Université de Valenciennes et du Hainaut-Cambrésis

Thèse de doctorat

Pour obtenir le grade de Docteur de l'Université de

VALENCIENNES ET DU HAINAUT-CAMBRESIS

Discipline, spécialité selon la liste des spécialités pour lesquelles l'Ecole Doctorale est accréditée:

Mécanique - Energétique

Soutenance prévue par Maryam PARSA

Le 11/12/2017, à VALENCIENNES

Ecole doctorale :

Sciences Pour l'Ingénieur (SPI)

Equipe de recherche, Laboratoire :

Laboratoire d'Automatique, de Mécanique et d'Informatique Industrielles et Humaines (LAMIH UMR CNRS 8201)

Mouillage et Évaporation de Gouttelettes de Nanosuspensions

JURY

Président du jury
- GRADECK, Michel. Professeur. LEMTA, Université de Lorraine.

Rapporteurs
- PONCET, Sébastien. Professeur. Université de Sherbrooke.
- PLOURABOUÉ, Franck. Professeur. IMFT, Université de Toulouse.

Examinateurs
- BIGERELLE, Maxence. Professeur. LAMIH, Université de Valenciennes.

Directrice de thèse
- HARMAND, Souad. Professeur. LAMIH, Université de Valenciennes.

Co-directeur de thèse
- SEFIANE, Khellil. Professeur. IMT, Université d'Édimbourg.

Membre invité
- DIEMUNSCH, Guy. Expert Thermique. Institut VEDECOM.

Acknowledgements

I would like to acknowledge all the people who supported me throughout my PhD study.

First, I would like to thank my supervisors Prof. Souad Harmand and Prof. Khellil Sefiane for their guidance during this research. Furthermore, I thank the VEDECOM Institute and LAMIH laboratory from which I received funding for my PhD study.

I truly thank Prof. Maxence Bigerelle and Dr. Raphaël Deltombe for their fruitful collaboration. Dr. Riadh Boubaker should also be acknowledged for his contribution, which can be seen in Chapter 4. Special thanks are reserved to our technicians, Mr. Jesse Schiffler, Dr. Marc Lippert, Mr. Jean-Michel Dailliet, and Mr. Herve Walkowiak. All of these people truly made an enormous contribution to my research.

I am grateful to many people from the University of Valenciennes for their insights and support in varying matters. I extend special thanks to the current and previous members of the LAMIH. Among them, I should mention Marie, Sabine, Celine, Fethi, Damien, Federico, Pin, Hiba, and Mira. Also, special thanks to Camila, Tariq and the other members of the “Los Amigos” collective for those afternoons and non-work-related moments. I apologise to those who are not named here.

In addition, I met many kind people during my stay in Valenciennes. I should thank Mr. Patrick Marechal and his family and Prof. Nicole Bringel for their friendly companionship. To Patrick and his family: thank you for those weekends and your kind help.

I am also deeply grateful to my friends with whom I shared the pain and pleasure of living abroad and conducting research. To Naghmeh, Faeghe, Neda, and Sofia, although you had your own difficulties, thank you for your insight, help, and continuous support during those dark years.

My deepest gratitude must go to my lovely family for their unconditional support and love despite the distance stands between us. I would like to specially thank my

parents, Fatemeh Nikkhah Khajehataei and Mohammad Parsa, my sisters Farkhondeh and Fariba, and my brother Salahaddin. To my mother: I can never thank you enough for your endless patience.

Maria

Contents

List of Publications

Peer-Reviewed Journals

Parsa, M., S. Harmand, K. Sefiane, M. Bigerelle and R. Deltombe,

Effect of Substrate Temperature on Pattern Formation of Bidispersed Particles from Volatile Drops.

The Journal of Physical Chemistry B **2017** *121* (48), 11002-11017.

Parsa, M., R. Boubaker, S. Harmand, K. Sefiane, M. Bigerelle and R. Deltombe,

Patterns from Dried Water-Butanol Binary-based Nanofluid Drops.

Journal of Nanoparticle Research **2017** *19* (8), 268.

Parsa, M., S. Harmand, K. Sefiane, M. Bigerelle and R. Deltombe,

Effect of Substrate Temperature on Pattern Formation of Nanoparticles from Volatile Drops.

Langmuir **2015** *31* (11), 3354-3367.

Conferences, Workshops and Meetings

Parsa, M., S. Harmand, K. Sefiane, M. Bigerelle and R. Deltombe,

Nanofluids: From Energetics to Microfluidics for Biology (Presentation)

*1st Bio2Val Workshop: Biomechanics and Biomaterial in Valenciennes, University of Valenciennes, Valenciennes, France, 11th June **2016**.*

Parsa, M., S. Harmand, K. Sefiane, M Bigerelle,

"Evaporation of Binary Mixture Nanofluid Drops: Pattern Formation."

*Biotech, Biomaterials and Biomedical TechConnect Brief: Micro, Nano & Bio Fluidics Chapter 6: Volume 3, Pages 196-197. 10th Annual TechConnect World Innovation Conference, Washington, United States, 22nd-25th May **2016**.*

Parsa, M.,

My thesis in 180 seconds. (Presentation)

*3rd Research Meeting of the VEDCOM Institute, Versailles Saint-Quentin-en-Yvelines University, Versailles, France, 23rd June **2015.***

Parsa, M.,

My thesis in 180 seconds. (Poster)

*3rd Research Meeting of the VEDCOM Institute, Versailles Saint-Quentin-en-Yvelines University, Versailles, France, 23rd June **2015**.*

Parsa, M., S. Harmand, K. Sefiane,

My thesis in First Year (Presentation)

*7th Doctoral Meeting of Mechanical, Civil, Energy and Materials Engineering of the EDSPI (the Doctoral School of Engineering Sciences of the University of Lille Nord de France), Lille University of Science and Technology, Villeneuve d'Ascq, France, 24th June **2014**.*

Parsa, M., S. Harmand, K. Sefiane,

Role of Drop Evaporation in Heat Transfer (Presentation)

*2nd Doctoral and Postdoctoral Meeting of the VEDECOM Institute, Versailles Saint-Quentin-en-Yvelines University, Versailles, France, 30rd April **2014**.*

Parsa, M., S. Harmand, K. Sefiane,

Role of Drop Evaporation in Heat Transfer (Poster)

*2nd Doctoral and Postdoctoral Meeting of the VEDECOM Institute, Versailles Saint-Quentin-en-Yvelines University, Versailles, France, 30rd April **2014**.*

Parsa, M., S. Harmand, K. Sefiane,

Enhancement of heat pipe performances using nanofluids (Poster)

*6th Doctoral Meeting of Mechanical, Civil, Energy and Materials Engineering of the EDSPI (the Doctoral School of Engineering Sciences of the University of Lille Nord de France), Lille University of Science and Technology, Villeneuve d'Ascq, France, 28th June **2013**.*

Parsa, M., S. Harmand, K. Sefiane,

Enhancement of heat pipe performances using nanofluids (Presentation)

*1st Doctoral and Postdoctoral Meeting of the VEDECOM Institute, the VEDECOM Institute, Versailles, France, 17th April **2013**.*

List of Figures

Chapter 1 Introduction

A part of this chapter is based on a manuscript submitted for publication in 2017. The author of this thesis wrote the manuscript. Prof. S. Harmand and Prof. K. Sefiane supported the author in writing the manuscript and granted approval for the final version.

1.1 Background

Wetting is an omnipresent, fundamental physical phenomenon in our daily life and refers to the study of intermolecular interactions between contacting liquid and solid. The phenomenon was likely first recognised by the Italian polymath Galileo Galilei (1564-1642) in 1612 who commented on spreading and wetting after the observation of a thin, dense flat solid floating on water while the free surface level of water was above the top of the solid [1,2]. When a liquid makes contact with a solid surface, an evolution in the liquid profile occurs until thermodynamic equilibrium between the three phases of liquid, solid, and vapour is reached at the three-phase contact line where the phases intersect each other. This equilibrium refers to the balance between the interactions at the interfaces of solid-liquid, solid-vapour, and liquid-vapour. In 1805, about two centuries after Galilei recorded his significant observation, one of the most famous figures in scientific research on wetting, Thomas Young (1773-1829), related the interface force balances at the contact line to the observed contact angle adopted between the liquid and solid phases [3]. Galilei did not understand the concept of surface tension at his time and as such was unable to measure the contact angle between the solid and liquid phases. Thus, his argument on wetting remained incomplete until Young introduced his famous explanation of the relation between contact angle and interfacial forces in the work titled *"An essay on the cohesion of fluids"* [1,3]. Since then, many researchers have attempted to further understand the mechanisms related to phenomena such as wetting and dewetting. For example, Dussan [4] and de Gennes [5] contributed extensively to the description of the static

and dynamics of the contact line, triggering further research for many practical applications such as microfluidics [6], polymers [7], lithography [8], and self-cleaning surfaces [9].

It has been established that having a solid-liquid-vapour system, such as a liquid drop deposited on a solid substrate, in equilibrium state is rare because fluid sensitivity to variations in environmental conditions, i.e., pressure, temperature, leads to the transition from one phase to another. Phase change is a process in which molecules of a certain phase (solid, liquid, or vapour) lose or gain enough energy to shift into another phase. Evaporation is a type of phase change whereby liquid molecules near the air-liquid interface have sufficient energy to transition from liquid phase to gas phase. At the same time, the atmosphere around the drop surface should not be saturated with the vapour of the liquid.

Drop evaporation phenomenologically may seem a rather simple problem. However, from a scientific perspective, it is a complex issue and has been an important topic to research communities for more than a century. The earliest investigation into the evaporation of micrometre-sized droplets was reported by Gudris and Kulikowa in 1924 [10]. Almost four decades later in 1962, Mangel and Baer [11] were the first to study the evaporation of sessile droplets on solid surfaces. Since then, the effect of various parameters, including ambient conditions, substrate properties and roughness, on these volatile sessile droplets has been extensively explored. The evolution of droplet profiles and dynamics of the contact line are dependent on these parameters. The nature and characteristics of the flow structure inside the evaporating droplets can also be influenced by these parameters. Continuity and Marangoni flows are commonly observed flows within the evaporating droplets. The former is mainly an outward flow towards the contact line induced by mass conservation. However, the latter is driven by non-uniform variation of surface tension along the air-liquid interface of the droplet. In 1855, physicist James Thomson (1822-1892) was the first to correctly explain the “tears of wine” phenomenon [12], which accounts for the tear-like droplets moving down a wineglass above the wine’s surface. Thomson argued that the spontaneous motion on

the wine's surface is due to surface tension gradients arising from non-uniform evaporation of alcohol [12]. As alcohol has a lower surface tension and higher volatility than water, the evaporation of alcohol results in local concentration gradients on the liquid-free surface. This process causes a surface tension gradient, prompting the liquid to move upward on the glass and form a thin film. Eventually, this liquid film converges to tear-like droplets that roll down into the bulk of wine along the glass. Although Thomson's publication was published first, this phenomenon was named after Italian physicist Carlo Giuseppe Matteo Marangoni (1840-1925) for his doctorate thesis titled *"On the spreading of liquid droplets".* In this publication, Marangoni reported that surface tension gradients can not only result from variations in chemical composition but also from temperature [13]. The Marangoni effect, i.e., that this phenomenon is driven only by a temperature gradient, is generally known as the thermocapillary effect.

Another topic that has attracted great interest amongst researchers in the past two decades is the evaporation of sessile droplets containing insoluble particles. The pioneering works of Deegan and colleagues [14–16] has demonstrated that particles can be moved towards the pinned contact line due to a convective outward flow and thus deposited at the droplet edge, forming a ring-like deposition pattern. This phenomenon is known as the "coffee-ring" effect. Following these pioneering publications, the evaporation of colloidal sessile droplets to control the morphology of deposition patterns left behind has been the subject of numerous studies for varying scientific and industrial applications [17,18]. The studies investigating the drying of colloidal suspension droplets have revealed that there are different mechanisms behind the final particles' distribution including the dynamics of the inner flow, evaporation kinetics, dynamics of the contact line, evolution of the droplet profile, and interparticle and interfacial interactions. These mechanisms that may lead to the formation of particular deposition patterns can be modified and controlled by manipulating of a series of factors such as solute (e.g., size, concentration) [19,20], base fluid composition (e.g., surfactant) [21–24], environmental conditions (e.g., temperature, pressure) [25,26], etc. Therefore,

understanding the effects of the aforementioned factors is critical for both the control and reproducibility of the deposition patterns [17,18].

In addition to these findings, another topic of interest is the evaporation of sessile droplets of complex fluids such as nanofluids, polymer suspensions, and biological fluids. The first study examining the dried patterns of biological fluids was conducted in the former Soviet Union about three decades ago [27]. Interestingly, it was later found that drying of the urine droplets of patients with urolithiasis would form a distinct pattern [28]. After these observations, the Ministry of Health of Russia developed the so-called “Litos” test system, which provides a preclinical diagnosis of urolithiasis [29]. In recent years, researchers have closely studied the pattern formation of biofluids (e.g., blood, tears, serum), which can be used as fast and cost-effective tools for the diagnosis of certain diseases [30–35]. Studying biofluid droplets is complicated as they consist of various components (e.g., electrolytes, proteins) that can interact and thus influence the underlying mechanisms involved in pattern formation [17]. Polymer solutions are also complex fluids, i.e., non-Newtonian fluids, and the mechanisms underpinning evaporation are not well understood [17]. Polymers play an important role in the study of droplet evaporation. For example, they are often added to the base fluids to modify the pattern formation for inkjet printing applications. A novel type of complex fluids are nanofluids, which arise from the dispersion of metallic or non-metallic particles with at least one dimension in the nanoscale (< 100 nm) into a base fluid [36]. Since 1995, the number of studies examining the evaporation of nanofluids has been rapidly increasing due to the range of applications for cooling electronics [37], boiling [38], solar energy [39], medicine [40], and the automotive industry [41]. Although myriad studies have investigated the applicability of nanofluids, a comprehensive understanding of the mechanisms underpinning the drying of nanofluid droplets and their pattern formation remains elusive.

1.2 Overall Aims and Specific Objectives

The rapidly increasing number of studies on particulate deposition of droplets is due to the fast-growing demand for its applications in fields such as inkjet printing [42–44], paints, nanotechnology [45], and biomedicine [30,46,47]. Despite the importance of controlling deposition patterns and the numerous published studies on the topic, the mechanisms behind the deposition morphology of droplets are also not yet fully understood [17]. Drying of even pure sessile droplets is a complex and difficult-to-control phenomenon and thus, much research on the drying of droplets from complex fluids is required.

The overall aim of this experimental research is to link the materials science, physics, chemistry, and engineering fields by assembling various techniques and methods to address problems that remain. Optical microscopy, infrared thermography, and white light interferometry techniques are widely used and their advantages to these fields are established. This thesis focuses on the effects several factors have on the pattern formation of drying sessile droplets from complex fluids including nanofluids and polymer solutions. Specifically, these factors are substrate temperature, composition of the base fluid, and the size of the particles. To determine how these factors affect the final patterns and mechanisms involved in the formation of those patterns, the flow structure and deposition of particles inside drying droplets are analysed by using a combination of the aforementioned techniques.

1.3 Outline of this Thesis

This thesis is organised into six chapters. The first and second chapters present scientific background and a review of other researchers' work to introduce the concepts discussed in this thesis. The structure of Chapter 2 is as follows: first, an introduction to the fundamentals of the wetting phenomenon, which is closely involved with the evaporation of sessile droplets, is provided; and second, the evaporation modes of drying droplets and the most important internal flow fields are described. Furthermore, Chapter 2 introduces the most common deposition patterns

left behind on solid substrates after the full evaporation of sessile colloidal droplets. Finally, the effects of several important factors on pattern formation and significant findings are explained. The subsequent chapters present the results obtained from the present research.

Chapter 3 details the investigation into the effects of substrate temperature on the deposition pattern of nanoparticles left after evaporation of water-based nanofluid droplets. Using different techniques, the dynamics of the contact line, movement of nanoparticles, and thermal flow patterns are studied to define the underlying mechanisms of the final deposition patterns.

Chapter 4 explains how the study in the previous chapter is extended to a different base fluid by adding butanol. The underlying mechanisms located using the same techniques as detailed in Chapter 3 are also discussed.

Chapter 5 explains the study investigating the effect of substrate temperature on pattern formation of two differently sized micro-particles from evaporating water-based droplets. In addition, the separation of micro-particles based on size near the droplets' edge is investigated using the techniques detailed in Chapters 3 and 4.

Chapter 6 presents the conclusions of the experimental work performed in the present research. Furthermore, some perspectives are suggested for future work. This experimental study applies current state-of-the-art infrared thermography, optical microscopy, and white light interferometry techniques to the formation of deposition patterns.

Chapter 2 Literature Review

This chapter is based on a manuscript submitted for publication in 2017. The author wrote the manuscript with the support of Prof. S. Harmand and Prof. K. Sefiane, who also granted approval for the final version.

2.1 Wetting and Droplets

Wetting is a ubiquitous phenomenon in nature and technology, and is defined as the ability of a liquid to spread/wet either a solid surface or immiscible liquid. The phenomenon is an area where physics, chemistry, and engineering intersect [48]. Researchers have studied the origins of wetting for hundreds of years [49]. Many of the studies conducted in the last 100 years have assumed it is controlled by the molecular interactions within the interfacial contact area between the liquid and solid [49]. However, there are now abundant studies showing that the phenomenon is determined by the interactions of the liquid and solid in the vicinity of the three-phase contact line (or the triple line) alone [49]. From the nanoscopic perspective, the contact line is the three-dimensional space where the solid-liquid interface meets the liquid-vapour interface (Figure 2.1) [49]. In other words, the molecules of the liquid, solid, and vapour phases interact with each other at the contact line.

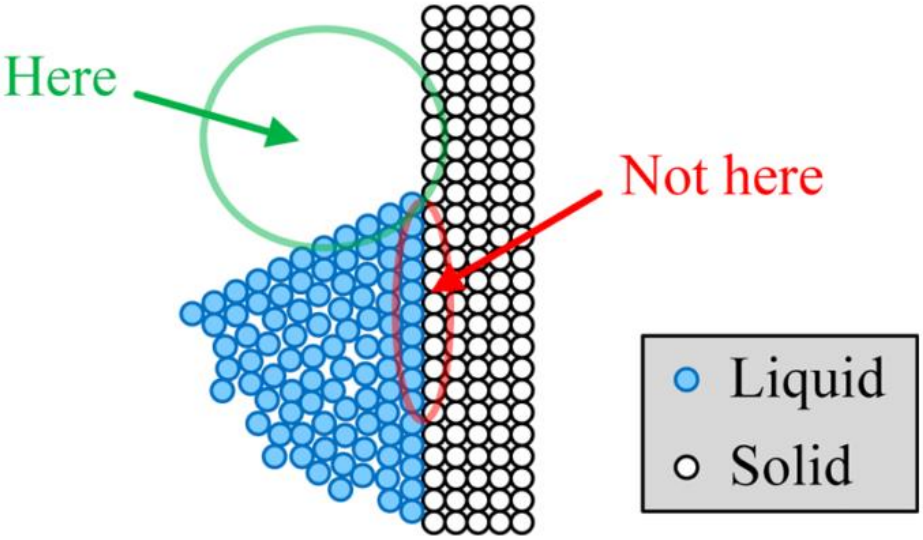

Figure 2.1 Contact line as a three-dimensional space composed of solid and liquid molecules. Image taken from Ref. [49].

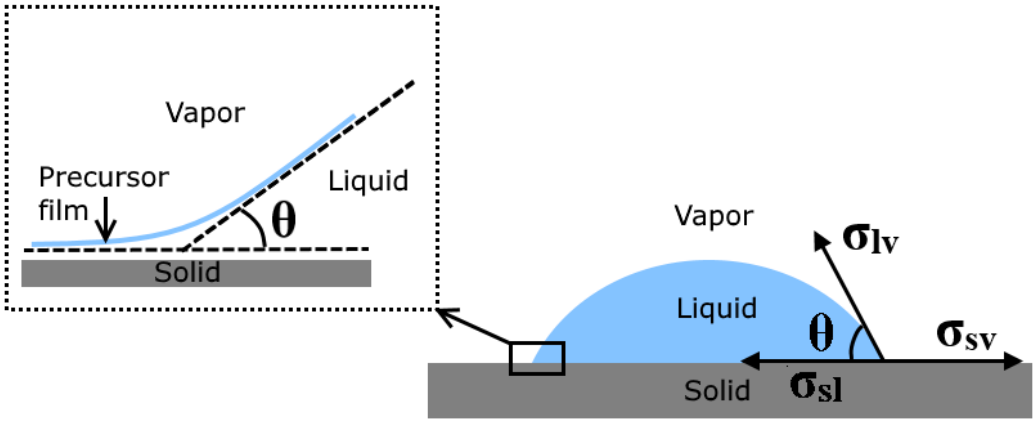

Figure 2.2 A droplet on a solid surface with three interfaces: liquid-vapour, solid-liquid, and solid-vapour. The shape of the droplet is determined by the apparent contact angle (θ). The contact line (here in the solid rectangle) is located at the intersection of the three phases. Inset: The precursor thin liquid film with micro- to nano-meter length is at the front of the macroscopic contact line. The thickness of the film varies from 10 to 100 nm.

When a liquid droplet is deposited on a solid substrate, three main boundaries can be macroscopically seen: a solid (the substrate), a liquid (the solvent), and a vapour phase (the surrounding air) (Figure 2.2). The contact line is created at the droplet's

edge where the three phases of liquid, vapour, and solid meet, as shown in Figure 2.2. Therefore, there are three interfacial tensions between each two phases: liquid-vapour (σ_{lv}), solid-liquid (σ_{sl}), and solid-vapour (σ_{sv}). Immediately after a droplet is gently deposited on an ideal, flat, smooth, and homogenous substrate, it spreads on the substrate due to the interactions of adhesive and cohesive forces. Then, when the three phases reach a thermodynamic equilibrium, the droplet stops spreading on the substrate and forms an equilibrium contact angle. The contact angle (θ) is the tangent of the droplet profile at the contact line, and it quantifies the extent to which the liquid is wetting the solid substrate. In 1805, Young was the first to express the relation between the equilibrium contact angle and the three interfacial tensions in words without proof [3]. Later, in 1869, Dupré described Young's statement mathematically in his work, which is widely known as Young's equation [50]:

$$\sigma_{sv} = \sigma_{sl} + \sigma_{lv} \times \cos\theta \tag{1.1}$$

According to Young's equation, there are three different possible wetting states, as shown in Figure 2.3. First, the liquid partially wets the surface if the contact angle is less than 90° (Figure 2.3b). Second, if the contact angle is zero, the liquid completely wets the surface; this is known as the perfect wetting state (Figure 2.3a). In contrast, if the contact angle is above 90°, the third state, non-wetting or bad wetting, is assumed (Figure 2.3c).

Young's equation is valid only for the system that meets the ideal conditions where the solid surfaces are flat, rigid, and chemically homogenous at an atomic scale [2]. If the solid surface is not truly homogenous, hysteresis of the contact angle occurs, and this angle (θ) lies between an advancing (θ_a) and receding (θ_r) contact angle. Thus, on practical surfaces, contact angle hysteresis (CAH) can be defined as the difference between the advancing and receding contact angles:

$$\text{CAH} \equiv \theta_a - \theta_r \tag{1.2}$$

The value of CAH ranges from 10° to larger. Sometimes, a value of 50° or more has been reported [2].

From the microscopic point of view, there is a very thin liquid film in front of the contact line of drops on substrates (inset in Figure 2.2), which can influence the contact angles [51]. Moreover, real solid surfaces are seldom truly smooth, and the actual (or microscopic) contact angle has not been experimentally observed [52]. Thus, the shape of a droplet on a real solid surface is determined with the apparent (or macroscopic) contact angle (Figure 2.2). The value of the contact angle is indicative of the wettability of the solid surface. A surface can be regarded as hydrophobic (with low wettability) when the contact angle is higher than 90°, or as hydrophilic (with high wettability) when the contact angle is below 90°.

Based on the above discussion, the nature of the interfacial interactions is of high importance as they affect wetting, and these parameters play a crucial role in many industrial applications such as oil recovery, inkjet printing, painting, and thin film coatings [53–56].

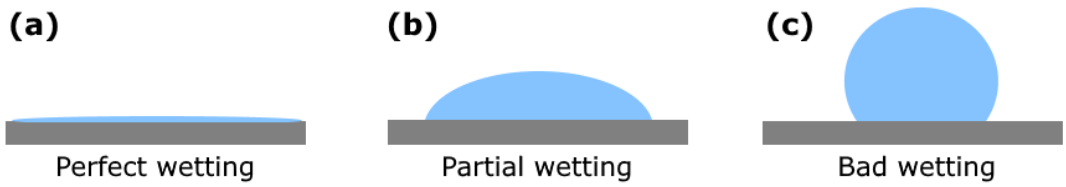

Figure 2.3 The wetting states of a droplet on ideal substrates: (a) Perfect wetting occurs when a contact angle approximates zero. (b) Partial wetting with a contact angle smaller than 90°. (c) Bad wetting or non-wetting is shown with a contact angle equal to or higher than 90°.

2.2 Sessile Droplet Evaporation

A sessile droplet is a liquid droplet that is placed on a solid substrate where its contact line limits the wetted contact area between the liquid and the solid surface; it is characterised by droplet height (H), radius (R), and contact angle (θ). The droplet evaporates if the atmosphere around its interface is not saturated with the vapour of the solvent. Evaporation of sessile droplets is an important topic of interest for many applications such as micro-electronic cooling [57], medical diagnostic techniques [30,46], nanotechnology [45], painting, and printing [42–44], among others. Thus, it

has attracted the attention of researchers and has led to a rapid increase in the number of publications on the topic since the 1980s.

2.2.1 Evaporation modes

Evaporation of sessile droplets tends to show four modes, all of which are depicted in Figure 2.4. These four evaporation modes are [58]:

i. The constant contact radius (CCR) mode, where the contact line is pinned and the contact radius and the wetted contact area between the droplet and substrate remain constant, whereas the contact angle decreases with time (Figure 2.4a). There is a linear evolution of volume loss with time, revealing a constant evaporation rate for the CCR mode [59–61]. This mode is often seen with sessile droplets on rough substrates.
ii. The constant contact angle (CCA) mode, where the wetted contact area shrinks and the contact angle remains unchanged, leading to a non-linear decrease of volume with time (Figure 2.4b) [62,63]. On smooth hydrophobic substrates, droplet evaporation is typically in the CCA mode.
iii. The mixed mode, where the evaporation mode gradually changes into another mode (Figure 2.4c) and sometimes both the radius and contact angle decrease simultaneously [58,64]. One of the most reported behaviours is the transition from CCR to CCA (Figure 2.4c) [58].

The “stick-slip” mode, where the droplet is in the CCR mode (corresponding to a “stick” phase), but the contact line suddenly slips/depins into a new position, leading to a smaller contact radius when the contact angle reaches a threshold, minimum value (corresponding to a “slip” phase). Then, the droplet is again in the CCR mode (“stick” phase) until the next depinning occurs. This pinning/stick and depinning/slip of the contact line may occur several times until the evaporation is complete (Figure 2.4d). The stick phase lasts longer and accounts for the majority of the droplet lifetime, whereas the slip phase occurs rapidly. In 1995, Shanahan introduced a simple theory for the stick-slip evaporation mode [65]. According to Shanahan [65] and colleagues [25,66,67], when a sessile droplet is in a thermodynamic equilibrium,

the free surface/interfacial energies of the system are at their minimum level. The decrease in the contact angle of the pinned droplet leads to an increase in this free energy above an energy barrier [25,67]. The pinning effect is also attributed to a potential energy barrier. When the excess free energy attains the energy barrier at a critical contact angle, the system has sufficient energy to overcome the energy barrier. Hence, the contact line slips to a new equilibrium position to dissipate the excess free energy [25,67]. The droplet evaporation may proceed with the successive repetition of this cycle of the stick and slip phases.

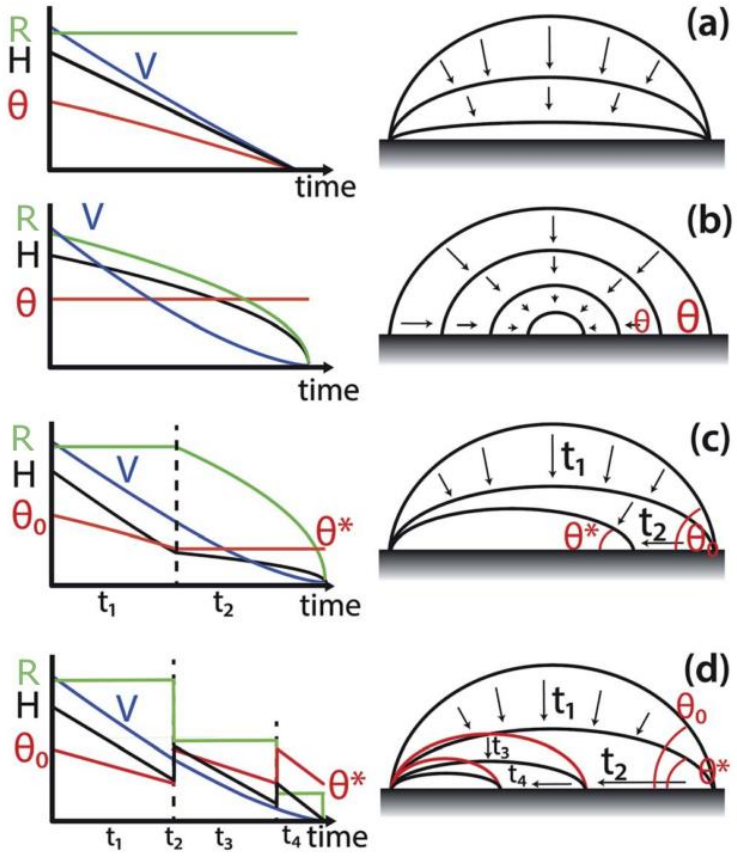

Figure 2.4 Schematic of the four possible evaporation modes of a sessile droplet: (a) constant contact radius mode (CCR); (b) constant contact angle mode (CCA); (c) mixed mode; and (d) stick-slip mode. The graphs show the evolution of the droplet profile (volume (*V*), height (*H*), contact radius (*R*), and contact angle (θ)) with time. Image modified from Ref. [58].

2.2.2 Flow fields within a drying droplet

The study of the effects of different flow fields within an evaporating sessile droplet is an important area in this research field. The capillary and Marangoni flows are two important flows commonly observed inside drying sessile droplets.

Once the contact line of a droplet is pinned on the solid surface, the fluid flows radially from the central region of the droplet towards the droplet edge due to the enhanced evaporation rate at the contact line. This radially outward flow replenishes the evaporated liquid at the edge, known as the capillary flow (Figure 2.5a) [14,68,69]. Within this particular flow field, the evaporating droplet usually follows CCR, where the radius is constant and the contact angle decreases [17,18,52].

The Marangoni flow is driven by the surface tension gradient along the free surface of the droplet [70]. This surface tension gradient is induced by the non-monotonous distribution of local temperature [70,71] and/or concentration along the liquid-vapour interface [21,68,70]. Usually, the flow is called the thermocapillary flow (or thermal Marangoni) in the case of the temperature gradient, and solutal Marangoni in the case of the concentration gradient. In an evaporating droplet, the liquid tends to flow from lower surface tension regions towards higher surface tension regions, creating Marangoni convection (Figure 2.5b). Therefore, the direction of the Marangoni flow can change depending on how the surface tension is distributed along the interface. Kim et al. [72] showed that the direction of the Marangoni flow can be changed within a water droplet containing polymers by controlling the substrate temperature. In the case of heated substrates, the temperature at the edge is higher than that at the apex, and the evaporation is enhanced at the edge, leading to the non-uniformity of the evaporation rate along the interface. As the surface tension of water decreases with increasing temperature, the liquid flows from the edge towards the top of the droplet along the interface (Figure 2.6a) [72]. Conversely, cooled substrates generate the Marangoni flow in the opposite direction (Figure 2.6b) [72].

The co-occurrence of the capillary and Marangoni flows inside the droplets is possible when the solvent evaporation causes a thermodynamic and/or hydrodynamic instability [26,73]. Kim et al. [72] found that the capillary flow is stronger than the

Marangoni flow when the substrate is heated, whereas the opposite is true in the case of cooled substrates.

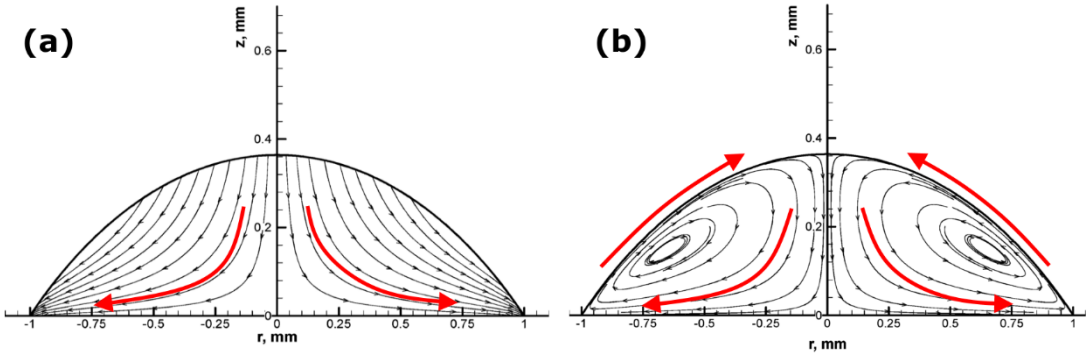

Figure 2.5 Streamline plots of the flow field within a drying water droplet. (a) Capillary flow without Marangoni flow; Image modified from Ref. [69]. (b) With Marangoni flow. The arrows indicate the direction of the flows. Image modified from Ref. [70].

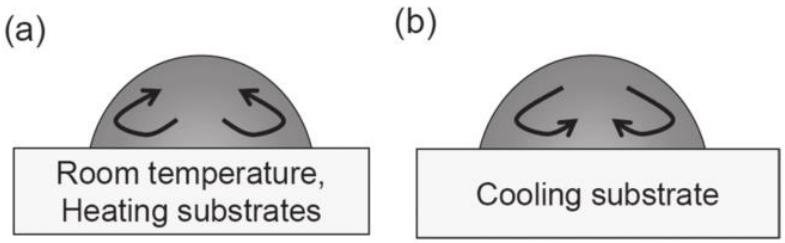

Figure 2.6 Schematic representation of the direction of the Marangoni flow inside drying water droplets: (a) drying droplet at room temperature and heating substrate; (b) drying droplet on cooling substrate. Image taken from Ref. [72].

2.3 Dried Patterns Formed by Particles on the Substrate

Drying liquid that contains non-volatile solutes is ubiquitous in daily life and nature, such as tea/coffee stains on solid surfaces, or rings of dust particles from dried rain drops on windows. The drying of sessile droplets with suspended particles forms various deposit patterns on solid surfaces. These interesting and complex patterns have a significant influence in many applications such as biology [30,46,74],

complex assembly [44], printing [42,75], and nanotechnology [45], among others. Numerous studies have been published over the past decades to improve the understanding and controlling of the deposition morphologies [17,18,52]. Macroscopic effects such as internal flow structure [15,76–78] and dynamics of the contact line [66,75,79,80], and microscopic effects such as particle-interface/particle-particle interaction [81–83] significantly affect the morphologies of the final deposits. The best-known deposit patterns are described in the following subsections.

2.3.1 Coffee-ring pattern

When a droplet of coffee completely evaporates on a solid surface, it leaves behind a ring-like deposit, known as the coffee-ring pattern (see Figure 2.7). The related flow to this pattern is called the outward capillary flow. The geometrical constraint of the droplet behind this effect was explained in the pioneering work of Deegan and colleagues in 1997 [14]. They also studied the growth rate of the deposited ring, and the flow velocity and distribution of the particles inside the droplet [15]. During the formation of this pattern, the evaporating droplet is in the CCR mode, thus the droplet keeps its shape as a spherical cap. The height of the pinned droplet is decreased, and the flow is hence pushed outward by the free surface. As the droplet is in the CCR mode and the radius is constant, liquid evaporated at the contact line must be replaced by liquid from the bulk (i.e., the centre of the drop). Thus, an outward flow inside the pinned droplet carries suspended particles towards the edge, leading to deposition of the particles near the contact line (Figure 2.8a). After complete evaporation, a ring of concentrated particles can be seen at the perimeter of the droplet, forming the coffee-ring pattern (Figure 2.8a) [14,35]. Uno et al. [84] studied the dried deposit of droplets on hydrophilic substrates. They found that thin layers of particle aggregates were formed at the perimeter of the droplet (Figure 2.9) and thus hindered the decrease of the wetted contact area (self-pinning). The rapid evaporation at the upper side of the layer induced the adsorption of particles to the substrate in the layer, forming the coffee-ring pattern. Thus, according to these explanations, there are two prerequisites for the coffee-ring effect: one is the droplet pinning (CCR); and the other is the higher evaporation rate at the pinned contact line

than in the rest of the droplet. Later, Hu and Larson [76] demonstrated that the two conditions of the pinned contact line and continuous evaporation of liquid alone are not sufficient to form the coffee-ring pattern; the suppression of a Marangoni flow is also required. The authors found that some particles deposit at the central region of the droplet due to a recirculating Marangoni flow induced by the surface tension gradient resulting from the evaporation [76]. Therefore, the Marangoni flow should be either reduced or eliminated by manipulating some parameters (i.e., substrate temperature) to create the coffee-ring pattern. Furthermore, besides the aforementioned conditions, droplet size is also an important factor for creating the coffee-ring pattern [85]. Shen et al. [85] showed that a very rapid evaporation process inhibits a successful coffee-ring formation, as the suspended particles do not have sufficient time to reach and deposit at the edge. The authors experimentally demonstrated that a lower limit of droplet size exists for the coffee-ring pattern. For particle concentration above a critical value, the lower limit of the droplet size can be estimated by the competition between liquid evaporation and the diffusive particle motion inside the droplet. The authors found the minimum diameter of the droplet with the coffee-ring pattern to be approximately 10 nm for the particle size of 100 μm [85].

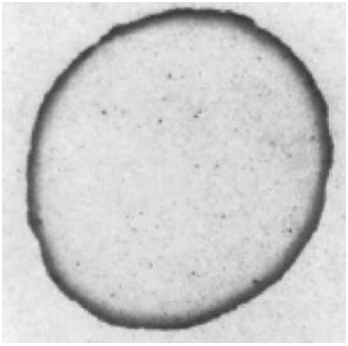

Figure 2.7 Stain left after the drying of a coffee drop following the CCR mode. Image modified from Ref. [16].

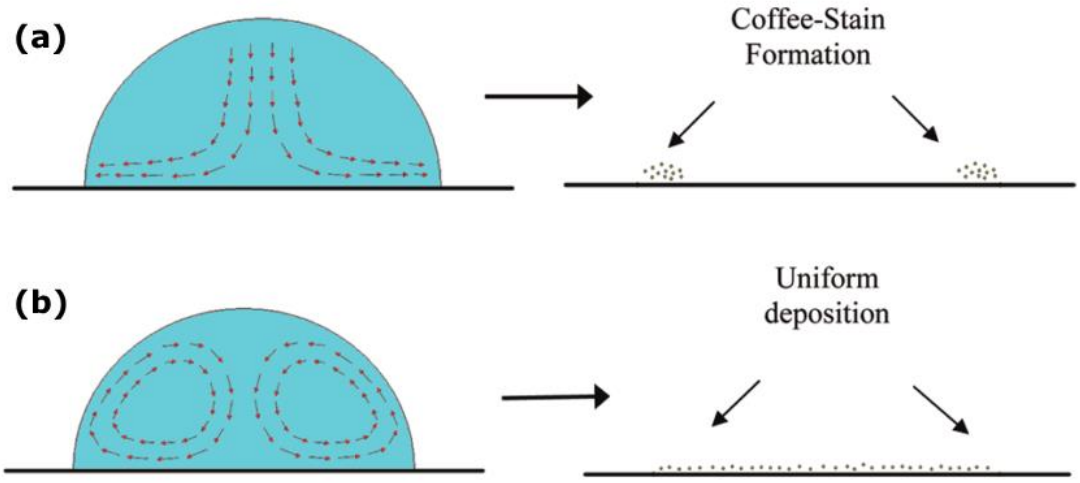

Figure 2.8 Evaporation of a colloidal drop under standard ambient conditions: (a) outward flow in a droplet creates a coffee-ring stain; (b) recirculating Marangoni flow creates a uniform pattern. Image taken from Ref. [77].

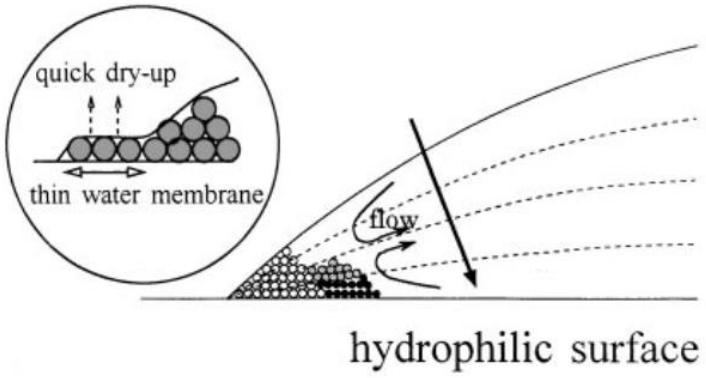

Figure 2.9 A schematic representation of particles' motion and pattern formation inside a drying droplet on a hydrophilic surface with CCR mode. Inset shows the magnification of the contact line. Image taken from Ref. [84].

2.3.2 Uniform pattern

Much attention has been devoted to altering the coffee-ring effect, as uniform deposition patterns are required in many research fields such as coating [86], inkjet printing [75], and biological assays [87]. However, such patterns are not easy to achieve due to the domination of the coffee-ring effect inside the droplet [87]. As mentioned in the previous section, the evaporation of droplets in CCR mode with

either the sufficient suppression or elimination of the Marangoni effect leads to the formation of the coffee-ring pattern. In the case of a high concentration of particles, a drying droplet in CCR (with the negligible Marangoni effect) may leave a ring-like pattern, but with a uniform distribution of particles in the region enclosed by the ring [88,89] (Figure 2.10). As an example, in Thokchom et al.'s [78] study, a monolayered, uniform nanoparticle structure was left behind after the dry-out of droplets on hydrophilic substrates in which the Marangoni effect was completely suppressed and the outward capillary flow dominated in the flow field. The concentration of nanoparticles was slightly higher than the theoretical concentration for filling the wetted contact area, inhibiting the coffee-ring effect.

The alteration of the internal flow may also form uniform patterns. Majumder et al. [77] showed that the recirculating Marangoni flow within a droplet on a hydrophilic substrate prevents particles from accumulating at the pinned edge and transports them towards the top of the droplet along the air-liquid interface (see Figure 2.8b). The Marangoni flow keeps the particle concentration homogenised, inhibiting the coffee-ring pattern and forming a uniform pattern instead (Figure 2.8b).

Uniform patterns can also be formed by controlling the evaporation kinetics and/or interactions inside the droplet (i.e., particle-particle, particle-substrate, and particle-liquid interactions) [82,83,90]. Bigioni et al. [82] reported the creation of a highly uniform, long-range-ordered compact monolayer of nanocrystals by enhancing the evaporation rate and attractive particles' interaction with the free interface of the droplet. Similarly, Li et al. [83] demonstrated that the sufficient enhancement of the evaporation rate leads to the accumulation of particles at the air-liquid interface instead of at the edge, thereby surpassing the coffee-ring effect. Those particles located at the interface deposit in the interior, and thus form a uniform deposition of particles in the interior with a thicker ring at the edge. In another study, Bhardwaj et al. [81] varied the solution pH to modify the particle-particle and particle-substrate interactions, which led to the alteration of the final deposit patterns. At a low pH value, particles in the vicinity of the substrate were attracted to it and formed a ring-like pattern with a uniform deposition of particles in the interior of the ring due to the

attractive particle-substrate interaction. At an intermediate pH value, the aggregation of particles was formed as the particle-substrate interaction was weaker than the particle-particle interaction. Aggregates randomly covered the entire initial wetted contact area. However, at a high pH value, the ring-like pattern was formed with almost no particles in the interior of the ring due to the strong repulsive particle-substrate interaction.

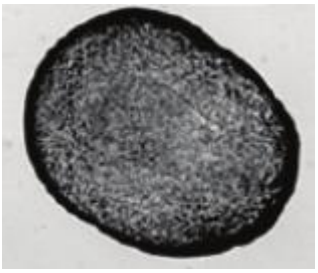

Figure 2.10 Uniform pattern with a thick outer ring. Image taken from Ref. [81].

2.3.3 Dot-like pattern

When a colloidal droplet follows the CCA mode while evaporating, a dot-like pattern can be found on the substrate after complete evaporation, as shown in Figure 2.11 [78,91]. Uno et al. [84] studied the pattern formation of evaporating drops in the CCA mode on hydrophobic surfaces. They reported that the shrinking of the contact line during the evaporation prevents particles from adsorbing onto the substrate at the early stages of the drying process. As evaporation proceeds, the concentration of particles increases, leading to the aggregation of particles. Then, the aggregates gather in the central region of the droplet and leave a random pattern of tiny spots after the dry-out. Similarly, other researchers have also observed such a dot-like pattern left in the centre of dried droplets that followed the CCA mode (see Figure 2.11) [79,88]. Thokchom et al. [78] attributed the formation of such patterns on hydrophobic surfaces to the dominant inward Marangoni flow capable of transporting particles to the central region during the drying process. The Marangoni flow becomes weaker as the contact angle decreases with time, and a radially outward flow is generated close to the substrate at the late stages of the evaporation.

However, the particle structures are already built within the droplet, and the outward flow is ineffective in transporting particles from the centre to the edge. Therefore, the dot-like pattern is formed on the substrate after the dry-out (Figure 2.11).

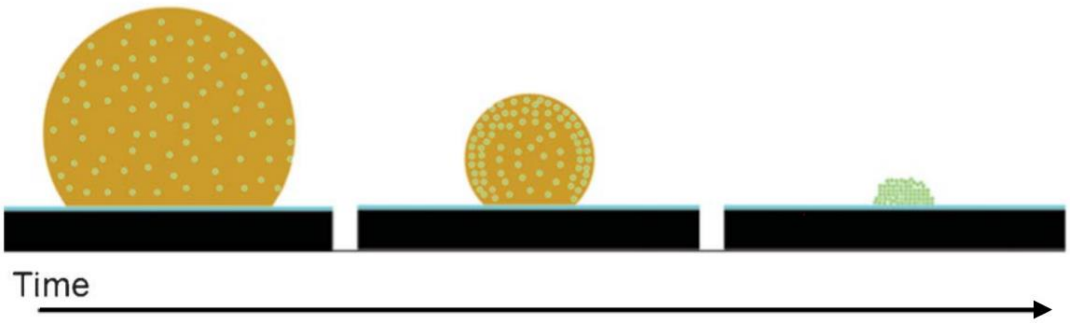

Figure 2.11 Evaporation of a droplet on a hydrophobic surface in the CCA mode leads to the dot-like pattern. Image modified from Ref. [91].

2.3.4 Stick-slip pattern

If a colloidal droplet evaporates following the stick-slip mode, a set of concentric rings are left on the substrate after complete evaporation [80], as shown in Figure 2.12a. During the stick phase of the stick-slip mode, particles accumulate at the contact line and form a ring. Then, the contact line slips to a new position, and particles form another ring. Consequently, the cycle of the stick and slip phases leads to the formation of multiple concentric rings of particles on the substrate. The contact line usually sticks and slips on one side of the droplet while remaining pinned on another side for all evaporation time, presumably due to the irregularities on the solid surface [88]. Unexpectedly, examination of the droplet profile has shown that the sticking of the contact line is not complete during the stick phase: there is a slight drift of the contact line, known as pseudo-pinning (see variation of the droplet radius over time in Figure 2.12b) [66,80,88,92]. Two explanations are proposed for this pseudo-pinning: one is the small-scale pinning of the contact line by the deposited particles; and the other is the increased local viscosity at the contact line by the higher concentration of particles [66,80,92]. Adachi et al. [93] formulated a mathematical model to explain the mechanism behind the oscillatory motion of the

contact line during the stick-slip mode, which leaves a striped pattern after complete drying. The contact line bears a friction force when the particles move from the centre to the edge. The competition between the friction force and surface tensions at the contact line results in the oscillatory motion of the contact line, forming the striped stain pattern. Hence, the pinning or depinning of the contact line is not important because the competition between the forces determines the behaviour of the contact line [18,93].

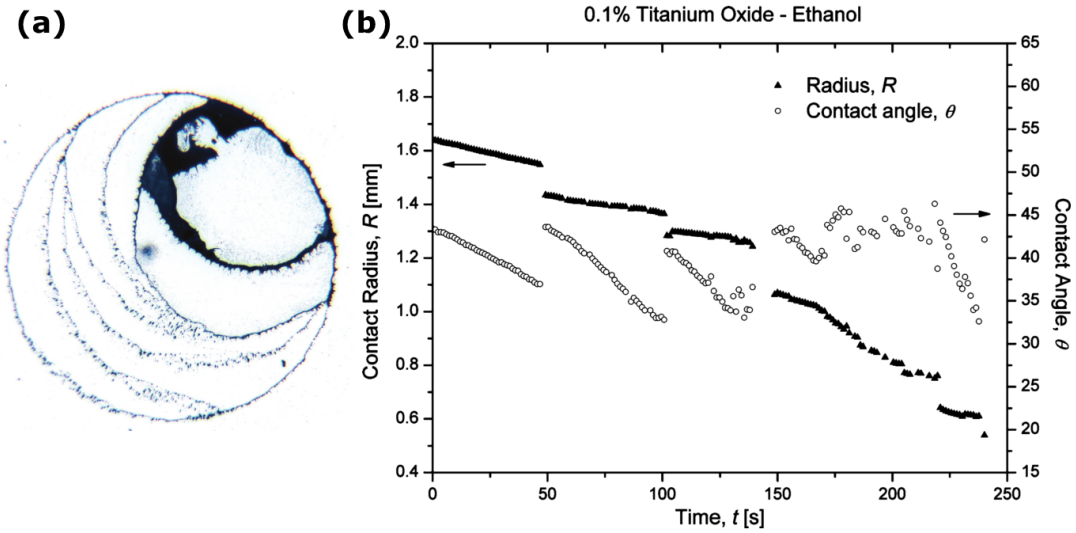

Figure 2.12 (a) Stick-slip pattern. Each ring of particles corresponds to the stick phase in the stick-slip mode. (b) Contact radius and contact angle versus evaporation time. Image modified from Ref. [80].

2.3.5 Fingering pattern

Besides the aforementioned pattern types, a fingering pattern has also been widely observed in many drop evaporation experiments [94–97]. When a thin film or a droplet spreads on a substrate, a pattern can be formed with fingering structures along the edge of the spreading film or droplet. The competition between the capillary effects and the force causing the spreading can result in a hydrodynamic instability, and consequently lead to the fingering phenomenon [98]. It is proved that the fingering instability is affected by the flow structures induced by temperature gradients [99], centrifugal forces [100], or gravity [101]. Weon and Je [102]

observed the fingering pattern inside the peripheral ring after the evaporation of a bidispersed colloidal drop, as shown in Figure 2.13. They attributed the formation of the pattern to the competition between the outward capillary flow and the inward Marangoni flow. In another study, Crivoi and Duan [97] reported the formation of both symmetrical and asymmetrical fingering patterns after the full drying of CuO water-based nanofluid droplets. They explained that the formation of the asymmetrical pattern could be due to the non-uniform evaporation rate or the movement of the contact line. Unexpectedly, a pinned droplet containing high concentrations of surfactants showed an outward fingering instability along the contact line [98]. The fluid was pushed outward in the fingering instability by local vortex cells arisen from both thermocapillary effects and the surfactant-induced Marangoni flow. As a result of this behaviour, the contact line was deformed and a finger protruded from the evaporating water droplet. This led to the collection of particles in the fingers of the droplet, as shown in Figure 2.14.

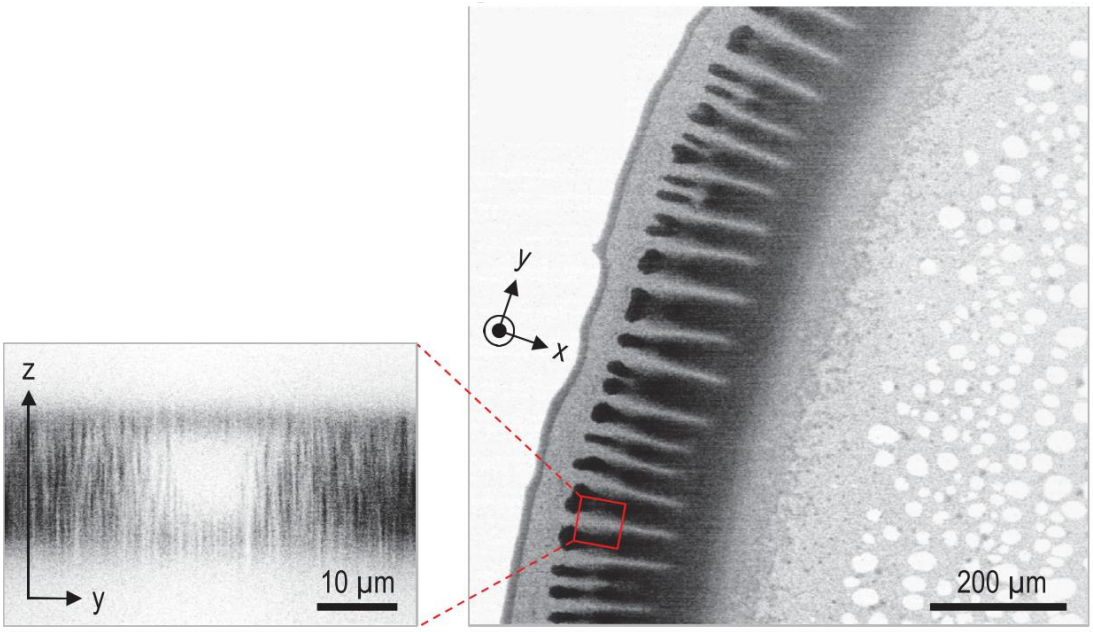

Figure 2.13 Fingering patterns inside the peripheral ring. Image taken from Ref. [102].

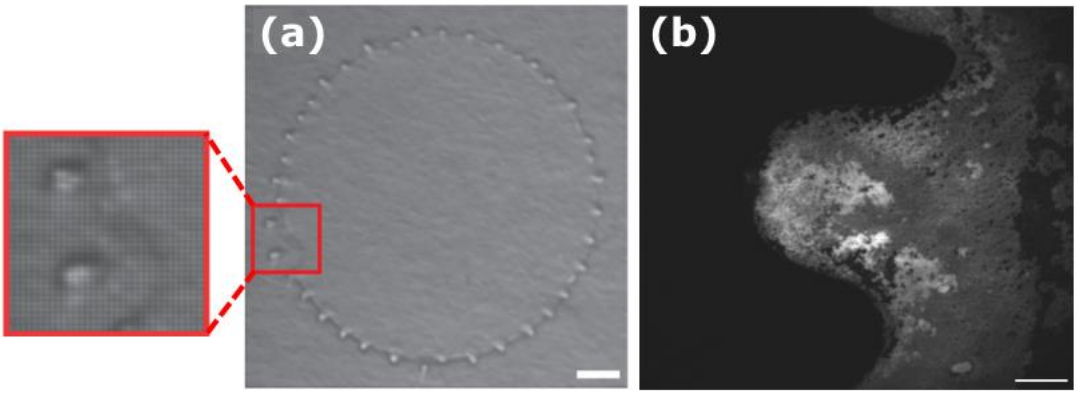

Figure 2.14 (a) Evaporating droplet fingering outward. (b) Particles in the fingers of the droplet. Image modified from Ref. [98].

2.3.6 Crack pattern

The investigation of cracking arising from desiccation of complex fluids is growing among scientific communities [31,33,35,47,52,103–107]. In one study, varying suspension salinity led to the formation of crack patterns with different morphologies after drying a colloidal drop on a flat surface (see Figure 2.15) [103]. At low salinities (Figure 2.15a), radial cracks were regularly formed at the drop edge, while a disordered crack pattern formed at intermediate salinities (Figure 2.15b,c). In contrast, at large salt contents (Figure 2.15d), a unique circular crack pattern was left after evaporation. These behaviours were explained by the drop shape evolution (Figures 2.15aI-dI). For intermediate salt content, the observed disordered crack pattern was related to the formation of a solid gelled skin (Figure 2.15bII), and also to the following buckling instability. Overall, the shape evolution of the drop affects the number and direction of the cracks [30]. The evolution of the drop shape depends on the salt content, thus the morphology of crack patterns is different for various salt contents [30,103]. Furthermore, crack patterns can be formed after drying of drops containing biological materials and fluids [31,33,35,47,104,107–109]. The higher evaporation rate at the edge of a droplet of blood plasma redistributes the suspended substances [52]. The accumulation of these substances at the edge region leads to the formation of a film (starting from the edge), which induces the gelation of the drying droplet. First, the drying starts from the edge, whereas the central region remains wet

[110]. The evaporation then induces the shrinkage of the droplet from the gelled edge, which causes a local stress. However, the adhesion of the droplet to the substrate constrains this shrinkage-induced local stress. As a result, an increased tensile stress in a drying drop is created by the competition between the adhesion to the substrate and the shrinkage [103,104]. Once the increased tensile stress exceeds the local tensile strength, cracks are formed on the surface of the film [52].

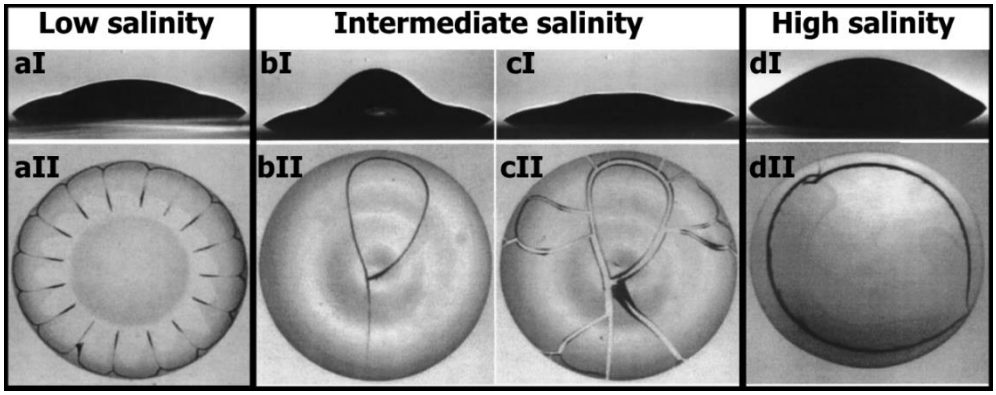

Figure 2.15 Influence of salt content on crack patterns from drying colloidal drops. (a) A regular radial crack pattern at low salinity. (b,c) A disordered crack pattern at intermediate salinity. (d) A circular crack pattern at high salinity. Side view of drops taken at: (aI) 15 min after deposition, (bI) 15 min after deposition, (cI) 20 min after deposition, and (dI) 15 min after deposition. Top view of drops taken at: (aII) 20 min after deposition, (bII) 20 min after deposition, (cII) 22 min after deposition, and (dII) 21 min after deposition. Image modified from Ref. [103].

2.3.7 Crystal pattern

Crystallisation is often observed in the central regions of dried droplets containing salts [111–113] (see Figure 2.16). For biological fluids containing salts, the combination of the two evaporation modes of CCR and CCA as drops dry contributes to the formation of salt crystallisation in the interior regions of a thick peripheral ring [30,114]. As an example, Gorr et al. [30] studied pattern formation from drying drops of aqueous lysozyme protein solutions with different NaCl concentrations. They reported that the early separation of protein from the fluid promoted an outward capillary flow during the CCR mode and hence formed the

thick outer ring. As evaporation proceeded, the salt remained in the fluid and crystallised while the drop experienced the CCA mode. Thus, a uniform layer of salt crystals was found in the centre of the dried drop. Some studies have reported that inorganic salts and the aggregation of macromolecular proteins are the main contributors to the formation of crystal patterns in the centre [114–116]. Some have posited that the increase in inorganic salt contents augments the aggregation of macromolecular proteins, thereby affecting the final morphology of crystal patterns [52,103,112]. However, another explanation for the formation of crystal patterns is that these patterns are the salt crystals in the gelled protein matrix, and proteins only have the role of seeds for the salt crystal growth [52,117,118]. All in all, the underlying mechanisms behind crystal patterns are not fully understood, as it is difficult to distinguish the main components of these patterns using current analytical techniques [52].

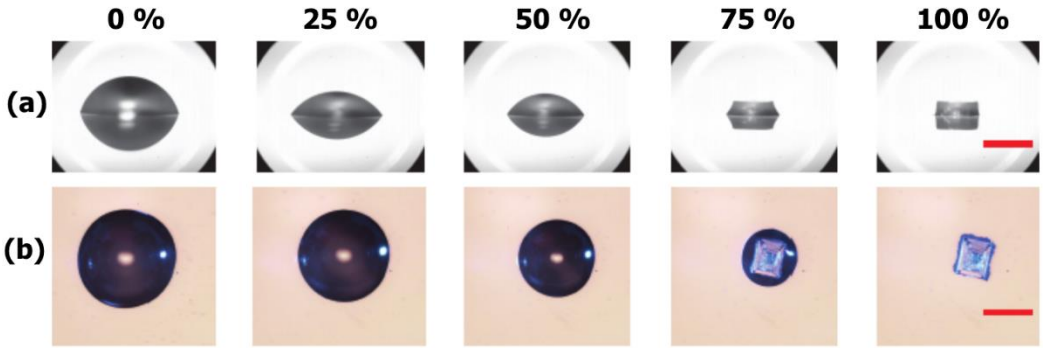

Figure 2.16 Lifetime of a saline droplet containing 10% salt: (a) side view and (b) top view. Scale bar, 1 mm. Image modified from Ref. [119].

2.3.8 Combined pattern

In some cases, a combination of two or more pattern types appears on a substrate. For example, Crivoi and Duan [120] reported the formation of the fingering pattern inside the coffee-ring after the complete evaporation of a water-based copper nanofluid droplet (Figure 2.17a). The authors found that the nucleation and growth process inside the peripheral ring results in the formation of this combined pattern. In another study, a combination of ring-like and dot-like patterns was observed after the

full evaporation of a drop containing a mixture of surface-inactive and surface-active solutes on a substrate with weak contact angle hysteresis, as shown in Figure 2.17b [121]. By analysing the drop shape evolution during the last stage of the evaporation, it was found that the contact line was pinned due to surfactant adsorption and this led to the ring-like pattern formation. Then, the depinning of the contact line started from a corner, and most parts of the contact line receded towards the part that was unpinned. Finally, the precipitation of surface-inactive solutes occurred close to the pinned part of the contact line, and led to the dot-like pattern formation inside the peripheral ring. In their work, Nguyen et al. [122] observed inner coffee-ring deposits (ICRDs) inside the initially pinned contact area of the dried water-based SiO_2 nanofluid droplets on smooth hydrophobic substrates (Figure 2.17c). In addition, they also found dendrite-shaped patterns inside ICRDs. Nguyen et al. explained the formation of the combined patterns by the late secondary pinning of the contact lines that occurred after the initial pinning. The balance of the forces on nanoparticles led to the secondary pinning. Furthermore, the authors found the size and patterns of ICRDs to be highly dependent on nanoparticle concentration, contact angle hysteresis, and nanoparticle interaction forces. Drying biofluid drops often form complex patterns that are combination of different deposition patterns. Figure 2.17d shows the dried pattern of blood serum from a healthy person; the pattern is a combination of two crack and crystal patterns [123]. As shown in Figure 2.17d, the deposit is characterised by two parts: the peripheral part, which is composed of radial and orthoradial cracks (Figure 2.17dI); and the central part, which is composed of different morphologies of crystal patterns, such as dendrites and inclusions (Figures 2.17dII,III).

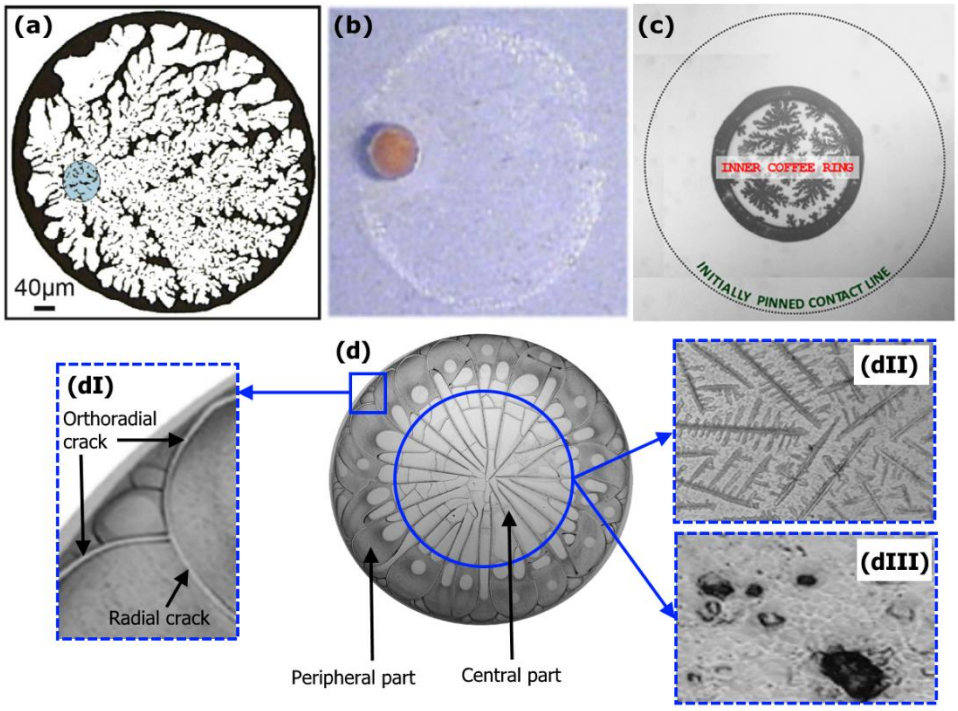

Figure 2.17 Combined patterns. (a) Fingering pattern inside the coffee-ring pattern. Image modified from Ref. [120]. (b) Dot-like pattern inside the coffee-ring pattern. Image modified from Ref. [121]. (c) Dendrite-shaped pattern inside the inner coffee-ring pattern. Image modified from Ref. [122]. (d) Crystal pattern enclosed within the crack pattern: (I) radial and orthoradial cracks in the peripheral part of the deposit, (II) dendrites in the central part of the deposit, and (III) inclusions in the central part of the deposit. Image modified from Ref. [123].

2.4 Effects of Different Factors on Deposit Patterns

The previous section discussed a series of dried patterns that are significantly affected by evaporation kinetics, the movement of contact line, inner flow structure, interfacial interactions, and particle-particle interaction. These effects are dependent on the factors that can be manipulated to control the pattern formation of drying drops. These factors are discussed in the following subsections.

2.4.1 Solute effect

2.4.1.1 Concentration

Particle concentration has a significant influence on the final deposition patterns. Sefiane [47] investigated the effect of concentration (0.1, 0.5, 1 and 2%) on the final deposition patterns of Al_2O_3 nanofluid drops. Ring-like patterns were observed for all concentrations and the thickness of the ring increased with increasing concentration. The author also found cracking patterns, which were more prominent at higher concentrations. Increasing concentration increased the thickness of these cells. Furthermore, Brutin [20] observed a transition between two patterns that corresponded to a critical concentration, as seen in Figure 2.18. For concentrations between 0.01 and 0.47 wt %, a coffee-ring pattern with no particles in the interior of the ring was formed. The width of the ring decreased with increasing concentration following a power law. For concentrations above 1.15 wt %, nanoparticles deposited in the central regions, forming a “flower petal” pattern. The deposition thickness increased with increasing concentration, whereas the number of flower petals decreased with concentration. As shown in Figure 2.19, the author observed a dot-like pattern at a polymer concentration of 0.5 wt %, but a ring-like pattern at 3 wt % [124]. In another study, Lee et al. [125] showed a transition from a coffee-ring pattern to a uniform pattern with increasing concentration at the nanoparticle size of 135 nm. However, there was no obvious relation between concentration and the type of deposit patterns at lower nanoparticle sizes. Therefore, the authors combined the effects of both concentration and nanoparticle sizes. Low nanoparticle concentrations and small nanoparticle sizes formed a coffee-ring pattern, while high concentrations and large particle sizes led to the formation of a uniform pattern. At moderate concentrations and particle sizes, an irregular pattern was formed. Moreover, Moffat et al. [92] showed that drying nanofluid droplets with a concentration of 0.01 wt % had a receding contact line with a distinct decrease in contact angle, whereas a concentration of 0.1 wt % resulted in the stick-slip behaviour. The increase in nanoparticle concentration enhances the stick-slip behaviour [66,92]. A direct correlation was found between the distance jump by the contact line and nanoparticle

concentration [66]. The higher concentration leads to a longer pinning of the contact line; thus, the deviation in the contact radius from equilibrium before a jump is higher and the steps of the contact line are greater [66].

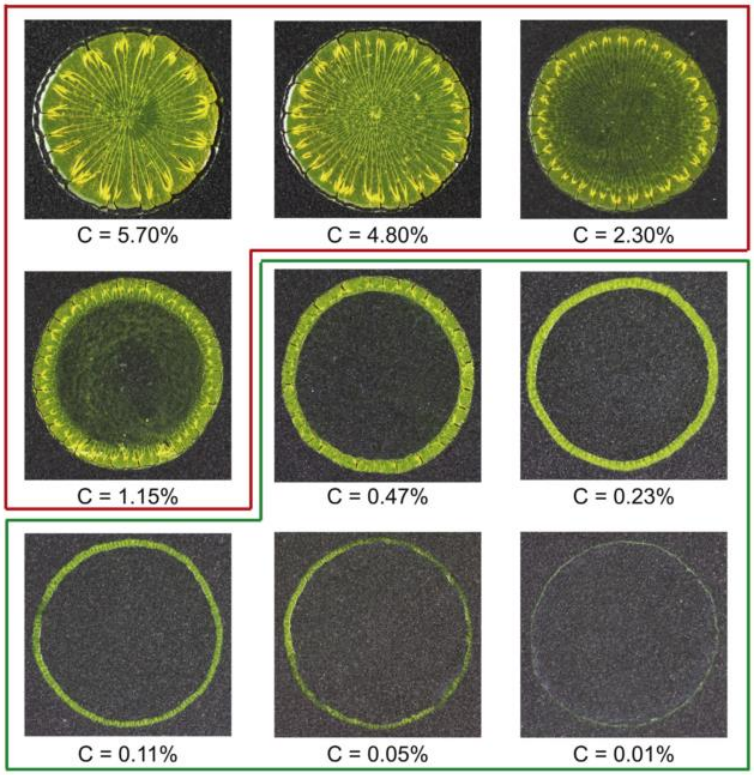

Figure 2.18 Influence of nanoparticle concentration on final deposition patterns. A coffee-ring pattern is formed for concentrations between 0.11 and 0.47 wt %, and a flower petal pattern is formed for concentrations between 1.15 and 5.7 wt %. Image taken from Ref. [20].

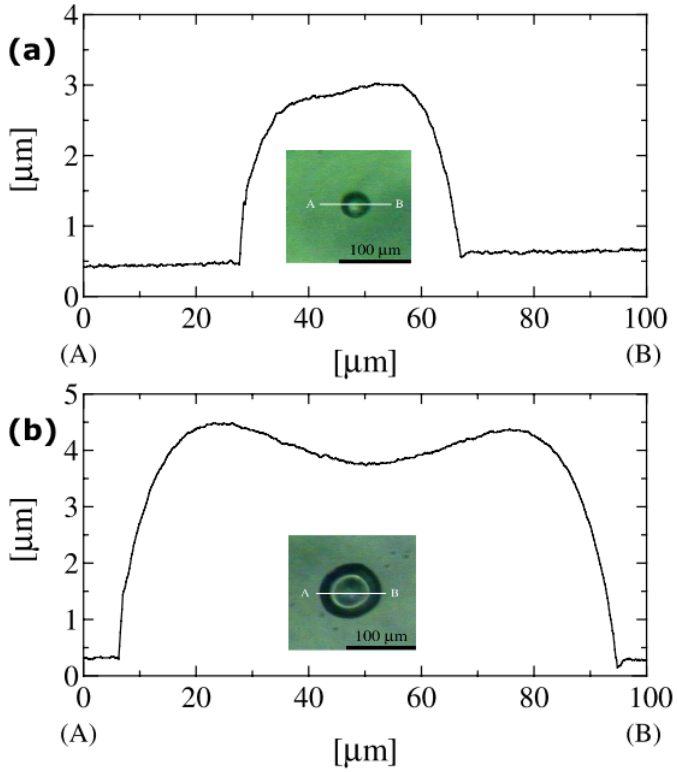

Figure 2.19 Dried patterns and thickness of polymer films. (a) A dot-like pattern at a concentration of 0.5 wt %. (b) A ring-like pattern at a concentration of 3 wt %. Image modified from Ref. [124].

2.4.1.2 Shape

Interfaces are significantly deformed by the anisotropic shape of particles, generating strong particle-particle interactions [126–132]. The outward flow, which is responsible for the generation of the coffee-ring effect for spherical particles, carries ellipsoidal particles to the air-liquid interface, causing strong long-ranged particle-particle attractions among ellipsoidal particles. Consequently, loosely packed aggregates are formed at the air-liquid interface [126,127,131,133]. Similarly, Yunker et al. [134] demonstrated that the addition of ellipsoidal particles to suspensions containing spherical particles can deteriorate the coffee-ring effect. They found that the coffee-ring persisted if the minor axis of ellipsoidal particles was larger than the diameter of spherical particles, whereas the coffee-ring was inhibited if the axis was smaller than the diameter. Thus, in the presence of ellipsoidal

particles with appropriate aspect ratio, a loosely packed structure can be formed at the free surface of evaporating drops, preventing particles from reaching the contact line and resulting in a uniform pattern after dry-out (Figure 2.20a). However, in the absence of ellipsoidal particles, the drying of drops containing spherical particles forms the coffee-ring pattern (Figure 2.20b). Dugyala and Basavaraj [135] studied the effect of both particle shape and the pH of a solution containing hematite ellipsoids. As shown in Figure 2.21, there was no considerable change in the deposit patterns for different particle aspect ratios at each pH value, while the type of deposit pattern changed for different pH values at each aspect ratio. The coffee-ring pattern was formed for low and high pH values, while the uniform pattern was formed for intermediate pH values. It is noteworthy that the particles in this study were hydrophilic, while the particles used in Yunker et al.'s [134] work were partially hydrophobic. In another study, a transition was found from radial to circular crack patterns by changing the particle shapes from spheres to ellipsoids [108]. The different aspect ratios of ellipsoidal particles had no significant effect on the crack patterns, and the same circular crack patterns were produced. It was found that the crack patterns formed by anisotropic particles are significantly affected by the particle ordering, and not their aspect ratio.

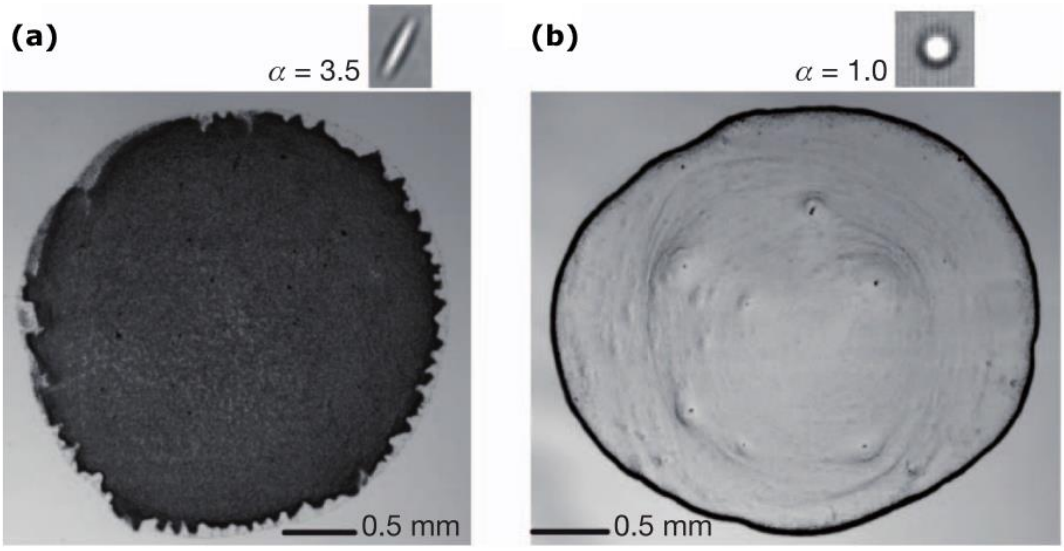

Figure 2.20 (a) Uniform pattern formed by ellipsoidal particles. (b) Coffee-ring pattern formed by spherical particles. α is the major-minor axis ratio. Image taken from Ref. [134].

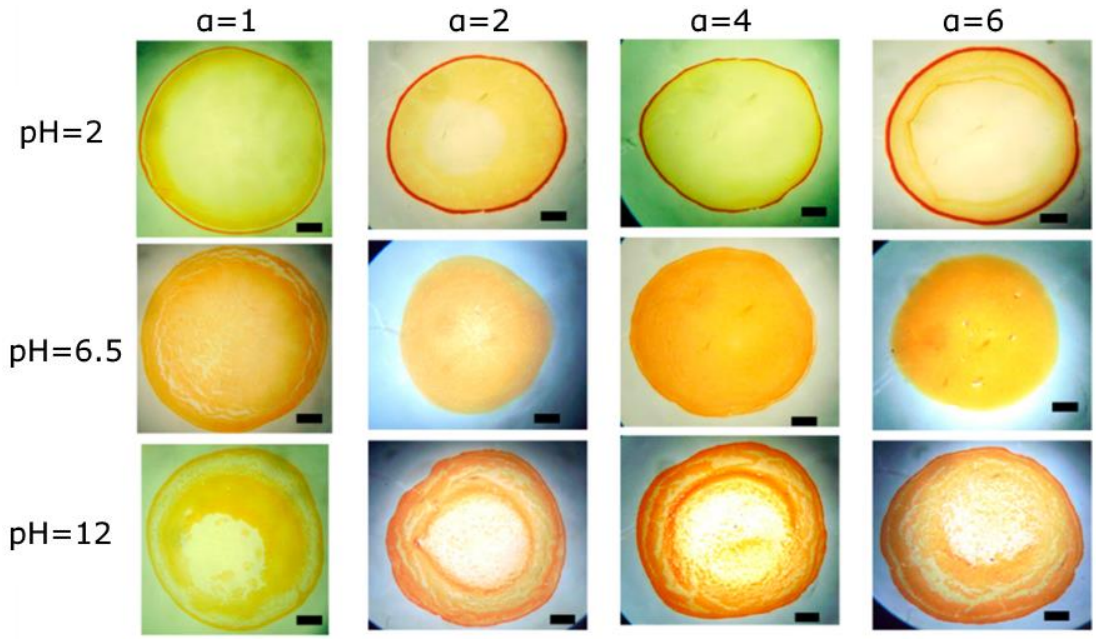

Figure 2.21 Effect of the hematite particle aspect ratio (α) and pH of a solution on final deposit patterns. Image modified from Ref. [135].

2.4.1.3 Size

Chon et al. [19] studied the influence of the different sizes of nanoparticles (2, 11, 30, and 47 nm) on the pattern formation. Larger nanoparticles led to the formation of the distinctive coffee-ring patterns, but smaller nanoparticles formed a thicker and more uniform deposition in the central region enclosed with a loosely defined wider ring. A different study by Choi et al. [136] investigated the pattern formation from evaporating water drops containing polystyrene particles (1 and 6 μm) and hollow glass spheres (9-13 μm). For the large-sized polystyrene particles, the contact line was not pinned and receded during the evaporation. Some particles deposited at the edge, but a considerable number of particles deposited in the interior region of the ring. The small-sized polystyrene particles moved towards the pinned edge and formed the coffee-ring pattern. In the case of hollow glass particles with a mix of small and large sizes, the contact line was not pinned and particles moved inward along the air-liquid interface and finally deposited in the centre of the droplet at the final stages of evaporation. Furthermore, Ryu et al. [137] obtained a phase diagram in terms of polymer concentration and poly(methyl methacrylate) (PMMA) colloid

size. As demonstrated in Figure 2.22, in the absence of polymer, small colloids form the coffee-ring pattern, while larger colloids are randomly distributed in the droplet forming bump-like patterns. At a low polymer concentration of 0.1 wt %, the coffee-ring effect is enhanced by increasing colloid size from 0.1 to 1 μm. The same trend is observed by increasing size from 5 to 10 μm, but the coffee-ring effect is more pronounced for the colloid size of 1 μm than for larger colloids. At each of the high polymer concentrations (0.5 and 1 wt %), the coffee-ring effect is enhanced with increasing colloid size, and large colloids form the coffee-ring patterns. The aggregation dynamics of colloids depends on their size. In the presence of polymer, small colloids are likelier to build aggregation than large ones, implying that the interactions between colloid and polymer for large-sized colloids become weak, and the coffee-ring effect thus becomes dominant.

Some studies have also investigated the effect of particles with multiple sizes in a single liquid drop on the final deposit. Among them, Sommer et al. [138] studied the effect of two different particle sizes (60 and 200 nm) in a liquid drop on the distribution of particles on a smooth substrate. The slow evaporation of drops resulted in well-ordered structures, where larger particles formed a peripheral ring in dense hexagonal structures surrounding the massive inner ring. However, a study by Jung et al. [139] showed that the mixture of multi-sized particles (500 nm and 5 μm) led to a different deposition pattern. During the evaporation process, nanoparticles moved towards the contact line and enhanced the pinning effect, while micro-particles moved towards the centre of the droplet resulting from the surface tension force of the liquid. As a result of this particle motion, larger and smaller particles separately deposited onto the substrate, with larger particles accumulating in the centre of the dried drop enclosed with a ring formed by smaller particles. Similarly, another study reported a separation of particles with three different sizes in a liquid droplet (Figure 2.23) [140]. Three well-separated rings were formed near the contact line by each size; the outermost ring was formed by the smallest particles, while the innermost ring was built by the largest particles. This concept of particle separation based on the particle-size effect can be a natural, cost effective method of disease diagnostics. The schematic phase diagram in Figure 2.24 shows the effect of particle

volume fractions of small and large particles on the final pattern after evaporation of a decalin-based colloidal droplet [102]. Coffee-ring patterns were formed for monodispersed small colloids, and grew as the concentration of the small colloids increased. For monodispersed large colloids, bump-like patterns were formed and grew when the concentration of the large colloids increased. For bidispersed colloids at a lower concentration, fingering patterns were left after complete evaporation due to the competition between the outward coffee-ring and inward Marangoni effects, particularly when the Marangoni flow was suppressed by the coffee-ring flow. The formation of multiple ring patterns for bidispersed colloids was attributed to the particle separation based on the size. For high concentrations of bidispersed colloids, a pronounced ring-like pattern was left behind. Recently, Zhong et al. [141] conducted experiments to study the effect of multi-sized particles on pattern formation. As shown in Figure 2.25, non-uniform deposition patterns were left either by 5 or 40 nm Al_2O_3 nanoparticles. For the weight ratios from 0:1 to 2:8 (Figure 2.25a), droplet shrinkage occurred in the middle of the evaporation, while those droplets with a weight ratio above 2:8 were pinned until the late stages of the evaporation (Figure 2.25b), preventing the large nanoparticles from making aggregates at the contact line and thus the formation of the fractal-like structures. By further increasing the 5 nm nanoparticles from the weight fraction of 30 to 50% (Figure 2.25b), the attraction between the small and large nanoparticles suppressed the movement of the small ones towards the central region. Therefore, the non-uniformity of the patterns left either by pure 5 or 40 nm nanoparticles was eliminated by combining the proper concentration of the two nanoparticle sizes.

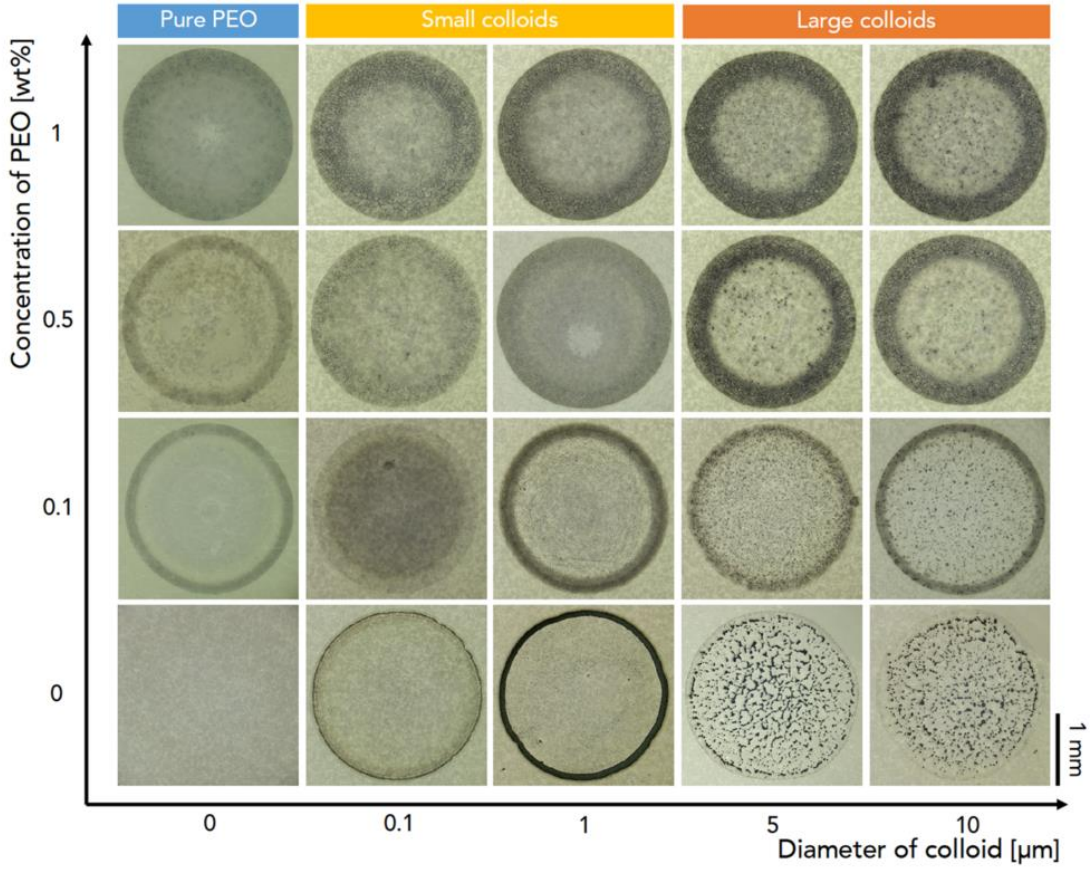

Figure 2.22 A phase diagram for polymer concentration and poly(methyl methacrylate) (PMMA) colloid size. Image taken from Ref. [137].

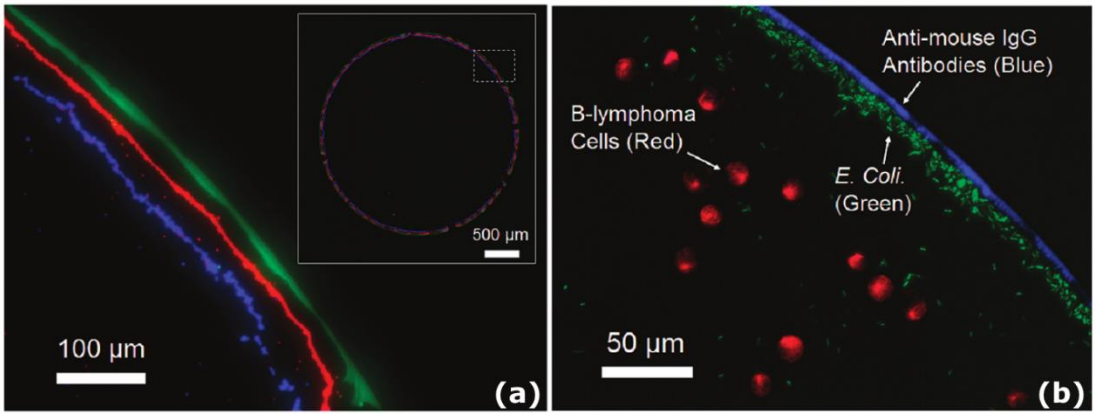

Figure 2.23 (a) Separation of particles with different sizes of 2 μm (blue), 1 μm (red), and 40 nm (green) after complete evaporation. (b) Separation of B-lymphoma cells (red), Escherichia coli (green), and antimouse IgG antibodies (blue). Image modified from Ref. [140].

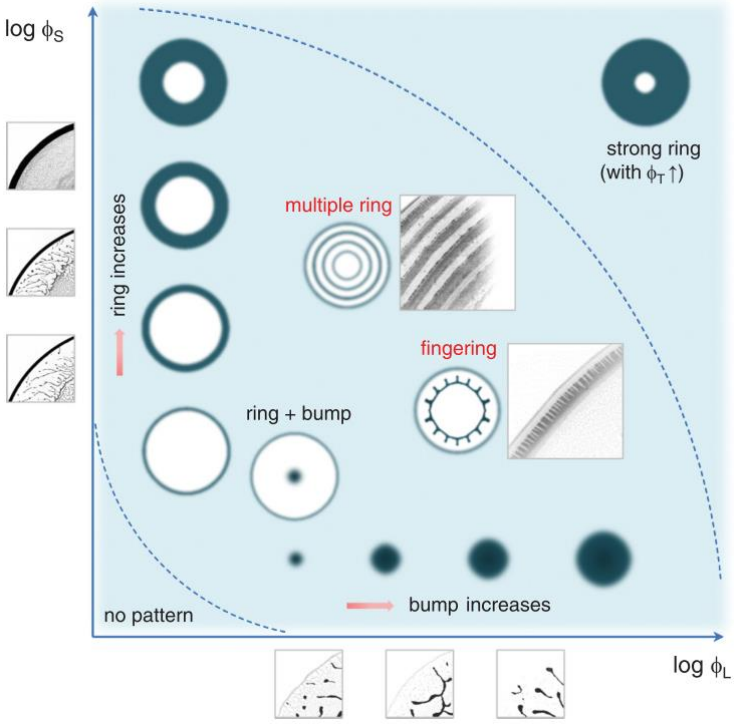

Figure 2.24 Schematic phase diagram of deposition patterns from monodispersed and bidispersed droplets. ϕ_L and ϕ_S are the volume fractions of large and small particles, respectively. Image taken from Ref. [102].

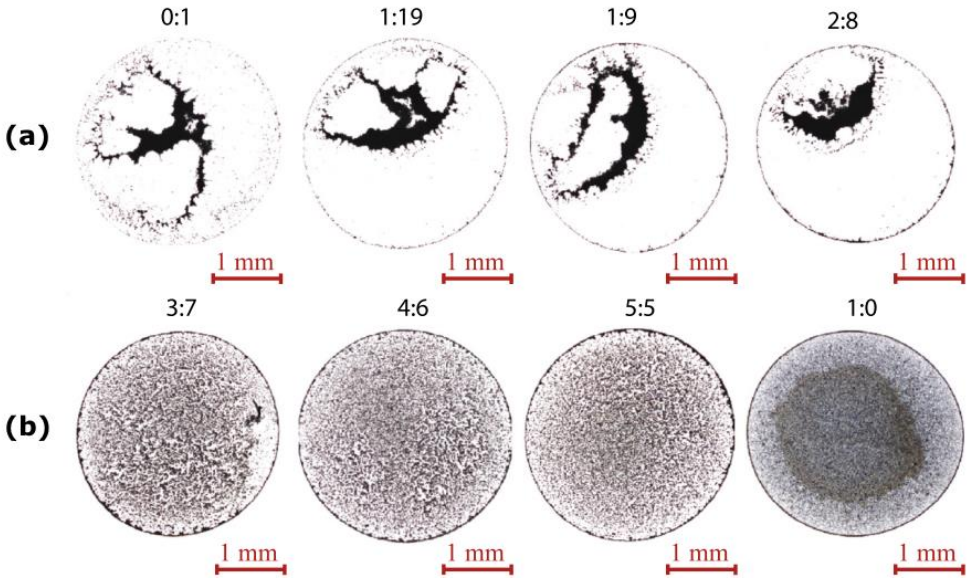

Figure 2.25 The deposition patterns formed by drying droplets with the weight ratio of 5-40 nm Al_2O_3 nanoparticles: (a) 0:1, 1:19, 1:9, and 2:8. (b) 3:7, 4:6, 5:5, and 1:0. Image modified from Ref. [141].

2.4.1.4 Material

Lee et al. [125] compared the deposition patterns of the 20 nm Al_2O_3 and 21 nm TiO_2 nanofluid drops at the same concentration of 0.05 vol % (Figure 2.26). The ring width of the Al_2O_3 nanoparticles was found to be smaller than that of TiO_2 nanoparticles. By considering the effect of different factors such as the material, size, and concentration of nanoparticles, the authors concluded that the material of nanoparticles has a less significant role on the pattern formation. As seen in Figure 2.27, the pattern formed by the mixture of the 5 nm graphite and the 5 nm Al_2O_3 nanoparticles is similar to the pattern of the Al_2O_3 nanoparticles [141]. However, the gap between the contact line and the centre-concentrated deposit is larger for the mixture pattern than that for the Al_2O_3 pattern. The effect of the combination of the two nanoparticles is found to be collaborative on the mixture pattern as they almost keep the positions they form individually.

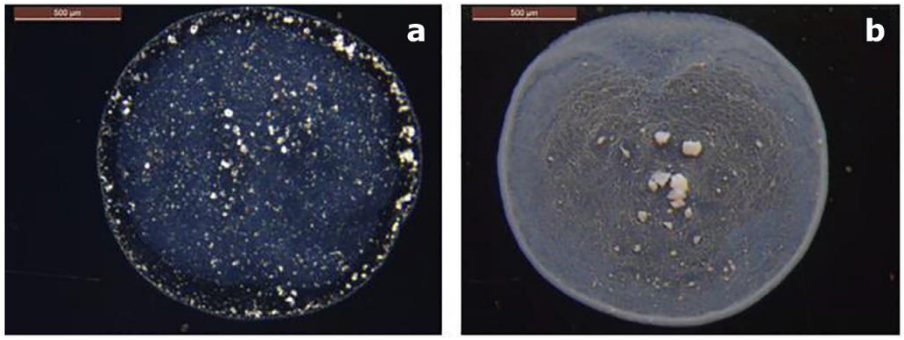

Figure 2.26 Deposition patterns after drying sessile drops containing different materials of nanoparticles: (a) 20 nm Al_2O_3 and (b) 21 nm TiO_2 with 0.05 vol % concentration on stainless steel. Image taken from Ref. [125].

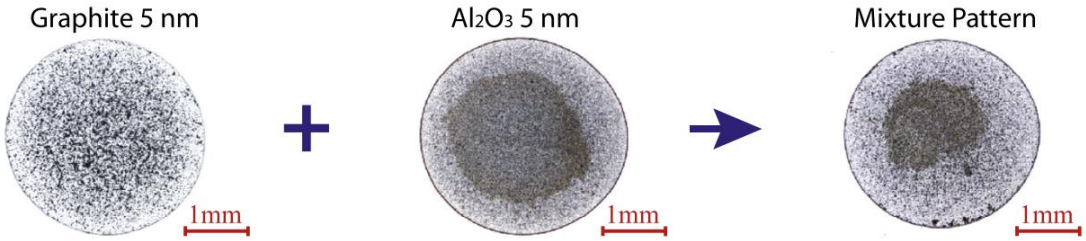

Figure 2.27 Deposition patterns after drying sessile drops containing single 5 nm graphite nanoparticles, single 5 nm Al_2O_3 nanoparticles, and the mixture of graphite and Al_2O_3 nanoparticles. Image taken from Ref. [141].

2.4.2 Environmental conditions

2.4.2.1 Relative humidity

Only few studies in the literature address the effect of relative humidity on the deposition pattern. Chhasatia et al. [142] examined the effect of relative humidity on the deposition patterns of picolitre-sized drops containing polystyrene beads. The rise in the relative humidity decreased the evaporation rate of a pinned drop, but increased the spreading of the drop with lower contact angle, leading to a larger deposition area. The authors concluded that the relative humidity was a key parameter for sufficient small drops in terms of the evaporation process and thus the final deposition patterns. Surprisingly, Brutin [20] showed that the deposition patterns of dried nanofluid drops were identical for different humidity values varying from 13 to 85%. They found that the diffusion coefficient of the nanofluid drops in humid air was different from that of pure water drops in dry air. The evaporation rate was enhanced due to the larger spreading area of the nanofluid drops and also the decrease of the contact angle. However, in another study the increase in the relative humidity affected the dried pattern of blood drops on glass substrates [32]. The deposition pattern was characterised by three distinctive areas, as shown in Figure 2.28: a fine peripheral area adhering to the substrate; a coronal area composed of wide mobile plaques with radial white cracks; and a central area composed of small cracks and a sticking deposit. By increasing the humidity, the width of the peripheral area grew; this is shown between the two yellow bars in Figure 2.28. The increase in

the humidity decreased the contact angle, and consequently increased the diameter of the deposition pattern and the width of the wedge near the contact line. This led to the formation of a wider peripheral area as the humidity rose. By increasing the humidity from 13.5 to 50%, the size of plaques in the corona grew, but then decreased with the further rise in the humidity from 50 to 78%. The difference in the size of plaques can be attributed to the evaporation rate, which affects the adhesion of the drop to the substrate [33].

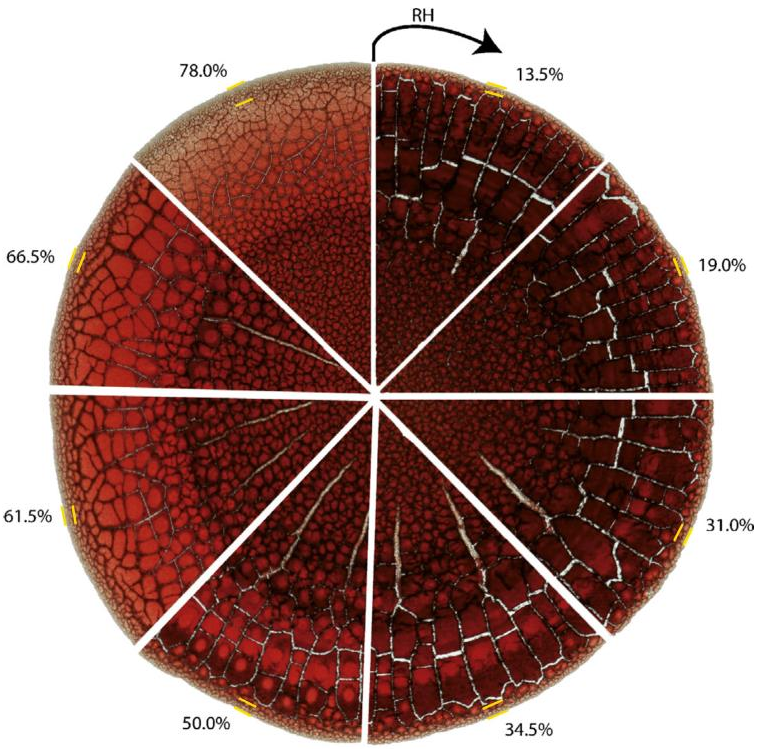

Figure 2.28 Influence of various ranges of relative humidity on the pattern formation of a sessile blood drop. Area between the two yellow bars indicates the peripheral area. Image taken from Ref. [32].

2.4.2.2 Ambient temperature and pressure

An investigation was conducted to identify the effect of the environmental temperature on the deposition patterns of dried TiO_2 and Al_2O_3 nanofluid drops [47]. At the same concentration, the deposition pattern of Al_2O_3 nanoparticles was relatively independent of the ambient temperature, but in the case of TiO_2 nanofluid,

increasing the temperature led to the ring-like pattern formation with concentric rings inside the peripheral ring.

Askounis et al. [25] examined the influence of reduced atmospheric pressure, varying from 750 to 100 mbar, on the final deposition patterns left after the full evaporation of water drops containing SiO_2 nanoparticles (see Figure 2.29). Reducing the atmospheric pressure enhanced the evaporation rate due to the increase in the effective diffusion coefficient of water vapour in the environment. The evaporating drop followed the stick-slip mode under 750 mbar pressure, hence the stick-slip pattern was formed (Figure 2.29a). In contrast, the ring-like pattern was formed under 500 mbar pressure (Figure 2.29b), and a wider and thicker ring was obtained with a further reduction of pressure to 250 mbar (Figure 2.29c). The outward flow contributed to the accumulation of nanoparticles at the contact line and thus enhanced the pinning effect, both of which led to the formation of the ring-like patterns, but the thicker ring resulted from the stronger outward flow caused by the further reduction of the pressure. At 500 mbar pressure, the authors also observed the assembly of hexagonal, closed-packed nanoparticle structures. A different ring-like pattern with an inner irregular shape was formed under 100 mbar pressure (Figure 2.29d). The high deposit was brought near the edge by the very strong outward flow induced by the extremely high evaporation rate. Moreover, the fast evaporation did not give sufficient time to the fluid to flow towards the edge; thus, it became frozen in place, forming different inner deposits than those drops under 250 and 500 mbar. From the nanoscopic point of view, nanoparticle pattern crystallinity was promoted by reducing pressure.

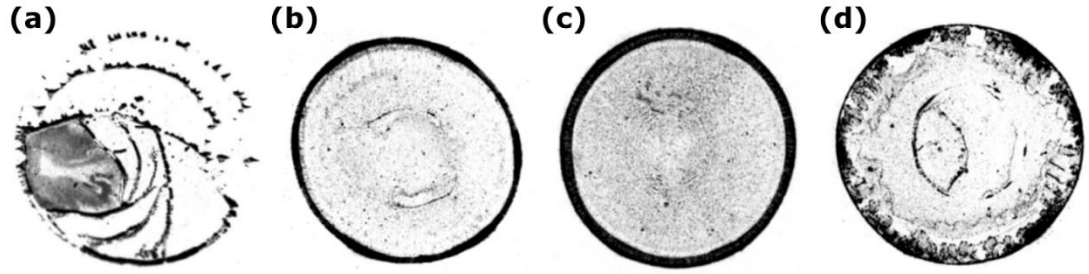

Figure 2.29 Influence of reduced environmental pressure on the pattern formation of a sessile SiO_2 nanofluid drop: (a) 750 mbar, (b) 500 mbar, (c) 250 mbar, and (d) 100 mbar. Image modified from Ref. [25].

2.4.2.3 Wettability of substrate

Section 2.3 mentioned that the coffee-ring pattern is more likely to occur on hydrophilic or high wettability substrates. In contrast, the dot-like pattern or central-like deposits are more likely to form on hydrophobic or low wettability substrates. Lee et al. [125] studied the influence of different substrate materials on deposition patterns of nanofluid droplets by using glass, stainless steel, and Teflon surfaces with the initial contact angles of 55.2°, 80.9°, and 90.4°, respectively. The authors confirmed that it was easier for drying droplets to form a ring-like pattern on the high wettability substrate with lower contact angle. On the other hand, more nanoparticles were found in the centre of the peripheral ring on the low wettability substrate with larger contact angle. For example, more nanoparticles concentrated in the centre of the pattern formed on stainless steel compared to that formed on glass. This was attributed to the droplet shape, as it is affected by the contact angle. A droplet with a larger contact angle has a greater height at the centre and a smaller base diameter; therefore, more nanoparticles should be found in the central region after complete evaporation. On the other hand, a droplet with a low contact angle has a smaller height at the centre and a larger base diameter, which enhances the evaporation rate and the flow velocity. This makes it easier for the droplet to form a ring-like pattern. By considering other factors such as particle size, particle concentration, etc., Lee et al. found the effect of substrate material to be less significant on the final deposition patterns [125]. However, the wettability of the substrate plays an important role in

the drying process and thus final deposition patterns [66,121,143]. For example, Orejon et al. [66] studied the effect of nanoparticles' presence on the dynamics of the contact line on substrates of various hydrophobicities; they observed the stick-slip behaviour only on hydrophobic substrates. Chhasatia and Sun [144] investigated the effect of substrate wettability on the pattern formation of droplets containing bidispersed particles. On the substrates with higher wettability, particles of different sizes were further separated than those on the substrates with lower wettability. This was attributed to the effects of the different evaporation modes, the substrate-particle interactions, the surface tension, and drag forces acting on particles on the rearrangement of particles near the contact line during evaporation. Furthermore, Jeong et al. [145] showed that the separation of nano- and micro-particles near the contact line only occurred on hydrophilic substrates. Conversely, hydrophobic substrates could not separate the suspended particles as the contact line was not pinned and receded during evaporation. In another study, Li et al. [121] demonstrated that the final deposition pattern of polymer particles could be manipulated by controlling contact angle hysteresis (CAH). Ring-like patterns were formed on substrates with strong CAH such as poly(vinyl pyrrolidone) (Figure 2.30a), and dot-like patterns were formed on substrates with weak CAH such as sodium polysulfonate (Figure 2.30b). Very recently, Zhong et al. [119] investigated the effect of various substrates on crystal patterns from saline droplets (see Figure 2.31). Cubic crystals were formed at the centre of the dried droplet deposited on silicon and PMMA substrates with a lower wettability and weaker pinning effect. However, the high wettability and the stronger pinning effect of the soda lemon glass resulted in the formation of a spherical profile composed of thin layers of salt and cubic crystals.

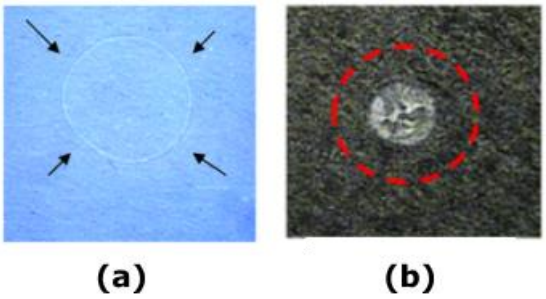

Figure 2.30 Deposition patterns of polymer particles on substrates with different values of contact angle hysteresis (CAH): (a) strong CAH and (b) weak CAH. Image modified from Ref. [121].

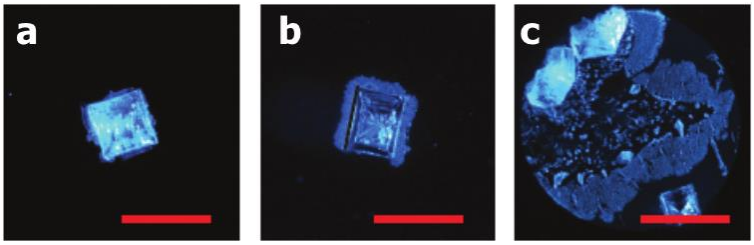

Figure 2.31 Dried deposits of saline droplets containing 10% salt on: (a) silicon wafer, (b) PMMA, and (c) soda lemon glass. Scale bar, 1 mm. Image modified from Ref. [119].

2.4.2.4 Substrate temperature

Unexpectedly, few studies have examined the effect of substrate temperature on dried patterns. One study found that a change in substrate temperature could change the flow direction at the late stages of the evaporation; thus, the dried deposition patterns of water-polymer droplets were different on a heated substrate than on a cooled one [72]. As shown in Figure 2.32a, the evaporation of a poly(ethylene oxide) (PEO) droplet formed a “puddle” structure on the isothermally heated substrate at 30 °C [146]. However, a peculiar “dual-ring” structure was left behind after full evaporation on the non-isothermally heated substrate at a rate of 20 °C/min (Figure 2.32b). At lower temperatures, the capillary flow was dominant and led to the formation of the peripheral ring. The further rise in temperature increased the surface stress gradient and decreased the viscous stress, resulting in the contact line

recession. Eventually, the Marangoni flow became dominant at the late stages of the evaporation process, forming the dual-ring structure.

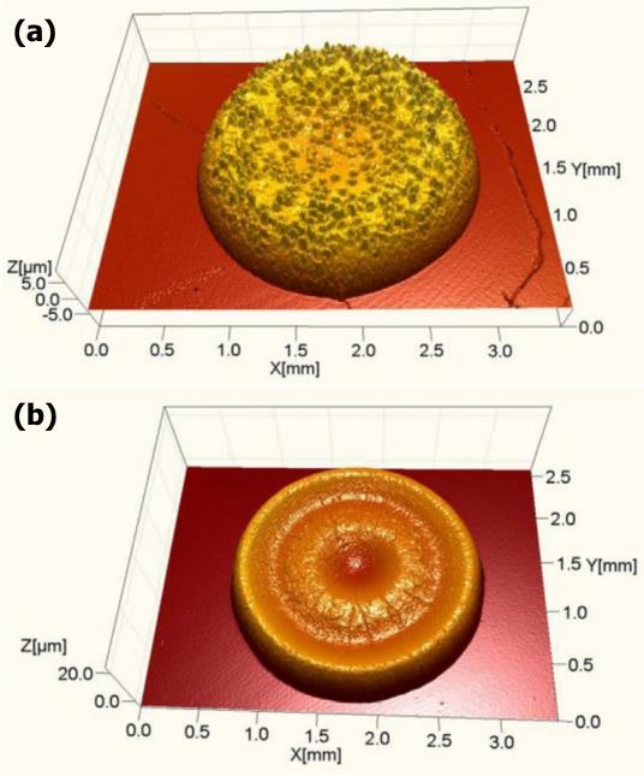

Figure 2.32 The surface profile of poly(ethylene oxide) film: (a) isothermal evaporation process; (b) non-isothermal evaporation process. Image modified from Ref. [146].

2.4.3 Base fluid

2.4.3.1 Surfactants

Adding surfactants to a base fluid is another way to alter the deposition pattern of drying sessile drops. In one study, the addition of ionic surfactant sodium dodecyl sulfate (SDS) significantly altered the coffee-ring effect inside an evaporating colloidal drop [21]. A strong inward Marangoni flow was created by SDS along the air-liquid interface of the drop, which prevented most particles from depositing at the contact line, forming a more uniform deposition pattern. Similarly, biosurfactants generated a surface tension gradient along the air-liquid interface, inducing a Marangoni flow [68]. The particles moved towards the drop edge but did not deposit

there and returned back inward along the free surface due to the Marangoni flow. Hence, the coffee-ring effect was inhibited and the particles were uniformly distributed on the substrate (Figure 2.33). In their work, Seo et al. [87] compared the pattern deposition of SDS (surfactant) and surfactant-like polymer solutions. Both surfactants altered the coffee-ring effect and led to the formation of multiple ring patterns. However, the rings formed by the surfactant-like polymer were more uniform due to the change of the depinning and receding of the contact line caused by the characteristics of the surfactant. The depinning of the contact line for the surfactant-like polymer was easier as it required less force. Therefore, the authors observed smaller distances between each ring, and more uniform multiple rings were left after full evaporation. In contrast to these studies, the addition of cetyltrimethylammonium bromide (CTAB) surfactant into graphite nanofluid drops promoted and formed the coffee-ring effect instead of the uniform one, as shown in Figure 2.34 [147]. The same transition from the uniform pattern to the coffee-ring pattern was observed after adding CTAB surfactant into Al_2O_3 nanofluid drops [148]. The authors used a two-dimensional diffusion limited cluster-cluster aggregation (DLCA) method to explain the transition. The simulation showed that the interparticle sticking probability has a significant influence on the pattern formation.

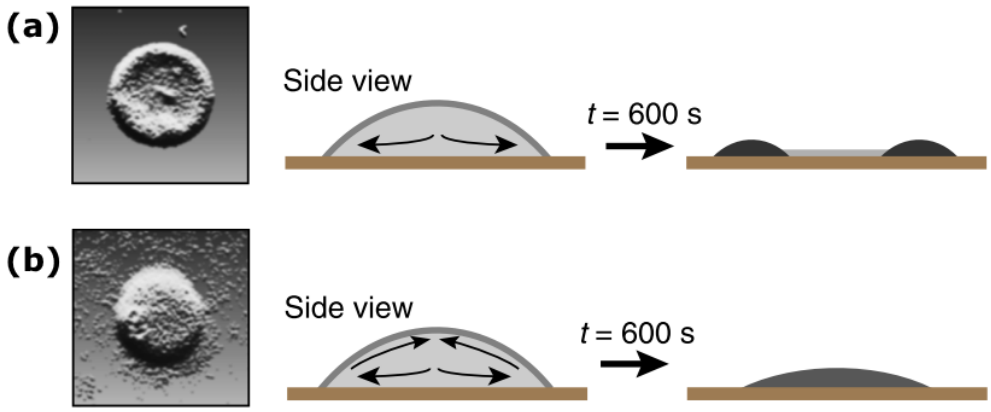

Figure 2.33 A coffee-ring pattern was formed without biosurfactants due to the coffee-ring effect. (b) A uniform pattern was formed with biosurfactants due to the strong Marangoni flow. Image taken from Ref. [68].

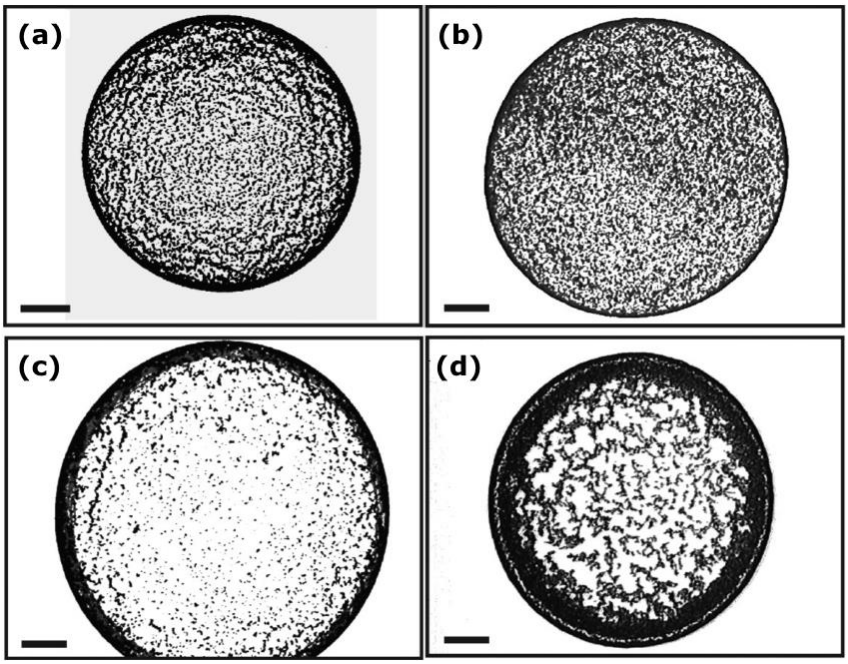

Figure 2.34 Deposition patterns left after full evaporation of graphite nanofluid drops. (a) At a concentration of 2 g/L without the CTAB surfactant. (b) At a concentration of 5 g/L without the CTAB surfactant. (c) At a concentration of 2 g/L with the CTAB surfactant. (d) At a concentration of 5 g/L with the CTAB surfactant. Image taken from Ref. [147].

2.4.3.2 Fluid composition

It is worth noting that pure water has been widely used as the base fluid in studies relevant to the pattern formation from sessile drops. Change in the base fluid composition can be a way to control the particle deposition morphology of a drying colloidal droplet. As an example, Choi et al. [136] compared the effect of Newtonian and non-Newtonian base fluids on the pattern formation of 6 μm polystyrene particles suspended in aqueous solutions of water, PEO, and xanthan gum (XG). The evaporation of the XG solution formed the coffee-ring pattern, while a more inner uniform pattern with no distinct ring was formed after the evaporation of the water and PEO solutions. The authors attributed the difference in the deposition patterns observed between the PEO and XG solutions to the difference between their viscosities. The viscosity of the XG solution remains high during low shear drying as it has a very high zero shear viscosity. For higher viscosity fluids, the capillary flow transports more particles towards the drop edge at the early stages of the evaporation,

thus leading to the formation of the coffee-ring pattern. In another study, Talbot et al. [149] examined deposition patterns from drying colloidal droplets influenced by two binary base fluids of water-ethylene glycol and water-ethanol. Uniform patterns enclosed with thick rings were formed at low concentrations (10 and 30 vol %) of ethylene glycol in water, as shown in Figure 2.35. In contrast, at higher concentrations of ethylene glycol (50-90 vol %), ring-like patterns were formed with the less dense interior regions. For concentrations above 70 vol %, unfilled regions were also observed inside the peripheral rings. Ethylene glycol-water mixture droplets showed rapid particle movement towards the contact line as water evaporates first. When ethylene glyol dominated the drying process, particle movement slowed down but still remained radially outward. At a high concentration of ethylene glycol (i.e., 90 vol %), no inward Marangoni flow was observed; thus, a slow radial flow dominated the evaporation, leading to the formation of the rings. On the other hand, for a low concentration of ethylene glycol (i.e., 10 vol %), there was a more rapid outward flow. The uniform coverage inside the rings was attributed to particles that did not have enough time to reach the edge after the evaporation process was dominated by ethylene glycol. Drying water-ethanol binary-based droplets formed ring-like deposits. The width of the rings grew with increasing ethanol concentration from 10 to 90 vol %. At the beginning of the evaporation for the ethanol concentrations between 10 and 50 vol %, inner flows showed particles collected at the central regions until the drying process was dominated by water. Then, the radial outward flow dominated the flow field. At an ethanol concentration of 90 vol %, the flow slowed down, and a lower contact angle facilitated pinning of the contact line, forming a ring-like deposit. As shown in Figure 2.36, the deposition patterns of water-ethanol binary-based nanofluid droplets are affected by the ethanol concentration [22]. The evaporation of pure water-based suspension formed a nearly uniform pattern (Figure 2.36a). However, at the ethanol concentration of 10 vol %, most nanoparticles deposited in the centre of the droplet and detached from the peripheral ring (Figure 2.36b). The dried pattern showed uniformity again as the ethanol concentration increased to 25 vol % (Figure 2.36c). However, the inner

deposit started to detach from the peripheral ring with a further increase in the ethanol concentration to 40 and 50 vol % (Figure 2.36d,e).

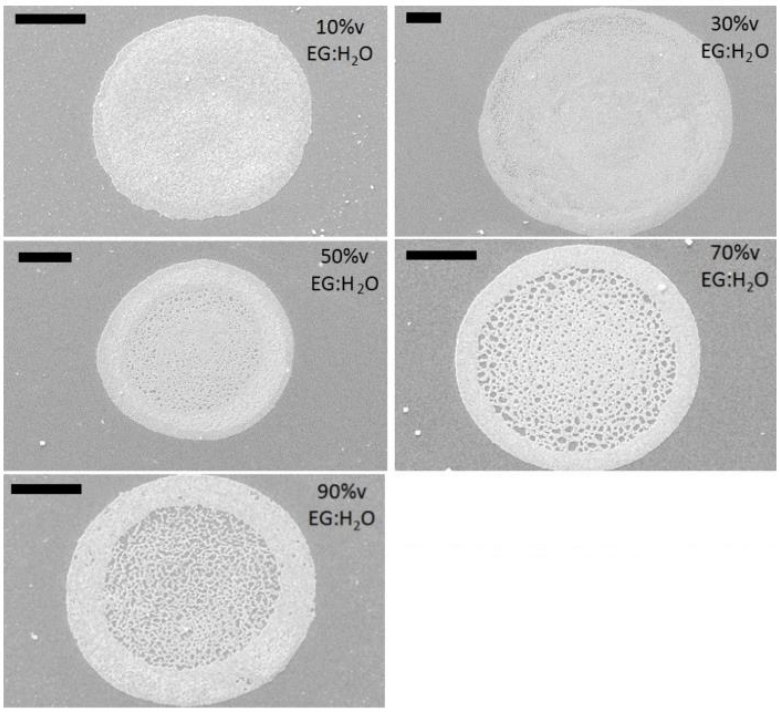

Figure 2.35 Deposition patterns from ethylene glycol-water binary-based droplets containing 1 vol % 220 nm spheres (scale bar 20 μm). Image taken from Ref. [149].

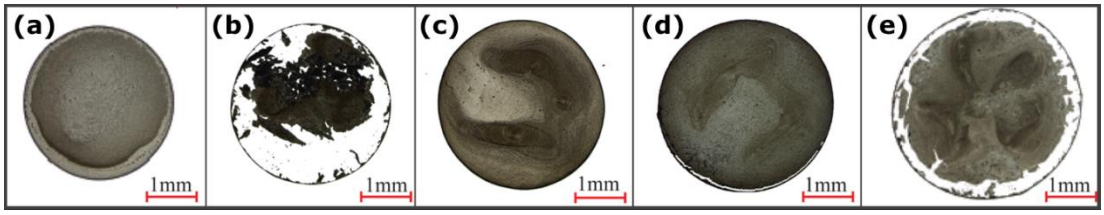

Figure 2.36 Influence of the ethanol concentration on the pattern formation of 1.5 g/L graphite-water nanofluid droplets: (a) 0 vol %, (b) 10 vol %, (c) 25 vol %, (d) 40 vol %, and (e) 50 vol %. Image modified from Ref. [22].

2.4.4 Electrowetting

In the studies discussed in the previous sections, the droplets evaporated freely and the deposition patterns were formed naturally. However, another efficient way to manipulate the deposition patterns is to apply electrowetting with a voltage to

colloidal droplets. Eral et al. [150] showed that an alternating current (AC) electrowetting suppressed the coffee-ring effect of droplets of different particle sizes and DNA solutions. As shown in Figure 2.37a-c, at frequencies of 6 Hz and 1 kHz, the electrowetting prevented the pinning of the contact line and generated the internal flow, which counteracted the evaporation driven flux and thus did not allow the particles to deposit at the contact line. However, at a higher frequency of 100 kHz (Figure 2.37d), the electrowetting led to a less pronounced coffee-ring pattern, but did not form a dot-like pattern similar to the one observed for the lower frequencies of 6 Hz and 1 kHz. The authors eliminated this problem by applying the amplitude modulation of the high frequency (100 kHz) with the low one (100 Hz), resulting in the formation of a very small dot-like pattern (Figure 2.37e). The electrokinetic mechanisms for a droplet under AC conditions can differ from those applied under direct current (DC) conditions [151]. Orejon et al. [151] studied the evaporation of TiO_2 nanofluid droplets under a DC potential. The stick-slip behaviour of droplets was suppressed, and instead the contact line receded monotonically for most of the evaporation time. Nanoparticles preferentially moved towards the substrate by electrophoretic forces instead of arriving at the contact line, and more uniform patterns were thereby formed.

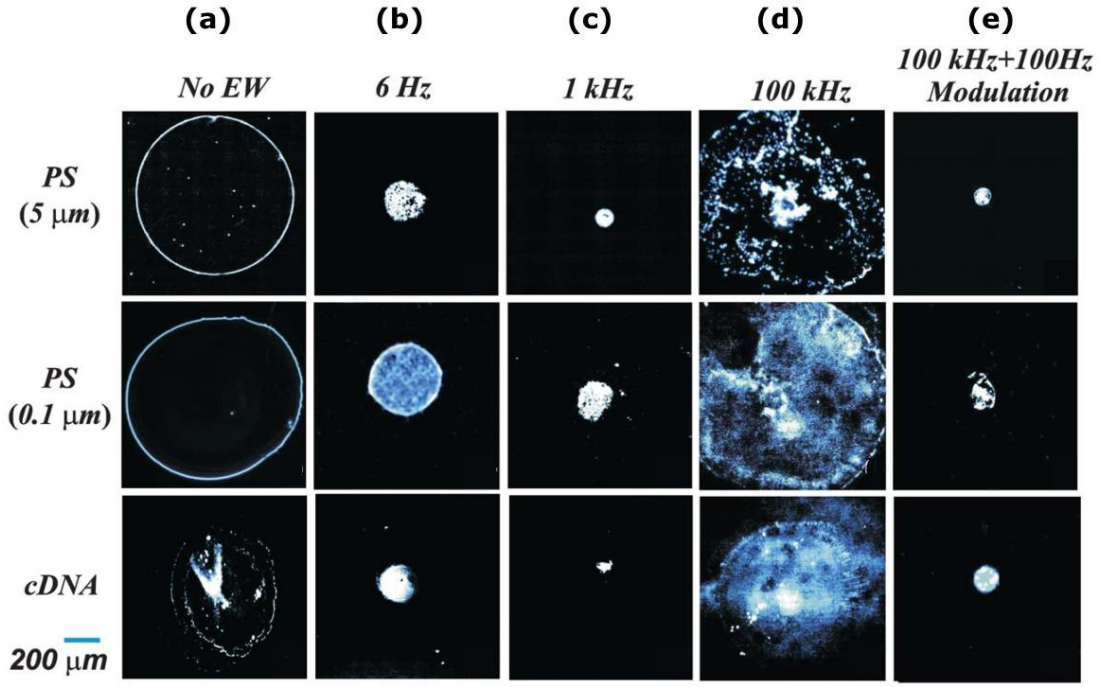

Figure 2.37 Influence of AC electrowetting (EW) on the pattern formation of colloidal droplets of different particle sizes and DNA solutions. Image modified from Ref. [150].

2.5 Summary

It is clear that the evaporation of a droplet containing particles, and consequently its pattern formation of particles, is dependent on many factors, such as environmental conditions, base fluid composition, and particle properties, among others. This literature review clearly shows researchers' interest in studying the driving factors that lead to a variety of deposition patterns. Nevertheless, because the evaporation of a droplet without particles remains a complex phenomenon, the full understanding of pattern formation from droplets of complex fluids is still lacking, and more research is needed to explain the mechanisms behind the final patterns.

According to subsection 2.4.2.4, the effect of substrate temperature on deposition patterns is still poorly understood. Therefore, the present study examined the influence of a wide range of substrate temperatures on deposition patterns, and the obtained results are presented in Chapter 3. Furthermore, from subsection 2.4.3.2, it is understood that few studies are related to the influence of binary- or

multicomponent base fluids on deposition patterns of droplets. Among these few studies, ethanol aqueous solutions are the most investigated binary base fluids. Similar to pure water, the surface tension of ethanol aqueous solutions decreases with increasing temperature. However, no studies have examined the effect of binary base fluids with a different surface tension behaviour from ordinary fluids like water. The surface tension of dilute aqueous solutions of some alcohols (i.e., butanol, pentanol) increases with enhancing temperature above a certain value. Chapter 4 investigates the deposition patterns from dried water-butanol binary-based droplets and compares these patterns with those from dried pure water-based droplets. Furthermore, the chapter also examines the effect of substrate temperature on the pattern formation of nanoparticles, as no study has considered the influence of substrate temperature on binary solvent mixture droplets. The majority of the works presented in this literature review have only investigated the effect of one factor on pattern formation. As shown in the review, the effects of the simultaneous combination of two or more factors on pattern formation are rarely studied. Whereas Chapter 4 investigates the combined effects of substrate temperature and fluid composition, Chapter 5 examines the combined effects of substrate temperature and size of particles.

Chapter 3 Patterns from Water-Based Nanofluid Drops on Heated Substrates

This chapter is based on an article published in Langmuir in 2015 [26]. The present author contributed to the design of the experiments, performed the experiments, and contributed to the data analysis and the writing of the manuscript. Dr. R. Deltombe scanned the deposits of nanoparticles using a white light interferometry technique. Prof. M. Bigerelle analysed the scans of the deposition patterns which are provided in Figures 3.1, 3.2, 3.3c. Prof. S. Harmand and Prof. K. Sefiane supported the author in writing the manuscript and granted approval for the final version.

Effect of Substrate Temperature on Pattern Formation of Nanoparticles from Volatile Drops by Maryam Parsa, Souad Harmand, Khellil Sefiane, Maxence Bigerelle and Raphaël Deltombe
Langmuir, 2015, *31* (11), pp 3354-3367
doi: 10.1021/acs.langmuir.5b00362

3.1 Abstract

This study investigates pattern formation during evaporation of water-based nanofluid sessile droplets placed on a smooth silicon surface at various temperatures. An infrared thermography technique was employed to observe the temperature distribution along the air-liquid interface of evaporating droplets. In addition, an optical interferometry technique is used to quantify and characterise the deposited patterns. Depending on the substrate temperature, three distinctive deposition patterns are observed: a nearly uniform coverage pattern, a “dual-ring” pattern, and multiple rings corresponding to “stick-slip” pattern. At all substrate temperatures, the internal flow within the drop builds a ring-like cluster of the solute on the top region of drying droplets, which is found essential for the formation of the secondary ring deposition onto the substrate for the deposits with the dual-ring pattern. The size of the secondary ring is found to be dependent on the substrate temperature. For the

deposits with the rather uniform coverage pattern, the ring-like cluster of the solute does not deposit as a distinct secondary ring; instead, it is deformed by the contact line depinning. In the case of the stick-slip pattern, the internal flow behaviour is complex and found to be vigorous with rapid circulating flow which appears near the edge of the drop.

3.2 Introduction

The evaporation of a sessile droplet has been a very important subject for research in many scientific communities (engineering, physics, chemistry, biology, etc.) over the past few decades [20,152]. Despite the numerous undertaken studies related to this fundamental phenomenon, there are still many outstanding questions about the complex behaviour of the internal flow during evaporation and the dynamics of the contact line [152]. This complexity can be attributed to the simultaneous involvement of three different phases, namely vapour, liquid, and solid [152]. The study of deposited patterns left after the drying of a drop containing suspensions has a significant role in various industrial and biological applications, such as inkjet printing [17,20,42,44,61,75,144,152–156], DNA/RNA microarrays [74,157–163], medical tests [17,30–32,46,164], coating technologies [152,165], and the fabrication of novel optical and electronic devices [43,166]. Studying drying nanofluid sessile droplets is also highly important for cooling purposes as well as for a better understanding of two-phase heat transfer [38].

The evaporation of a liquid drop containing suspensions on a solid surface leaves a non-uniform deposition, typically like a ring-shape stain, known as the “coffee-ring” effect [14]. In this process, the contact line remains pinned, and particles are brought to the drop perimeter by an outward capillary flow; as a result, particles deposit in the vicinity of the contact line [14,61,167]. The outward flow is driven by evaporation mainly concentrated near the contact line [168]. However, there are critical factors that can reverse the coffee-ring effect, leading to a more uniform coverage formation which arises from surface tension gradients [68,76]. Non-uniform evaporative cooling at the free surface of a liquid droplet induces

temperature gradients along the air-liquid interface of the drop and further results in surface tension gradients [169,170], which drive a convective Marangoni flow [70,76,171–173]. The Marangoni convection flows from regions of lower surface tension to those of higher surface tension. The flow fundamentally exists at the air-liquid interface of evaporating droplets [21]. Therefore, depending on surface tension gradient direction, the Marangoni effect can either counteract the outward capillary flow or enhance it. It is worth stressing that the Marangoni effect in general can have a significant role in many practical applications such as heat and mass transfer, coatings, and production of materials [69,70,76,171,172,174,175].

Apart from temperature gradients, the addition of surfactants can induce surface tension gradients and hence generate the Marangoni effect. The phenomenology of surfactant-driven Marangoni flows is different from temperature-dependent Marangoni flows [21], which occur without the presence of surfactants [76]. The deposition patterns could be altered by the addition of ionic surfactant sodium dodecyl sulfate (SDS) to aqueous colloidal drops. Studies have shown that the presence of surfactants leads to a rather uniform deposition of small solid particles after the dry-out of drops [21,68,176]. As the concentration of SDS is increased near the pinned contact line, surface tension decreases. The resulting gradients of surface tension drive the colloidal particles towards the drop centre. This strong radial Marangoni flow prevents the particles from depositing at the contact line and significantly alters the coffee-ring effect [21]. Sempels et al. [68] studied the influence of biosurfactants on the flow pattern. They observed complex flow patterns near the contact line of drying droplets generated by localised vortices. These Marangoni eddies dramatically affect the deposition pattern at higher concentrations of self-produced biosurfactants. Still et al. [21] have also confirmed that the addition of SDS to liquid droplets creates Marangoni eddies, which prevents particles depositing at the contact line, finally leading to the depinning of the contact line, and as a result, the deposition pattern of particles is significantly altered.

Temperature-dependent Marangoni flows are rarely observed in pure water due to very weak Marangoni flows, which (perhaps) can be attributed to the widely known

difficulty of keeping water interfaces sufficiently clear of contaminants [76]. Xu and Luo [177] showed that the Marangoni flow exists in drying pure water droplets using fluorescent nanoparticles. A stagnation point where the surface tension, the surface temperature gradient, and the surface flow change direction at the droplet surface was deduced. This reveals that the surface temperature and the surface tension vary non-monotonously along the droplet surface [177]. The formation of deposition pattern is strongly affected by the flow motion within the liquid droplet during the evaporation [16,153]. A different deposition pattern could be formed when the Marangoni effect dominates the coffee-ring formation within the evaporating droplet containing suspensions [69]. The solute travels towards the droplet centre driven by surface tension gradients and preferentially deposits there, inhibiting the coffee-ring formation [76]. The difference in deposition pattern was studied by Hu and Larson [69], who showed that solutes are carried by Marangoni convection near the droplet free surface inward to the centre of the droplet and then plunge downward where a part of solutes could be either returned to the edge or be adsorbed onto the substrate at the central region. Xu et al [178]. studied the formation of the colloidal ring in the presence of the Marangoni effect. The authors showed that when the Marangoni flow appears inside the droplet, the ring mass increases linearly with time, which contradicts the power-law growth by Deegan et al. [15,167], who showed almost all the particles inside the droplet are transported to the edge and form a dense ring of deposits. It was concluded that only the particles in the outward flow region form the colloidal ring, not all the particles in the droplet, indicating the co-occurrence of the outward capillary flow and Marangoni flow inside the drying droplet [178]. Hu et al. [146] reported that an uncommon “dual-ring” pattern was formed by non-isothermal evaporation of poly (ethylene oxide) droplets on a heated substrate at temperatures above 60 °C due to change of microflows at elevated temperatures as well as the dominant Marangoni convection. However, heating the substrate isothermally at 30 °C led to a completely different pattern called a “puddle” structure due to the dominant outward capillary flow and then resulted in a pinned contact line during the whole evaporation process [146]. Kim et al. [72] demonstrated that the substrate temperature affects the direction of polymer solute inside the evaporating droplet,

particularly at the end of the evaporation process. Jeong et al. [145] employed a technique to separate particles based on their size, ranging from 100 nm to 15 μm, using strong temperature-driven Marangoni flow within evaporating droplet on hydrophilic substrates. The authors showed that the smallest particles deposited at the outermost ring in the vicinity of the contact line. The ring diameter became smaller with increasing particles size. In other words, the larger the particles, the smaller are the rings [145].

In spite of abundant experimental studies on evaporating sessile droplets, investigations on the formation of nanoparticle deposits caused by the dry-out of droplets on substrates heated at different temperatures are still scarce. In this study, the formation mechanism of deposited CuO nanoparticles during evaporation of sessile droplets onto heated smooth silicon wafers at various temperatures is investigated. Reflection optical microscopy is employed to study the flow within evaporating nanofluid water-based droplets and demonstrate how different substrate temperatures affect the deposits features of nanoparticles. To the best of our knowledge, for the first time, the effects of a wide range of substrate temperatures (from 25 to 99 °C) on the deposition features left behind after the evaporation as well as the internal flow structure during the whole evaporation time are studied. The experiments contribute to the comprehensive understanding of the influence of temperature and internal flows on the resulting deposition patterns.

3.3 Experimental Methods

3.3.1 Solution

The nanofluid was obtained from copper (II) oxide (CuO) nanopowders (Sigma-Aldrich, molecular weight = 79.55, diameter < 50 nm) with a mass concentration of 0.05 wt % dissolved in distilled water using the two-step method and then stabilised in the ultrasonic bath (Elma, S 10/H) for at least 1 hour before use.

3.3.2 Deposition

Smooth silicon wafers were cleaned and ultrasonicated in distilled water for at least 30 minutes prior to each experiment test. Then, they were rinsed with acetone and distilled water for several times and dried with an air dryer (Elma Company). The silicon substrate was placed on a hot plate controlled at four different temperatures of 47, 64, 81, and 99 °C. The experiment was also carried out at ambient conditions without heating the substrate (25 °C). The 0.5 µL droplet of CuO/water nanofluid was deposited onto the hot silicon substrate using a programmable syringe pump (KdScientific, legato 100), leading to the deposition diameter of about 2 mm. At all temperatures, the experiment was repeated at least six times, showing consistent temperature-dependent behaviour. The room temperature and relative humidity were recorded as 25 °C and 29%, respectively, during the experiment by means of a sensor (Hygrosens Company).

3.3.3 Characterisation

The evaporation process of droplets was observed and recorded using a high-speed camera (Keyence, VW600C) mounted on an optical microscopic lens (Keyence, VH-Z100R, magnification zoom from 100× to 1000×). Video editing/analysis software (Keyence, VW-9000 Motion Analyzer) was used to visually track the clusters of nanoparticles movement and also measure a specific distance inside droplets with a proper calibration. The images of dried deposits were taken by means of an optical microscopic lens (VH-Z20R, magnification zoom from 20× to 200×). An infrared camera (FLIR, SC7200) mounted on a lens (FLIR, MW G1 L0905) was employed to visualise the air-liquid interface temperature of the evaporating droplets as well as the silicon surface. Water being mostly opaque to infrared, we expect to be able to read the surface temperature of the drop during evaporation. The deposits left behind after the evaporation were later scanned by a white light interferometer (Zygo, NewView 7300) for further analysis of the deposition distribution along the droplet diameter. The white light interferometer is also used to characterise and quantify substrate roughness. In this regard, it is important to distinguish between two surface

characteristics, i.e., waviness and roughness. A spectral fractal analysis showed that the wafer possesses two levels of surface topography: a waviness and a nanoroughness. Careful analysis of all used substrates has shown that the waviness is isotropic i.e. does not depend on the directions. The characteristic length roughness parameter is close to 50 μm with mean height amplitude of 1 nm (mean diameter 70 μm). The roughness, on the other hand, can be seen as nanostructure over an area of about 10 μm^2 and height 0.2 nm and a mean diameter of 3 nm. Because the size of nanoparticles is around 50 nm, these two roughnesses are deemed too fine to significantly affect the interaction between the substrate and nanoparticles.

Furthermore, in order to characterise the deposits of nanoparticles on the wafer, the inspected surfaces must be defined on a square of 2.5 mm × 2.5 mm. The first step consists in dissociating the surface topography of the wafer and the nanoparticle deposits. Figure 3.1 represents the wafer topography. As it can be seen, the wafer macroscopic forms exhibit amplitude of 1 μm on a 1000 μm length.

3.3.4 Supporting Information

Supporting Information associated with this chapter is available in the online version.[1]

[1] http://www.pubs.acs.org/doi/suppl/10.1021/acs.langmuir.5b00362

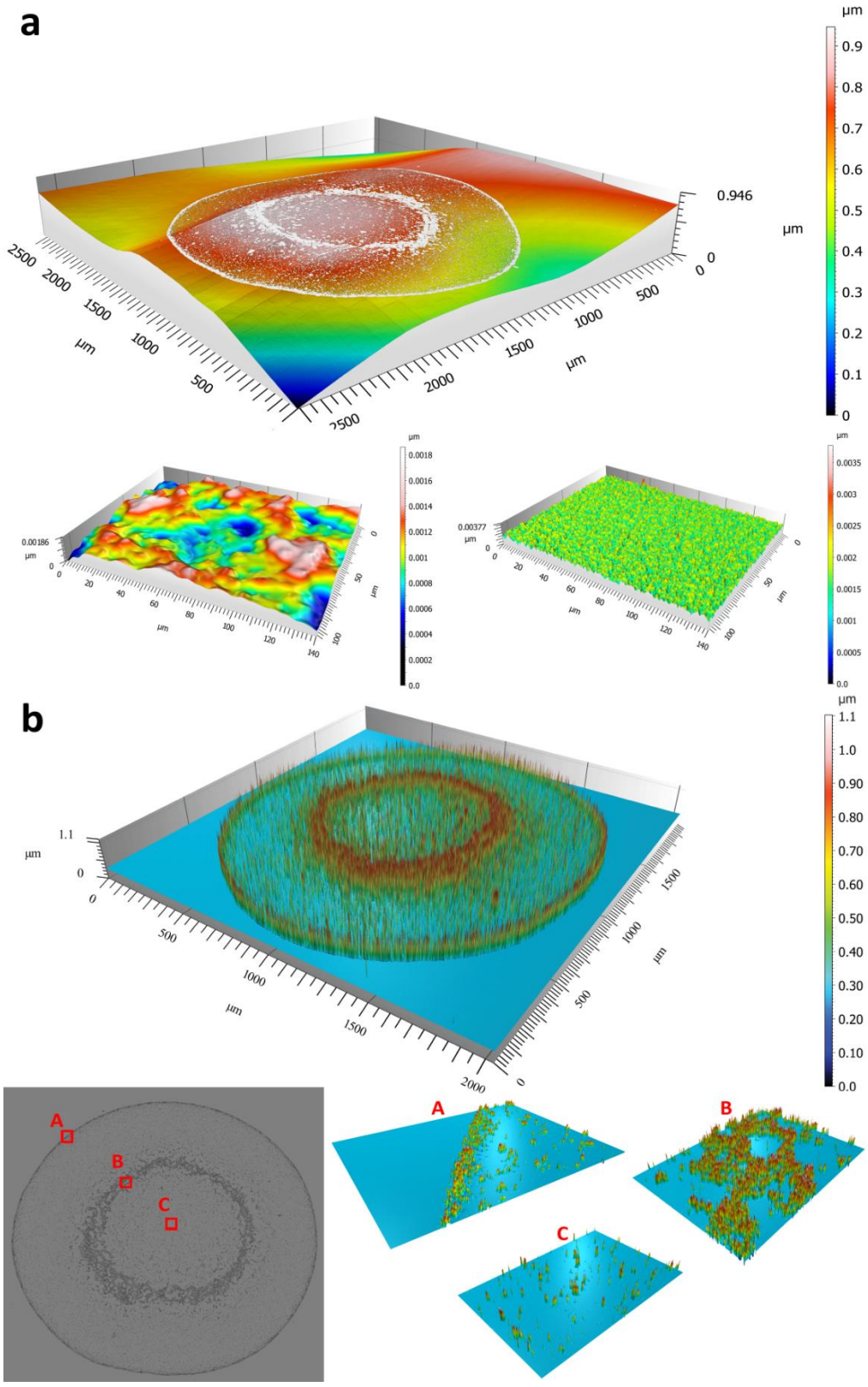

Figure 3.1. Surface topography of the wafer. (b) Topography of the nanoparticle deposits.

3.4 Results and Discussion

3.4.1 Deposition pattern after evaporation

Images obtained from the interferometry analysis for various substrate temperatures are shown in Figure 3.2. These images are later analysed to extract the density corresponding to the concentration of nanoparticles deposited on the substrate. It is worth mentioning that for most of the experiments performed the contact line is mostly pinned and the base of the drops remains fairly constant for the most part. During evaporation, the wetting contact angle on the other hand monotonously decreases (Figure 3.3a).

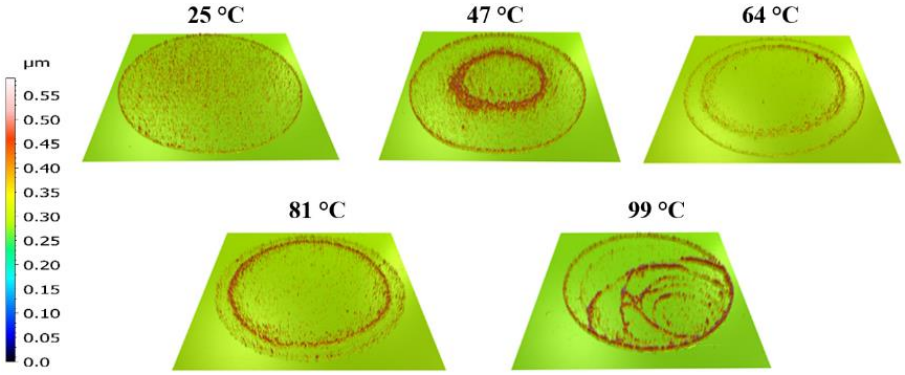

Figure 3.2. Interferometry image of the deposits at various temperatures.

Top views of deposition patterns from dried CuO-water nanofluid droplets at different substrate temperatures ranging from 25 to 99 °C are shown in Figure 3.3b. The density profiles (normalised relative volume per unit area μm^{-2}) from interferometry are shown in Figure 3.3c, beside the corresponding images. The dimensionless distance in the density profile graphs indicates the drop diameter. For sample I at 25 °C, the highest density of the nanoparticles indicates the initial contact line, and the nanoparticles occupy mainly the central region of the drop. Overall, a nearly uniform coverage deposition is formed when the silicon substrate is not heated. In the case of heating (samples II-V), the non-uniform nanoparticles distribution is left after evaporation. However, the central regions of samples II-IV are more uniform compared with the central region of sample I. As shown in Figures

3.3bII-3.3bIV, at temperatures of 47, 64 and 81 °C, the corresponding patterns exhibit two rings; one is the outer ring at the edge (peripheral ring), and the other (secondary ring) is the inner ring deposited interior of the peripheral ring. This dual-ring phenomenon has previously observed by Hu et al. [146]. For samples II-IV, the majority of nanoparticles accumulate at the secondary ring, and the second largest density of the nanoparticles is at the periphery. The nanoparticles are uniformly deposited inside the secondary ring and in the areas between the peripheral and secondary rings (see Figures 3.3bII-3.3bIV). Only at a temperature of 47 °C, the secondary ring is deposited in the middle of the droplet, and its size is smaller than the secondary ring of other samples at temperatures of 64 and 81 °C (see Figures 3.3bII and 3.3bIV). The distance between the two rings is indicated by three oval arrows in Figure 3.3cII-IV. The density distribution profiles reveal that there is an increase in the size of the secondary ring with enhancing the temperature from 47 to 81 °C. In other words, the secondary ring deposits closer to the perimeter when increasing the substrate surface temperature. Sample V at a temperature of 99 °C exhibits a completely different deposition pattern feature from the other examined temperatures. Apart from the initial contact line, about 60% of the total area is covered by several distinct deposition lines fixed to the right side of the droplet (see Figure 3.3bV). Obviously, sample V presents the most non-uniform nanoparticles distribution which originates from the aforementioned deposition lines (see Figure 3.3cV). The density value rises at the deposition lines and decreases between two consecutive lines, thus causing several peaks in the density distribution profile on the right side of the square (sample area) shown in Figure 3.3bV (see the right side of Figure 3.3cV), reveal that the deposition lines at the regions near the fixed contact line (the right side of the square in Figure 3.3bV) contain much more nanoparticles compared with those on the left side of the square in Figure 3.3bV (see the left side of Figure 3.3cV).

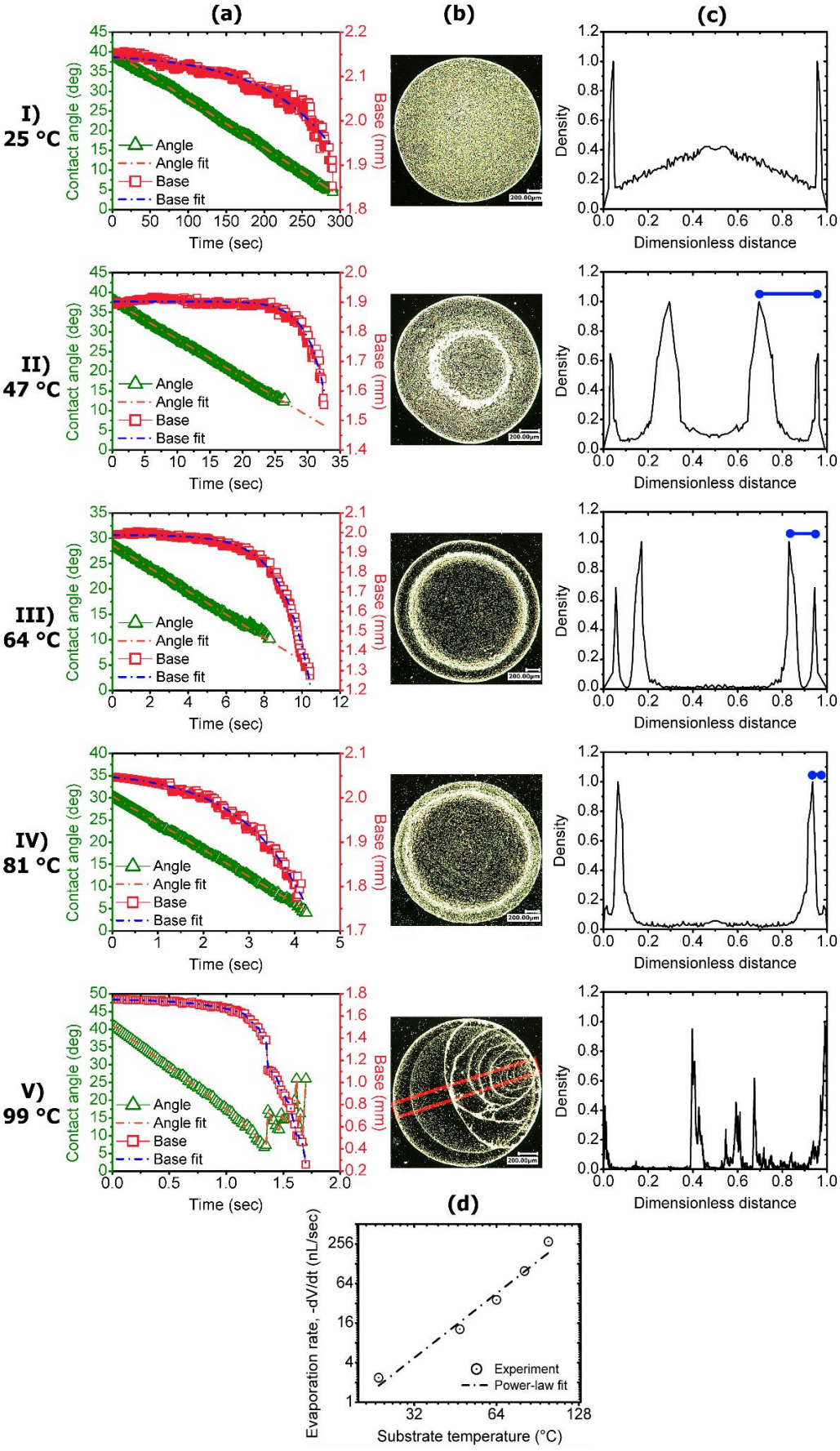
(a)
(b)
(c)
I)
25 °C
II)
47 °C
III)
64 °C
IV)
81 °C
V)
99 °C
Contact angle (deg)
Base (mm)
Time (sec)
Angle
Angle fit
Base
Base fit
Density
Dimensionless distance
200.00μm
(d)
Evaporation rate, -dV/dt (nL/sec)
Substrate temperature (°C)
Experiment
Power-law fit

Figure 3.3. (a) Evolution of base and contact angle for evaporating 0.05 wt % CuO-water nanofluid droplets on a non-heated substrate at 25 °C and heated substrates at different temperatures of 47, 64, 81, and 99 °C. (b) Dried deposits of 0.05 wt % CuO-water nanofluid droplets on a non-heated substrate at 25 °C and heated substrates at different temperatures of 47, 64, 81, and 99 °C. The scale bar is 200 μm. (c) Density distribution profiles of dried CuO-water droplets at different temperatures of 25, 47 °C, 64, 81, and 99 °C. The dimensionless distance in (c) for samples I-V indicates the droplets diameter (from edge to edge). For sample V, the distance is from the left to the right side of the square shown in the deposit. Note that the line profiles are relative measurements of the density distribution of the nanoparticles. The oval arrows in (c) indicate the distance between the peripheral and secondary rings at 47, 64, and 81 °C. (d) Effect of substrate temperature on evaporation rate.

3.4.2 Flow pattern and deposition formation during evaporation

To understand the deposition features in Figure 3.3, the evaporation process of droplets at all studied temperatures was observed via optical microscopy (see Supporting Information). The microscope was focused on the initial contact line. The sequential images of all videos are shown in Figures 3.4-3.9, and 3.12, and 3.13. The first sequence shows the temporal evolution of the drying droplet on the non-heated substrate (25 °C). The 500× magnification consecutive still images from this sequence are provided in Figure 3.4. It can be clearly seen that the contact line is pinned during all the evaporation time due to the outward capillary flow, which makes the nanoparticles drift towards the contact line. The number of nanoparticles transported away from the droplet centre and to reach the edge increases as the evaporation time proceeds [16,21]. However, from the early stages of the evaporation, some nanoparticles move outward to the edge but do not deposit there. These nanoparticles are convected back on the droplet surface towards the central region of the droplet, building a ring-like collection (cluster) of nanoparticles close to the air-liquid interface (see Figure 3.4h-k). The outgoing nanoparticles are in the same plane of those deposited at the pinned contact line, implying that these nanoparticles are close to the substrate surface, but the images of the convected backward nanoparticles are out of focus, indicating that the nanoparticles are near the air-liquid interface when they move inward to the top of the droplet [21,177]. The

region between the contact line and the ring-like nanoparticles cluster forms an eddy region, as indicated in between two bars in Figure 3.4h-k. There is a clear eddy between the two lines, which points towards a convection roll in this region. The nature and origin of this convection will be discussed later. In the final stages of the evaporation, the ring-like cluster drifts towards the drop centre, increasing the width of the eddy, as shown in Figure 3.4h-k. The depinning of the contact line pushes back the ring-like cluster towards the central area (Figure 3.4k,l), and then the cluster deposits at the centre when the evaporation is completed. However, the deposition feature does not show a ring-like pattern at the droplet centre (see sample I in Figure 3.3b). The density profile also represents the higher fraction of the nanoparticles at the central region of the droplet, except at the contact line (see Figure 3.3cI). The video corresponding to this case shows the formation of the nearly uniform deposition as some nanoparticles do not deposit at the edge from the early stages of evaporation, preventing the coffee-ring effect [21].

Sequences showing the evaporation of the droplets on the substrates heated at 47 and 64 °C, respectively are analysed to further examine deposition mechanisms. The consecutive images of the aforementioned sequences are given in Figures 3.5 and 3.6 for temperatures of 47 and 64 °C, respectively. Although nanoparticles motion at 47 °C and 64 °C is similar to what was observed inside the evaporating droplet on the non-heated substrate, the ring-like cluster of the nanoparticles at 47 and 64 °C deposits as a distinct secondary ring (Figures 3.5l and 3.6l) unlike the non-heated case (25 °C), in which the cluster deposition does not show a ring-like pattern (Figure 3.4l). When most of water evaporates, and the contact line depins (Figures 3.5j and 3.6j), the nanoparticles at the edge deposit on the substrate, and then the ring-like cluster travels towards the depinned contact line until they reach the edge (Figures 3.5k and 3.6k) and deposit onto the substrate (Figures 3.5l and 3.6l). Figure 3.7 shows top views of the evaporating droplet at 64 °C at a magnification of 100×. The eddy identified previously is believed to be driven by surface tension gradients, Marangoni convection, as reported by previous studies [69,146,177]. The Marangoni eddy and deposition of the secondary ring is clearly shown in Figures 3.7d-j and 3.7k,l, respectively.

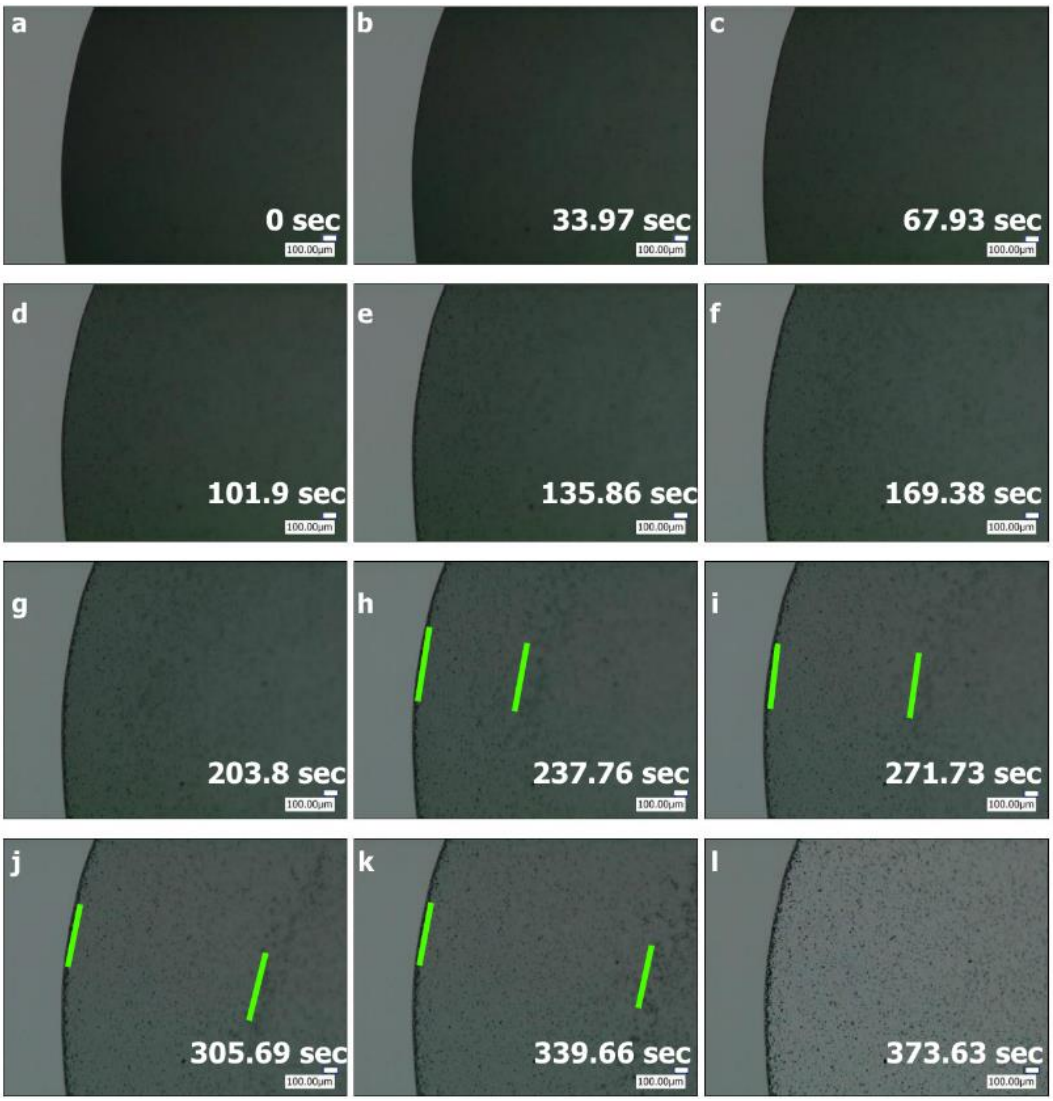

Figure 3.4. Snapshots from a video microscopy of the evaporation process of a water droplet containing 0.05 wt % CuO nanoparticles deposited onto a non-heated silicon substrate (at 25 °C). The Marangoni eddy is indicated in between the bars. The optical micrographs are recorded at a temporal resolution of 60 fps and at 500× magnification. The scale bar is 100 *μ*m.

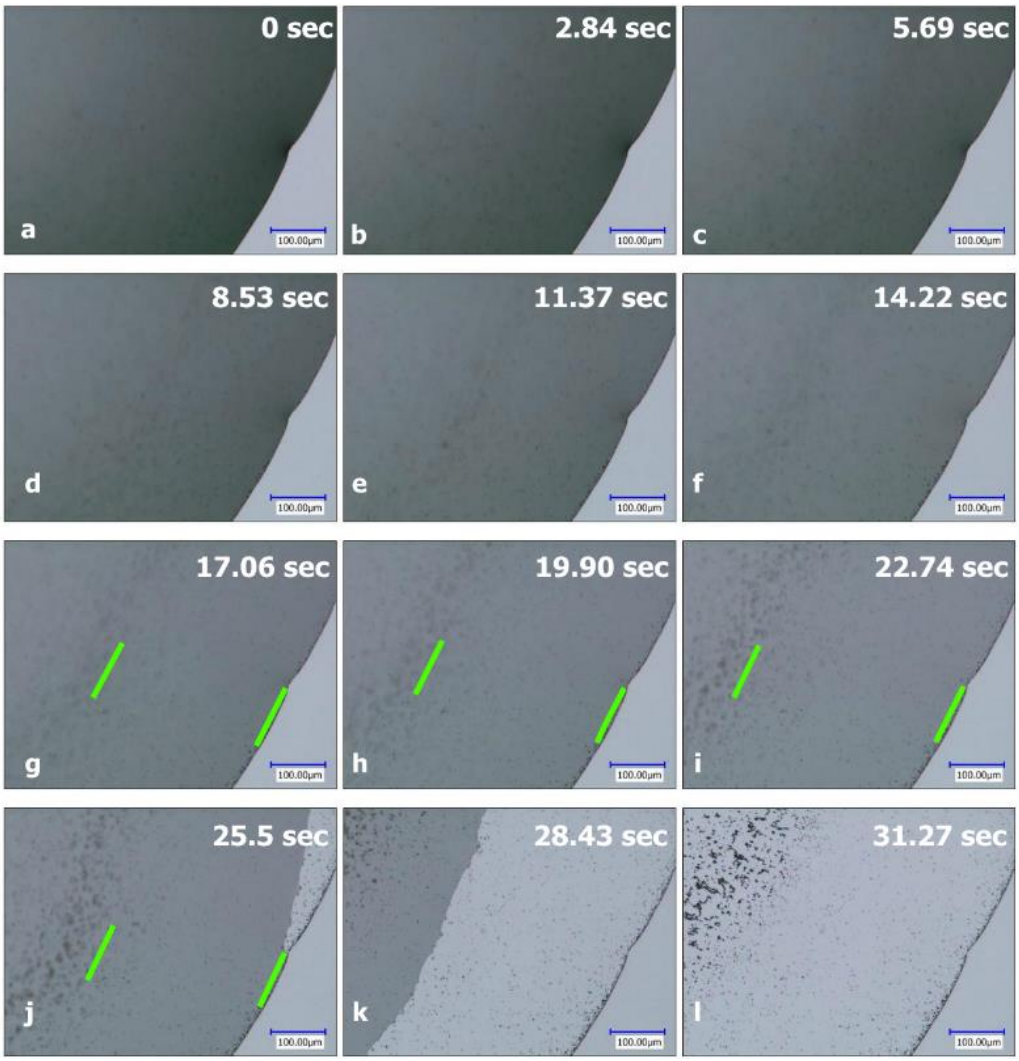

Figure 3.5. Snapshots from a video microscopy of the evaporation process of a water droplet containing 0.05 wt % CuO nanoparticles deposited onto a heated silicon substrate at 47 °C. The Marangoni eddy is indicated in between the bars. The optical micrographs are recorded at a temporal resolution of 60 fps and at 500× magnification. The scale bar is 100 μm.

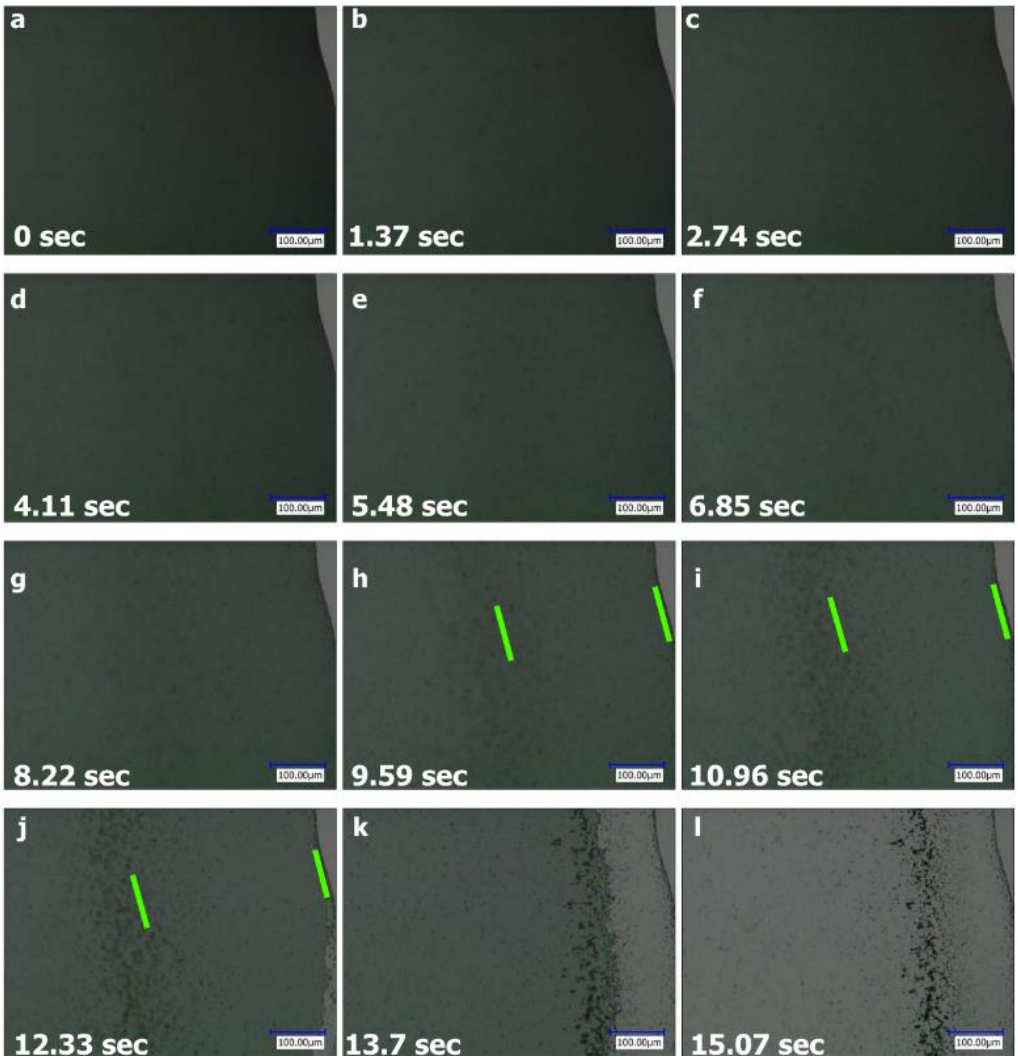

Figure 3.6. Snapshots from a video microscopy of the evaporation process of a water droplet containing 0.05 wt % CuO nanoparticles deposited onto a heated silicon substrate at 64 °C. The Marangoni eddy is indicated in between the bars. The optical micrographs are recorded at the temporal resolution of 60 fps and at 500× magnification. The scale bar is 100 μm.

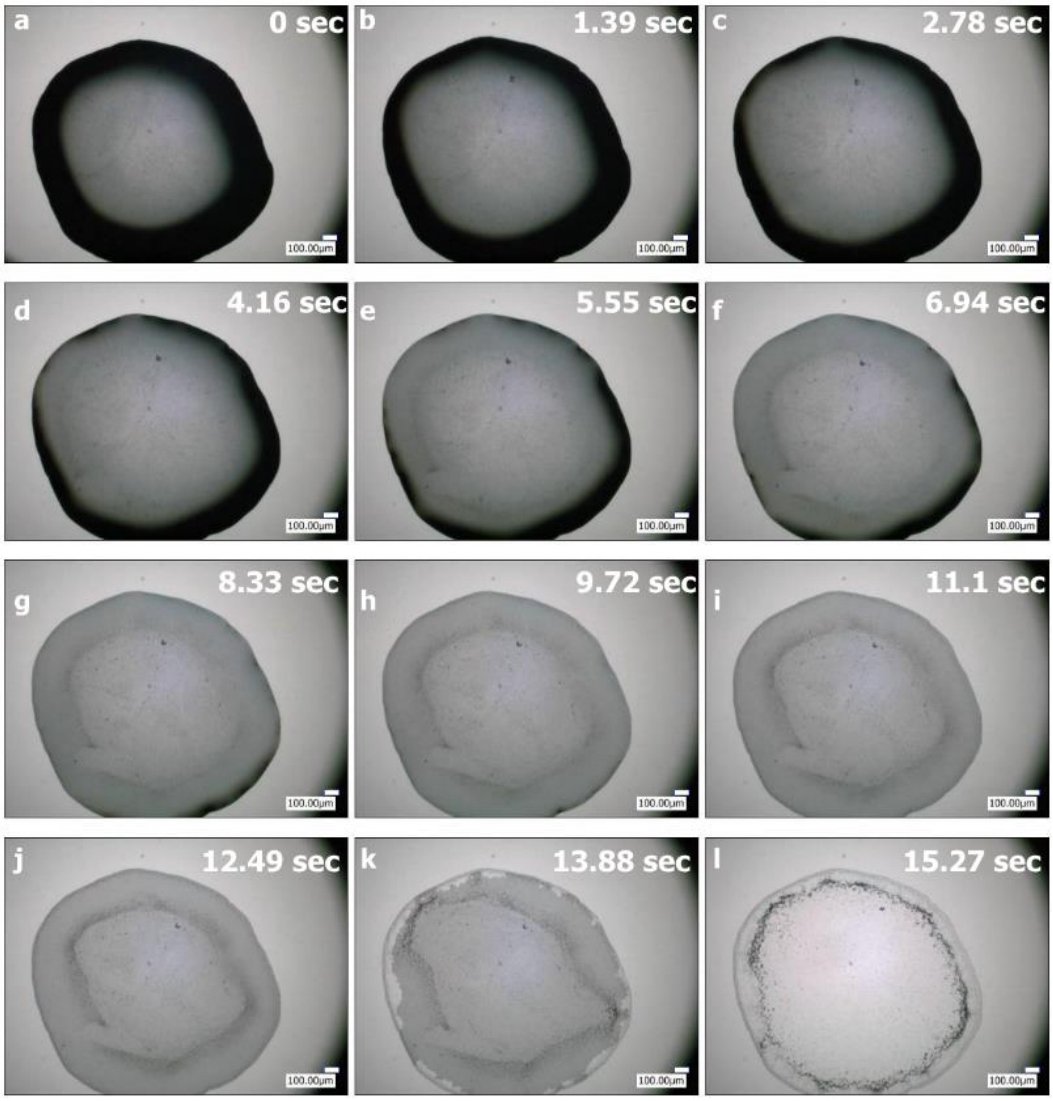

Figure 3.7. Snapshots from a video microscopy of the evaporation process of a water droplet containing 0.05 wt % CuO nanoparticles deposited onto a heated silicon substrate at 64 °C. The optical micrographs are recorded at a temporal resolution of 60 fps and at 100× magnification. The scale bar is 100 μm.

The 500× magnification consecutive still images of the drying droplet at 81 °C are given in Figure 3.8. Similarly to Figures 3.5-3.7, after depinning of the initial contact line, the secondary ring deposits on the substrate due to the ring-like nanoparticles cluster on the top region of the droplet caused by the Marangoni effect (Figure 3.8). Snapshots in Figure 3.9 (taken from Supporting Information Video S6) show the formation of the secondary ring at 81 °C with lower magnification of 100×. The

secondary ring deposition on the hot surface when reaching the depinned edge is clearly presented in Figure 3.9k.

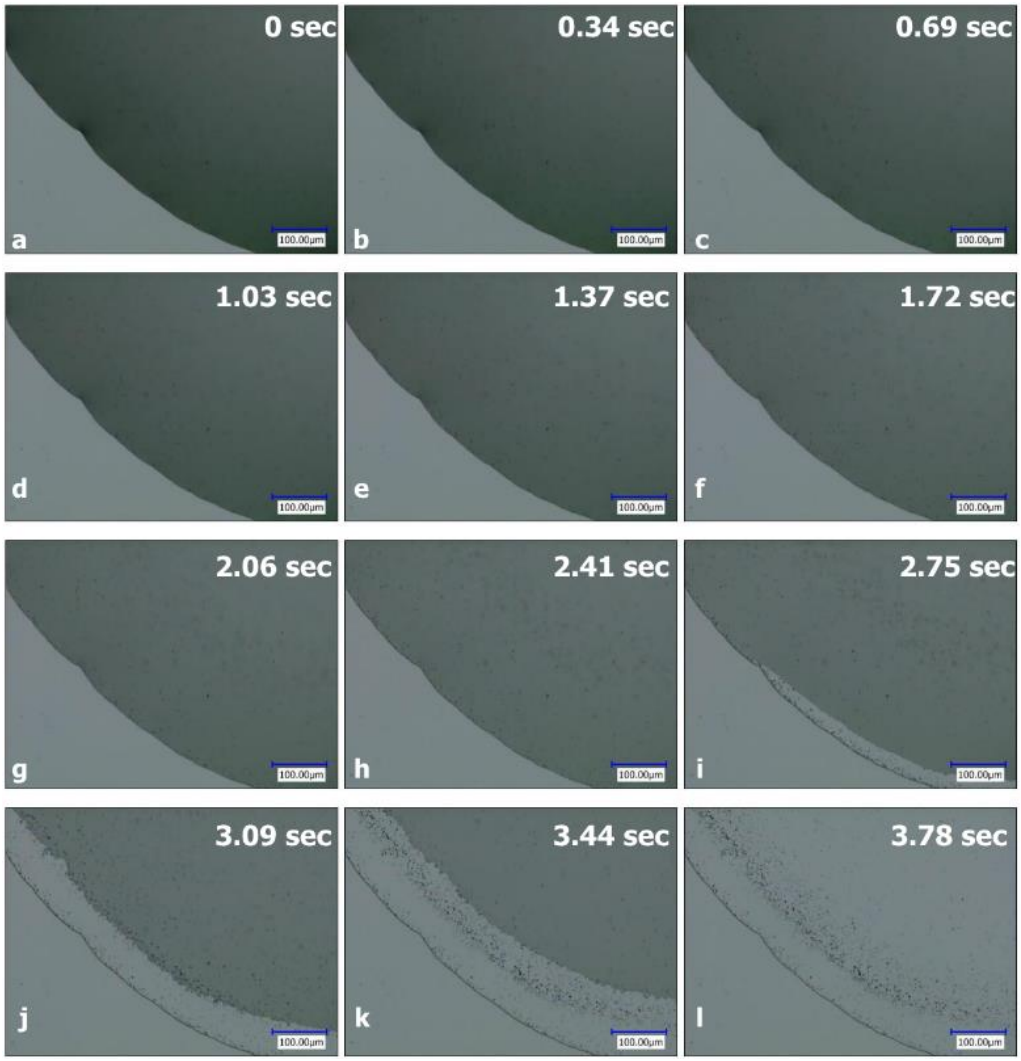

Figure 3.8. Snapshots from a video microscopy of the evaporation process of a water droplet containing 0.05 wt % CuO nanoparticles deposited onto a heated silicon substrate at 81 °C. The optical micrographs are recorded at a temporal resolution of 60 fps and at 500× magnification. The scale bar is 100 μm.

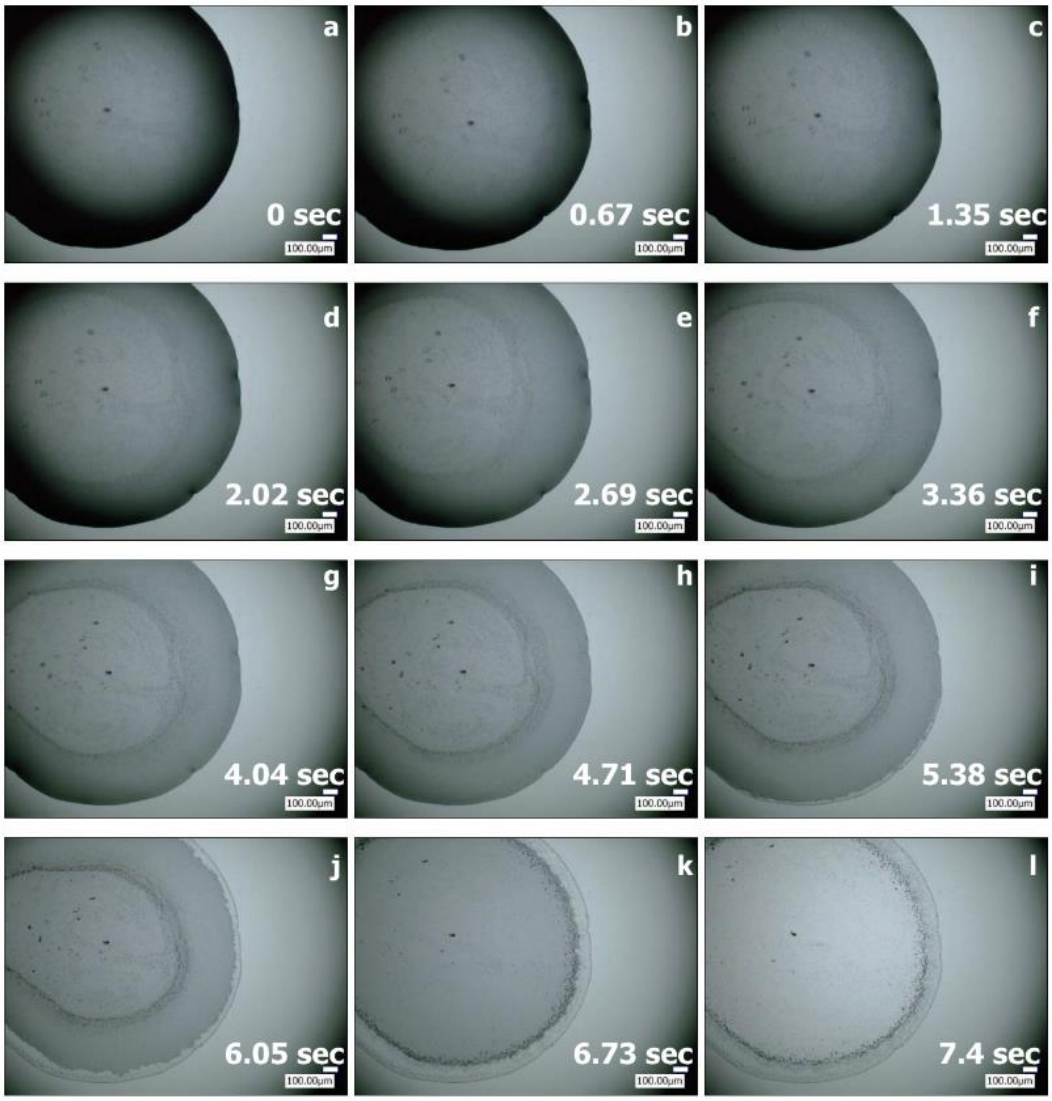

Figure 3.9. Snapshots from a video microscopy of the evaporation process of a water droplet containing 0.05 wt % CuO nanoparticles deposited onto a heated silicon substrate at 81 °C. The optical micrographs are recorded at a temporal resolution of 60 fps and at 100× magnification. The scale bar is 100 μm.

Side views of a drying droplet at 47, 64, and 81 °C are sketched in Figure 3.10 based on the above analysis. In Figure 3.10a, two mechanisms responsible for the outward capillary and Marangoni flows for the deposition features of samples II-IV given in Figure 3.3 are indicated by the dotted and dashed arrows, respectively. First, the nanoparticles move adjacent to the substrate surface in the direction of the dotted arrow to reach the initial edge and deposit near the contact line. A fraction of these

nanoparticles do not deposit at the edge and move back inward farther away from the substrate surface, as shown by the dashed arrow (Figure 3.10). The repelled nanoparticles stop near the air-liquid interface, leading to a ring-like nanoparticles collection in the top part of the droplet. As evaporation progresses, more nanoparticles attach to the edge and also on the top region of the droplet (Figure 3.10b,c). Finally, the initial contact line depins and moves radially (Figure 3.10c,d), resulting in nanoparticles deposition at the edge, named the peripheral ring in Figure 3.10. At the final stage of the evaporation, the ring-like nanoparticles cluster is very close to the substrate surface; the cluster drifts outward to reach the depinned contact line (Figure 3.10d) and deposits as a secondary ring on the substrate surface (Figure 3.10e).

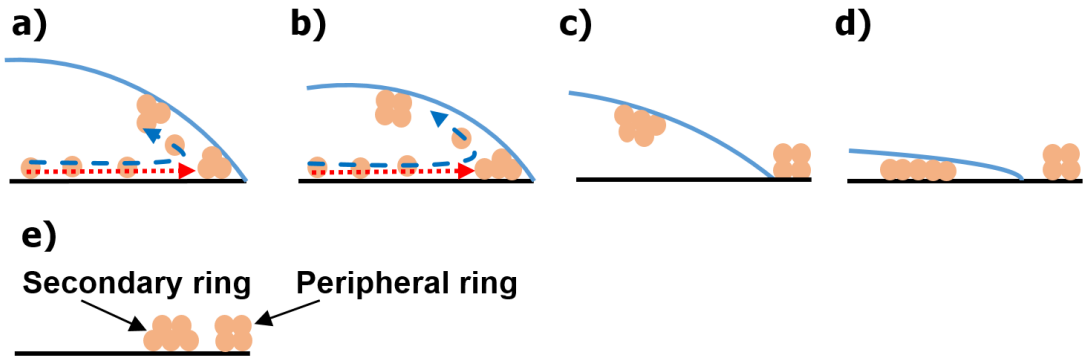

Figure 3.10. Formation mechanism schematic of the secondary ring deposited after dried droplet of CuO-water 0.05 wt % onto a hot substrate (47, 64, and 81 °C): (a) The edge is pinned; the nanoparticles move outward to the edge (shown by the dotted arrow), some arrive at the contact line, and some move back radially in to the top of the drying droplet (indicated by the dashed arrow). (b) As time proceeds, the concentration of the nanoparticle increases at the pinned edge and on the top region of the droplet. A ring-like cluster is also built by the repelled nanoparticles near the air-liquid interface. (c) The contact line depins and left behind a peripheral ring on the substrate surface. (d) The nanoparticles cluster on the top region drifts to the edge after the initial depinning; the ring-like cluster stops traveling when it reaches the edge and finally deposits on the substrate as a secondary ring. (e) Two distinct rings of deposits left behind when the evaporation has been completed.

Amongst three temperatures of 47, 64, and 81 °C, the lowest (47 °C) and highest (81 °C) substrate temperatures show the longest (~310 μm) and shortest (~190 μm)

eddy widths just before the initial contact line depins, respectively, as illustrated in Figures 3.11aI, 3.11bI, and 3.11cI. It is found from Figure 3.11aI-II that there is an increase of approximately 80 μm in the eddy width after the complete evaporation compared with that before the edge depinning, whereas the eddy width is decreased after the evaporation about 190 and 130 μm at temperatures of 64 °C (Figure 3.11bI-II) and 81 °C (Figure 3.11cI-II), respectively. Figure 3.5j,k shows that the depinning of the contact line pushes back the ring of nanoparticles inward to the droplet centre (Supporting Information Video S2), which can be a delay for nanoparticles to reach the edge. This reveals that depinning of the contact line significantly affects the location of the secondary ring deposition as well as the eddy width after the complete evaporation. Even after the evaporation, the longest (~390 μm) and shortest (~60 μm) eddy widths occurred at the lowest (47 °C) and highest (81 °C) substrate temperatures, respectively. Therefore, the eddy width increases with decreasing the substrate temperature. This is also confirmed by the oval arrows shown in the density profiles (Figure 3.3cII-IV), which indicate the distance between the initial contact line and the secondary ring. Despite the shorter eddy width at 64 and 81 °C before depinning compared with that at 47 °C, the ring-like cluster (at 64 and 81 °C) arrives at the edge sooner than that at 47 °C after the edge begins depinning, and hence the secondary rings at 64 and 81 °C deposit closer to the peripheral rings. Higher substrate temperature (81 °C) enhances nanoparticles velocity because of higher evaporation rate, and thus the particles attach rapidly to the depinned contact line, leading to a shorter eddy width after the complete evaporation.

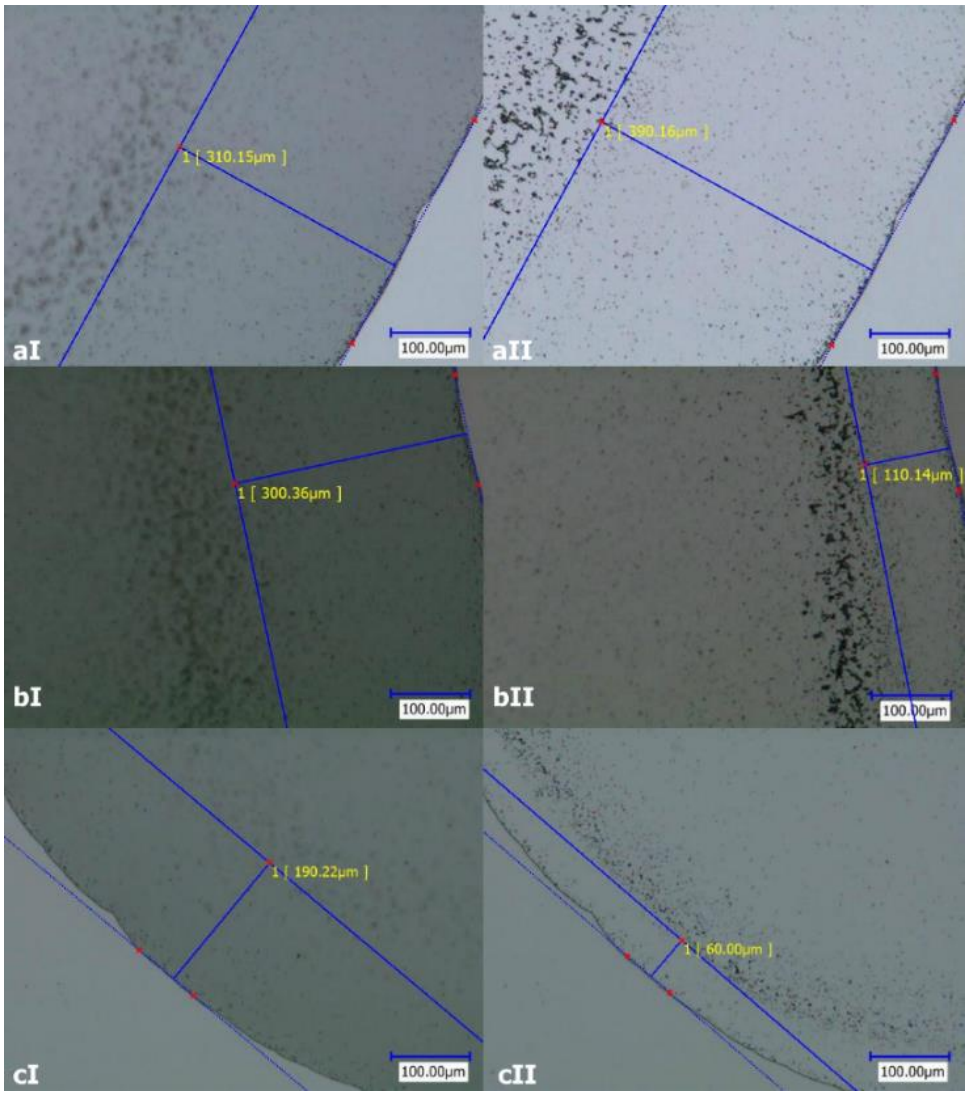

Figure 3.11. 500× deposit images of water droplets containing 0.05 wt % CuO nanoparticles just before the depinning of the initial contact line (left side, shown by I) and after the complete evaporation (right side, shown by II): (aI) before depinning at 47 °C, (aII) after evaporation at 47 °C, (bI) before depinning at 64 °C, (bII) after evaporation at 64 °C, (cI) before depinning at 81 °C, and (cII) after evaporation at 81 °C. The distance between the peripheral and secondary rings is shown in square brackets. The scale bar is 100 μm.

At higher temperatures of 81 and 99 °C, in the very beginning stages of evaporation process ($t < 0.3t_{evap}$, t_{evap} is total evaporation time) (99 °C, Figure 3.12), two counter-rotating vortices are obviously seen. To illustrate the flow direction at 99 °C, two small clusters of nanoparticles on both sides of the evaporating droplet (shown inside the circles in Figure 3.12a-d) are tracked to indicate the different positions of the

nanoparticles at different times. The arrows indicate the direction of the nanoparticles movement, which is clockwise and counter-clockwise on the right- and left-hand sides of the drying droplet, respectively. It is noteworthy to mention that the nanoparticles participating in the vortices are on the top region of the evaporating droplet. After two vortices stop rotating, a ring-like collection of nanoparticles remains on the top region of the droplet until the end of evaporation. At the late stages of the evaporation process ($t > 0.7t_{evap}$) (Figure 3.12i-l), the initial contact line jumps to a new contact line which depins and repins for several times, resulting in a set of rings pinned to one side of the droplet (left part of Figure 3.12i-l), leading to the well-known "stick-slip" behaviour [25,65,145]. The temporal evolution of the drying droplet at 99 °C at higher magnification of 500× is given in Figure 3.13. The velocity of the nanoparticles at 99 °C is much higher because of the higher substrate temperature compared with that at 47, 64, and 81 °C. Some nanoparticles close to the substrate leave the central region of the droplet, arrive near the edge, and deposit there. An example of these nanoparticles movement during the evaporation is shown in Figure 3.14a by a line which indicates a trace of a specific small cluster of nanoparticles movement from its first location (far away from the edge) to the final location (close to the edge). On the other hand, a group of nanoparticles are simultaneously trapped in an eddy region, frequently traveling inward and outward in this region, and finally join the ring-like collection of the nanoparticles on the top region. This rapid circulating flow motion near the edge region can be seen by tracking an individual small cluster of nanoparticles as shown in Figure 3.14b, and it continues for the other suspended nanoparticles until the contact line depins. A ring-like collection of nanoparticles appears on the top of the drying droplet, which is formed by the vortices as well as the repelled nanoparticles (Figure 3.13a-i). As shown in Figure 3.13j-o, the contact line jumps, leading to repinning of a new contact line, towards which nanoparticles move (Figure 3.13n) and deposit (Figure 3.13o).

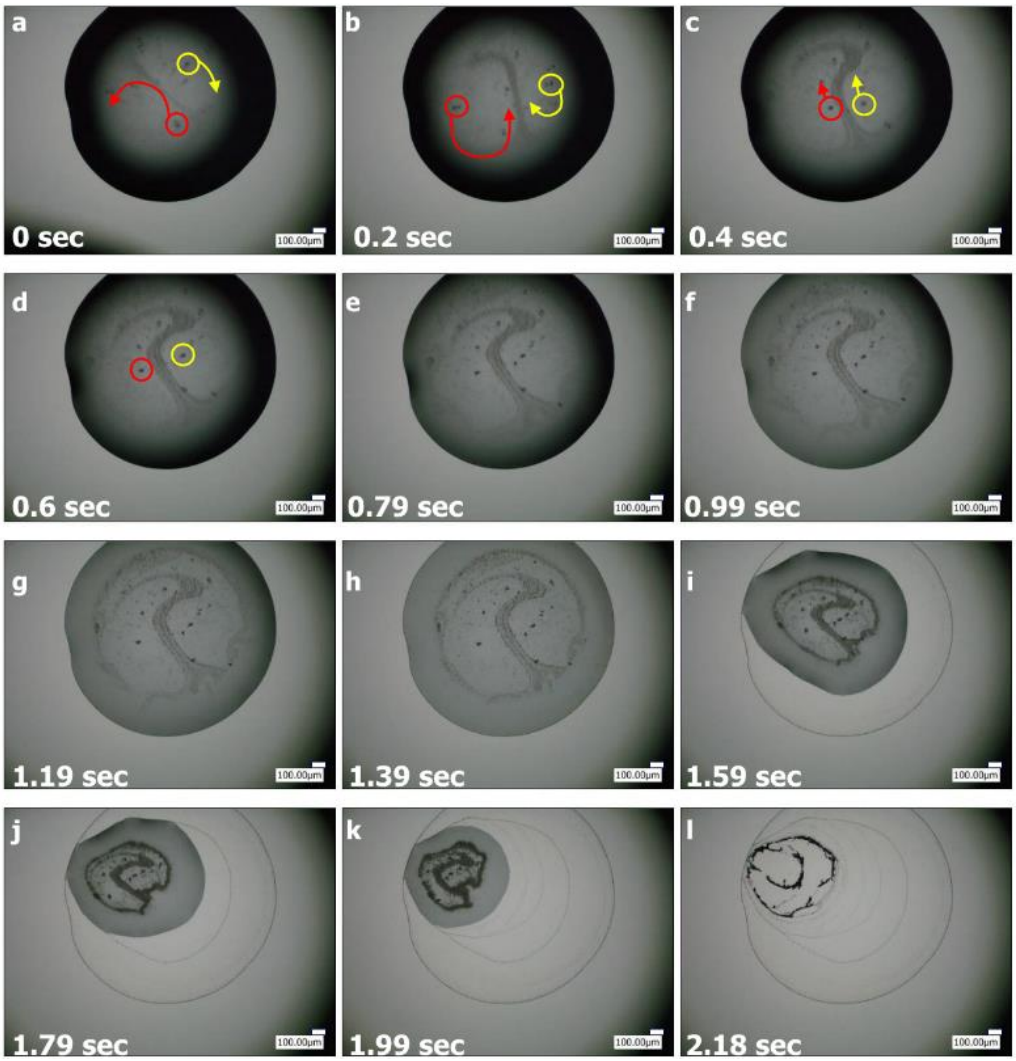

Figure 3.12. Snapshots from a video microscopy of the evaporation process of a water droplet containing 0.05 wt % CuO nanoparticles deposited onto a heated silicon substrate at 99 °C. The optical micrographs are recorded at a temporal resolution of 125 fps and at 100× magnification. The arrows indicate the movement direction of nanoparticles, which are shown by the circles. The scale bar is 100 μm.

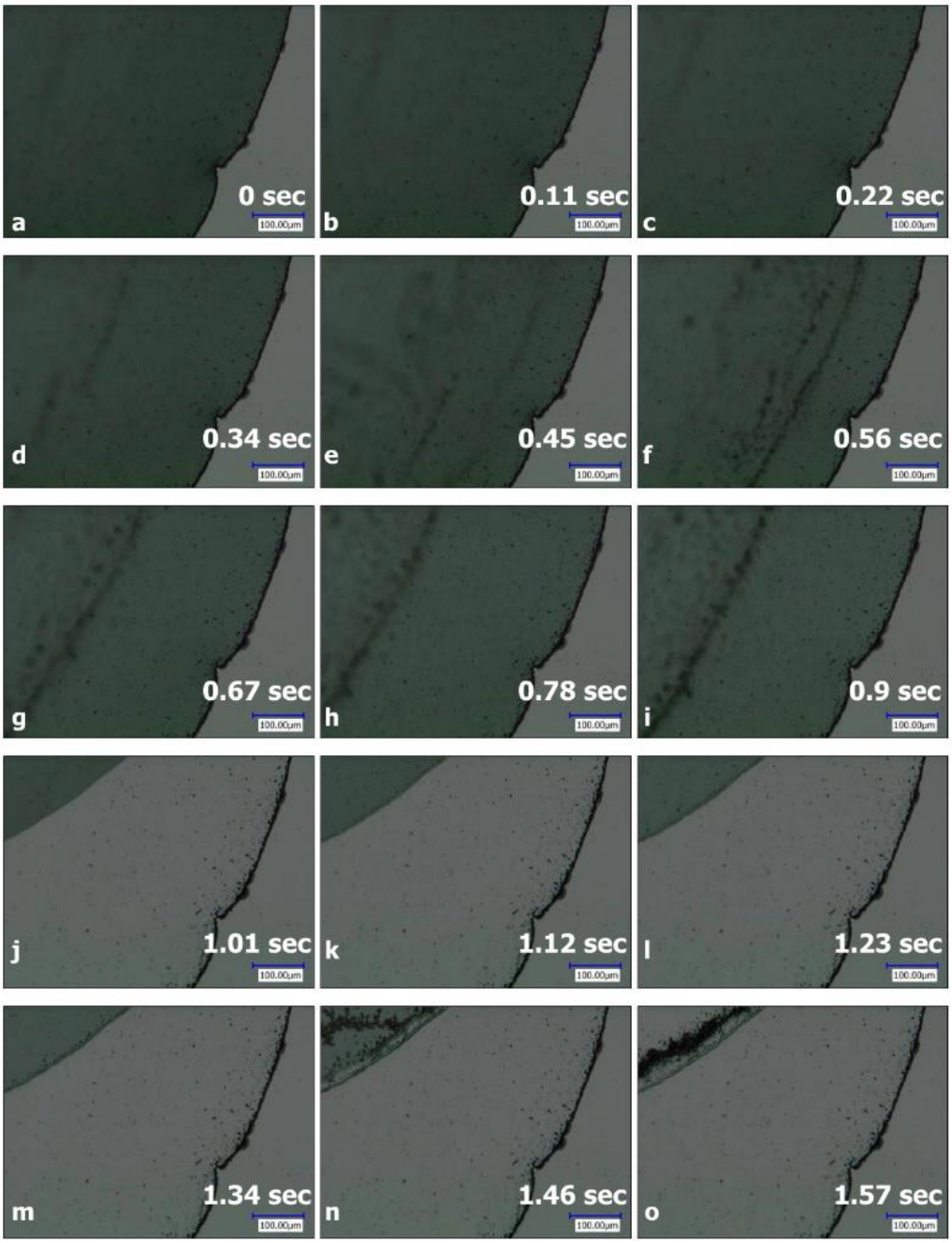

Figure 3.13. Snapshots from a video microscopy of the evaporation process of a water droplet containing 0.05 wt % CuO nanoparticles deposited onto a heated silicon substrate at 99 °C. The optical micrographs are recorded at a temporal resolution of 60 fps and at 500× magnification. The scale bar is 100 μm.

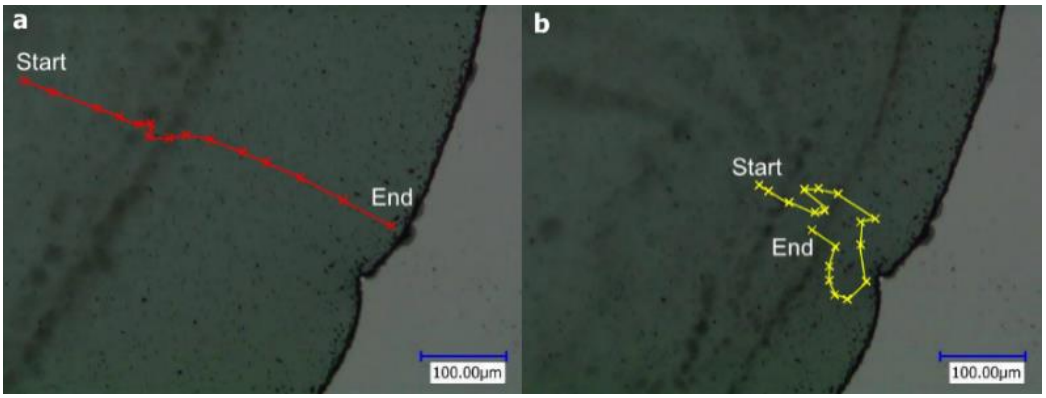

Figure 3.14. 500× still images of a water droplet containing 0.05 wt % CuO nanoparticles deposited onto a heated silicon substrate at 99 °C: (a) The line shows a tracer nanoparticle which moves towards the edge and deposit near the edge; the start and end points of the movement are at evaporation times of 0.08 and 0.68 s, respectively. (b) The line shows the movement direction of a specific nanoparticle cluster which circulates in the region very close to the edge; the start and final evaporation time of the movement are at 0.2 and 0.52 s, respectively. The optical micrographs are recorded at a temporal resolution of 60 fps and at 500× magnification. The scale bar is 100 μm.

3.4.3 Infrared thermography

It is well understood from the previous section that the Marangoni effect is potentially a responsible mechanism for the formation of the secondary ring as it pulls the suspended nanoparticles from the area in the vicinity of the edge to the top surface of the drying droplets. Marangoni flow is created by a surface tension gradient along the surface of a liquid droplet which is induced by either temperature or concentration gradients. In other words, the presence of a temperature gradient on the liquid droplet's surface induces the Marangoni effect. For this reason, the surface temperature distributions of the drying droplets shown in Figure 3.1a were visualised during the evaporation by means of an infrared camera, and the corresponding temperature profiles at different evaporation time are given in Figure 3.15. The infrared thermography results show that the surface temperature at the edge is the highest for all samples I-V shown in Figure 3.3 (see Figure 3.15). Thus, the droplet apex is the coolest position. Fluids naturally tend to flow from the region with lower surface tension to that of higher surface tension. The surface tension of ordinary

liquids (e.g., water) decreases as temperature increases. Therefore, a radially inward surface flow is expected to be driven from the edge to the top region along the air-liquid interface since the temperature decreases from the edge to the surface centre, as shown in Figure 3.15. In addition, a stagnation point should appear somewhere at the air-liquid interface close to the contact line, beyond which there is an outward surface flow (see Figure 3.16). Deegan et al. [15] also confirmed the existence of such a stagnation point which occurs at the radial point at which the drag on the surface from an underlying liquid, which is diverging with the velocity as the contact line is approached, overcomes the oppositely directed surface tension gradient (see Figure 3.16). According to the experimental study of Xu and Luo [177], there are two flow regions in the evaporating droplets: one is the outward flow, in which particles move outward adjacent to the surface and stop at the edge; the other is the convective flow, in which particles move towards the contact line but then change their direction and move inward along the vapour-liquid interface. The authors found these two different flow regions by tracking the motion of particles and concluded that a stagnation point exists on the droplet surface closer to the contact line than the turning point of particles [177]. Moreover, the theoretical analysis of Xu et al. [178] confirmed that, when the thermal Marangoni effect is remarkable and a stagnation point exists on the droplet surface, only the particles participating in the outward flow region can reach the contact line and form the deposit ring. In other words, all the particles inside the evaporating droplet do not form the deposit ring due to the existence of the stagnation point, and thus a group of particles appears in the convective flow region near the droplet surface [178]. This behaviour is in good agreement with the observations of the present study showing that some nanoparticles stop at the edge and form the outer ring (shown by the solid arrows in Figure 3.16), and some nanoparticles move to the droplet surface and trapped in the convective flow region leading to the formation of the inner ring (shown by the dashed arrows in Figure 3.16). The main reason behind the formation of the inner ring is the stagnation point. When the nanoparticles are within the stagnation point (the convective flow region), the nanoparticles stop near the droplet surface and do

not return back to the edge because this region is induced and dominated by the thermal Marangoni effect which counteracts the outward flow.

Snapshots from optical microscopy at 47, 64, 81, and 99 °C have revealed that the repelled nanoparticles have a significant role on the formation of the ring-like nanoparticles collection near the top surface of the droplet and, therefore, the deposition of a distinct secondary ring on the substrate at 47, 64, and 81 °C (Supporting Information Videos S2, S3, and S5). Similarly, when the substrate temperature is at 25 °C, the ring-like collection of the nanoparticles has been found at the top section of the droplet, but the corresponding deposit feature does not show a distinct secondary ring (Figure 3.3aI and Supporting Information Video S1), which has been seen for 47, 64, and 81 °C. Moreover, when the substrate is at the highest temperature of 99 °C, a distinct secondary ring cannot be seen on the substrate after the evaporation but several deposition lines left behind the evaporation instead (Figure 3.3bV and Supporting Information Video S7). As shown in Figure 3.15aI-aV, the value of the temperature difference of the air-liquid interface between the centre and the edge increases with increasing the substrate temperature. The dimensionless thermal Marangoni number ($M_a{}^T$) which is induced by temperature gradient is defined as

$$M_a{}^T = \frac{-\frac{d\sigma}{dT}R}{\mu\alpha}\Delta T \tag{3.1}$$

where $\mathrm{d}\sigma/_{dT}$ is the change in surface tension with temperature, in N m/°C; R is the droplet radius, in m; ΔT is temperature difference between the droplet centre and edge, in °C; μ is dynamic viscosity, in Pa.s; and α is thermal diffusivity, in m²/s. The dynamic viscosity of nanofluid at different temperatures is calculated and found that there is a negligible change in the values compared to those of pure water. This can be due to the very low concentration of CuO nanoparticles (0.05 wt %). Since the addition of the nanoparticles does not affect pure water properties, the temperature-dependent Marangoni number of pure water is calculated for each substrate temperature at different times, as shown in Figure 3.15b. The thermal Marangoni number increases with substrate temperature. In addition, the thermal Marangoni

numbers at all substrate temperatures exceed the critical value, revealing the occurrence of surface-tension driven convection along the interface [179]. It can be deduced that the formation of the distinct secondary ring depends on the Marangoni strength. Regarding the central region of all samples I-V in Figure 3.3c, those (samples II-IV) with the initial thermal Marangoni numbers (at $t = 0.45$ s) between 2.4×10^5 and 9.9×10^5 (Figure 3.15b) show the more "uniform" deposition feature in the centre (inside the secondary ring) in comparison with that of sample I (25 °C, Figure 3.3cI) with the thermal Marangoni number equal to 0.4×10^5. For sample V (99 °C, Figure 3.3cV) with the thermal Marangoni number of 13.7×10^5, the central region is completely non-uniform due mainly to the stick-slip behaviour.

In the previous section, it was mentioned that the eddy width can be attributed to the substrate temperature. Here, it may be noteworthy to mention that the eddy width of the drying droplets (47, 64, and 81 °C) at the initial depinning time (Figures 3.11aI, 3.11bI, and 3.11cI) increases with the suppression of the Marangoni (Figure 3.15b). In addition, after the complete evaporation, the possibility of the secondary ring deposition in the regions closer to the peripheral ring is increased with increasing the thermal Marangoni number from 2.4×10^5 (case of 47 °C) to 9.9×10^5 (case of 81 °C) (see Figures 3.11aII, 3.11bII, and 3.11cII).

The vigorous, rapid circulating flow motion (i.e., "Marangoni eddies") near the edge region (99 °C, Figure 3.14b and Supporting Information Video S8) can be attributed to the large thermal Marangoni number (Figure 3.15b). The evaporating droplet at 99 °C has a higher surface temperature difference between the centre and edge at the initial time of the evaporation ($t = 0.45$ s), which makes an extremely strong Marangoni flow, and thus a somewhat different internal flow pattern appears within the evaporating droplet. The Marangoni flow induces the velocity of nanoparticles inside the droplet. As the evaporating droplet at 99 °C has the strongest Marangoni flow amongst all of the studied cases, the velocity of nanoparticles at 99 °C is the highest compared with that at lower temperatures.

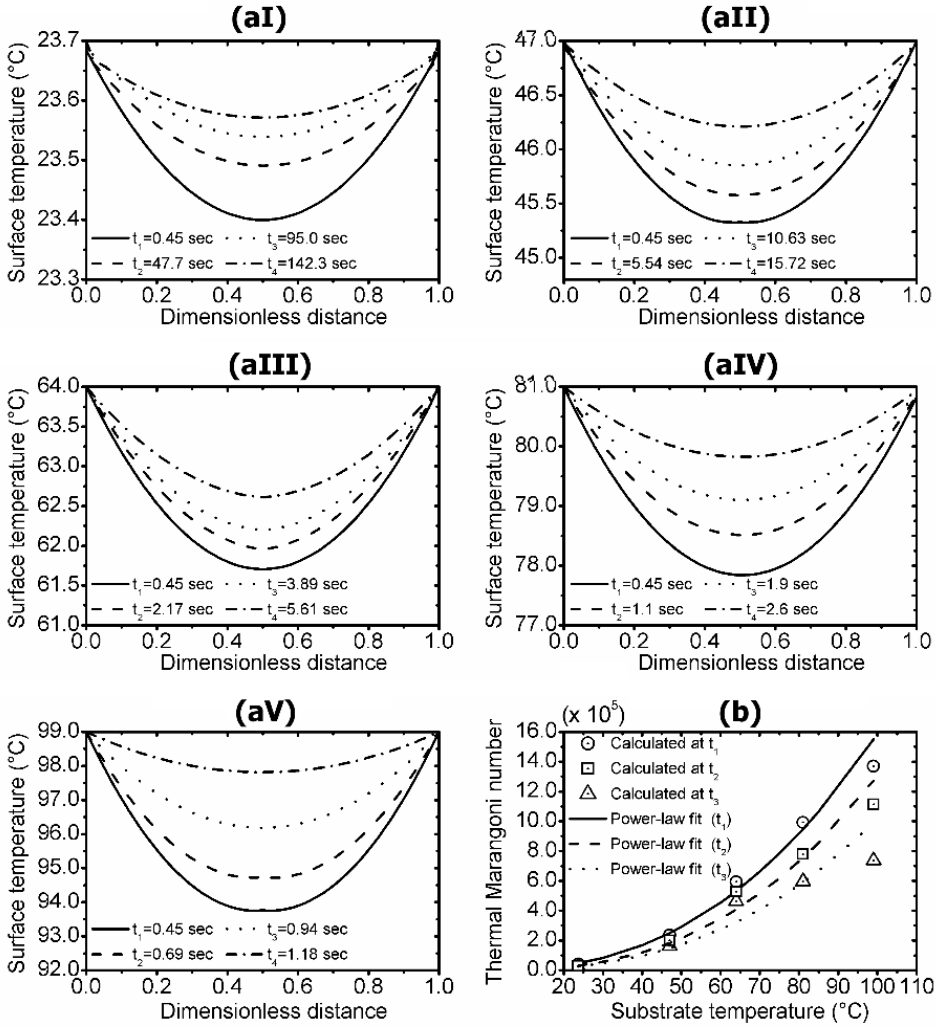

Figure 3.15. Surface temperature distribution profiles of the droplets at different evaporation time: (aI) a non-heated silicon substrate at 25 °C (θ_i = 40°), (aII) heated substrates at temperatures of 47 °C (θ_i = 39°), (aIII) 64 °C (θ_i = 29°), (aIV) 81 °C (θ_i = 30°), and (aV) 99 °C (θ_i = 41°). The dimensionless distance indicates the normalised diameter of the droplets (from edge to edge). θ_i is the initial contact angle of the droplets. (b) Effect of substrate temperature on thermal Marangoni number calculated at different times.

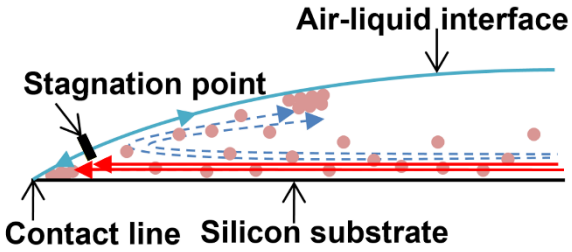

Figure 3.16. Schematic description of the flow pattern inside an evaporating water droplet containing CuO nanoparticles placed on a heated silicon substrate; the solid and dashed arrows indicate the outward capillary and thermally driven Marangoni flows, respectively. The black bar in the picture indicates a stagnation point where the direction change of the surface flow occurs.

3.5 Conclusions

In this study, a series of experiments were carried out to provide detailed observations of how a wide range of substrate temperatures can lead to three different deposition patterns from evaporating water droplets containing CuO nanoparticles. The presence of temperature gradients along the air-liquid interface induces a radial Marangoni flow that prevents nanoparticles from depositing near the edge and returns particles to build a ring-like collection of the solute on the top surface of the drop. Meanwhile, part of the remaining nanoparticles moves towards the contact line and finally deposits at the edge due to the outward capillary flow which counteracts the Marangoni flow. The ring-like cluster of the solute deposits onto the substrate, eventually forming a distinct secondary ring, but this was found only at three substrate temperatures of 47, 64, and 81 °C. Therefore, it can be concluded that the Marangoni effect is a prerequisite for the ring-like cluster inside the droplet and thus the dual-ring deposition pattern on the substrate. The analysis of the deposition feature reveals that the eddy width corresponding the size of Marangoni convection roll (or distance between the perimeter and secondary ring) decreases with enhancing the increasing temperature. At very early stages of the evaporation process at 81 and 99 °C, two counter-rotating vortices appear on the top region of the drying droplets. Apart from the repelled solute, these two vortices driven by Marangoni flow have key roles in the formation of the ring-like cluster. In

the case of the drying droplet on the heated substrate at 99 °C, a complex flow motion can be seen in the near edge region, where a portion of the solute circulates rapidly for a period of time; this is caused by the strong Marangoni effect. The latter substrate temperature also showed the most non-uniform deposition feature containing several deposition lines due to the stick-slip of the contact line at later evaporation stages. The deposition patterns with the secondary ring (47, 64, and 81 °C) show more uniform deposition of the nanoparticles at the centre (interior of the secondary ring) than that of the pattern left after the evaporation at 25 °C. The video microscopy analysis reveals that there exists a stagnation point on the evaporating droplets surface in the vicinity of the edge at which the change in the surface flow direction occurs.

The infrared thermography results of all studied cases show that the droplet apex has the lowest temperature while the surface temperature increases with approaching the contact line and reaches its highest value at the edge. For the non-heated case, this temperature difference between the apex and edge can be due to the temperature difference between the drop and substrate. The surface temperature distribution as well as flow observation through microscopy confirm the existence of a thermally driven Marangoni flow within the evaporating droplets at all substrate temperatures. The surface temperature difference between the edge and centre of the droplets increases with increasing substrate temperature, leading to a stronger Marangoni flow inside the drying droplets. The dual-ring deposition pattern can be obtained when the thermal Marangoni number in the range of 2.4×10^5 and 9.9×10^5. Beyond this range (${M_a}^T > 9.9 \times 10^5$), the probability of having the stick-slip regime increases, as shown by the case of 99 °C. The present study may contribute to the further understanding and better prediction of pattern formation of nanoparticles in the presence of the Marangoni effect.

Chapter 4 Patterns from Binary-Based Nanofluid Drops on Heated Substrates

This chapter is based on an article published in the Journal of Nanoparticle Research in 2017 [24]. The author contributed to the design of the experiments, performed the experiments, and contributed to the data analysis and the writing of the manuscript. Dr. R. Deltombe scanned the deposits of nanoparticles using a white light interferometry technique. Prof. M. Bigerelle analysed the scans of the deposition patterns which are provided in Figure 4.2c. Dr. R. Boubaker estimated the concentration of butanol within evaporating droplets which is shown in Appendix A.1.1. Prof. S. Harmand and Prof. K. Sefiane supported the author in writing the manuscript and granted approval for the final version.

Patterns from Dried Water-Butanol Binary-Based Nanofluid Drops by
Maryam Parsa, Riadh Boubaker, Souad Harmand, Khellil Sefiane, Maxence Bigerelle and Raphaël Deltombe
Journal of Nanoparticle Research, 2017, *19* (8), pp 268
doi: 10.1007/s11051-017-3951-2

4.1 Abstract

In this work, the behaviour of evaporating binary-based nanofluid sessile droplets deposited on a smooth silicon substrate at different temperatures is explored. The formation of deposition patterns during the evaporation is studied by tracking particle clusters using optical microscopy. Similarly to evaporation of pure water-based nanofluid droplets, three distinctive deposition patterns are left behind the complete evaporation: a relatively uniform coverage pattern (on a non-heated surface); a "dual-ring" pattern at higher temperature, i.e., 81 °C; and a "stick-slip" pattern at 99 °C. Infrared thermography technique was employed to visualise the evolution of thermal patterns on the surface of the drying droplets. Thermal imaging shows that the evaporation of binary mixture droplets can be classified into three regimes. In the

first regime, multiple convection vortices can be observed at the droplet interface, corresponding to the chaotic motion of nanoparticles captured by video microscopy. This flow regime is believed to be driven by surface tension gradients arising from local concentration gradients. As evaporation time proceeds, the number of convection vortices decreases in regime I, and a few numbers of those are left in the second regime. The flow slows down and a rapid transition (the second regime) occurs; this is followed by the last regime. At the two highest temperatures of 81 and 99 °C, the end of the transition regime is associated with the existence of two distinctive counter-rotating vortices. For the third regime, the results from both infrared thermography and video microscopy show identical behaviour to those of water-based nanofluid droplets at the same substrate temperatures. This reveals that most of the more volatile component (not all) has evaporated after the first two regimes; hence, the solutal Marangoni driven by local concentration gradients is significantly weakened and has no further role in the flow structure in the last regime. Instead, the thermocapillary effect and continuity are the underlying reasons for the internal flow structure of the evaporating droplets during the last regime.

4.2 Introduction

Droplet evaporation is a natural and omnipresent phenomenon in many practical applications ranging from technological applications such as heat transfer [38], combustion [180], polymers [84], and inkjet printing [75] to biological applications such as medical diagnostic techniques [46]. The number of publications on the study of droplet evaporation has been considerably increasing since the 1980s [181]. However, the study becomes more complex for the droplets deposited onto a solid surface (the so-called sessile drops) as three phases of liquid, solid, and vapour coexist, forming a three-phase contact line (or the triple line) at the periphery.

The presence of insoluble solid particles, ranging from few microns to nanometres in size, inside a drying sessile droplet causes further complications in such studies because of adsorption of particles at the liquid-vapour interface and their interaction with the solid surface during evaporation [182]. After the dry-out of a sessile drop

containing suspensions, different deposition patterns can be formed on the substrate by the suspended particles. The most commonly known deposit is the “coffee-ring” effect or ring-shaped pattern. Deegan et al. [14,15] were first to find the physical mechanism behind this pattern formation. They observed that the solutes are dragged towards the pinned triple line by the outward capillary flow, and deposit at the edge. The number of solutes arriving at the edge increases with evaporation time; and hence, a distinct ring-like pattern is left on a solid surface after complete evaporation. Hu and Larson [76] found that the inward Marangoni flow inside the drying droplet can prevent the formation of the coffee-ring pattern as some particles are dragged to the central region of the drying droplet and deposit there. Therefore, not only continuous evaporation of liquid and pinning of the triple line are not sufficient for the generation of the coffee-ring pattern, but also the Marangoni effect should be suppressed or even eliminated. The Marangoni effect is driven by non-uniform surface tension distribution at the free surface of droplets as a result of either inhomogeneity of temperature or concentration at the liquid-vapour interface. Uneven temperature distribution at the free surface of sessile droplets arises from non-monotonous evaporative cooling at the liquid-vapour interface and/or non-uniformity of heat transfer from the solid surface [182]. Hu et al. [146] studied evaporation of poly(ethylene oxide) (PEO) droplets on both isothermally and non-isothermally heated substrates. In the case of isothermal heating, a usual “puddle” structure was formed on the substrate as the capillary flow was dominant, whereas non-isothermal substrate (at above 60 °C) led to an unusual volcano-like pattern as a result of the dominant Marangoni flow [146]. Maillard et al. [183] reported that the evaporation of silver nanocrystals in hexane left a ring made of hexagonal arrays, but no rings were observed when hexane was replaced with decane. The difference in the deposit was attributed to the evaporation time. The shorter evaporation lifetime induced the formation of such rings. It was found that increasing the evaporation time led to a decrease in the Marangoni number as well as temperature gradient. Thus, the system reached equilibrium faster and instabilities disappeared. Under such conditions, nanocrystals were not organised and no rings were formed [183]. Parsa et al. [26] carried out a series of experiments to understand the effect of substrate

temperature on the deposition process of water-based nanofluid droplets. The authors found that the strength of the thermally induced Marangoni flow significantly affects the deposited patterns. On the non-heated substrate, a nearly uniform coverage was formed while at higher substrate temperatures, the stronger thermal Marangoni flow results in the formation of the "dual-ring" as well as the "stick-slip" patterns [26]. For the dual-ring patterns, the authors also demonstrated that the distance between the peripheral (outer) and secondary (inner) rings decreases with increasing substrate temperature. Zhong and Duan [184] studied the effect of substrate temperature from cooling to heating on the evaporation of water-based graphite nanofluid drops. Increase in the substrate temperature led to the transformation of the dried deposits from a uniform disk-like profile to a dual ring. For the low substrate temperatures cooler than the atmosphere, most nanoparticles either deposited in the internal regions or contributed to the peripheral ring, leaving an annular gap between them. For higher substrate temperature above the atmosphere, the inward Marangoni flow carried more nanoparticles to the liquid-vapour interface. Meanwhile, nanoparticles were driven towards the triple line by an enhanced outward radial flow. The co-occurrence of these two flows produced a dual-ring pattern after the complete evaporation [184]. Zhong et al. [185] studied the influence of substrate temperature on the morphology of water-based graphite nanofluid drops. They observed the dual-ring pattern due to the co-occurrence of both the inward thermal Marangoni flow and the radial outward flow. The annular gap between the exterior (peripheral) and interior (secondary) rings was decreased by increasing substrate temperature (from 22 to 64 °C), and finally with the further increase of temperature to 84 °C, the interior ring merged with the exterior ring. The expansion of the interior ring with increasing temperature was attributed to the enhanced outward flow [185].

Another way to create the Marangoni effect is the manipulation of base fluids by adding surfactants or diverse liquids (i.e., high-carbon alcohols), which induces the concentration gradients at the free surface of drying droplets and consequently leading to a surface tension gradient along the free surface. This concentration-induced Marangoni flow (also known as the solutal Marangoni) can have a dramatic effect on the deposited patterns and also the evaporation process of sessile droplets.

Still et al. [21] reported that the addition of ionic surfactant sodium dodecyl sulfate (SDS) leads to a more uniform deposition pattern as the surfactant-induced Marangoni eddies inhibit the coffee-ring effect. However, Crivoi and Duan [147] showed the nanofluid droplets with surfactant had a tendency to promote the coffee-ring pattern instead of the uniform coverage. Recently, it has been shown that thermocapillary effects superimpose the surfactant-dependent Marangoni, and hence, nanoparticles deposit in a flower-like pattern along the undulated triple line [98].

Rather limited attention has been paid to the study of drying binary- or multicomponent-based drops, as compared with that of single component-based drops [186,187]. In general, the main focus of researchers has been on studying pure binary-based droplets without nanoparticles [188–192]. Sefiane et al. [188] studied the evolution of the profile of water-ethanol mixture drops on polytetrafluoroethylene (PTFE) substrate and reported that there are three distinct evaporation regimes contrary to evaporation of single-component drops. Cheng et al. [189] and Liu et al. [190] studied the evaporation of ethanol-water sessile droplets on different substrates, and both confirmed the existence of three evaporation regimes before complete drying. Christy et al. [192] used particle image velocimetry (PIV) technique to measure the flow field along the base of a drying ethanol-water droplet. The authors showed that the flow field inside drying droplets can be divided into three regimes. The first regime is dominated by multiple vortices, which reduce in number with evaporation time. This stage arises from surface tension gradients induced by concentration gradients. In the second regime, there is an exponential decay in vorticity and there is also a transition from multiple vortices to a radial flow towards the triple line (the third regime) [192]. The third regime is dominated by an outward flow, which is identical to the evaporation of a pure water droplet. Zhong and Duan [22] studied the effect of concentration of both ethanol and graphite nanoparticles on the evaporation dynamics and pattern formation of ethanol-water nanofluid droplets. They used microscopy technique to observe nanoparticle movement during evaporation to understand the underlying process behind the deposition pattern after the dry-out of these droplets [22]. Zhong and Duan [22] showed that the evaporation of water-based graphite nanofluid drops led to a

relatively uniform dried pattern. The authors have reported that the dried patterns were sensitive to the ethanol concentration. With 10 vol % ethanol, most nanoparticle residuals detached from the drop edge and deposited in the central region. With 25 vol % ethanol, the uniform deposition was reported similar to the water-based drop. By increasing ethanol concentration to 40 and 50 vol %, the detachment occurred between the drop edge and interior deposits. This detachment was intensified by increasing ethanol from 40 to 50 vol % [22]. Zhong and Duan [193] also investigated the effect of ethanol concentration on the flow regimes and the deposition pattern of binary mixture nanofluid droplets. They reported the dried pattern from the water-based Al_2O_3 nanofluid showed the uniform deposit in the internal region enclosed with a distinct coffee-ring. With 10 vol % ethanol, aggregates of nanoparticles were produced due to the chaotic flow and strong vortices. These aggregates either stay at the interior area or are driven to the edge. With 20 vol % ethanol, an evident gap was observed between the outer ring and interior stain. By increasing ethanol to 40 vol %, the non-uniformity of the interior region was increased resulting from evident agglomerations of nanoparticles. Meanwhile, the outer coffee-ring was attenuated. By further increase of ethanol to 50 vol %, the agglomeration of nanoparticles was intensified, and hence, the disorder of the interior area was increased and the coffee-ring was weakened so that it was hardly an exterior ring [193].

As mentioned above, different factors are involved in the formation process of the final dried deposits such as the fluid compositions [22], environmental conditions [25,26], and internal flows including capillary and Marangoni effects [16,153]. According to Zhong and Duan [22], the formation process of deposition patterns by nanoparticles from nanofluid drops affected by the complex flows has not been comprehensively studied. A very recent work of Parsa et al. [26] extensively studied the internal flow structure within evaporating water droplets containing nano-suspensions on heated substrates via an optical microscopy technique. Kim et al. [86] studied the influence of a combination of an ethanol-water mixture, surfactant, and surface-adsorbed polymer on the final deposition pattern as well as the flow field. Despite the aforementioned studies [22,26,86,193], there is still a lack of knowledge

about the underlying mechanism of nanoparticle deposition, in particular for multicomponent droplets evaporating on heated substrates.

It is noteworthy to mention that ethanol has been widely used in the majority of the studies on the evaporation of binary mixture drops [22,86,188–190,192,193]. It is well known that ethanol aqueous solutions and pure water are ordinary fluids as their surface tension decreases with the increasing of their temperature. For the first time, Vochten and Petre [194] observed that the surface tension of dilute aqueous solutions of some high-carbon alcohols (number of carbon atoms ≥4) such as butanol increases as temperature exceeds a certain value. This is known as the inverse Marangoni effect. Petre and Azouni [195] contributed to the study of these particular fluids by creating a temperature gradient on the surface of alcohol solutions. They found that there is the possibility of controlling the direction of the surface motion by employing the thermocapillary effect [195]. Some experiments were also carried out to study these fluids in microgravity conditions [196,197]. The term "self-rewetting" fluids was first used in the work of Abe and Iwasaki [197] who studied the Marangoni direction around two adjacent vapour bubbles at a heater surface for aqueous solution of butanol. Unlike ordinary fluids, the aqueous solution of butanol spreads towards the hot surface due to the inverse Marangoni effect, preventing the coalescence of bubbles and improving the boiling heat transfer [197]. These so-called self-rewetting fluids with the peculiar temperature dependence of surface tension have been attracting the attention of many researchers in thermal management for both terrestrial and space applications [198–202]. Savino et al. [199] conducted experiments to investigate the behaviour of self-rewetting fluids inside wickless heat pipes. They found that the size of vapour slugs at the hot side were much smaller in comparison to water [199]. There was also more liquid in the evaporation region of the heat pipe filled with self-rewetting fluids compared to that filled with water, leading to better thermal performances for the heat pipes filled with self-rewetting fluids [199]. For the first time, Sato et al. [203] reported the improvement in the critical heat flux of the heat pipe filled with the self-rewetting fluid containing silver nanoparticles. Since then, there has been increasing interest of using these so-called self-rewetting nanofluids in heat-transfer devices

[200,202,204,205]. A recent work by Su et al. [205] demonstrated the heat-transfer enhancement of oscillating heat pipes charged with self-rewetting nanofluids due to both the inverse Marangoni effect and higher thermal conductivity. Despite these abovementioned studies relevant to the evaporation of self-rewetting nanofluids [200,202,204,205], the literature shows that the understanding of mechanisms behind the deposition patterns left from the self-rewetting nanofluids is still lacking.

In the present study, the effect of silicon substrate temperatures (from ambient to 99 °C) on the evaporation of binary-based CuO nanofluid sessile droplets is investigated. Optical microscopy is used to study the flow dynamics within an evaporating droplet until the complete drying to understand the role of nanoparticle movement on the deposition pattern. In addition, the interfacial thermal activity at the liquid-vapour interface is studied during evaporation by means of infrared thermography. The formation of patterns from these drying binary droplets is discussed and related to the end of the underlying physical mechanism.

4.3 Experimental Methods

4.3.1 Solution

The binary mixture is an alcohol aqueous solution consisting of distilled water and 1-butanol (with a concentration of 5 wt %). This specific concentration was selected based on literature indicating self-rewetting behaviour [198–202]. It is noteworthy to mention that the saturation vapour pressure of water is 3.166 and 97.75 kPa at 25 and 99 °C, respectively. For butanol, the saturation vapour pressure is 0.905 and 49.937 at 25 and 99 °C, respectively. The nanofluid was prepared by dissolving copper(II) oxide (CuO) nanopowders (Sigma-Aldrich, molecular weight = 79.55, diameter < 50 nm) with a concentration of 0.05 wt % in the aforementioned binary mixture. Then, the suspensions of CuO nanoparticles were thoroughly mixed and kept in an ultrasonication bath for at least 1 h prior to the evaporation experiments. The term “binary-based nanofluid” in the text refers to the binary mixture containing nanoparticles.

4.3.2 Droplet deposition

Smooth silicon wafers were ultrasonicated in distilled water for at least 30 min before the experiments. Then, they were carefully cleaned and rinsed with distilled water and acetone and then dried by using an air dryer. Detailed description of the characterisation and quantification of substrate roughness is provided in the study of Parsa et al. [26] and will not be repeated here. The droplet of 0.05 wt % nanofluid-based butanol aqueous solution (with varying size from 0.5 to 1.1 μL) was deposited onto the heated silicon substrates by means of a motor-driven dosing system of a DSA30 drop shape analyser (KRÜSS GmbH). A tempering chamber (KRÜSS GmbH, TC40) in combination with a humidity chamber (KRÜSS GmbH, HC10) was mounted on the DSA30, inside which the experiments were carried out under controlled environmental conditions of pressure, temperature, and relative humidity of 1 atm, 25 °C, and 30%, respectively. The substrate temperature was controlled at four different temperatures of 47, 64, 81, and 99 °C. Besides, the experiment was carried out on the non-heated substrate. In order to establish reproducibility, the experiment was repeated at least five times at each substrate temperature.

4.3.3 Imaging

The DSA30 was equipped with a uniform LED lighting unit and a high-resolution charge coupled device (CCD) camera. Two windows mounted on the right and left sides of the TC40 chamber allowed the CCD camera to capture the shadow images of an evaporating sessile droplet over time creating by the illumination of the LED light (see Figure 4.1). The evolution of the droplet profiles (volume, base diameter, contact angle, and height) as a function of time was determined by transferring the recorded shadow images to the drop shape analysis software (KRÜSS GmbH, DSA4). The measurement resolution of the contact angle was 0.1°. An infrared (IR) camera (FLIR, X6580sc) mounted on a lens (FLIR, G1) recorded the evaporation of the sessile droplet through the top window on the chamber to observe the liquid-vapour interface during the evaporation time (see Figure 4.1). A high-speed camera (Keyence, VW600C) mounted on an optical microscopic lens (Keyence, VH-Z100R)

was employed to record the evaporation process of drying droplets at magnification zoom of 100× and 500×. For this part of the experiment, the droplet was deposited onto the substrate by means of a syringe pump (KdScientific, legato 100) under ambient conditions at the aforementioned temperature and relative humidity. A white light interferometer (Zygo, NewView 7300) was also used to scan the deposits after the complete evaporation to analyse the deposition distribution along the droplet base.

4.3.4 Supporting Information

Supporting Information associated with this chapter is available in the online version.[2]

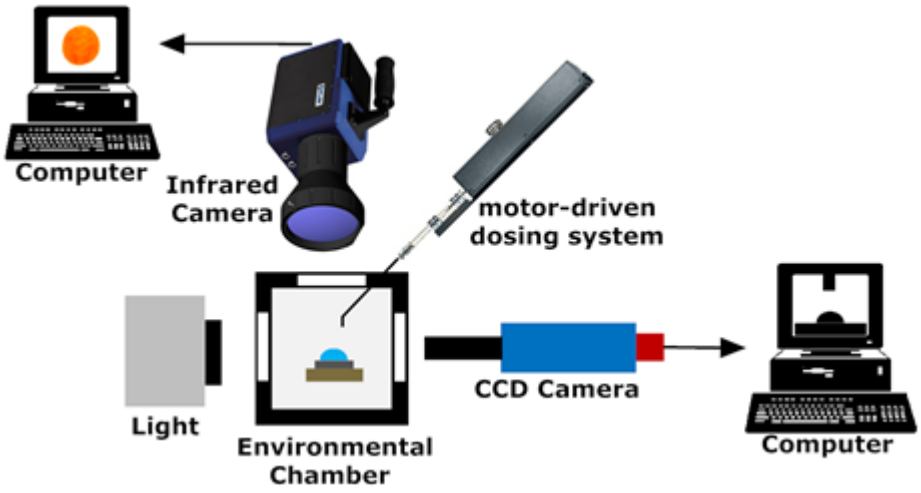

Figure 4.1 Schematic diagram of the experimental apparatus.

4.4 Results and Discussion

4.4.1 Deposition patterns formed by nanoparticles

Figure 4.2a shows that the evaporation occurs mainly in the constant contact base mode, and the contact line remains pinned for the majority of the evaporation time.

[2] https://link.springer.com/article/10.1007/s11051-017-3951-2

However, the contact angle decreases throughout the evaporation process. Figure 4.2b shows deposition patterns left behind after evaporation of butanol-water (5:95 wt %) mixture nanofluid droplets at a wide range of substrate temperatures from ambient to 99 °C. The corresponding graphs in Figure 4.2c show density profiles of those samples shown in Figure 4.2b. The density profiles, or concentration of particles on substrates, are obtained from interferometry after further analysis on deposition features. Sample I in Figure 4.2b indicates that in the case of non-heating, a nearly uniform coverage can be formed with higher concentration of nanoparticles at the triple line (see also Figure 4.2cI). Figure 4.2cII-V shows that heating the silicon substrate increases the possibility of non-uniformity of nanoparticle distribution on the surface. Apart from the outer ring (peripheral ring), a small inner ring (secondary ring) can be seen in the central region of the dried droplet at 47 °C (see Figure 4.2bII). Similarly, the secondary rings can be found interior of the peripheral ring at 64 (Figure 4.2bIII) and 81 °C (Figure 4.2bIV). Such patterns (or the dual-ring phenomenon) have been previously observed in Parsa et al. [26] for pure water droplets. However, a closer examination of inner areas of secondary rings in the present study reveals several faint ring-like (or line) patterns interior of the secondary rings (see samples II-IV in Figure 4.2b). Moreover, the secondary rings in the study by Parsa et al. [26] are found to be more distinguishable as there was only one distinct inner ring without the aforementioned faint lines inside the secondary ring. It implies that the addition of butanol to the base fluid alters the distribution of nanoparticles within the secondary rings. The size of the secondary ring at a higher temperature of 81 °C is larger than those at lower temperatures of 47 and 64 °C (Figure 4.2cII-IV), which has been previously shown by Parsa et al. [26]. In other words, the decrease in the substrate surface temperature leads to smaller secondary rings or a larger distance between the peripheral and secondary rings (Figure 4.2cII-IV). At the highest substrate temperature of 99 °C (Figure 4.2bV), the nanoparticle deposition pattern changes dramatically as there are a set of distinct deposition rings inside the perimeter, which cover about 60% of the total dried area (see Figure 4.2cV). These distinct deposition lines on one side of the dried droplet cause non-uniform distribution of nanoparticles as shown in Figure 4.2cV. The same behaviour

known as stick-slip was reported by some researchers [25,26,66]. Parsa et al. [26] observed the stick-slip behaviour for the evaporation of CuO-water nanofluid drop let at 99 °C. It is clear that butanol has no noticeable effect on the deposition pattern at 99 °C.

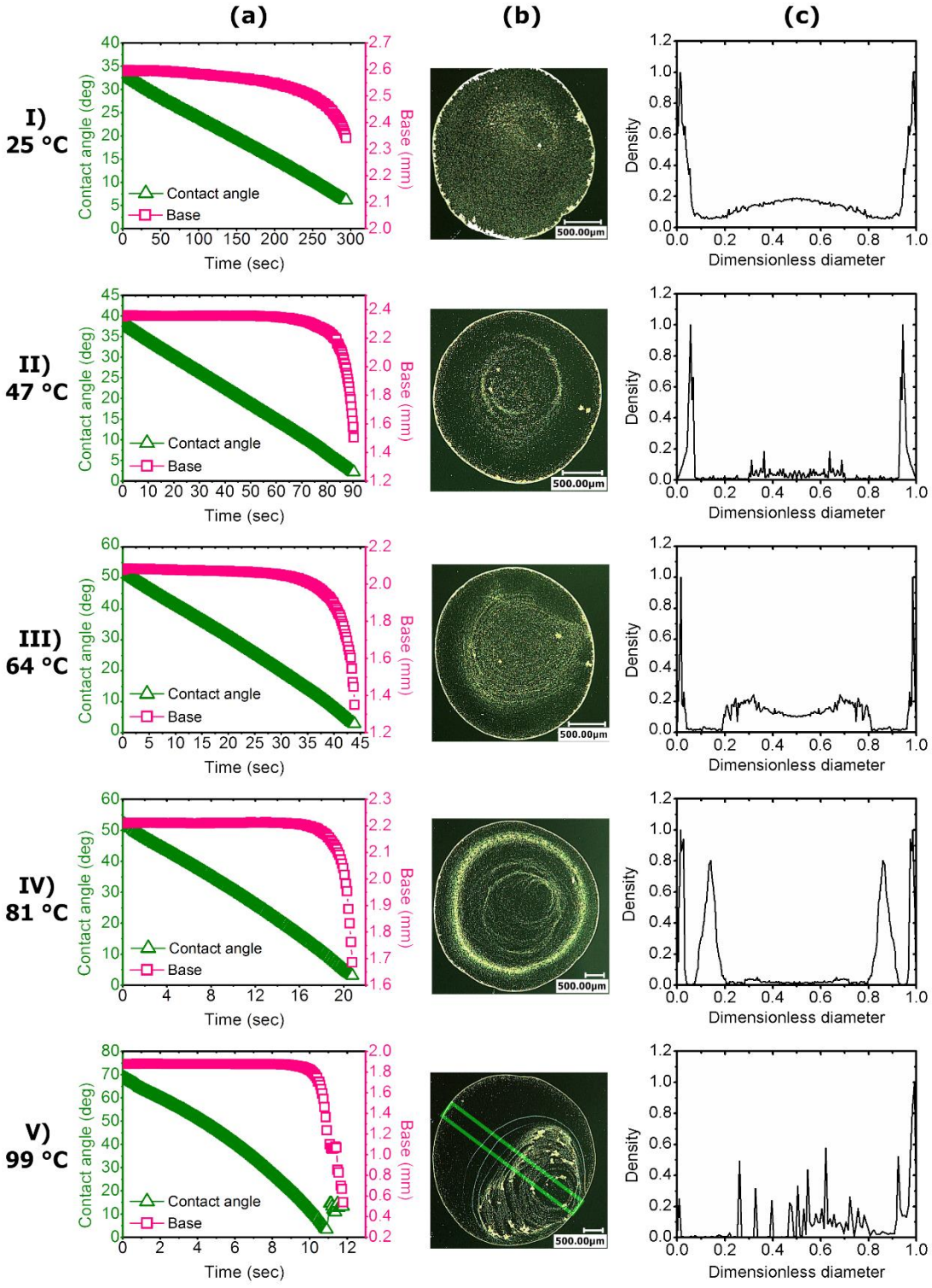

Figure 4.2 (a) Temporal variation of base diameter and contact angle for drying 0.05 wt % binary-based CuO nanofluid droplets on non-heated and heated substrates at 47, 64, 81, and 99 °C. (b) Dried deposits of 0.05 wt % binary-based CuO nanofluid droplets on non-heated and

heated substrates at 47, 64, 81, and 99 °C (scale bar: 500 μm). (c) Density distribution profiles of dried deposits of binary-based CuO nanofluid droplets at substrate temperatures of 25, 47, 64, 81, and 99 °C. Note that the density distribution profiles are relative measurements. The dimensionless diameter indicates the distance from edge to edge. At 99 °C, the diameter is from the left to the right side of the square shown in the dried deposit.

4.4.2 Internal flow pattern

Optical microscopy was employed to observe the evaporation process of binary-based CuO nanofluid droplets at all examined temperatures, and consequently to understand the mechanism behind the deposition patterns shown in Figure 4.2b (see Supporting Information). It is worth noting that single nanoparticles cannot be observed with the optical microscope. Instead, clusters of particles are observed and followed as indicators of the flow. The microscope was focused on the initial triple line. The clusters motion and formation of some structures within evaporating droplets are best visualised in the supporting videos (Supporting Information), and it is highly recommended to view these videos. The 500× magnification snapshots from video microscopy in Figure 4.3 show temporal evolution of the evaporating droplet on the non-heated substrate. From the beginning of the evaporation, rapid chaotic motion of nanoparticles can be clearly seen (see Supporting Information Video S1). Simultaneously, some nanoparticles reach the initial triple line and deposit there as the accumulation of nanoparticles at the edge increases with time (see Figure 4.3a-e). Then, the flow gradually slows down and a cluster of nanoparticles involved in chaotic motion remains at the liquid-vapour interface as they are out of focus. Some nanoparticles are also transported to the edge adjacent to the substrate due to the outward capillary flow. However, very few numbers of nanoparticles do not deposit at the edge and move inward along the liquid-vapour interface arisen from a weak thermal Marangoni effect. It is obvious that the outward flow is the dominant flow after the end of the chaotic motions of nanoparticles. In the final stages of the evaporation, those nanoparticles on the top surface which were out of focus become more visible as the droplet height decreases with the evaporation time and the nanoparticles are on the same plane as those deposited at the pinned

triple line (see Figure 4.3i-k). They later move to the drop centre (Figure 4.3g-j) until the triple line depins, and eventually, they deposit onto the substrate surface (see Figure 4.3 k,l and Supporting Information Video S1).

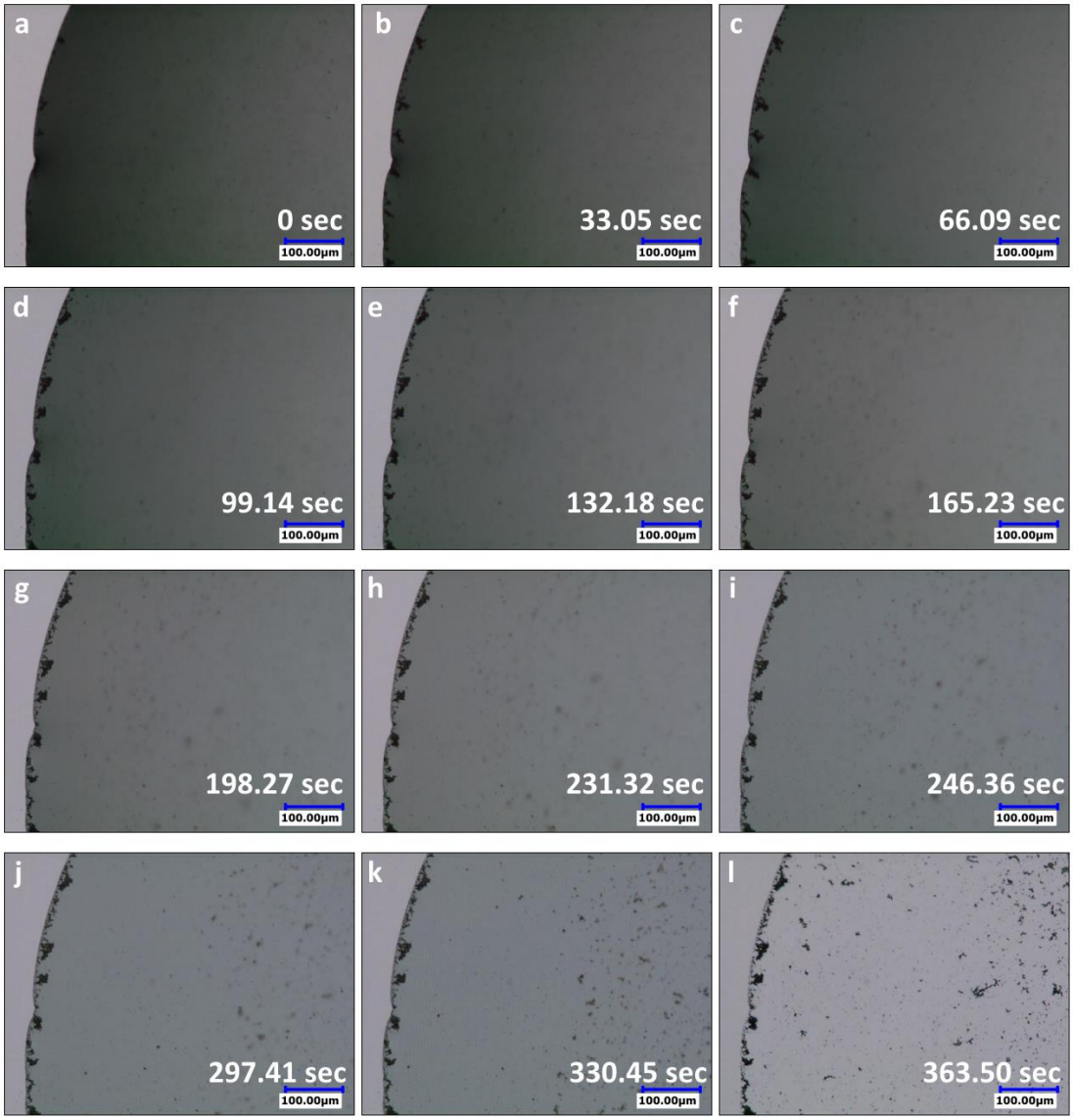

Figure 4.3 Sequential images from a video microscopy of the drying droplet on a non-heated silicon substrate (at 25 °C). The optical micrographs are recorded at a temporal resolution of 60 fps and at 500× magnification (scale bar: 100 μm).

The 500× magnification micrographs of the evaporating droplet on the substrate heated at temperatures of 47 and 64 °C are presented in Figures 4.4 and 4.5,

respectively. The nanoparticles' motion within the drying droplet at 47 and 64 °C is found to be similar to that of the non-heated substrate. First, the vigorous chaotic flow is observed (Figures 4.4a-f and 4.5a-c), and then, the outward capillary flow drives nanoparticles to move towards the triple line and stop at the edge (shown by the dashed arrows in Figure 4.6). Meanwhile, a considerable number of nanoparticles traveling towards the edge return back from the areas close to the edge towards the drop surface (shown by the solid arrows in Figure 4.6; Supporting Information Videos S2 and S3). Unlike the non-heated case, after the end of the chaotic flow, more nanoparticles move inward along the liquid-vapour interface which shows the outward capillary flow is not dominant for the substrate temperatures of 47 and 64 °C. When the substrate temperature increases, the temperature difference between the apex and the edge increases. The thermal Marangoni flow which is dependent on this temperature difference becomes stronger, and thus, more nanoparticles move back radially to the top surface of the drying droplet. The nature and origin of the chaotic and Marangoni flows will be later discussed in detail in the next section.

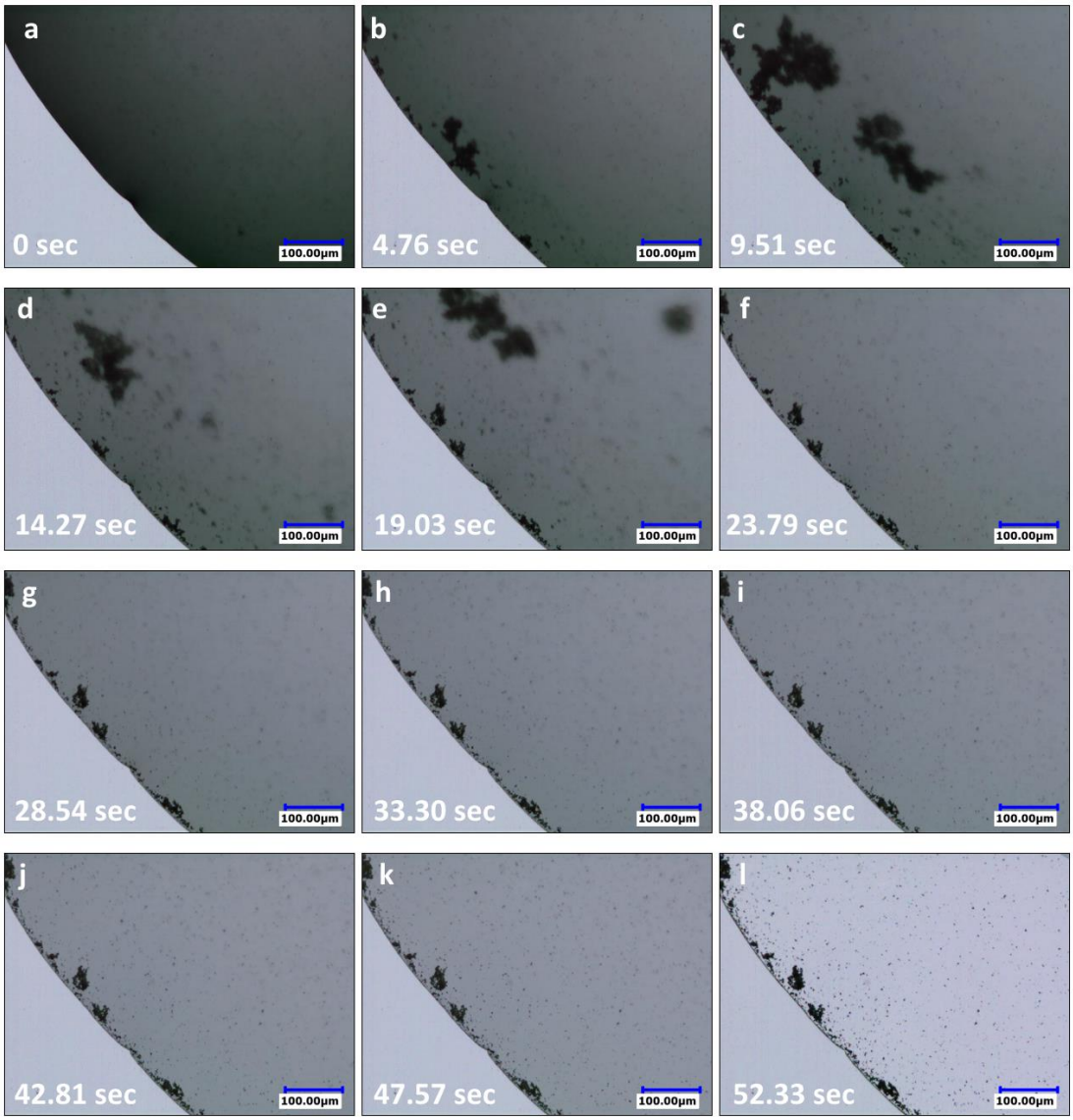

Figure 4.4 Sequential images from a video microscopy of the drying droplet on a heated silicon substrate at 47 °C. The optical micrographs are recorded at a temporal resolution of 60 fps and at 500× magnification (scale bar: 100 μm).

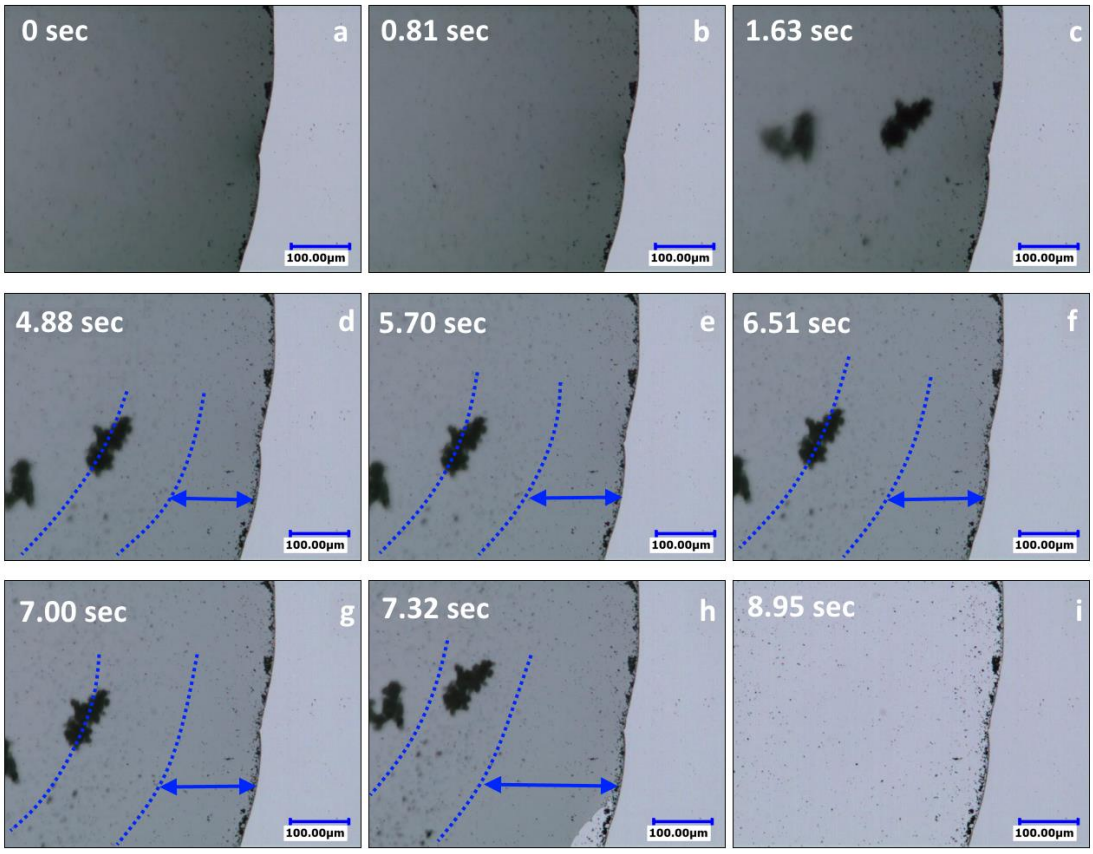

Figure 4.5 Sequential images from a video microscopy of the drying droplet on a heated silicon substrate at 64 °C. The area in between the two dotted curves shows the ring-like cluster. The arrows denote the eddy region between the triple line and ring-like cluster. The optical micrographs are recorded at a temporal resolution of 60 fps and at 500× magnification (scale bar: 100 μm).

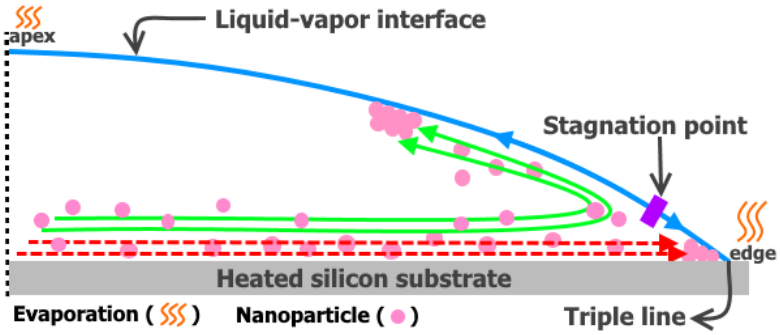

Figure 4.6 Schematic description of the flow pattern (after the end of the chaotic flow) within drying binary mixture-based nanofluid droplets deposited on a heated substrate; the solid and dashed arrows indicate the Marangoni and outward capillary flows, respectively.

Figure 4.7 shows the consecutive still images of the drying droplet on the substrate heated at 64 °C and at 100× magnification. The chaotic flow carries a group of nanoparticle clusters to the liquid-vapour interface; thus, those nanoparticles participating in the chaotic flow at the liquid-vapour interface remain there after the chaotic motion stops (see Figure 4.7a-d) [18,193]. The rapid growing of the aggregates of nanoparticles is observed due to the strong vortices and chaotic motions. These aggregates stay close to the perimeter of the drop during the chaotic flow (Figure 4.7a,b); then, they are transported from the drop edge towards the apex of the droplet (Figure 4.7c), covering the central liquid-vapour interface at the end of the chaotic flow (Figure 4.7d) [22,193]. As shown in Figure 4.7d-h, the presence of some of those nanoparticle clusters at the drop free surface forms a ring-like cluster of nanoparticles. Meanwhile, the other group of those nanoparticles is located in the inner region of the ring-like cluster (Figure 4.7d-h). The repelled nanoparticles from the edge also contribute to the formation of the ring-like nanoparticle cluster on the top of the evaporating droplet (shown in between the arrows in Figure 4.7e,f). The ring-like cluster can be more clearly observed, revealing that it descends onto the substrate due to the decrease in the droplet height (Figure 4.7e-h). An eddy region is also observed between the pinned triple line and this ring-like cluster, as shown by the double arrows in Figure 4.5d-h. The eddy width increases as the ring-like cluster drifts towards the central region of the evaporating droplet. At the final stage of the evaporation (Figure 4.7g,h), the triple line depins and the aforementioned nanoparticle cluster arrives at the depinned triple line, leading to the deposition of the ring-like cluster on the substrate as a secondary ring (see Figure 4.7i). The same deposition process at 47 °C is found for temperature of 64 °C.

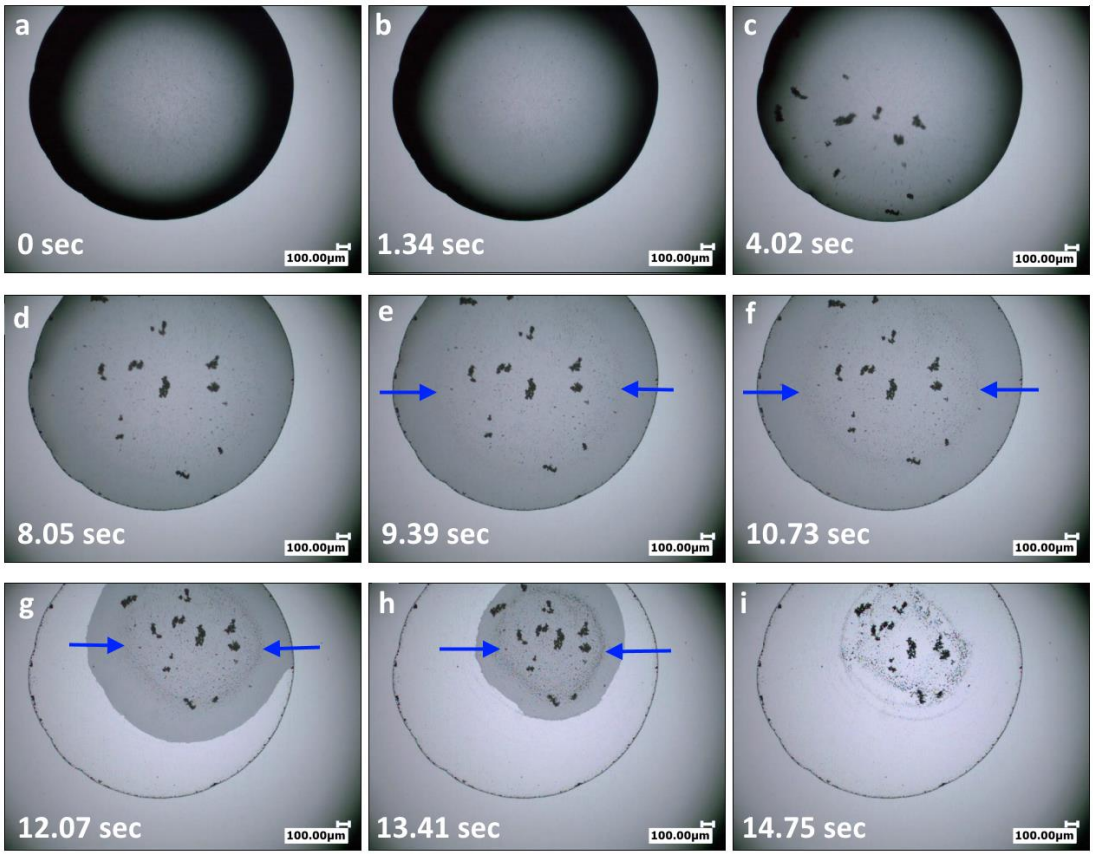

Figure 4.7 Sequential images from a video microscopy of the drying droplet on a heated silicon substrate at 64 °C. The arrows show the right and left sides of the ring-like cluster. The optical micrographs are recorded at a temporal resolution of 60 fps and at 100× magnification (scale bar: 100 μm).

Sequences showing top views of the drying droplets on the substrate heated at 81 °C are given in Figures 4.8 and 4.9, at magnifications of 500× and 100×, respectively (taken from Supporting Information Videos S5 and S6). Similarly to the substrate temperatures of 47 and 64 °C, the secondary ring deposits onto the substrate after the depinning of the triple line due to the formation of the ring-like cluster close to the liquid-vapour interface formed by both the rapid chaotic flow and the repelled nanoparticles (see Figures 4.8d,e and 4.9d,e). The previously observed eddy can also be clearly seen in between the edge and dotted curve, as indicated by the arrows in Figure 4.8d,e. According to some studies [26,69,146,177], this eddy is driven by surface tension gradients, Marangoni convection.

According to the aforementioned analysis, side views of a n evaporating droplet at 47, 64, and 81 °C are depicted in Figure 4.10. First, the chaotic flow leads to the random motion of nanoparticles (shown by the solid arrows), as sketched in Figure 4.10a. The flow slows down (Figure 4.10b), and finally, the random motion of nanoparticles stops (Figure 4.10c). Those nanoparticles brought to the top regions of the droplet by the chaotic flow remain at the central liquid-vapour interface after the chaotic motion stops (Figure 4.10c). A group of these nanoparticles contributes to the formation of a ring-like cluster at the top of the free surface (Figure 4.10c), while the remainders are located inside the ring-like cluster (Figure 4.10c). The chaotic flow is replaced by the capillary (indicated by the dashed arrows, Figure 4.10c), and thermal Marangoni flows (shown by the solid arrows, Figure 4.10c). The nanoparticles travel outward to reach the edge and deposit there due to the outward capillary flow (shown by the dashed arrows in Figure 4.10c,d). However, some of these nanoparticles change their direction due to the Marangoni flow and move inward along the liquid-vapour interface to join the ring-like cluster at the top part of the droplet (shown by the solid arrows in Figure 4.10c,d). A peripheral ring deposits on the substrate after the triple line depins, as shown in Figure 4.10e. The ring-like cluster drifts towards the depinning triple line (Figure 4.10e) and deposits on the substrate when it reaches the edge, leaving behind a secondary ring (Figure 4.10f). In the present work, the number of isolated nanoparticles is reduced due to the effect of butanol on the particle-particle interactions during the chaotic flow, which augments the aggregation of nanoparticles. In addition, a group of nanoparticles remaining in the central region of the liquid-vapour interface (at the end of the chaotic flow) is located inside the ring-like cluster. Hence, the number of nanoparticles contributing to the formation of the secondary ring (caused by the thermal Marangoni flow) is expected to be lower than that in the work of Parsa et al. [26]. This is (perhaps) the reason that the secondary ring in the dried nanofluid-based water-butanol droplet is less distinguishable as that in the nanofluid-based pure water. The existence of the faint lines inside the secondary ring can be attributed to the deposition of those nanoparticles located in the inner area of the ring-like cluster at the liquid-vapour interface onto the substrate at the end of the evaporation process.

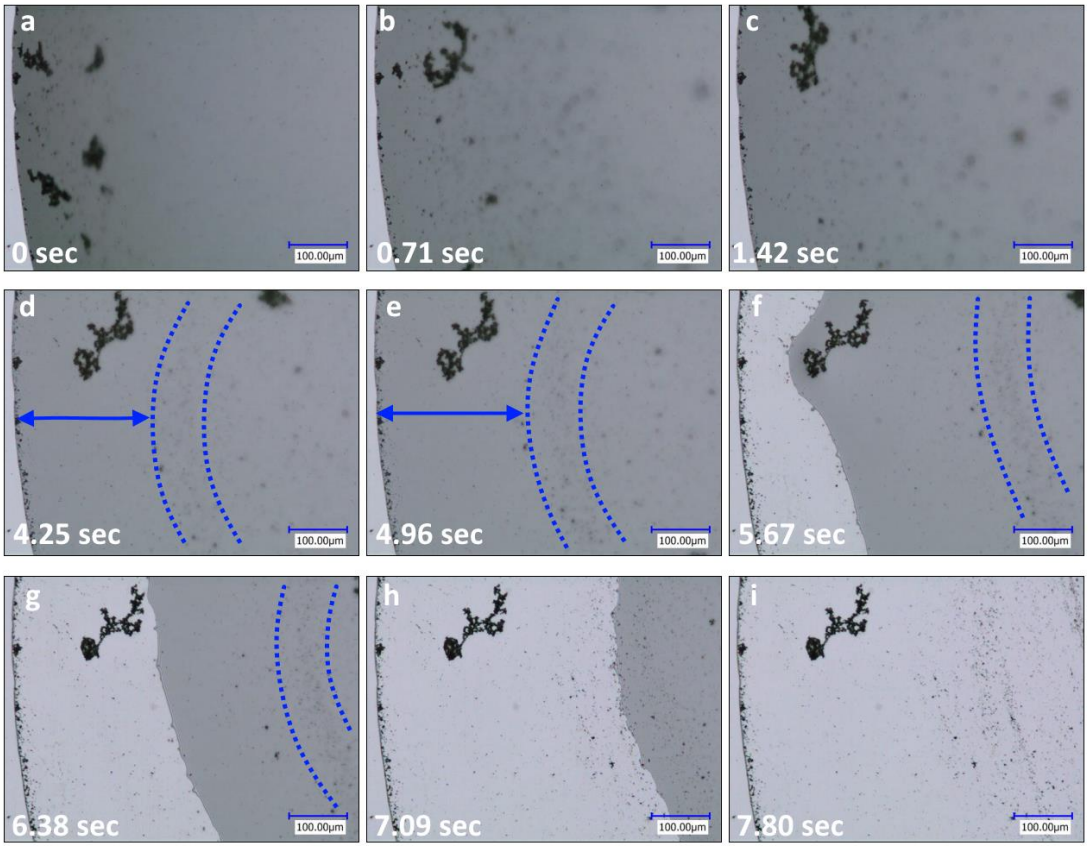

Figure 4.8 Sequential images from a video microscopy of the drying droplet on a heated silicon substrate at 81 °C. The area in between the two dotted curves shows the ring-like cluster. The arrows denote the eddy region between the triple line and ring-like cluster. The optical micrographs are recorded at a temporal resolution of 60 fps and at 500× magnification (scale bar: 100 μm).

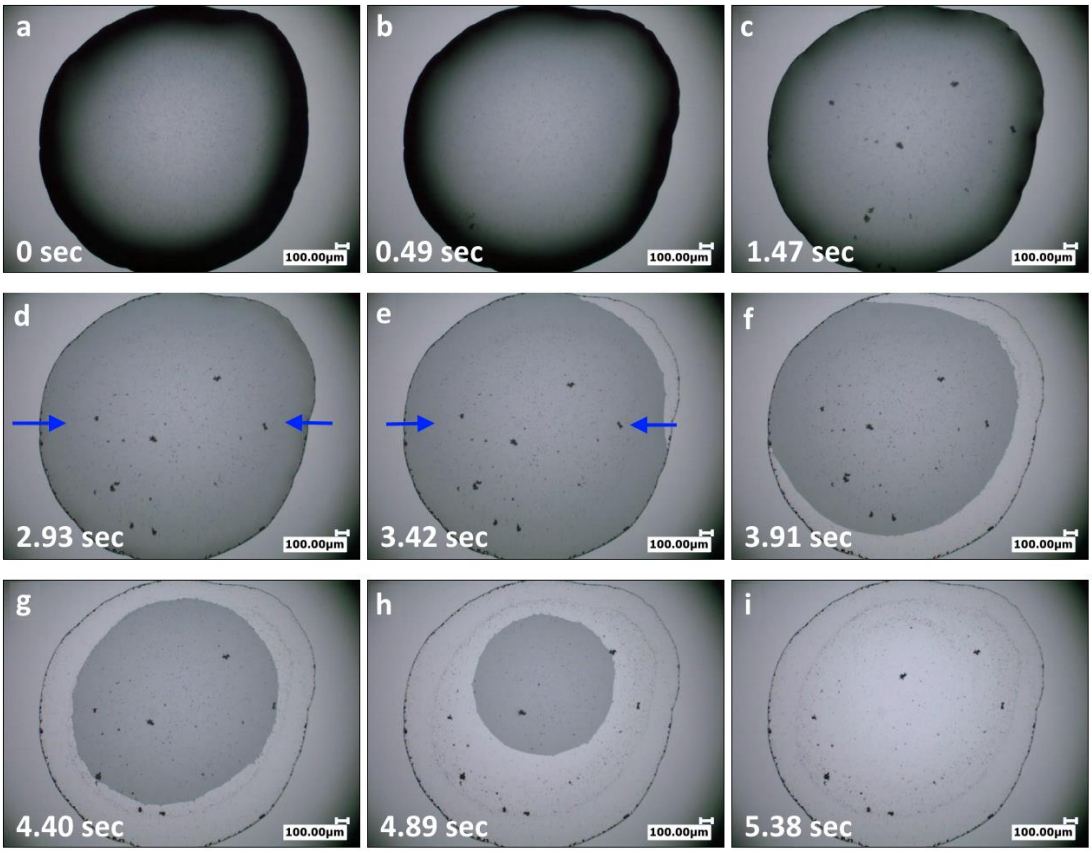

Figure 4.9 Sequential images from a video microscopy of the drying droplet on a heated silicon substrate at 81 °C. The arrows show the right and left sides of the ring-like cluster. The optical micrographs are recorded at a temporal resolution of 60 fps and at 100× magnification (scale bar: 100 μm).

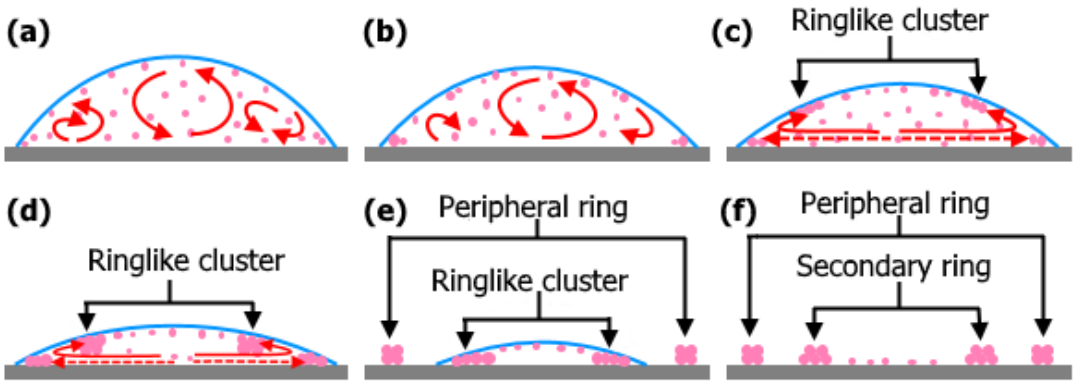

Figure 4.10 Formation mechanism schematic of the dual-ring pattern deposited after the dry-out of a droplet on a heated substrate (47, 64, and 81 °C): (a) Nanoparticles move randomly within a drying pinned droplet due to the strong chaotic flow (indicated by the solid arrows). During this time, some nanoparticles also deposit at the edge. (b) The strength of the chaotic

flow decreases with time, and then the flow slows down. (c) The chaotic flow stops, and those nanoparticles which were carried to the liquid-vapour interface (at the end of the chaotic flow) stay there, building a ring-like cluster at the top region of the droplet near the liquid-vapour interface. The capillary (indicated by the dashed arrows) and thermal Marangoni flows (indicated by the solid arrows) form the internal flow structure inside the pinned droplet. (d) The capillary flow makes nanoparticle move towards the triple line and deposit there (indicated by the dashed arrows). Some of these nanoparticles do not deposit at the edge due to the thermal Marangoni flow and return back towards the top regions of the droplet along the liquid-vapour interface (indicated by the solid arrows), contributing to the formation of the ring-like structure. (e) The triple line depins and a peripheral ring is left behind; following the initial depinning, the ring-like cluster drifts towards the edge, and it stops traveling when it reaches the triple line. (f) After the complete evaporation, the ring-like cluster deposits on the substrate as a secondary ring.

After the complete evaporation of the droplets at temperatures of 47, 64, and 81 °C, the highest (81 °C) and the lowest (47 °C) substrate temperatures show the longest (~1841 μm) and the shortest (~1106 μm) diameters of secondary rings, respectively, as shown in Figure 4.11. In other words, the higher the substrate temperature, the larger is the secondary ring. By analysis of the video microscopy (Supporting Information Videos S4 and S6), it is understood that the deposition of the secondary ring occurs when the depinned triple line reaches the ring-like cluster, revealing that the size of the secondary ring or the eddy width after the complete evaporation is significantly affected by the depinning of the triple line [26]. Parsa et al. [26] reported that the higher evaporation rate enhances nanoparticle velocity, and hence, nanoparticles arrive more rapidly at the depinned triple line, leading to a larger secondary ring (or a shorter eddy width) after the evaporation is completed.

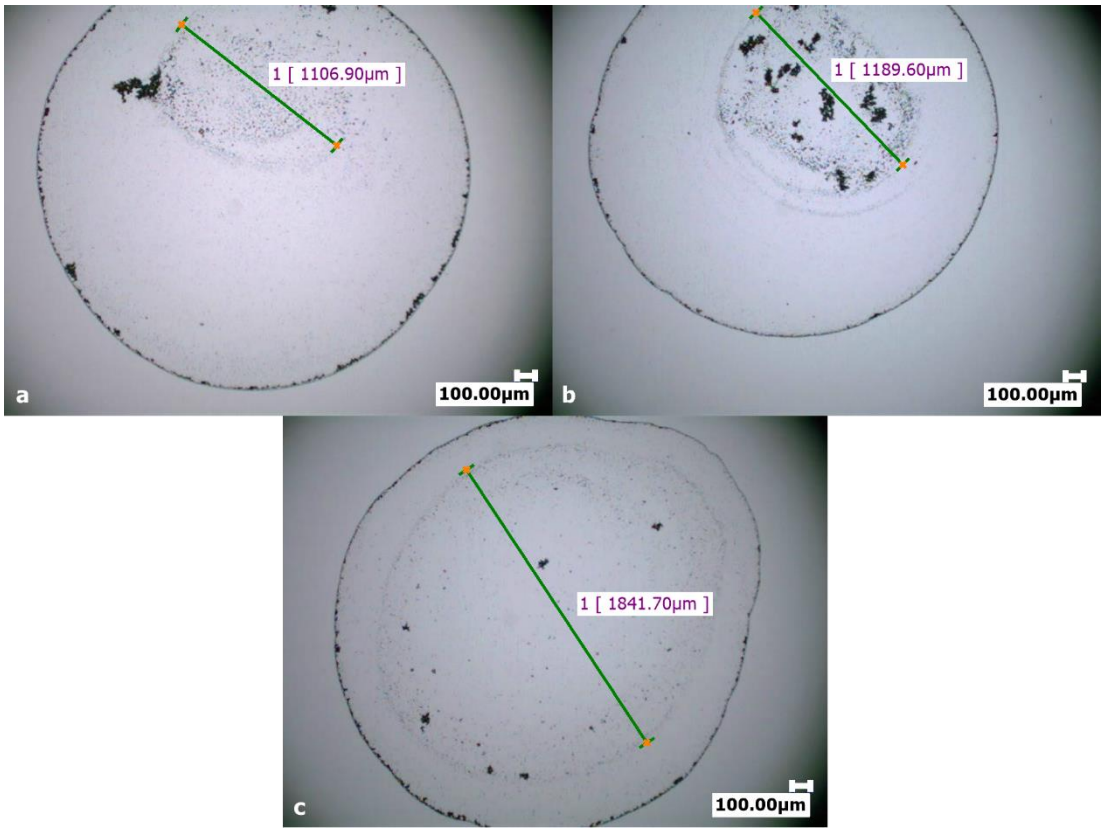

Figure 4.11 100× deposit images of binary droplets containing CuO nanoparticles after the complete dry-out: (a) at 47 °C, (b) at 64 °C, and (c) at 81 °C. The secondary ring size is shown in square brackets (scale bar: 100 μm).

The similar vigorous chaotic flow is seen inside the drying droplet deposited onto the silicon substrate heated at a temperature of 99 °C (see Figure 4.12a-c, Supporting Information Videos S7). As it has been previously mentioned, the chaotic flow as well as the thermal Marangoni effect builds a ring-like collection of nanoparticles at the liquid-vapour interface of the evaporating droplet (Figure 4.12g,h). At substrate temperatures of 81and 99 °C, the transition from the chaotic flow to the thermal Marangoni flow is associated with the presence of two counter-rotating vortices, as illustrated in Figure 4.13. Two clusters of nanoparticles on the top region are tracked on both sides of the drying droplets (shown inside the circles in Figure 4.13) to indicate the location of the clusters. The arrows show the direction of the clusters' movement. Parsa et al. [26] also observed similar pairs of counter-rotating vortices in the very beginning stages of evaporation of CuO-water nanofluids at the same

temperatures of 81 and 99 °C. After the complete transition, the flow becomes slow and the same flow pattern at lower temperatures of 47, 64, and 81 °C is observed for the highest temperature of 99 °C. However, the triple line at 99 °C depins in a completely different way compared to the other examined temperatures. In the case of the highest temperature, one side of the initial triple line jumps and leads to the formation of a new triple line (see Figure 4.12i,j), while the other side of the initial triple line remains pinned. The new triple line also depins and repins consecutively until the end of evaporation (see Figure 4.12j-l and 4.14j-l). Multiple concentric rings are deposited on the substrate by several depinnings and repinnings of the triple line, which is known as the stick-slip pattern. This behaviour prevents the deposition of the ring-like cluster at the liquid-vapour interface (Figure 4.12h,i) onto the substrate, thereby the dual-ring pattern cannot be seen at 99 °C. The pinning allows more nanoparticle deposit at the triple line of an evaporating droplet, acting as a potential energy barrier preventing the depinning of the droplet [66]. It is known that the droplet depins when this energy barrier is overcome by an excess of free energy arisen from the change in the shape of the droplet (or the system is out of equilibrium) [25,66]. In the pinning cases, the excess free energy is insufficient to depin the triple line; thus, the energy barrier is unachievable [25]. Increasing the substrate temperature and hence enhancing the evaporation rate cause the higher accumulation of nanoparticles, leading to higher particle concentration at the triple line [25]. The value of the excess free energy is an increasing function of nanoparticle concentration [66]. Therefore, in some cases with a high evaporation rate (i.e., 99 °C), the excess free energy can be equivalent to the energy barrier causing the slip (or jump) of the triple line. The depinning triple line tends to reach a more energetically favourable position (i.e., a new pinning phase or the stick of the triple line) which should be indicative of both the nanoparticle concentration at the triple line as well as the potential energy barrier [25,66].

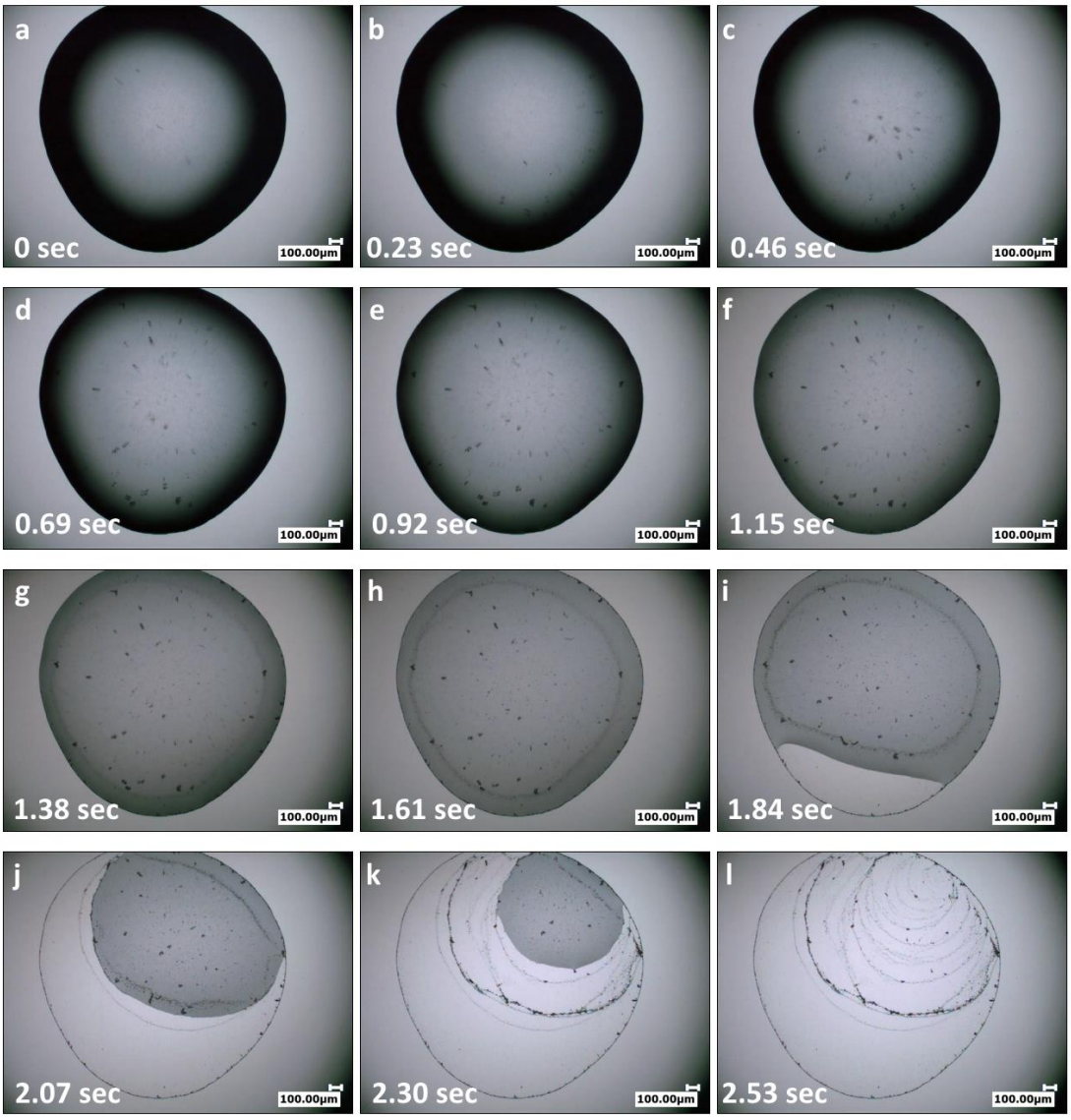

Figure 4.12 Sequential images from a video microscopy of the drying droplet on a heated silicon substrate at 99 °C. The optical micrographs are recorded at a temporal resolution of 125 fps and at 100× magnification (scale bar: 100 μm).

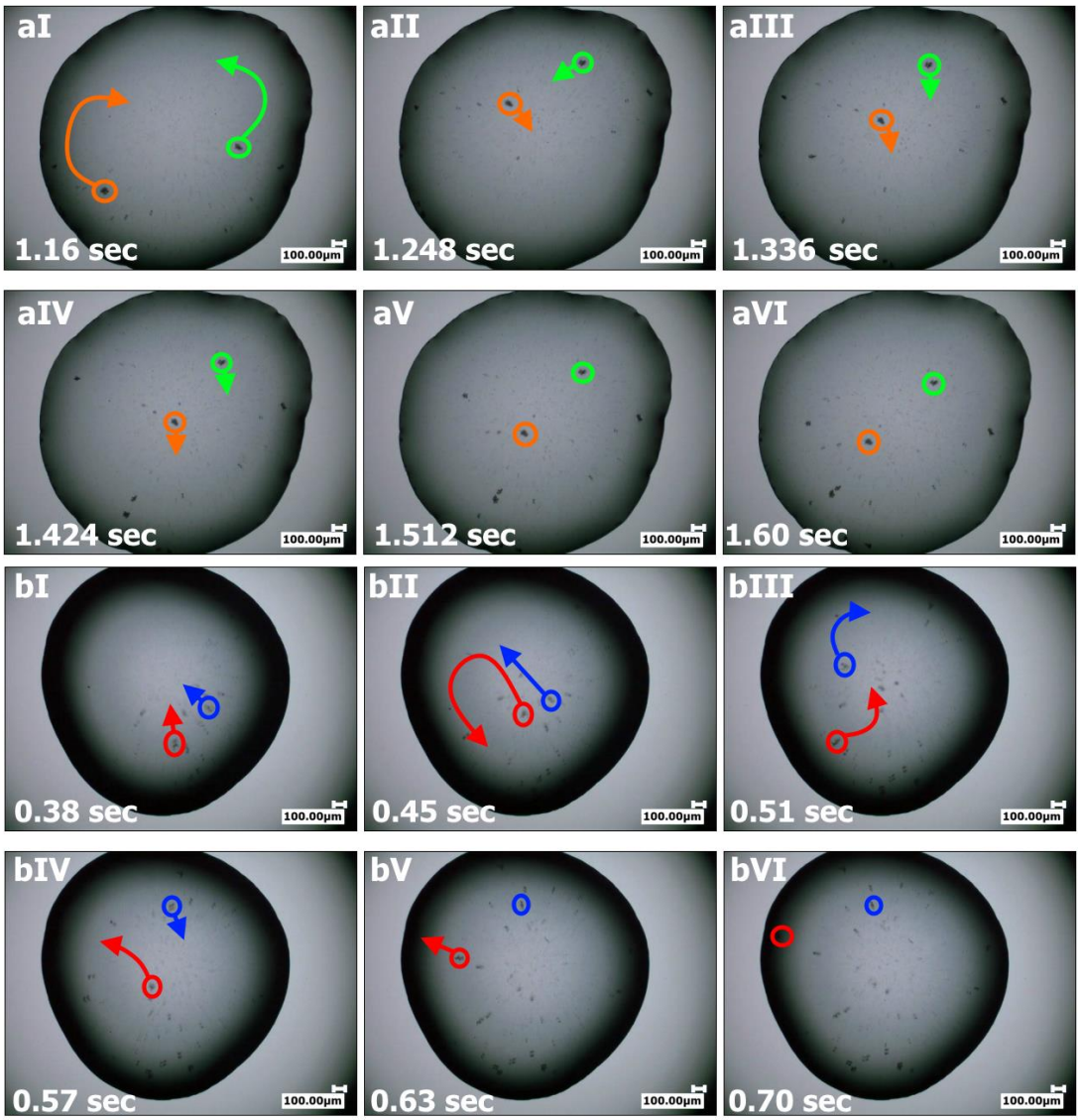

Figure 4.13 Sequential images from a video microscopy of the drying droplets on a heated silicon substrate: (aI-VI) at 81 °C, and (bI-VI) at 99 °C. The arrows show the nanoparticle cluster movement, which are indicated by the circles (scale bar: 100 μm).

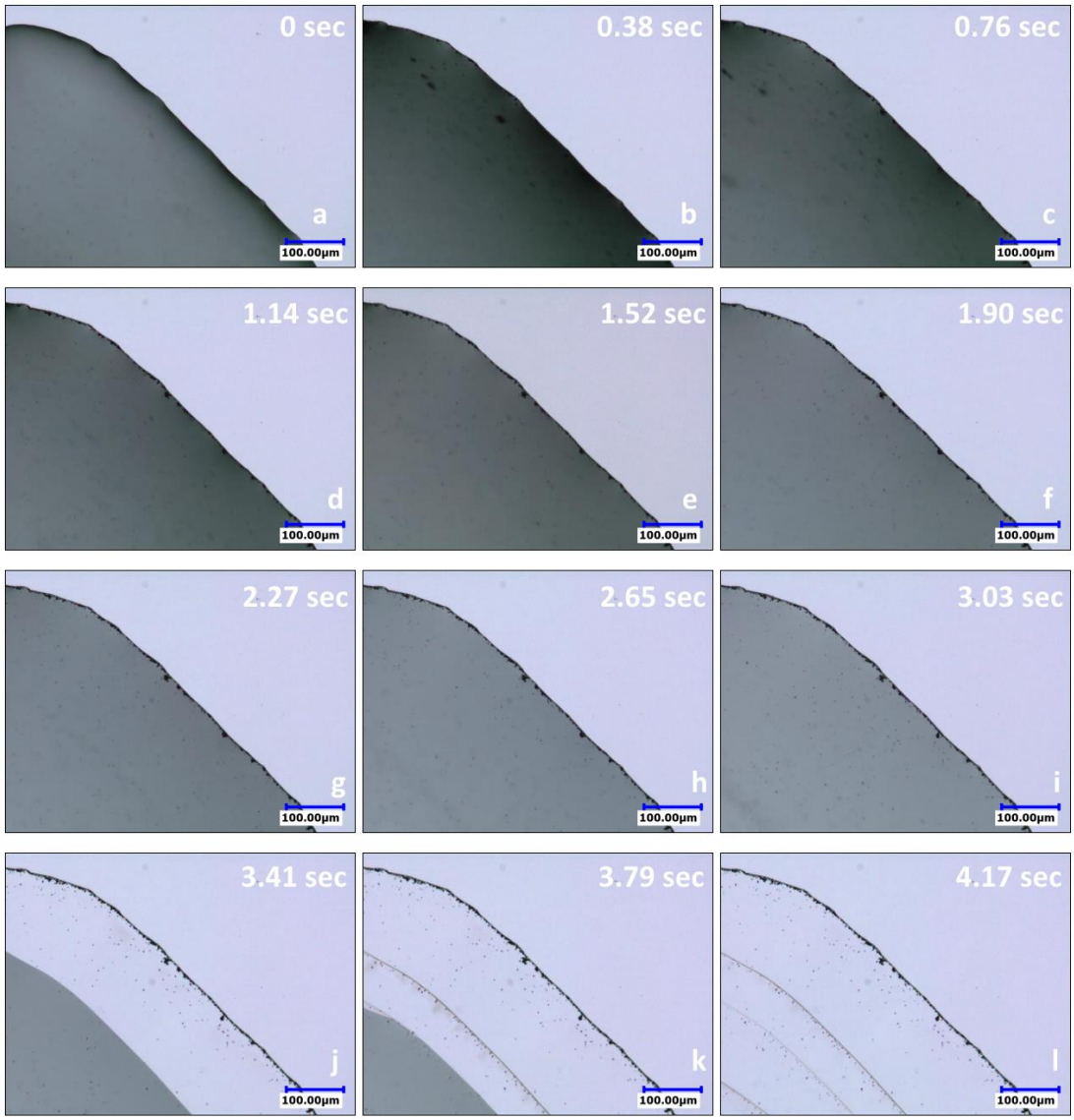

Figure 4.14 Sequential images from a video microscopy of the drying droplet on a heated silicon substrate at 99 °C. The optical micrographs are recorded at a temporal resolution of 125 fps and at 500× magnification (scale bar: 100 μm).

4.4.3 Thermal imaging and Marangoni effect

It is known that for pinned binary mixture drops, the contact angle decreases, whereas the change in characteristics at the triple line is shown in terms of the change in the evaporation rate [192]. In Figure 4.15, the evaporation rate of a pinned butanol-water mixture drop (at 64 °C) is divided into three regimes. The first (regime I) and last regimes (regime III) have the highest and lowest evaporation rates,

approximately. These regimes are identified by evolution of volume for all drops, and then, the transition time between two consecutive regimes is correlated to the infrared thermography data. Figures 4.16 and 4.17 show the thermal imaging of evaporating droplets corresponding to the dried droplets shown in Figure 4.2b at substrate temperatures of 64 and 81 °C. Infrared thermography results (for all studied temperatures) reveal that the evaporation of binary mixture droplets can be divided into three regimes in terms of thermal patterns [192,206]. In regime I, a high number of multiple convection vortices appear on the surface of drying droplets (see Figures 4.16a-h and 4.17a-h). As the droplets are very small with a radius (R ≈ 0.94 − 1.18) smaller than the capillary length $l_c = \sqrt{\sigma/\rho g}$ in a range between 1.92 and 2.62, the observed convection cannot be due to buoyancy-driven flows. In addition, the multiple vortices in regime I were not seen for the evaporation of pure water-based nanofluid droplets on the same substrate and similar temperatures [26]; thus, neither buoyancy-driven flow nor gravity is considered to be driving the vortices. By using thermal imaging, small temperature differences at the droplets' surface were observed; hence, thermocapillary is unlikely to be the mechanism behind convection [192,206]. It is believed that the multiple vortices in regime I may be arising from concentration gradients at the liquid-vapour interface, which affect local surface tension [192,206]. However, there is the possibility that non-uniform evaporation resulting from concentration variation is likely to cause small temperature variations, which may also lead to surface tension gradients [192]. To check the effect of the Marangoni flow on the thermal patterns, the variations of both the solutal Marangoni (M_a^S), and the thermal Marangoni (M_a^T) numbers throughout the evaporation process are provided in Figure 4.18aI-III (for 47, 64, and 81 °C). Estimation of the Marangoni numbers is explained in detail in Appendix A.1.1 and Appendix A.1.2. During regime I, the solutal Marangoni decreases with the evaporation time due to the decrease of the alcohol concentration, but instead the thermal Marangoni increases. Meanwhile, the order of the magnitude of the solutal Marangoni is larger than that of the thermal one, showing that the solutal Marangoni is dominant during regime I (Figure 4.18aI-III). In other words, the occurrence of multiple convection vortices in regime I leading to the chaotic motion of nanoparticles is mainly due to

the strong Marangoni flow driven by the local concentration gradient. For the self-rewetting fluids, as far as dilute composition regions are concerned, alcohol is a more volatile component and evaporates first, despite the fact that pure alcohols have a higher boiling point than water [198]. The variation in local concentration at the droplet interface could be due to diffusion from the bulk liquid inside droplets to the interface, evaporation, and diffusion into the gas phase [192,206]. As evaporation proceeds, the number of multiple vortices decreases [206]. Regime II or the transition regime rapidly occurs when the flow slows down. Convection vortices remain on one side of the drying droplet to disappear near the triple line (see Figures 4.16k-o and 4.17k-m). In the previous section, it is understood that there is an exception for the transition regime at substrate temperatures of 81 and 99 °C, where two distinctive counter-rotating vortices can be observed following the chaotic flow (or regime I). Those two vortices can be seen in Figure 4.17o (81 °C) indicated by two arrows. Two physical mechanisms could be considered for the observations during the transition regime: One is diffusion of the final and limited content of butanol from the bulk liquid to the interface leading to very weak concentration gradients at the interface [192]; the other could be viscous dissipation [206]. Bennacer and Sefiane [206] have shown that once the driving force for the solutal Marangoni switches off, viscous forces dictate the flow evolution. Therefore, the decay in vorticity intensity is completely determined by viscous dissipation [206]. After the complete transition, no vortices are left on the droplet's surface similar to thermal imaging of evaporating CuO-water droplets (see Figures 4.16p and 4.17p). As shown in Figure 4.18aI-III, the solutal Marangoni continues to decrease after the transition regime (regime II), whereas the thermal Marangoni remains constant, and then decreases at the late stages of regime III. The order of the magnitude of the solutal Marangoni becomes lower quickly after regime II compared to that of the thermal Marangoni, indicating the dominance of the thermal Marangoni flow in regime III. This indicates that the majority of butanol may be depleted during regimes I and II. The absence of vortices at the interface and also identical thermal imaging to pure water-based droplets also show the solutal Marangoni is no further responsible for regime III. Furthermore, regime III corresponds to that observed by

video microscopy showing some particles moving outward to the triple line and deposit at the edge, whereas some other particles return from the area close to the periphery towards the centre along the liquid-vapour interface. Both thermal imaging and tracing of nanoparticles during regime III demonstrate that the internal flow structure is identical to that found for evaporation of CuO-water droplets [26]. Therefore, the main source of flow motion in regime III (except for non-heated substrate) is the thermal Marangoni driven by inhomogeneous temperature distribution along the droplet surface. For non-heated substrate, the outward capillary flow is dominant as there is a rather weak temperature gradient along the droplet surface [26]. For heated substrates, temperature gradients are strong enough to induce the Marangoni effect. Similarly to evaporation of CuO-water droplets [26], the thermal imaging results for the last regime show that the droplet apex is the coolest position while the edge has the highest temperature. As the surface tension of water decreases with increasing temperature, water flows from lower surface tension to higher surface tension regions. This is confirmed by tracking nanoparticles within evaporating droplets, showing a radially inward surface flow from the edge to the top region along the droplet interface. However, a cluster of nanoparticles is simultaneously driven by the outward capillary flow adjacent to the substrate. Some of these nanoparticles deposit at the edge, and some others are the aforementioned repelled nanoparticles driven by the thermal Marangoni effect. Both experimental and theoretical studies confirm that a stagnation point exists on the droplet surface very close to the triple line when the thermal Marangoni effect is significant (see Figure 4.6) [26,177,178]. Because of this point, flow regions within drying droplets are divided in to two regions. The first region is the outward flow, in which the particles reach the triple line and form the peripheral ring (Figure 4.6). The second region is the convective flow, in which the particles move towards the triple line but then change their direction and inwardly return to the top surface along the liquid-vapour interface (Figure 4.6). The convective flow region is dominated by thermally driven Marangoni flow counteracting the outward flow. The same observations for water-based nanofluid droplets show that most of the butanol (not all) has evaporated prior to the start of regime III. In addition, the competition between the Marangoni

numbers (Figure 4.18aI-III) has revealed that thermal Marangoni is responsible f or regime III and hence the solutal Marangoni effect is dominated by the thermal Marangoni effect for the last regime of evaporation. Figure 4.18bI-III shows the absolute interfacial velocities driven by both the concentration gradient (or the solutal Marangoni velocity ($U_{M_a}^S$)) and by the temperature gradient (or the thermal Marangoni velocity ($U_{M_a}^T$)) as a function of M_a^S and M_a^T, respectively (at 47, 64, and 81 °C). Estimation of the Marangoni velocity can be found in Appendix A.1.3. It can be clearly seen that the solutal Marangoni velocity decreases linearly during all regimes with a decrease in the solutal Marangoni number. In other words, the solutal Marangoni velocity decreases with the evaporation time (see the direction of the dashed arrow in Figure 4.18bIIII). On the other hand, the thermal Marangoni velocity increases linearly during regimes I and II as the thermal Marangoni number increases. In regime III, there is a sudden decrease in the thermal Marangoni velocity, whereas the thermal Marangoni number remains almost constant. It can be deduced that the thermally driven velocity increases with evaporation time in regimes I and II, but it decreases during regime III. As mentioned, there is a linear relation between the solutal Marangoni velocity and the solutal Marangoni number ($U_{M_a}^S = \alpha_S M_a^S + \beta_S$). In addition, there is the same relation between the thermal Marangoni velocity and the thermal Marangoni number ($U_{M_a}^T = \alpha_T M_a^T + \beta_T$) during the first two regimes. The orders of magnitude of the slopes (α_S , α_T) for both the solutal and thermal Marangoni are of 10^{-6} and 10^{-5} m/s, respectively. Only at 47 °C is the order of magnitude of α_S of 10^{-7} m/s.

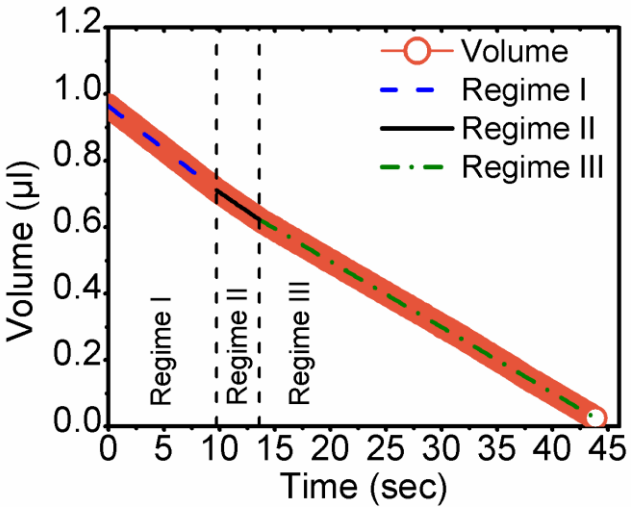

Figure 4.15 Volume variation with time at 64 °C.

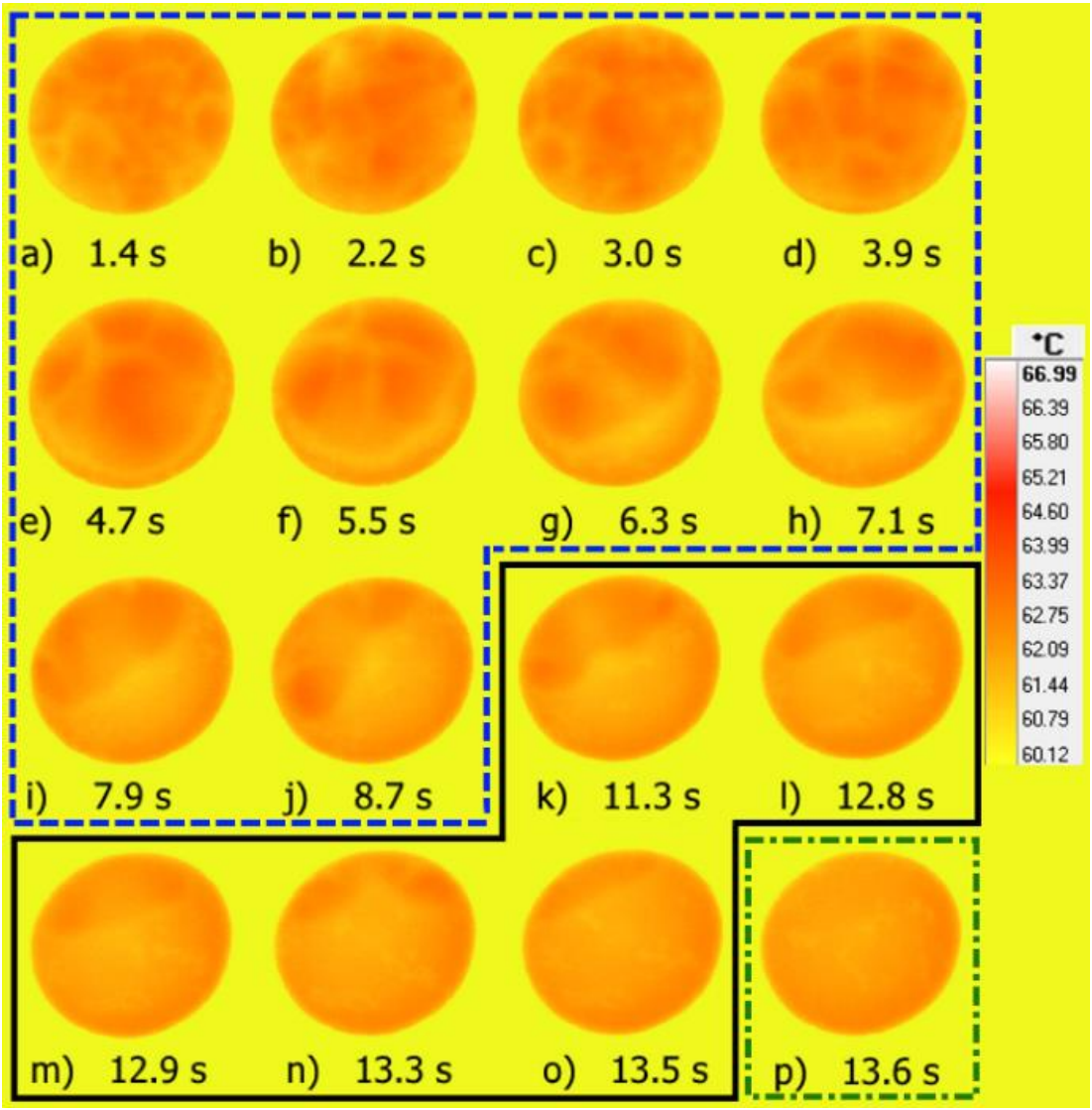

Figure 4.16 Thermal imaging. Evolution of thermal patterns observed during the evaporation of binary-based CuO nanofluid droplets on heated silicon substrates at 64 °C.

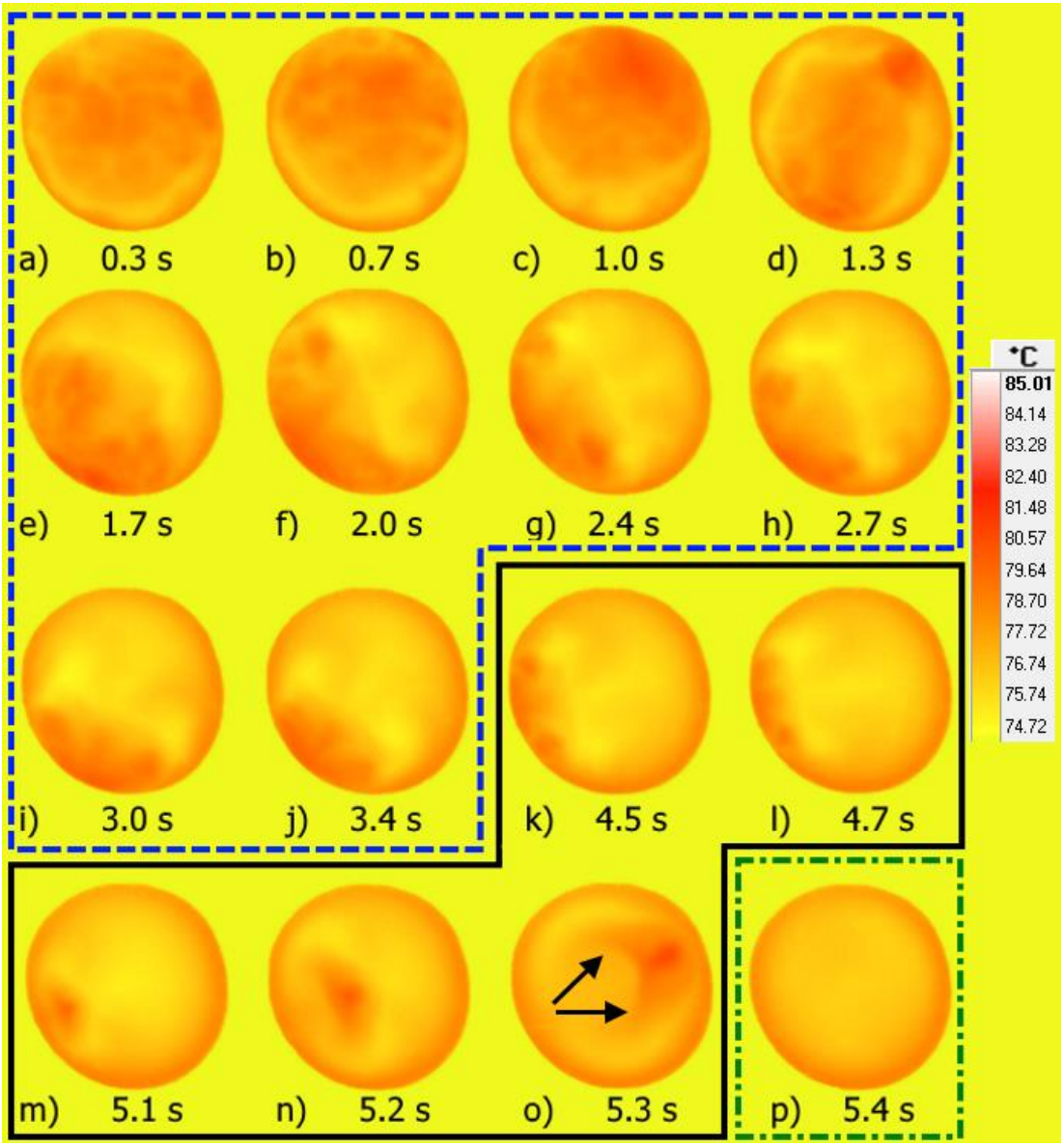

Figure 4.17 Thermal Imaging. Evolution of thermal patterns observed during the evaporation of binary-based CuO nanofluid droplets on heated silicon substrates at 81 °C.

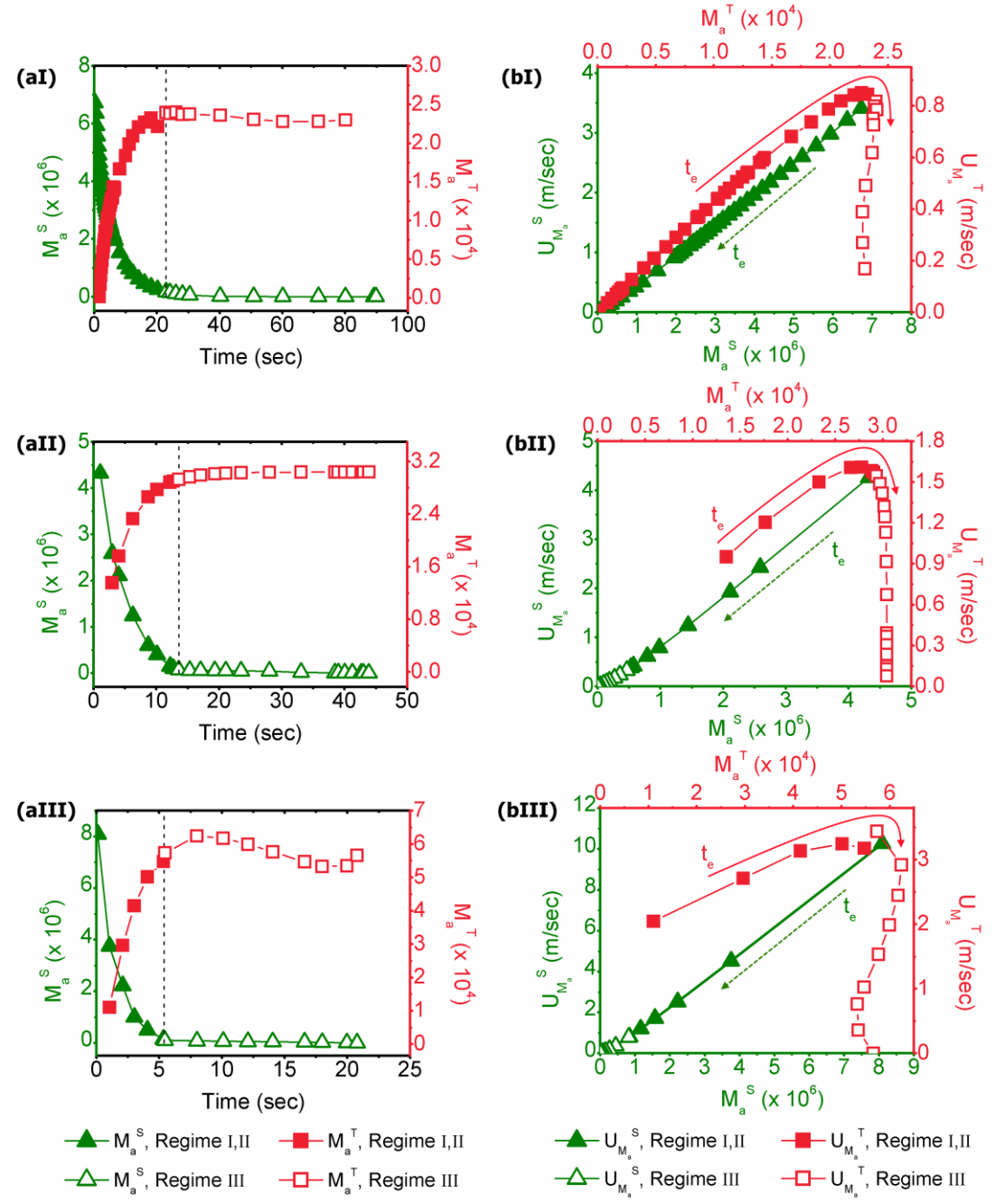

Figure 4.18 (a) Solutal and thermal Marangoni numbers calculated during evaporation time: (I) 47, (II) 64, and (III) 81 °C. (b) Solutal and thermal Marangoni velocities calculated during evaporation time as function of solutal and thermal Marangoni, respectively: (I) 47, (II) 64, and (III) 81 °C. The solid arrow shows the increase direction of the evaporation time for the thermal Marangoni velocity; the dashed arrow shows the increase direction of the evaporation time for the solutal Marangoni velocity. t_e is the evaporation time. The calculated velocities are the absolute values.

4.5 Conclusions

This study investigates the evaporation of binary-based sessile droplets containing CuO nanoparticles placed on silicon substrates at a wide range of temperatures. Depending on the substrate temperature, different deposition patterns were left on the silicon surface. The patterns were found to be similar to those left behind after the dry-out of water-based nanofluid droplets. The analysis of the video microscopy shows that the chaotic motion of nanoparticles is from the beginning of the evaporation. Then, the flow slows down and rapidly transits to a regular motion of the particles. At temperatures of 81 and 99 °C, the transition from the chaotic flow to slower and regular flow is accompanied with two distinctive counter-rotating vortices. After the complete transition, the nanoparticles move towards the triple line adjacent to the solid surface due to an outward flow. Some of those deposits at the edge forming the peripheral ring, whereas the remaining nanoparticles return back from the area in the vicinity of the triple line towards the top centre of the droplet along the liquid-vapour interface driven by the thermal Marangoni effect. This regular motion of the solute within the drying droplets was also observed for water-based nanofluid droplets. The repelled solute builds a ring-like cluster on the top of the droplets, which has a significant role on the deposition of the secondary ring interior of the peripheral ring at temperatures of 47, 64, and 81 °C. Unlike the evaporation of CuO-water droplets, there are several faint line patterns inside the secondary ring of binary mixture droplets. The ring-like cluster on the top of the evaporating droplet at 99 °C does not deposit the secondary ring on the substrate, as a part of the triple line pins and depins for several times leading to the stick-slip pattern.

Both the thermal imaging and volume evolution show that the thermal patterns of drying binary-based nanofluid droplets go through three distinct regimes. Regime I is characterised by multiple convection vortices driven by the solutal Marangoni arising from local concentration gradient, corresponding to the chaotic motion of the solute seen in video microscopy. The competition between the solutal Marangoni and thermal Marangoni numbers also demonstrates that the flow is dominated by the

former one. During regime II, the flow slows down, and the number of multiple vortices reduces until all of those disappear. At 81 and 99 °C, the same pairs of counter-rotating vortices in video microscopy are found for the transition regime (regime II). Regime III is identical to the thermal pattern of CuO-water nanofluids. In other words, the majority of the more volatile component has been depleted during the two first regimes (regimes I and II); thus, the thermal Marangoni effect drives the flow in regime III. For this reason, the internal flow structure in regime III is identical to that of the evaporating CuO-water droplets. This flow structure is corresponding to the regular motion of the solute, as shown in video microscopy.

Chapter 5 Patterns from Water-Based Bidispersed Drops on Heated Substrates

This chapter is based on a manuscript submitted for publication in 2017 [207]. The author contributed to the design of the experiments, performed the experiments, and contributed to the data analysis and the writing of the manuscript. Dr. R. Deltombe scanned the deposits of nanoparticles using a white light interferometry technique. Prof. M. Bigerelle analysed the scans of the deposition patterns which are provided in Figures A.3, A.4, and A.5 in Appendix A.2. Prof. S. Harmand and Prof. K. Sefiane supported the author in writing the manuscript and granted approval for the final version.

Effect of Substrate Temperature on Pattern Formation of Bidispersed Particles from Volatile Drops by Maryam Parsa, Souad Harmand, Khellil Sefiane, Maxence Bigerelle and Raphaël Deltombe
The Journal of Physical Chemistry B, 2017, *121* (48), pp 11002-11017
doi: 10.1021/acs.jpcb.7b09700

5.1 Abstract

In this study, pattern formation during evaporation of bidispersed drops (containing 1 and 3.2 μm particles) placed on a smooth substrate at different temperatures is investigated. Five distinctive deposition patterns are observed depending on the substrate temperature: a relatively uniform pattern enclosed by a disk-shaped ring, a nearly non-uniform pattern inside a thick outer ring, a "dual-ring" pattern, a "rose-like" pattern, and a set of concentric rings corresponding to the "stick-slip" pattern. At drops edge, the particle size effect leads to the formation of three rings: an outermost ring formed by the non-volatile additives smaller than 1 μm, a middle ring built by particles with size of 1 μm, and an innermost ring formed by the mixture of 1 and 3.2 μm. For temperatures between 64 and 99 °C, the depinning of the contact line causes the same particle sorting at the other deposition lines in the interior of the

drop. However, the width of the zone between the outermost ring and the middle ring at the initial edge of the drop is found to be smaller than that at the other deposition lines. The size of the width is found to be dependent on the contact angle. Particle velocity is measured by tracking particles during the evaporation. It is shown that particle slightly increases with time, but it rapidly increases at the last stage of the drying process, known as “rush-hour” behaviour. The sudden change in the increase of the velocity occurs between the normalised time of 0.7 and 0.8 for temperatures from 22 to 81 °C. The increasing trend of velocity with time matches well with the theoretical model. The tracer particles are also used to measure the distance between the contact line and the nearest turning point of those particles return back towards the top of the drop due to the inward Marangoni flow. It is found that this distance decreases with increasing the substrate temperature.

5.2 Introduction

The drying of a sessile droplet containing non-volatile solute can lead to the formation of a deposition pattern on the substrate. A full understanding of the pattern formation is of vital importance as it plays a crucial role in many industrial applications, such as inkjet printing [43,44,208,209], lithography [210], micro-patterning of electronics [136], and photonics [211]. Moreover, the study of the pattern formation is of increasing biological importance [31,35]. The most commonly observed pattern is the “coffee-ring” effect or the ring-like deposit, which is created by the deposition of particles at the edge arisen from the net outward capillary flow on the liquid-solid interface [14,15]. It is well known that the coffee-ring effect can be reversed by the inward Marangoni flow driven by the surface tension gradient along the liquid-vapour interface [76]. The inward Marangoni flow causes some particles to travel towards the centre along the free surface and deposit in the central regions of the drying droplet. This phenomena leads to the formation of different patterns such as the uniform deposition, “dual-ring” [26], “stick-slip” [26], and volcano-like patterns [146]. There are a number of factors affecting the pattern formation, which can be manipulated to control internal flow motion as well as the

dried deposits for use in the aforementioned applications, such as altering environmental conditions (i.e., atmospheric pressure [25], substrate temperature [26,146], relative humidity [20]), applying electrowetting [150,151], manipulating the base fluid [22,193], adding surfactants [21,68,147], varying the solute (i.e., shape [134], size, and concentration [19,125]).

Another factor that affects the deposition patterns is employing different particle sizes inside a drying droplet simultaneously. Huang et al. [212] showed that the mixture of 50 nm silver and 100 nm gold nanoparticles in water forms well-aligned stripe patterns onto a silicon dioxide/silicon substrate through dip-coating. Jung and Kwak [213] reported that 1 and 6 μm polystyrene particles can be separated using the dielectrophoretic (DEP) force created by the micro-patterned gold electrode on the silicon dioxide layer and the drag force generated by the outward flow in an evaporating droplet. The authors showed that the two sized particles self-assembled near the contact line. The smaller particles deposited at the edge, whereas the larger ones deposited separately with a constant distance (of $\sim$ 67 μm) from the smaller ones. The separation of the red blood cells and Escherichia coli was also observed by the same method [213]. Erb et al. [214] applied the magnetostatic interaction between 1 and 2.7 μm Fe_2O_3 particles to assemble diverse sets of structures such as rings (a large particle is surrounded by smaller particles) and poles (small particle aggregates on two sides of a large particle). Jung et al. [139] divided the dispersing of the polystyrene micro- (5 μm) and nanoparticles (500 nm) in an evaporating droplet into the three phases by using particle-tracking velocimetry. In the first phase, the micro- and nanoparticles migrated towards the pinned contact line and deposited there. In the second phase, the separation of the two sized particles near the contact line was observed similar to Jung and Kwak [213]. In the third phase, the receding contact line causes the movement of the micro-particles towards the centre of the droplet. Sangani et al. [215] also reported that the small particles (of 3 μm) moved towards the contact line and deposited at the drop edge, leading to the contact line pinning. On the other hand, the larger particles (of 50 μm) collected as a chain, keeping a distance from the small ones. The distance between the chain of the large particles and the edge increases slowly with time as the drop height decreases, and

thus the chain moves inward. However, unlike the bidispersed suspension, this distance between the particles and the edge remained nearly constant in most monodispersed suspension cases [215]. Weon and Je [216] also observed the increasing distance between the chain of large polystyrene particles (20 μm) and the drop edge, whereas small particles (2 μm) segregated at the edge. The authors concluded that the reversal motion of large particles happens when the inward force driven by the capillary force overcomes the outward force driven by the coffee-ring effect. This competition between these two forces affected the pattern left after the evaporation of 0.2 and 3.6 μm diameter poly(methyl methacrylate) (PMMA) particles in water [216]. At first, the initial ring of small particles at the edge was formed, and then, the large particles moved inwardly to the central regions; then, a new ring of deposits was formed when the reverse motion was stopped by rupture. This behaviour was repeated several times and consequently multiple rings were formed on the substrate [216]. Chhasatia and Sun [144] studied the evaporation of bidispersed drop containing 0.1 and 1.1 μm particles on substrates with different wettabilities (receding contact angle varied from 85 to 0°). Because the state of substrate wettability significantly affects the duration of evaporation modes (i.e., constant contact area, constant contact angle, and mixed modes), different microflow patterns within evaporating drops were observed for each evaporation mode. As a result, different deposition patterns were found for substrates of varying wettabilities [144]. Monteux and Lequeux [217] showed a thin liquid film without particles at the edge in the case of monodispersed drop. The width of the depleted zone was found to be controlled by the particle size and contact angle. This phenomenon was reported to be useful to sort two different particle sizes inside the drop as the smaller particles can penetrate further into the edge, leading to the separation of smaller particles from the larger ones. Wong et al. [140] studied the deposition of three different-sized polystyrene particles (of 40 nm, 1, and 2 μm) in a water droplet. The largest and smallest particles formed the innermost and outermost rings on the substrate after the dry-out of the droplet, respectively. Devlin et al. [218] investigated the effect of the gravity direction on the deposition patterns of two different (1 and 3.2 μm) sized particles in a sessile and a pendant drop both deposited onto silicon substrates. For

the pendant drop, only small particles deposited at the edge and the dried central region contained the large particles. However, for the sessile drop, the mixture of 1 and 3.2 μm sized particles deposited at the edge [218,219], and both two particle sizes were found in the centre of the dried drop [218]. Zhong et al. [141] reported that the evaporation of water sessile droplets with 40 nm Al_2O_3 nanoparticles left behind a fractal-like deposit, whereas the 5 nm nanoparticles formed a coffee-ring pattern with a thick deposition in the centre of the dried droplet. The authors demonstrated that the coexisting of 5 and 40 nm Al_2O_3 nanoparticles eliminated the non-uniform pattern formed either by the 5 or 40 nm nanoparticles, leading to a more uniform mixture pattern.

A review of the relevant literature indicates that most studies have been devoted to understanding the behaviour of multi-sized particles in liquid drops evaporating on non-heated substrates [139–141,144,212–219]. However, only a few works have investigated the influence of heated substrates in this field [145,220,221]. Han et al. [220] showed that two different particle sizes of 50 and 500 nm can self-assemble into arranged stripe patterns by confining the solution between a cylindrical lens and heated hydrophobic silicon substrate at 80 °C. Jeong et al. [145] showed that a combination of the coffee-ring and strong Marangoni effects can be used to sort different-sized particles (from 100 nm to 15 μm) on a hydrophilic substrate heated at 36 °C. The particles were not separated on hydrophobic substrates due to the constant, large contact angle as well as the unpinned contact line during the evaporation, leading to the transportation of the particles away from the contact line. Eventually, the particles of different sizes were overlapped at the contact line on hydrophobic surfaces. Hendarto and Gianchandani [221] investigated the effect of Marangoni convection on the size sorting of multiple-sized hollow glass spheres (ranging from 5 to 200 μm in diameter) suspended in an isopropyl droplet by heating a glass substrate for a wide range of temperatures (55-85 °C). Although the smaller spheres (< 50 μm) were found everywhere throughout the dried droplet at 55 °C, the larger spheres (150-200 μm) were mainly deposited in the centre of the dried region. At 85 °C (over the boiling point of isopropyl), most of the smaller spheres were deposited at the areas near the edge.

To the best of our knowledge, there is no article available to study the effect of various temperatures on the mixture of two sized particles suspended in water-based sessile droplets. In this study, the effect of a wide range of substrate temperatures (from 22 to 99 °C) is investigated on the internal flow structure as well as the deposit features of two different-sized particles in water droplets drying on smooth silicon substrates. In addition, for the first time, the motion of two sized particles is tracked within a drying droplet on a heated substrate using reflection optical microscopy.

5.3 Experimental Procedure

5.3.1 Solution

The aqueous suspension was made from yellow-green fluorescent carboxylate-modified polystyrene latex beads with mean diameter of 1 μm (Sigma-Aldrich), and Fluoro-Max^{TM} red fluorescent polymer microspheres with diameter of 3.2 μm (Thermo Scientific) in MilliQ water. The mass concentration of particles was 0.025 wt % with equal parts of each particle size.

5.3.2 Deposition

Smooth silicon wafers were ultrasonicated and thoroughly rinsed with deionised water and acetone, followed by air drying (Elma Company) to remove the moisture. A programmable syringe pump (KdScientific, legato 100) was used to deposit the drop solution (with varying size from 0.5 to 6 μL) onto the hot silicon substrate, which was placed on a plate heated at temperatures of 51, 64, 81, and 99 °C. The experiment was also carried out onto non-heated substrate (22 °C). Each set of experiments was repeated at least five times. The atmospheric conditions were monitored during the experiments using a sensor (Hygrosens Company). The room temperature and relative humidity were 22 °C and 30%, respectively.

5.3.3 Imaging and microscopy

Thermal imaging was conducted by means of an infrared (IR) camera (FLIR, X6580 sc) mounted on a lens (FLIR, MW G1WD30) to read the temperature at the air-liquid interface of the drying droplets, as water is mostly opaque to IR. A high-speed camera (Keyence, VW600C) equipped with a lens (Keyence, VW Z2) and an LED backlight (CCS Inc.) were employed to record side view images of evaporating droplets at 30 frames/s. The drop shape analysis software (KRÜSS GmbH, DSA4) was used to monitor the evolution of drop shape parameters such as the base diameter and contact angle. The top-view images of evaporating droplets were recorded by means of the high-speed camera mounted on an optical microscopic lens (Keyence, VH-Z100R, magnification zoom from 100× to 1000×). The particles' movement was tracked using video editing/analysis software (Keyence, VW-9000 Motion Analyzer). The images of the final deposition patterns were taken by using an optical microscopic lens (Keyence, VH-Z20R, magnification zoom from 20× to 200×). To investigate the deposition distribution along the droplet base diameter, the dried deposits were scanned by means of a white light interferometer (Zygo, NewView 7300). The further information about characterisation and quantification of substrate roughness can be found in the study of Parsa et al. [26].

5.3.4 Supporting Information

Supporting Information associated with this chapter is available in the online version.[3]

5.4 Results and Discussion

5.4.1 Deposition pattern after dry-out of drops

Figure 5.1a shows the contact line of drops remain pinned for majority of the evaporation time and the contact angle monotonously decreases. Dried Patterns of

[3] https://pubs.acs.org/doi/suppl/10.1021/acs.jpcb.7b09700

bidispersed drops at different temperatures from 22 to 99 °C are presented in Figure 5.1b. Using an algorithm, the 3.2 μm particles are separated from the 1 μm particles and the density corresponding images are provided in Appendix. Dried deposits of drops, density distribution, and topography of the particle deposits are shown in Figures A.3, A.4, and A.5, respectively.

As shown in Figures 5.1b, A.4 and A.5, sample I at 22 °C exhibits a relatively uniform coverage of particles enclosed with a distinct disk-shaped ring of particles. For sample II at 51 °C, the observed pattern shows nearly non-uniform distribution of particles inside the outer ring with a higher density. As shown in Figures 5.1b, A.4, and A.5, samples at temperatures of 64, 81, and 99 °C exhibit completely non-uniform patterns compared to the examined lower temperatures. At 64 and 81 °C, the dual-ring pattern is observed with the irregular distribution of particles in the interior of the smaller ring (see Figures 5.1bIII,IV, A.4III,IV and A.5III,IV). At 99 °C, both samples V and VI exhibit the stick-slip patterns but in two different shapes; one resembles a “rose” flower wherein both the stick and slip phases occur on all sides of the drop and end in the drop centre (Figures 5.1bV, A.4V and A.5V); and the other resembles a set of multiple concentric rings wherein the drop sticks on one side (the left side of Figures 5.1bVI, A.4VI and A.5VI) and slips from the opposite side (the right side of Figures 5.1bVI, A.4VI and A.5VI). The density of particles increases at the deposition lines and decreases between two consecutive lines (see Figures A.4V,VI and A.5V,VI).

5.4.2 Deposition formation during the drying process

Using optical microscopy, the evaporation process of bidispersed drops at all substrate temperatures was observed (see the Supporting Information). The readers are strongly encouraged to view the high-magnification videos provided in the Supporting Information, as the motion of particles cannot be unambiguously ascertained from still images. Top-view snapshots from all real-time videos of the drying bidispersed drops are provided in Figures 5.2,5.3,5.6,5.7, and 5.10-5.15. In all figures, the microscope lens was focused on the contact line of drops. The 1000×

magnification consecutive optical micrographs of the drop evaporating on the non-heated substrate are shown in Figure 5.2 (Supporting Information Video S1). Insets in Figure 5.2 show the regions highlighted in solid rectangles at higher magnification. It can be clearly seen that the accumulation of particles at the edge increases with time due to an outward radial flow driven by the coffee-ring effect (see Figure 5.2a-i). It is known that the thickness of the meniscus decreases towards the drop edge; thus, particles stop moving further towards the contact line at a position where their size matches the thickness of the meniscus [140]. In other words, the smaller particles move closer to the pinned contact line as compared to the larger ones, leading to the separation of particles with different sizes (insets in Figure 5.2b,e,h). Magnified images of the CL region show that there is a thin liquid film between the initial contact line and leading edge of the ring consisting of particles with mean diameter of 1 μm (shown between two arrows in inset in Figure 5.2e). A peripheral ring of particles is left behind at the drop edge after the complete evaporation, confirming that the thin liquid film did not only consist of pure water (see the outermost ring in inset in Figure 5.2i). Besides, Figure 5.3 shows a depleted zone is left behind between the peripheral ring and the leading edge of 1 μm particles after the complete evaporation of the thin liquid film separating the two rings from each other. To ensure the origin of the deposits at the peripheral ring, the evaporation of drops containing monodispersed particles was conducted (Figure 5.4). As presented in Figure 5.4aI, the drop containing 1 μm particles leaves a thin liquid film which is between the particles and the contact line. After the complete evaporation, only a single ring at the periphery is left and thus the thin liquid film of pure water is completely evaporated (see Figure 5.4aII). Figure 5.4bI shows the 3.2 μm particles travel towards the edge and stop from the edge with a distance, which is filled with the thin liquid film. As shown in Figure 5.4bII, two rings of particles are left behind after the drop dries out. The inner ring is formed by 3.2 μm microspheres; the outer (or peripheral) ring is formed by the particles obviously smaller than 3.2 μm microspheres (Figure 5.4bII). This results from the deposition of the non-volatile additives, which are used in the monodispersed 3.2 μm particle suspension by the manufacturer to inhibit agglomeration and promote stability of the suspension. The

same peripheral ring can be seen for dried bidispersed drops. This reveals that the smallest particles probably with diameters lower than 1 μm penetrate further inside the contact line region, and reach the drop edge, leading to the deposition of particles there. Therefore, three separate rings of particles can be observed during the drying process of bidispersed drops (see insets in Figure 5.2h): the first is the outermost ring at the contact line consisting of particles smaller than 1 μm; the second is the middle ring forming by 1 μm particles; and the third is the innermost ring consisting of 3.2 μm particles. To better understanding of the deposition features in the vicinity of the contact line, the individual particles within the droplet were tracked, as shown by the blue and red arrows in Figure 5.5aI-aVI. The arrows show that those 1 μm particles arriving behind the 3.2 μm particles can travel around the larger particles and reach the middle ring. Besides, some 1 μm particles pass from between the two adjacent 3.2 μm particles and then deposit at the middle ring (shown by the circle in Figure 5.5bI-bIV). Such movements by small particles can be observed until the late stages of the evaporation. On the other hand, some other small (1 μm) particles are trapped at the innermost ring and cannot move further towards the edge due to the presence of high number of large particles at the innermost ring at the late stages of the evaporation (see the increase in the number of particles of the innermost ring with time in Figure 5.2a-h). In addition, there is a dramatic increase in the velocity of particles approaching the edge in the late stages of the drop's lifetime [222,223], causing the sudden increase in the number of small particles at the innermost ring. In other words, there is not enough space for these small particles to pass through the inner ring and reach the middle one, leading to the aggregation of small particles at the innermost ring, and hence the innermost ring is formed by the mixture of both small (1 μm) and large (3.2 μm) particles after the dry-out of the drop (see the innermost ring in insets in Figure 5.2i). Insets in Figure 5.2b,e,h show that the distance between the innermost ring and the contact line increases with the evaporation time. In other words, the innermost ring moves inward towards the drop centre, repelling the coffee-ring effect. The reversal motion of the innermost ring can be attributed to the inward force driven by the capillary force [224,225], which is found to be a kind of lateral immersion capillary force [224]. The latter acts when

there is a contact between the particles and the air-liquid interface during the drying process [224,225]. The inward migration of particles takes place whenever the outward coffee-ring flow is overcome by the net capillary force between particles and the air-liquid interface, which is consistent with literature [216]. This reverse effect is a unique transport mechanism that is related to the geometric constraints of particles and drop (i.e., drop size, contact angle) [216], instead of other mechanisms, such as the Marangoni [76,177], gravity, standard effects [14,15], etc.

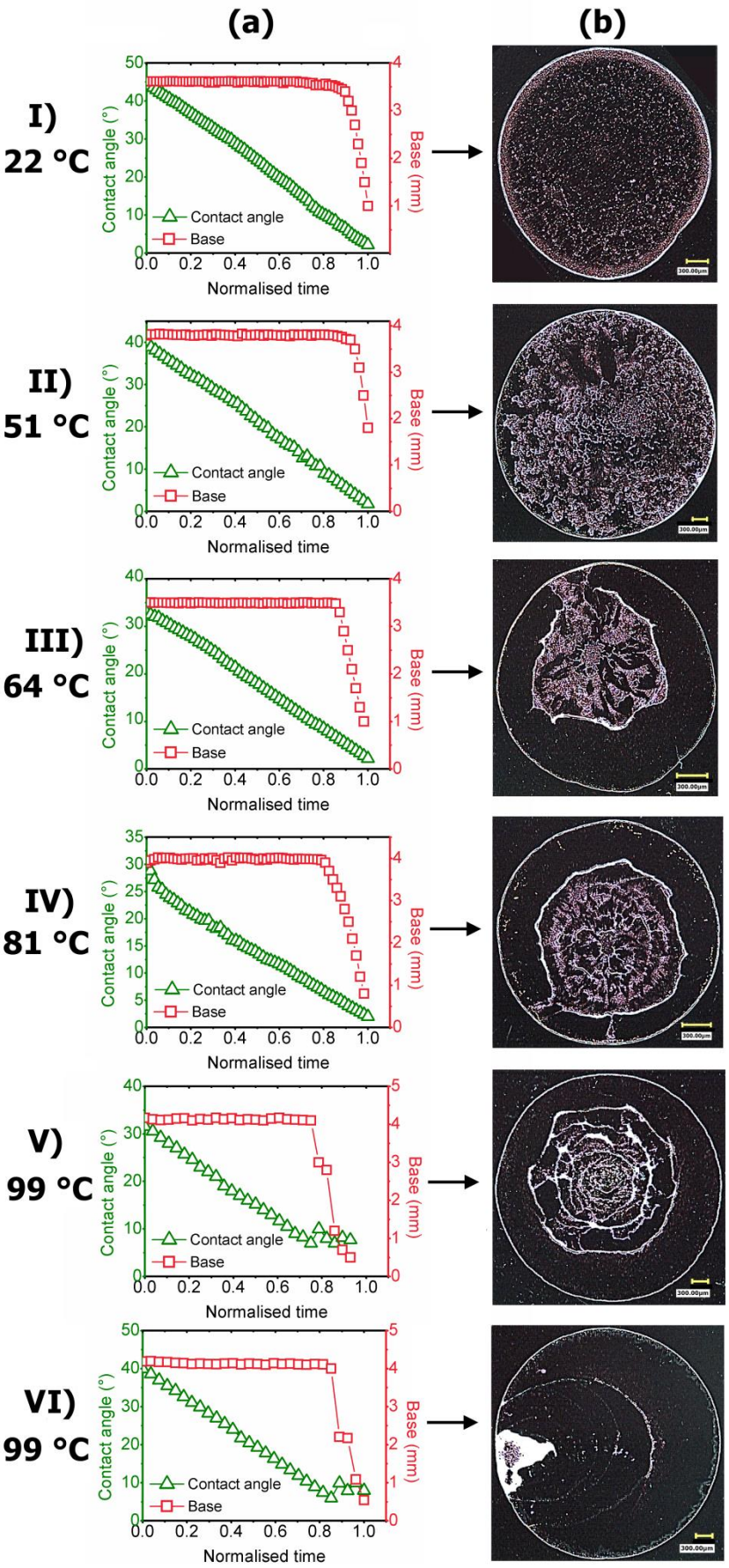
(a)
(b)
I)
22 °C
II)
51 °C
III)
64 °C
IV)
81 °C
V)
99 °C
VI)
99 °C
Contact angle (°)
Base (mm)
Normalised time
Contact angle
Base

Figure 5.1 (a) Evolution of base and contact angle for evaporating water-based bidispersed drops containing a mixture of 3.2 μm diameter particles (mass concentration of 0.0125 wt %) and 1 μm mean diameter particles (mass concentration of 0.0125 wt %) onto a non-heated silicon substrate (at 22 °C) and heated substrates at different temperatures of 51, 64, 81, and 99 °C. (b) Dried deposits of bidispersed drops onto a non-heated silicon substrate (at 22 °C) and heated substrates at different temperatures of 51, 64, 81, and 99 °C. Scale bars, 300 μm.

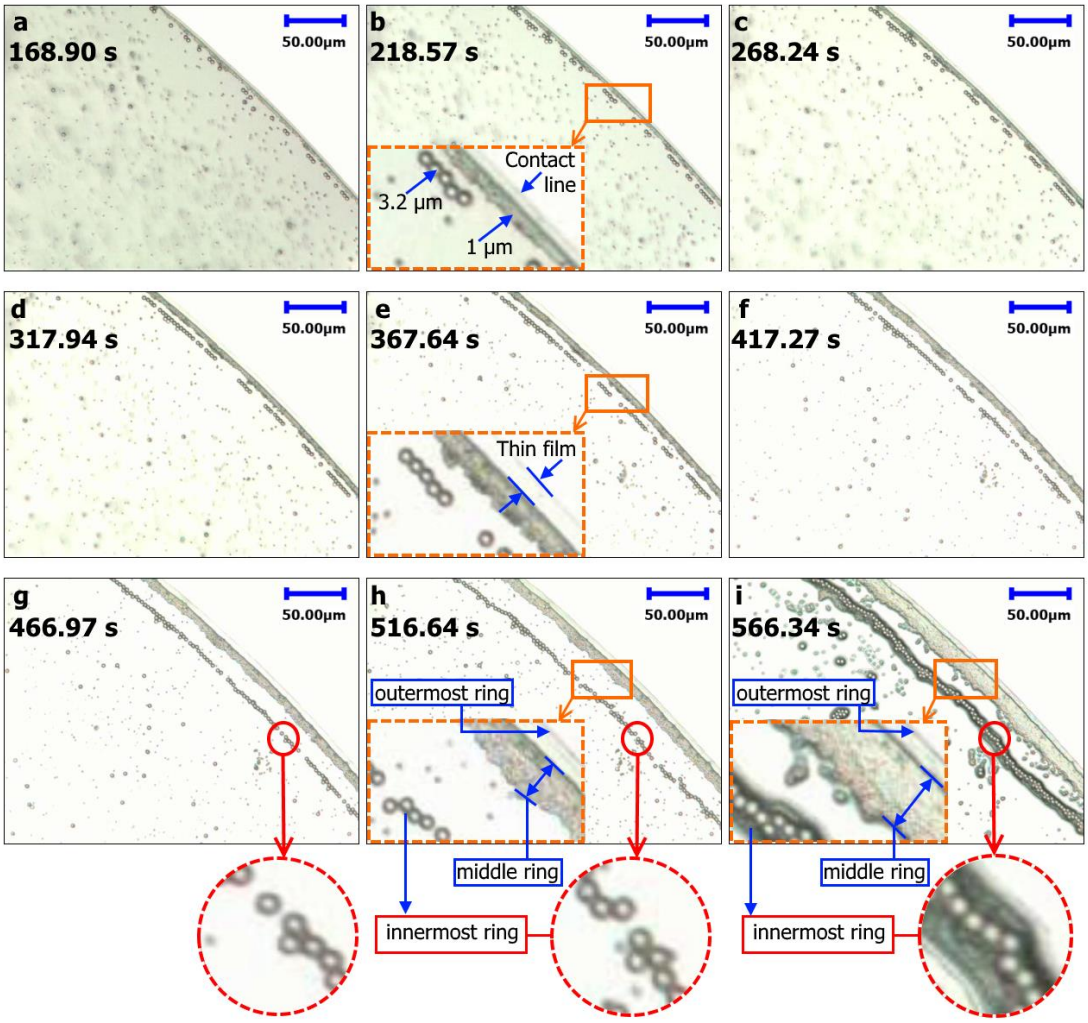

Figure 5.2 Snapshots from a video microscopy of the evaporation process of a water-based bidispersed drop containing a mixture of 3.2 μm diameter particles (mass concentration of 0.0125 wt %) and 1 μm mean diameter particles (mass concentration of 0.0125 wt %) onto a non-heated silicon substrate (at 22 °C). Insets show the zoomed-in regions highlighted in the solid rectangles and circles. The micrographs are recorded at a temporal resolution of 30 fps and at 1000× magnification. Scale bars, 50 μm.

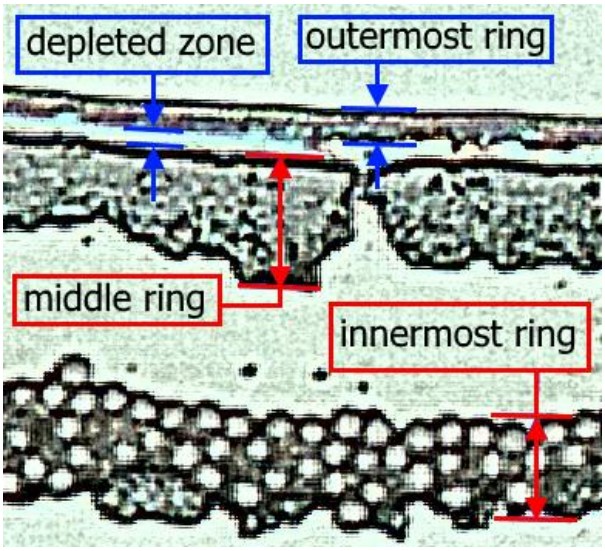

Figure 5.3 Zoomed-in picture (2×) of a completely dried water-based bidispersed drop containing a mixture of 3.2 μm diameter particles (mass concentration of 0.0125 wt %) and 1 μm mean diameter particles (mass concentration of 0.0125 wt %) onto a non-heated silicon substrate (at 22 °C). The complete evaporation of the thin liquid film leaves a depleted zone between the leading edge of the middle and outermost rings. The original micrograph is taken at magnification of 1000×.

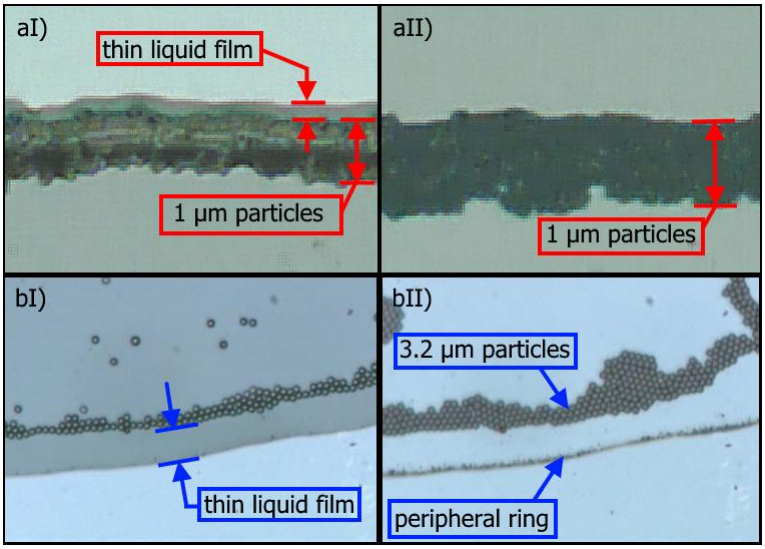

Figure 5.4 (a) Images taken from a video microscopy of the evaporation process of a water-based monodispersed drop containing 1 μm mean diameter particles (mass concentration of 0.0125 wt %) onto a heated silicon substrate at 51 °C: (I) the 1 μm particles leave a thin liquid film during the evaporation; (II) the thin liquid film dries out at the end of the evaporation, and only the ring of 1 μm particles is left behind. (b) Images taken from a video microscopy of the

evaporation process of a water-based monodispersed drop containing 3.2 μm diameter particles (mass concentration of 0.0125 wt %) onto a heated silicon substrate at 51 °C: (I) the thin liquid film is formed between the edge and the ring of 3.2 μm particles during the drying; (II) the thin liquid film dries out at the end of the evaporation and leaves the peripheral ring of non-volatile additives behind, apart from the inner ring of 3.2 μm particles.

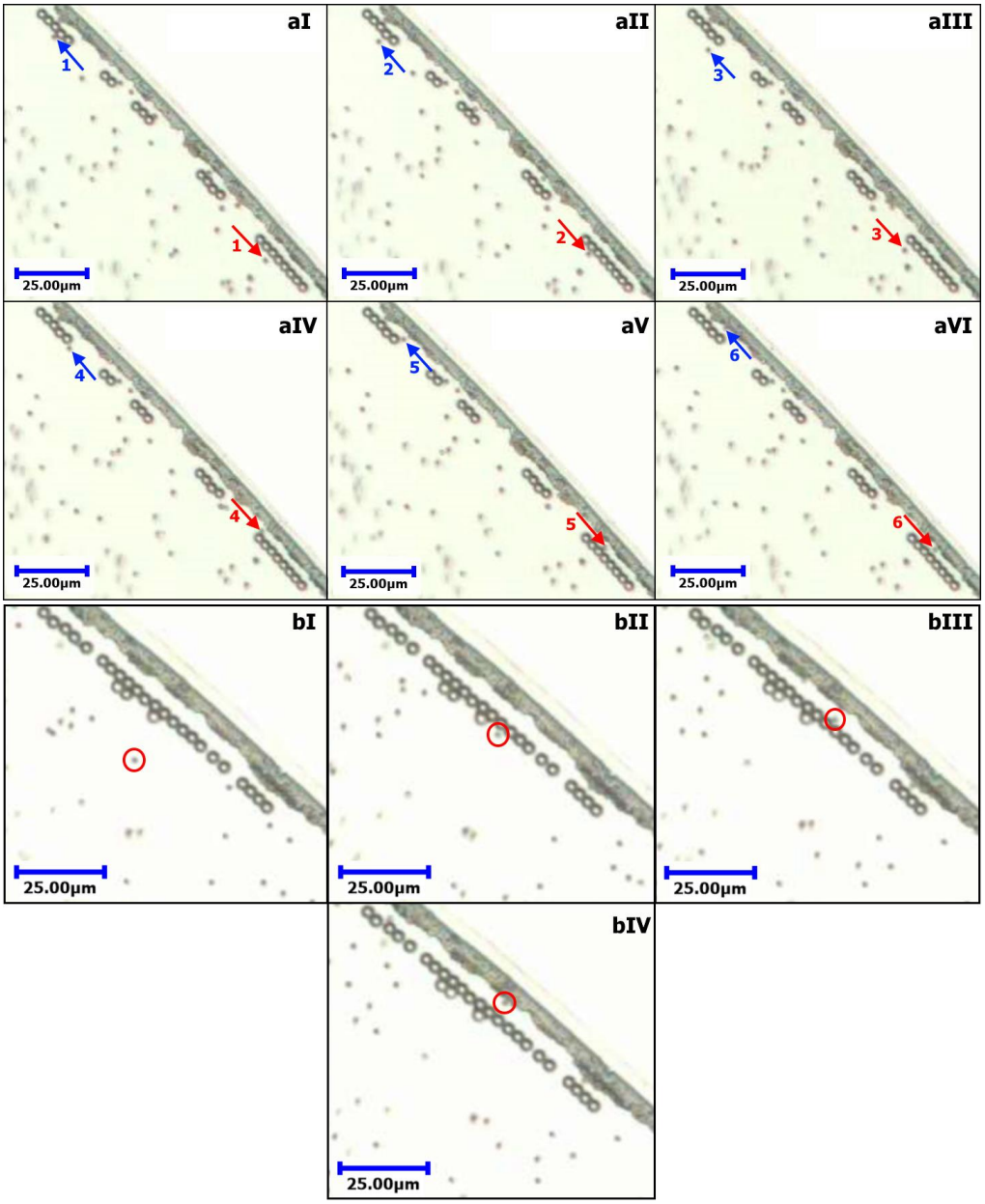

Figure 5.5 Zoomed-in snapshots from a video microscopy of the evaporation process of a water-based bidispersed drop containing a mixture of 3.2 μm diameter particles (mass concentration of 0.0125 wt %) and 1 μm mean diameter particles (mass concentration of 0.0125 wt %) onto a

non-heated silicon substrate (at 22 °C). (aI-VI) The two-colour arrows indicate two tracer 1 μm particles which move towards the edge; the particles become close to the 3.2 μm particles and then travel around them and deposit at the middle ring near the edge. (bI-IV) The circle indicates a tracer 1 μm particle that moves towards the edge; the particle passes from between the two adjacent 3.2 particles and deposits at the middle ring. The micrographs are recorded at a temporal resolution of 30 fps and at 1000× magnification. Scale bars, 25 μm.

The 1000× and 100× magnification consecutive micrographs of the evaporating droplets on the substrates heated at 51 °C are given in Figures 5.6 and 5.7, respectively (Supporting Information Videos S2 and S3). A thin liquid film can be seen between the contact line and leading edge of the middle ring (formed by 1 μm particles) similar to what was observed for the non-heated case (see inset in Figure 5.6g). The 3.2 μm particles also deposit in the vicinity of the middle ring forming the innermost ring, but they are not well organised as those observed at 22 °C (see insets in Figure 5.6g,h). Unlike the non-heated case, the reverse effect (observed for the non-heated case) is not seen at 51 °C, and thus the innermost ring is not transported inwardly towards the centre. Instead, the Marangoni effect plays an important role in the transportation of particles in the reverse direction of the outward flow. The tracking of particles reveals that in the early stages of the evaporation, a group of particles approach the drop edge but do not reach the edge. Instead, they move back radially towards the top of the drop surface along the air-liquid interface. These repelled particles stop near the top of the drop surface, building a ring-like collection (or cluster) of particles there (see Figure 5.7a-e). The transportation of particles towards and away from the drop edge forms an eddy region between the ring-like cluster at the top region of the drop and the edge, as shown by the double arrows between the dashed curve and edge in Figure 5.6a-h. It is well understood that there is a surface tension gradient along the air-liquid interface as the temperature on the top centre of the drop is lower than that at the edge [24,26]. The surface tension of water decreases with increasing temperature, and water tends to flow to high surface tension regions; thus, the radially inward flow is driven from the edge to the top surface of the drop. Moreover, the existence of a stagnation point at the air-liquid interface near the contact line is divided the internal flow inside the evaporating drop

into two regions (see Figure 5.8) [177]: one is an outward surface flow which is beyond the stagnation point, leading to the motion of particles towards the contact line close to the solid surface and their deposition at the edge; the other is the convective flow, in which particles move radially outward towards the drop edge but then their direction is changed and move backward along the air-liquid interface (Figure 5.8). It is reported that in the case of having both the strong Marangoni effect and stagnation point, only those particles participating in the outward flow region can deposit in the edge regions [178] and build the three ring structures. Therefore, those particles participating in the convective flow region lead to the formation of the ring-like cluster of particles at the top surface of the drop. During the late stages of the evaporation (just before the depinning of the contact line), the ring-like cluster moves towards the contact line (Figure 5.7f), and a group of particles deposit near both the middle and innermost rings, merging these two rings completely (see inset in Figure 5.6i). On the other hand, as both the arrival of the ring-like cluster towards the edge and depinning are two immediate, consecutive processes, a group of particles at the free interface of the drop may not have the time required to reach the edge and thus freezes in place, forming a non-uniform distribution of particles inside the drop (Figure 5.7f-i). In the merging process of the two inner rings, the majority of smaller particles (1 μm) deposit closer to the edge compared with the larger ones (3.2 μm). This is because of further penetration of the small particles into the regions near the contact line in comparison with the larger ones. The contact line depinning occurs just after the merging of the middle and innermost rings, preventing the deposition of the ring-like cluster as a new ring-like structure in the central region of the drop. Side views of an evaporating droplet deposited onto a heated substrate is sketched on the basis of the aforementioned analysis. In Figure 5.9a,b, the solid and dashed arrows indicate the direction of the outward and thermal Marangoni flows, respectively. First, the outward flow causes the particles to move adjacent to the substrate surface towards the initial contact line and deposit near the edge (Figure 5.9a,b). However, the Marangoni flow prevents a fraction of these particles from depositing at the edge and leads them to return inward along the air-liquid interface (Figure 5.9a,b). The collection of these particles at the top surface of the drop results in a ring-like cluster.

The cluster approaches the drop edge before the depinning of the contact line (Figure 5.9cI), joining the particles deposited near the edge (Figure 5.9dI). The depinning occurs quickly after the merging (Figure 5.9dI); hence, the ring-like cluster does not deposit as a distinct ring-like structure in the central regions of the droplet, unlike the other studies [23,24,26]. Parsa et al. [26] reported the similar ring-like cluster at the top of the evaporating CuO-water nanofluid droplet (Figure 5.9a,b), which deposited as a distinctive secondary ring in the central regions of the dried droplet. The authors observed that first the contact line depinned (Figure 5.9cII) and then the cluster drifted towards the depinned contact line (Figure 5.9dII) [26]. Consequently, a new ring-like structure was formed when the ring-like cluster reached the depinned contact line (Figure 5.9dII,eII) [26]. By comparing the present observations (Figure 5.9cI,dI,eI) with those of Parsa et al. [26] (Figure 5.9cII,dII,eII), it can be concluded that the depinning time of the contact line plays an important role in the final deposition pattern. The previously observed thin liquid film between the contact line and leading edge of the middle ring dries out only at the last moments of the evaporation process (insets in Figure 5.6g,h,i). After the complete evaporation, a new peripheral ring appears at the drop edge that is separated from the merged ring by a depleted zone (see inset in Figure 5.6i). A similar ring was also observed for the non-heated case (marked as the outermost ring in Figure 5.6i).

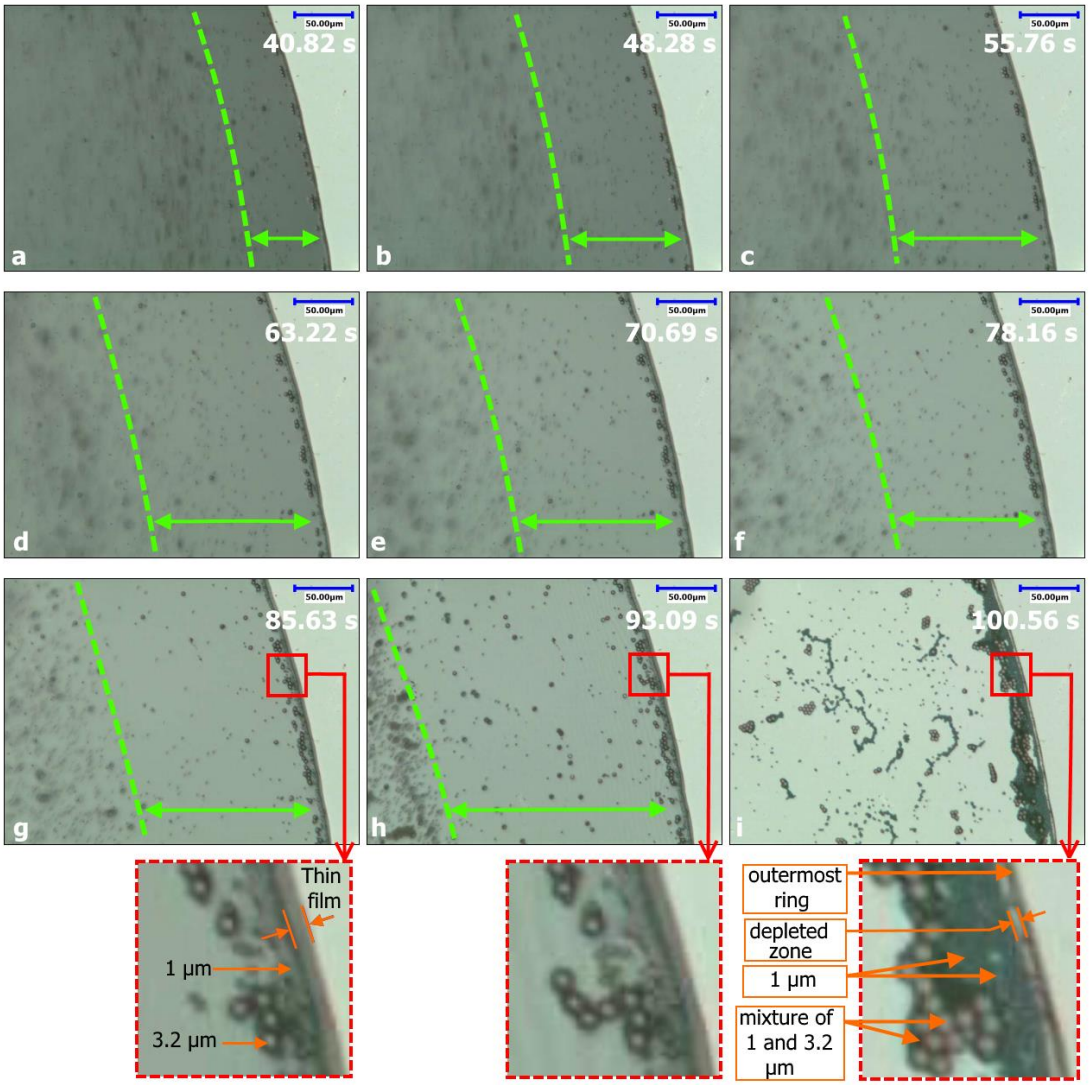

Figure 5.6 Snapshots from a video microscopy of the evaporation process of a water-based bidispersed drop containing a mixture of 3.2 μm diameter particles (mass concentration of 0.0125 wt %) and 1 μm mean diameter particles (mass concentration of 0.0125 wt %) onto a heated silicon substrate at 51 °C. The double arrows denote the eddy region between the ring-like cluster and edge. Insets show the zoomed-in regions highlighted in the solid rectangles. The micrographs are recorded at a temporal resolution of 125 fps and at 1000× magnification. Scale bars, 50 μm.

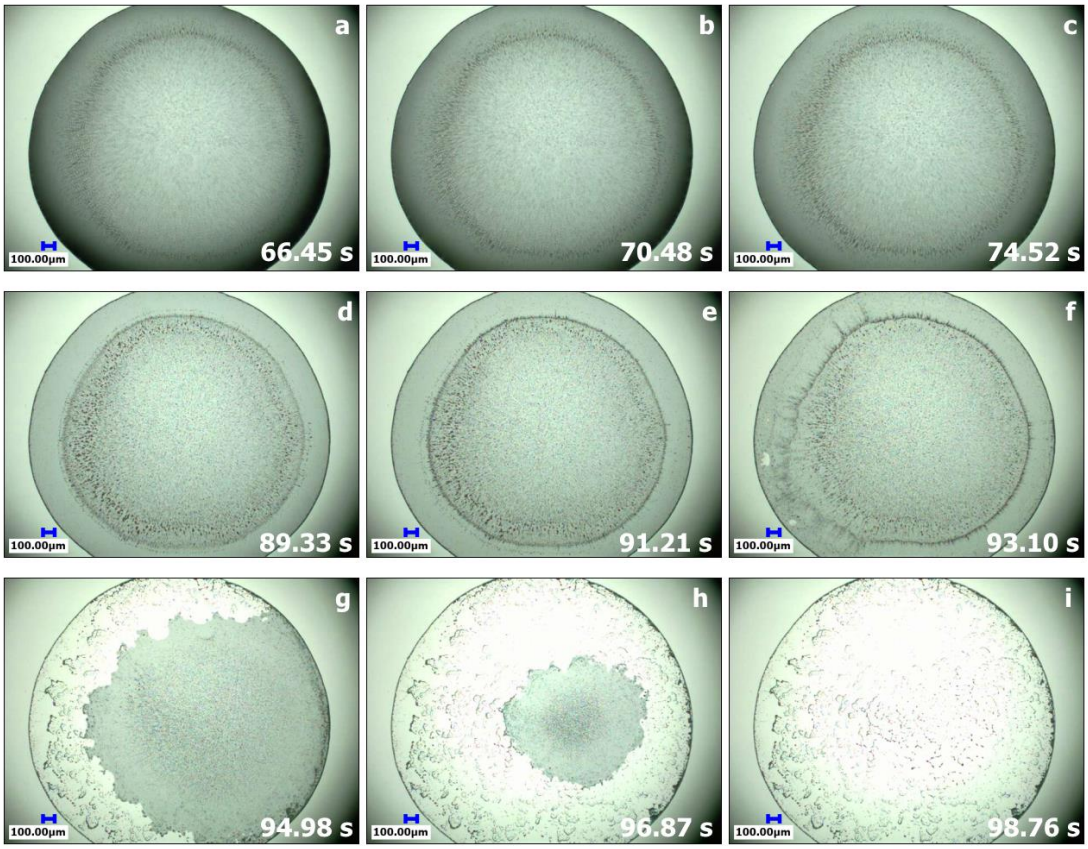

Figure 5.7 Snapshots from a video microscopy of the evaporation process of a water-based bidispersed drop containing a mixture of 3.2 μm diameter particles (mass concentration of 0.0125 wt %) and 1 μm mean diameter particles (mass concentration of 0.0125 wt %) onto a heated silicon substrate at 51 °C. The micrographs are recorded at a temporal resolution of 125 fps and at 100× magnification. Scale bars, 100 μm.

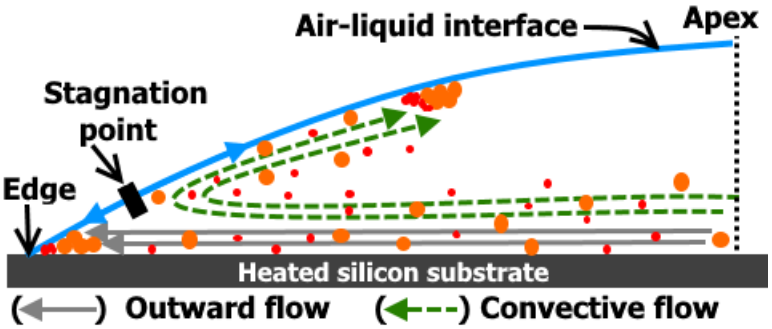

Figure 5.8 Sketch of the internal flow pattern inside an evaporating water-based bidispersed drop containing a mixture of 3.2 μm diameter particles and 1 μm mean diameter particles onto a heated silicon substrate; the outward and temperature-dependent Marangoni flows are

indicated by the solid and dashed arrows, respectively. The black bar indicates a stagnation point where the surface flow changes its direction.

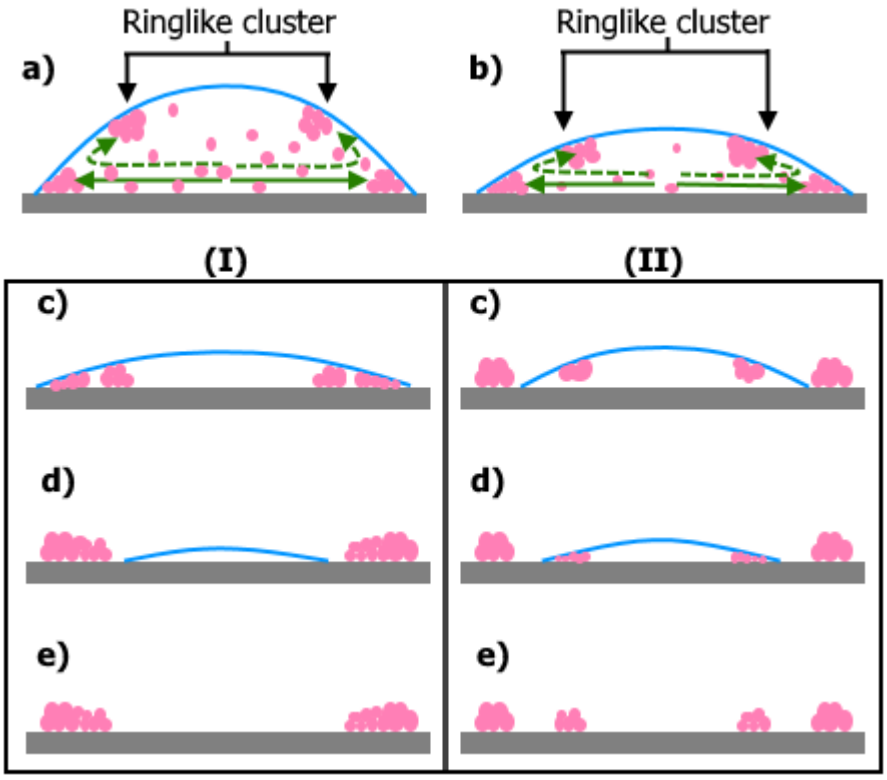

Figure 5.9 Deposition mechanism schematic of the ring-like cluster onto the heated silicon substrate during and after the evaporation of water-based drop containing particles: (a) The particles move towards the pinned edge (shown by the solid arrow), some deposit at the edge, and a fraction of the particles moves back inward to the top surface of the drop. (b) The number of particles increases with evaporation time at the top surface and edge, leading to the formation of a ring-like cluster at the top region of the droplet near the air-liquid interface. (cI) The ring-like cluster moves towards the pinned edge and joins particles deposited at the edge. (dI) The contact line depins. (eI) After the complete evaporation, the ring-like cluster deposited in the edge regions, merged with the other particles at edge. (cII) The contact line depins, and the ring-like cluster moves towards the depinned contact line. (dII) The ring-like cluster reaches the depinned contact line and deposits in the central region. (eII) Apart from the particles deposited in the edge regions, the deposition of the ring-like cluster leads to a new distinct ring-like structure in the central regions after the complete dry-out of the drop.

The 1000× and 100× magnification consecutive still images of the evaporating drop at 64 °C are provided in Figures 5.10 and 5.11, respectively (Supporting Information

Videos S4 and S5). The temporal evolution of the evaporating drop at 81 °C is given in Figures 5.12 and 5.13 at magnifications of 1000× and 100×, respectively (Supporting Information Videos S6 and S7). Similar to the drying drop at 51 °C, a ring-like cluster can be observed at the top of the drop caused by the Marangoni effect (see Figures 5.11a-e and 5.13a-e). The Marangoni eddy identified previously at 51 °C is clearly shown between the edge and ring-like cluster by the dashed arrows in Figures 5.10b-h and 5.12a-g. As shown in insets in Figure 5.10g,h, the particles sorting near the edge is similar to that of the drying drop at 51 °C. However, unlike 51 °C, the depinning of the contact line prevents the ring-like cluster from reaching the initial contact line. The depinned contact line pushes back the ring-like cluster towards the central regions of the drop (Figures 5.11f,g and 5.13f). Then, the ring-like cluster reaches the depinned contact line (Figures 5.11h and 5.13g), building a new distinctive ring-like structure in the drop centre (Figures 5.11i and 5.13h,i). Subsequently, those particles trapped inside the ring-like cluster at the free interface deposit in the interior of the new ring-like structure, leading to the observed irregular distribution of particles there (see inside the secondary ring in the Figures 5.11g-i and 5.13g-i). The formation mechanism of the inner ring-like structure deposited in the central region is schematised from the side view in Figure 5.9a,b,cII,dII,eII. Contrary to the what is observed for the case of 51 °C, the ring-like cluster did not reach the initial edge, and thus the rings (formed by 1 and 3.2 μm particles) in the edge region are distinctive (insets in Figures 5.10i and 5.12i). Figure A.6 (in Appendix A.2) shows that the depinning time of the initial contact line decreases with increasing temperature. Hence, at 51 °C, the depinning time is longer than that at higher temperatures. The longer depinning time at 51 °C leads to the arrival of the ring-like cluster to the edge region and prevents from the formation of the secondary ring-like structure in the interior of the drop. However, the slightly earlier depinning at temperatures of 64 and 81 °C prevent from the arrival of the ring-like cluster to the edge, and hence the cluster deposits in the interior of the drop. In a manner similar to that of the heated case at 51 °C, a depleted zone (between the two bars in insets in Figures 5.10i and 5.12i) appears after the dry-out of the thin liquid film (shown between the two bars in inset in Figure 5.10g), which separates

the ring built by 1 μm particles (marked as the middle ring in insets in Figures 5.10i and 5.12i) and the ring formed by particles smaller than 1 μm (marked as the outermost ring in Figures 5.10i and 5.12i). The innermost ring is formed by the mixture of both 1 and 3.2 μm particles (insets in Figures 5.10i and 5.12i). The depinning of the initial contact line also pushes the innermost ring and consequently leads to the deformation or rupture of some parts of the ring (see the regions highlighted by the ovals in Figures 5.10f-i and 5.12f-i).

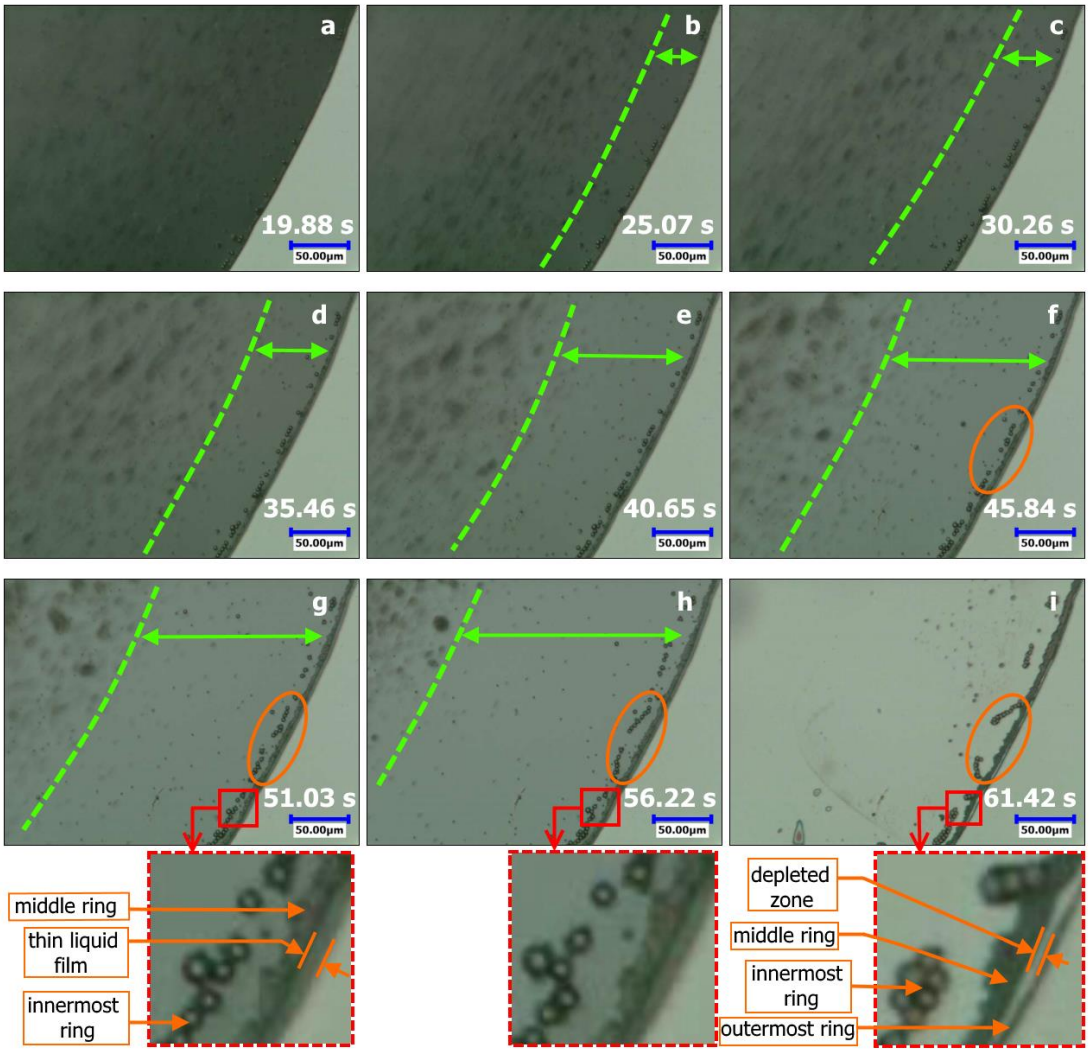

Figure 5.10 Snapshots from a video microscopy of the evaporation process of a water-based bidispersed drop containing a mixture of 3.2 μm diameter particles (mass concentration of 0.0125 wt %) and 1 μm mean diameter particles (mass concentration of 0.0125 wt %) onto a heated silicon substrate at 64 °C. The double arrows denote the eddy region between the ring-

like cluster and edge. Insets show the zoomed-in regions highlighted in the solid rectangles. The micrographs are recorded at a temporal resolution of 125 fps and at 1000× magnification. Scale bars, 50 μm.

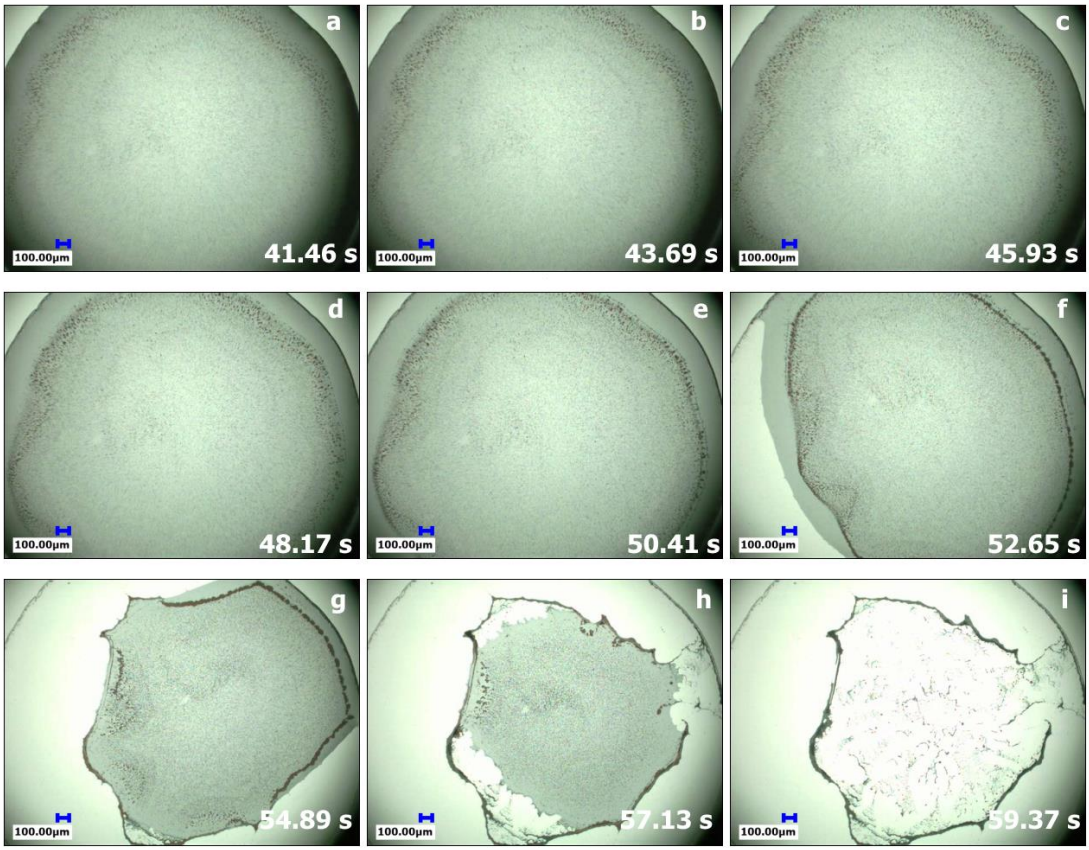

Figure 5.11 Snapshots from a video microscopy of the evaporation process of a water-based bidispersed drop containing a mixture of 3.2 μm diameter particles (mass concentration of 0.0125 wt %) and 1 μm mean diameter particles (mass concentration of 0.0125 wt %) onto a heated silicon substrate at 64 °C. The micrographs are recorded at a temporal resolution of 125 fps and at 100× magnification. Scale bars, 100 μm.

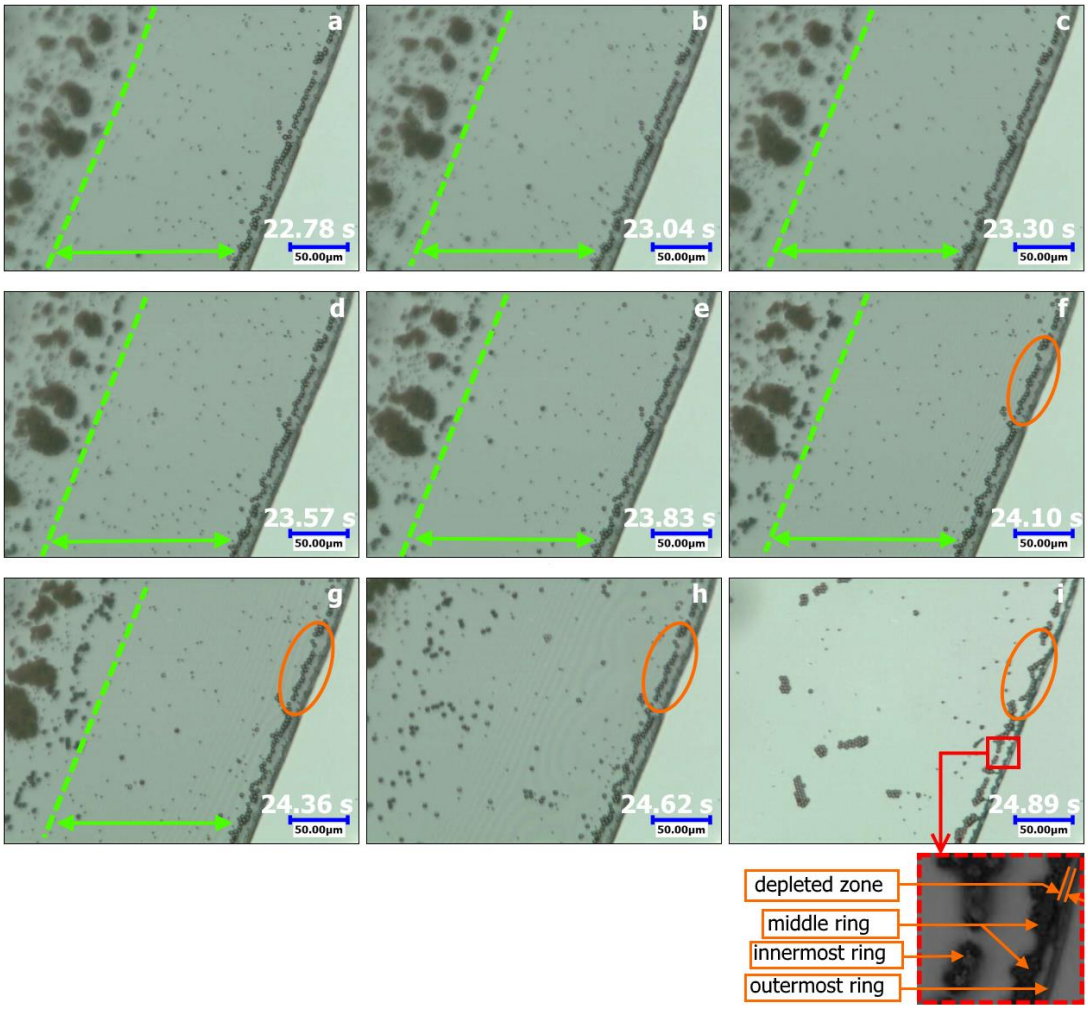

Figure 5.12 Snapshots from a video microscopy of the evaporation process of a water-based bidispersed drop containing a mixture of 3.2 μm diameter particles (mass concentration of 0.0125 wt %) and 1 μm mean diameter particles (mass concentration of 0.0125 wt %) onto a heated silicon substrate at 81 °C. The double arrows denote the eddy region between the ring-like cluster and edge. The micrographs are recorded at a temporal resolution of 125 fps and at 1000× magnification. Scale bars, 50 μm.

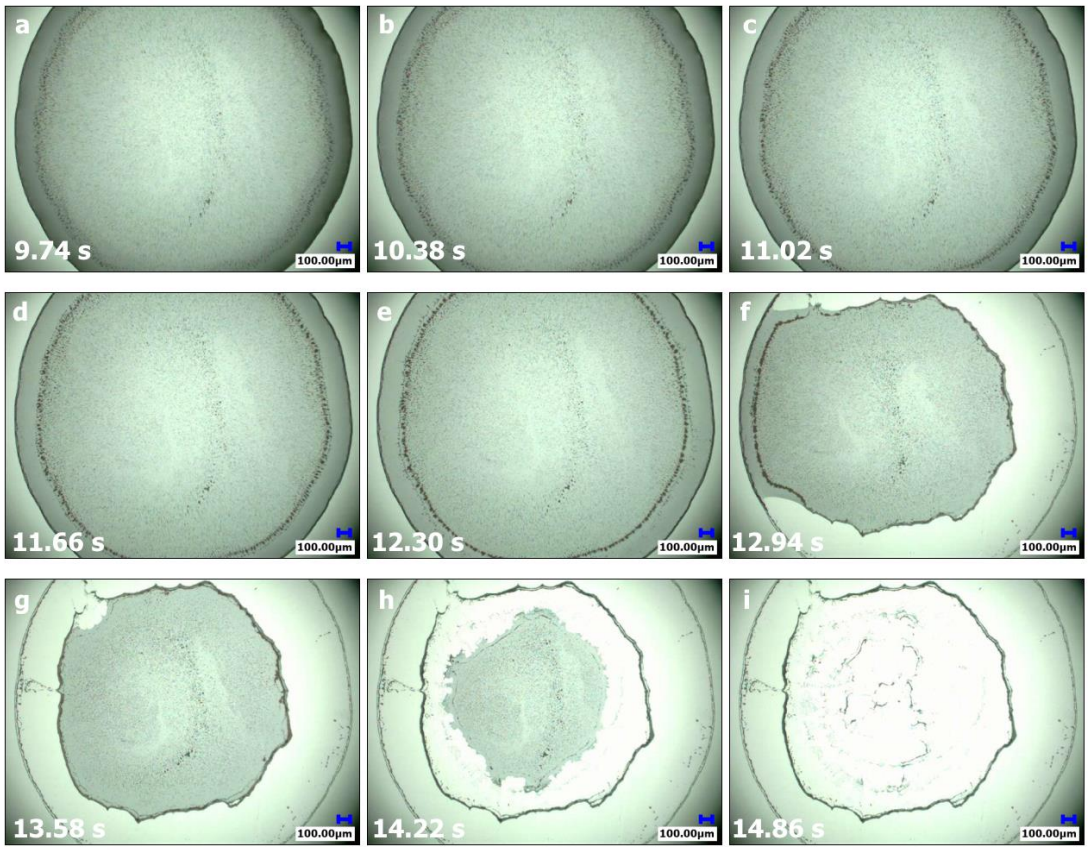

Figure 5.13 Snapshots from a video microscopy of the evaporation process of a water-based bidispersed drop containing a mixture of 3.2 μm diameter particles (mass concentration of 0.0125 wt %) and 1 μm mean diameter particles (mass concentration of 0.0125 wt %) onto a heated silicon substrate at 81 °C. The micrographs are recorded at a temporal resolution of 125 fps and at 100× magnification. Scale bars, 100 μm.

Figures 5.14 and 5.15 show top views of the drying drops at 99 °C at magnifications of 500× and 100×, respectively (Supporting Information Videos S8 and S9). The transportation of the particles participating in the eddy region can be observed due to the Marangoni effect (shown by the double arrows between the edge and dashed curve in Figure 5.14a-f). The ring-like cluster at the top region of the drying drop is found to be identical to the drops evaporating at 64 and 81 °C (Figure 5.15a-c). In a similar manner to the droplets evaporating at 64 and 81 °C, the contact line depins before the ring-like cluster moving towards the edge (Figure 5.15d). The depinned contact line reaches the ring-like cluster, depositing it onto the substrate (Figure 5.15e). After that, the contact line jumps to a new position and remains pinned

(Figure 5.15f,g). The contact line jumps several times after each pinning stage (Figure 5.15g,h), leaving behind distinct deposition lines in the central region of the dried drop (Figure 5.15i). This evaporation process is known as the stick-slip behaviour. The stick and slip of the contact line occurs from all sides of the drop (Figure 5.15d-h), leading to the formation of a rose-like pattern (Figures 5.15i and 5.16a). However, in some cases (at 99 °C), the typical stick-slip behaviour is observed during which the contact line is pinned on one side of the drying drop (left side in Figure 5.16b), and it slips and sticks on the other side (right side of the drop in Figure 5.16b). Thus, the multiple concentric rings are formed with a preferential/initial pinning to one side, as shown in Figure 5.16b. That pinning of the contact line on one side of the droplet is (perhaps) due to irregularities on the surface [88]. A close examination of the initial contact line after the complete evaporation reveals that the observed outermost ring at lower temperatures (22, 51, 64 and 81 °C) almost overlaps the leading edge of the middle ring (see insets I in Figure 5.16a,b). Thus, the depleted zone between the contact line and the ring of 1 μm particles is not easily distinguishable (insets I in Figure 5.16a,b). There are two obvious rings of particles at the initial periphery of the dried drops (insets I in Figure 5.16a,b): one is the outermost ring, which is formed by 1 μm particles overlapping the non-volatile additives, and the other is the innermost ring which is built by the mixture of 1 and 3.2 μm particles. A magnified image of the initial contact line on the pinned side of the drop (inset II in Figure 5.16b) also shows the similar particle sorting but with larger aggregation of 1 and 3.2 μm particles at the innermost ring which is due to the continuous pinning on that side of the drop during the evaporation. Inset II in Figure 5.16a and inset III in Figure 5.16b show the magnified pictures of the second deposition lines which are the remnants of the ring-like cluster deposited on the solid surface. Unlike the initial deposition line (shown by inset I in Figure 5.16a and insets I,II in Figure 5.16b), the second line consists of rings which are easily distinguishable from each other (inset II in Figure 5.16a and inset III in Figure 5.16b): the outermost ring formed by the non-volatile additives, the middle ring built by 1 μm particles, and the innermost ring formed by the mixture of all particle sizes. The width of the depleted zone is known to be a function of the geometric parameters

(i.e., contact angle (θ), particle size (d_p)), and is relatively equal to $d_p/\tan\theta$ (see Figure 5.17) [217]. As the width of the depleted zone is the distance between the initial contact line (or the outermost ring) and the ring of 1 μm particles (or middle ring), d_p should be equal to 1 μm and is constant for all studied cases. Thus, the width of the zone becomes larger with decreasing the contact angle (Figure 5.17). In other words, the larger the contact angle, the smaller becomes the zone. It is obvious that the initial contact angle of the drop at the initial contact line is larger than the contact angle (just after the first jump) at the second deposition line (see Figure 5.17aI,bI). Hence, the width of the zone at the initial contact line (inset I in Figure 5.16a and insets I,II in Figure 5.16b) is smaller than that at the second deposition line (inset II in Figure 5.16a and inset III in Figure 5.16b). Similarly, at 81 °C, the width at the initial deposition line is smaller compared to that at the inner ring-like structure (see Figure 5.17aII,bII). This is because the initial contact angle of the drop is larger than that of the drop at the deposition time of the ring-like cluster (see Figure 5.17aI,bI). As previously mentioned, several deposition lines are formed on the solid surface due to the stick-slip behaviour. For the rose-like pattern, the structure of the other internal lines left by the stick-slip (apart from the second line) are similar to what was explained for the second deposition line (inset II in Figure 5.16a). However, the typical stick-slip deposit (Figure 5.16b) exhibits a different pattern (for the internal deposition lines) where there is a faint single ring connecting some triangular structures (see insets IV,V in Figure 5.16b). This can be attributed (perhaps) to the weak pinning of the contact line during the evaporation [226]. Thus, the retracting contact line carries the particles towards the pinned side of the drying drop and builds these triangular structures.

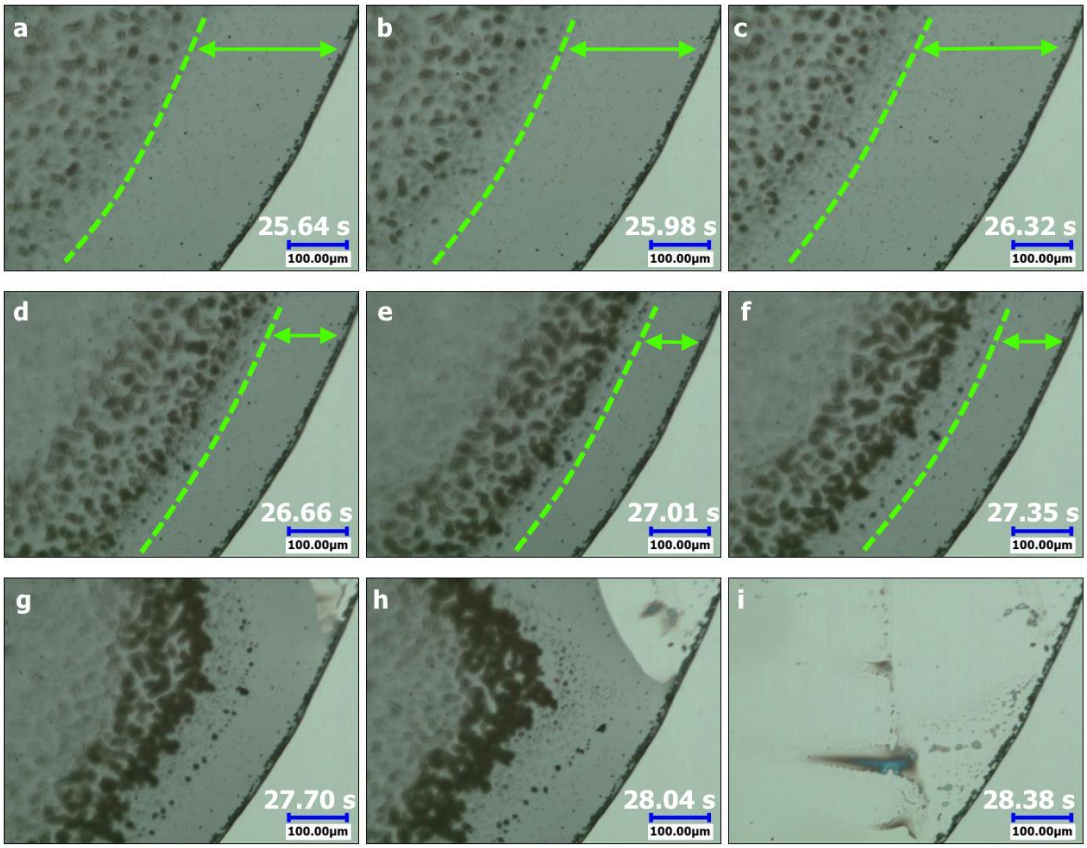

Figure 5.14 Snapshots from a video microscopy of the evaporation process of a water-based bidispersed drop containing a mixture of 3.2 μm diameter particles (mass concentration of 0.0125 wt %) and 1 μm mean diameter particles (mass concentration of 0.0125 wt %) onto a heated silicon substrate at 99 °C. The double arrows denote the eddy region between the ring-like cluster and edge. The micrographs are recorded at a temporal resolution of 125 fps and at 500× magnification. Scale bars, 100 μm.

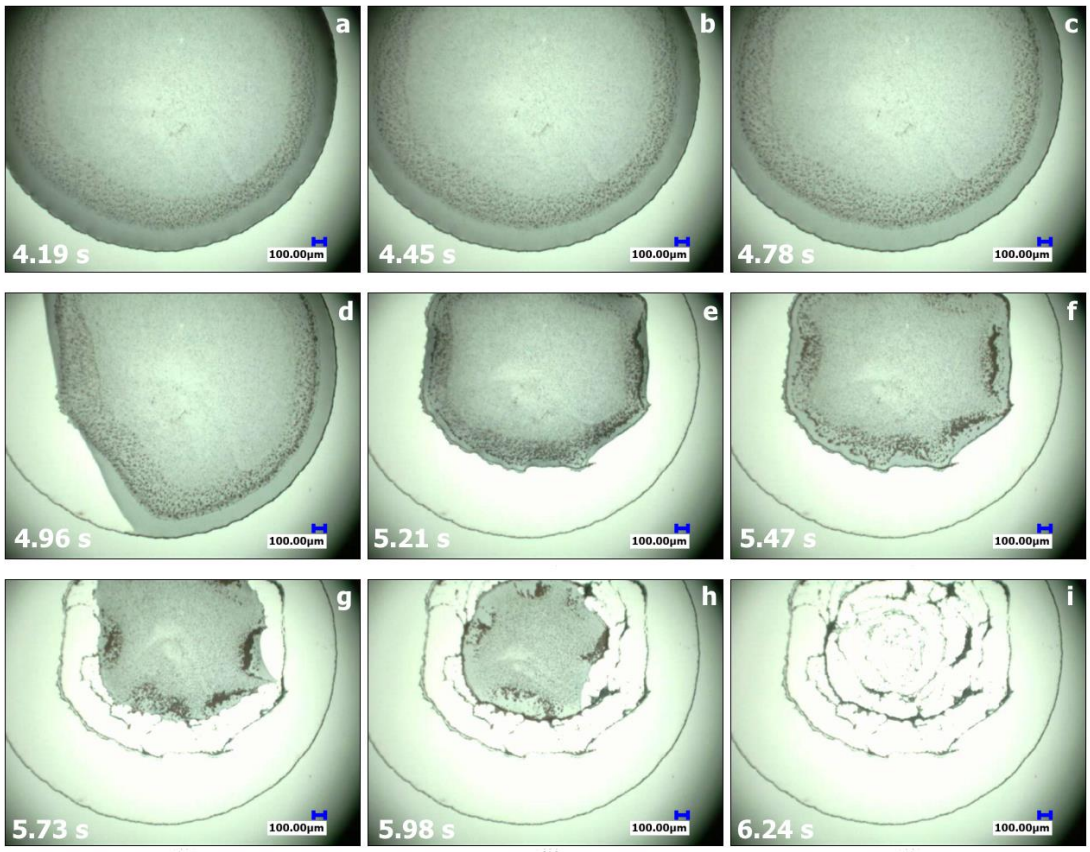

Figure 5.15 Snapshots from a video microscopy of the evaporation process of a water-based bidispersed drop containing a mixture of 3.2 μm diameter particles (mass concentration of 0.0125 wt %) and 1 μm mean diameter particles (mass concentration of 0.0125 wt %) onto a heated silicon substrate at 99 °C. The micrographs are recorded at a temporal resolution of 125 fps and at 100× magnification. Scale bars, 100 μm.

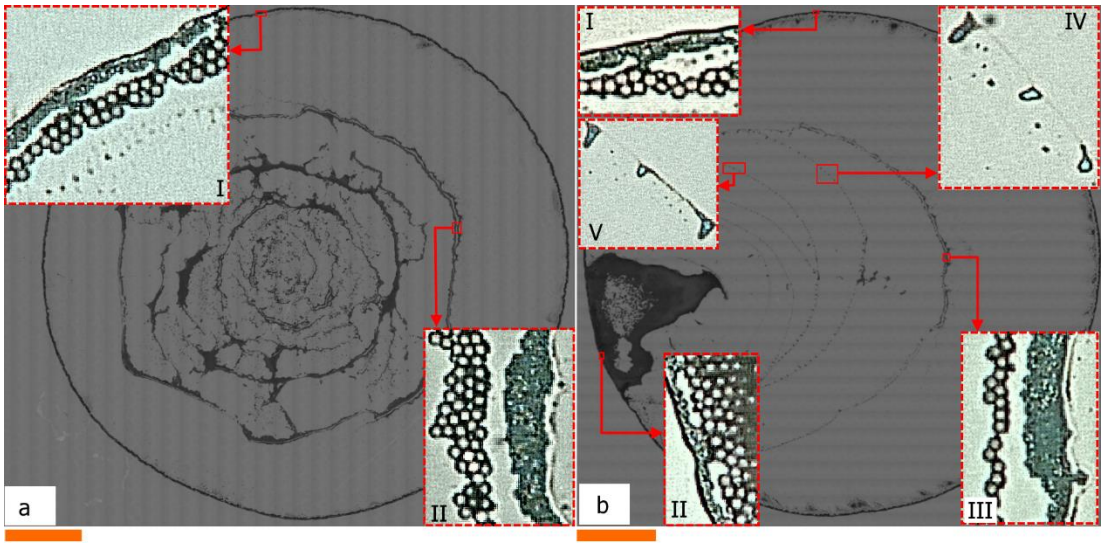

Figure 5.16 Dried deposits of bidispersed drops containing a mixture of 3.2 μm diameter particles (mass concentration of 0.0125 wt %) and 1 μm diameter particles (mass concentration of 0.0125 wt %) onto a heated substrate at temperature of 99 °C: (a) the rose-like pattern: (I) initial contact line, and (II) the second deposition line. (b) The typical stick-slip pattern: (I) initial contact line on the depinned side, (II) initial contact line on the pinned side, (III) the second deposition line, (IV) the third deposition line, and (V) the fourth deposition line. Insets show the zoomed-in regions highlighted in the solid rectangles. Scale bars, 600 μm.

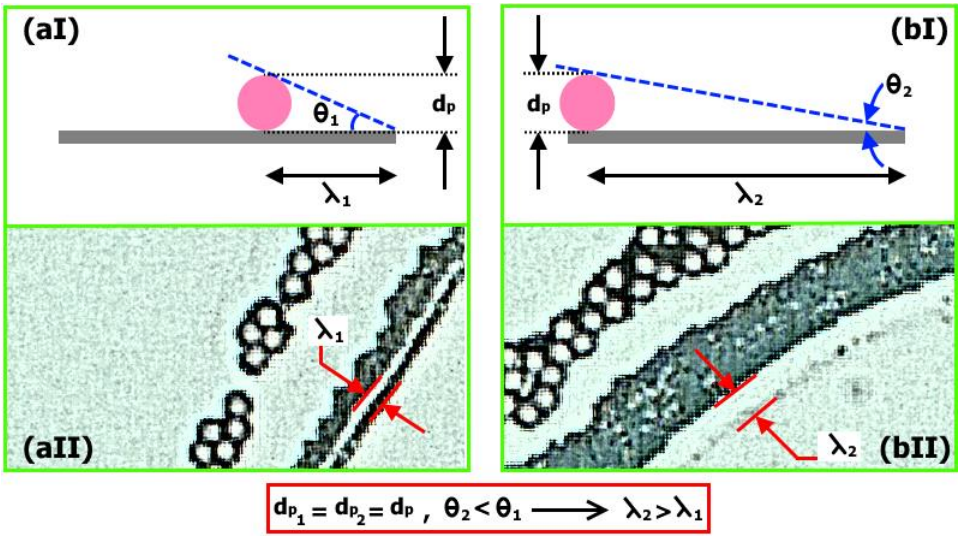

Figure 5.17 (aI) Schematic diagram of a bidispersed drop's edge at the initial evaporation time. (aII) Particle sorting at the initial edge after the complete evaporation. (bI) Schematic diagram of the drop's edge at the deposition time of the ring-like cluster. (bII) Particle sorting after the deposition of the ring-like cluster. λ is the distance between the ring of non-volatile additives and the ring of 1 μm particles. θ is the contact angle. d_p is the diameter of the 1 μm particle.

In studies related to the evaporation of monodispersed drops on heated substrates, the thermal Marangoni effect is the main mechanism behind the pattern formation of particles [26]. For monodispersed drops on heated substrates, the dual-ring pattern was observed for temperatures between 47 and 81 °C, but this pattern is not observed for bidispersed drops at temperature of 51 °C. Instead, a non-uniform deposition of particles enclosed by a thick ring is observed. This can be attributed to the different particle sorting near the contact line which (perhaps) affects the depinning time and thus the final deposition pattern. In the case of bidispersed drops at highest temperature of 99 °C, two different patterns from the stick-slip behaviour are observed, whereas only one particular pattern (similar to sample VI in Figure 5.1b) was reported after the stick-slip behaviour for monodispersed drops [26]. Overall, the final deposition pattern of bidispersed drops on heated substrates is significantly dependent on the thermal Marangoni effect rather than the particle size effect. However, the size effect plays an important role in the deposition pattern of the regions near the contact line, and it is quite different from the monodispersed cases.

5.4.3 Particle velocity

The particle velocity is measured at the distance of 50 μm from the contact line and presented as a function of normalised time in Figure 5.18. It should be noted that only those particles deposited at near the edge are considered for this measurement. In other words, the particles inside the outward flow region are tracked for the measurement of velocity (see solid arrows in Figure 5.8). Hence, the repelled particles in the Marangoni flow region are not included in this measurement (see dashed arrows in Figure 5.8). Using the models by Deegan et al. [15], the theoretical height-averaged velocity is calculated close to the contact line, which is given by [223]:

$$\tilde{u}(r,t) = \frac{R}{4\left(\frac{r}{R}\right)(t_e - t)}\left(\frac{1}{\sqrt{1-\left(\frac{r}{R}\right)^2}} - \left[1-\left(\frac{r}{R}\right)^2\right]\right) \tag{5.1}$$

where R is the drop radius; r, the distance from the drop centre; t, the evaporation time; and t_e, the total evaporation time. For the plots in Figure 5.18, the value of r is equal to the difference between the drop radius and the distance of measurements from the contact line ($r = R - 50$ μm). As it can be seen in Figure 5.18, both the experimental and theoretical velocities gradually increase with time but they increase abruptly at the last stages of the evaporation. This sudden change in the velocity is known as the "rush-hour" behaviour [222,223]. The observation of the rush-hour behaviour has been reported previously for drying drops on non-heated substrates [222,223]. Here, the similar behaviour is observed for evaporating bidispersed drops on both non-heated and heated substrates. The outward flow towards the contact line is generated to replenish the evaporated liquid, whereas the drop height is vanishing with the evaporation time. Thus, the liquid is squeezed through the vanishing area, leading to a diverging radial velocity. The critical time at which the radial velocity diverges is indicated by the dashed line, which is estimated between the normalised time of 0.7 and 0.8 for all temperatures between 22 and 81 °C (Figure 5.18). Despite the trend of the theoretical velocity matching well with the experimental one, there is a difference between the measured and calculated values. This discrepancy can be attributed to the distance between the objective lens and substrate for experimental measurements, which is not considered in the model. In addition, the increase of temperature changes the properties of the liquid and vapour (i.e., liquid density, vapour concentration, and vapour diffusivity) and it is also not included in the model. Marín et al. [222] introduced a more developed model to calculate the theoretical height-averaged velocity that includes all abovementioned and other extra parameters (i.e., contact angle, height). However, it cannot be used in this study as the simultaneous side view and top-view visualisations of drops were not possible.

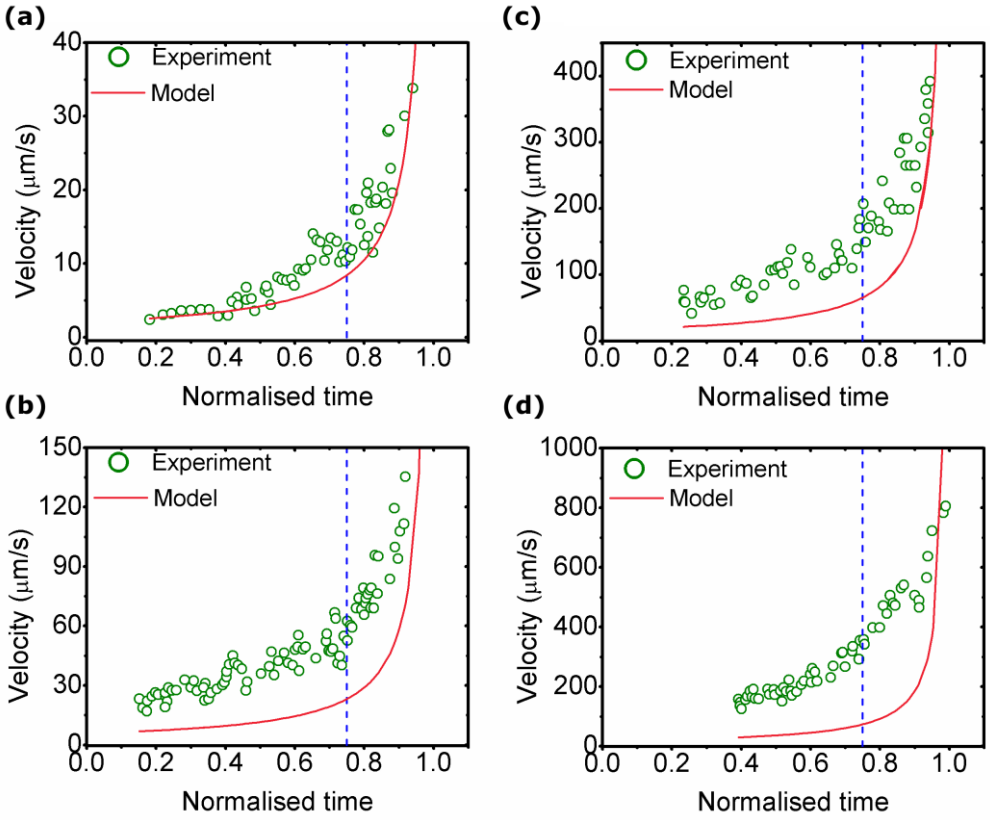

Figure 5.18 Particle velocity versus normalised time for drying bidispersed drops containing a mixture of 3.2 μm diameter particles (mass concentration of 0.0125 wt %) and 1 μm mean diameter particles (mass concentration of 0.0125 wt %) onto heated substrates at: (a) 22 °C, (b) 51 °C, (c) 64 °C, and (d) 81 °C. The dashed line indicates the start of the rush-hour behaviour.

5.4.4 Location of stagnation point

To determine the location of the stagnation point in evaporating bidispersed drops onto heated substrates, the 1 μm particles are tracked and the turning points of these particles returning back to the top surface of the drops are shown by the crosses in Figure 5.19. The crosses show that the particles can change the direction in different distances from the contact line. During the entire evaporation of drops at 51 and 64 °C, the nearest turning points to the contact line are found to be adjacent to the ring of 3.2 μm particles (innermost ring) (see insets in Figure 5.19a,b). On the other hand, it is observed that those other particles that reach the region between the innermost ring and the ring of 1 μm particles do not turn back and finally deposit at the ring of 1 μm (middle ring). These observations reveal that the distance between the stagnation

point and the contact line (the so-called stagnation distance) is smaller than that between the innermost ring and contact line; thus, the stagnation point should be located somewhere between the innermost and the middle rings (for evaporating drops at 51 and 64 °C). At substrate temperature of 81 °C, the nearest turning point to the contact line is observed between the innermost and middle rings (see inset in Figure 5.19c). Hence, at 81 °C, the stagnation point should be in the immediate vicinity of the middle ring. The measured distances between the nearest turning point and the contact line are approximately 11, 9, and 7 μm for substrate temperatures of 51, 64, and 81 °C, respectively. This shows that increasing the substrate temperature decreases the stagnation distance within drying bidispersed drops.

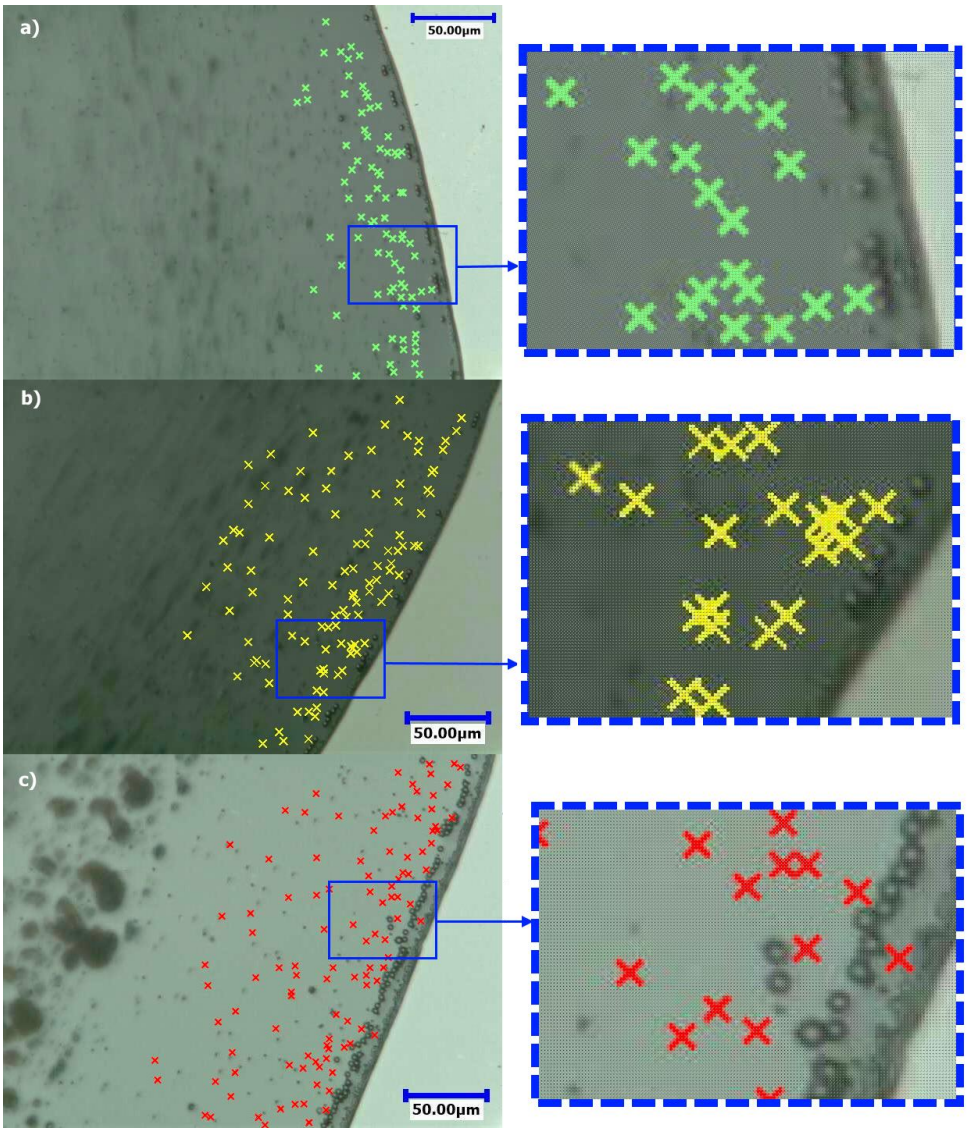

Figure 5.19 Turning points of 1 μm particles are shown by the crosses inside bidispersed drops containing a mixture of 3.2 μm diameter particles (mass concentration of 0.0125 wt %) and 1 μm mean diameter particles (mass concentration of 0.0125 wt %) onto heated substrates at (a) 51 °C, (b) 64 °C, and (c) 81 °C. Insets show the zoomed-in regions highlighted in the solid rectangles.

5.5 Conclusions

In summary, the results of the deposition patterns from evaporating bidispersed drops onto both non-heated and heated silicon substrates were reported. On non-heated substrate, a nearly uniform deposition pattern enclosed by the disk-like ring was

observed. On heated substrates, the inward thermal Marangoni flow formed a ring-like cluster of particles on the top surface of the drops, which had a significant role in the final deposition patterns. The internal flow was divided into two regions of the outward coffee-ring flow and the Marangoni flow by a stagnation point where the flow changed its direction. At the substrate temperature of 51 °C, the ring-like cluster reached the initial edge just before the depinning of the contact line, and thus a relatively non-uniform deposition pattern enclosed by the thick ring was formed. From temperatures from 64 to 81 °C, the depinning of the initial contact line occurred before the arrival of the ring-like cluster towards the edge, forming a ring-like structure on the surface. Hence, a dual-ring pattern was left after the full evaporation: one is the ring-like structure at the periphery; the other is the inner ring-like structure left by the cluster. However, at 99 °C, the stick-slip behaviour of the contact line led to the formation of a stick-slip pattern. Magnification at the drops edge showed three rings in the regions near the contact line after the complete evaporation: one was the outermost ring formed by the non-volatile additives smaller than 1 μm, the second was the middle ring formed by the 1 μm particles, and the other is the innermost ring formed by the mixture of 1 and 3.2 μm particles. However, in some cases, the outermost ring was found to be nearly overlapping the middle ring. The width of the zone between the outermost ring and the middle ring was shown to be different at the initial edge and the edge of the inner ring-like structure (for temperatures from 64 to 99 °C). The width of the zone at the initial edge was found to be smaller than that at the edge of the inner ring-like structure. This was explained by the difference between the values of the contact angles at the initial time and the deposition time of the inner ring-like structure. Furthermore, velocity of small particles was measured and compared with a theoretical model. The theoretical trend fitted well with the experimental one, but there was a discrepancy between the theoretical and experimental values. Particle velocity slightly increased with time but it rapidly increased at the last stages of the evaporation, known as the rush-hour behaviour. At all examined temperatures, the rush-hour behaviour began between the normalised times of 0.7 and 0.8. Moreover, the 1 μm particles were tracked during the evaporation and the nearest position of the turning point of tracer

particles was found. For the substrate temperatures of 51 and 64 °C, the nearest turning point was observed adjacent to the innermost ring. However, the nearest turning point at 81 °C was found to be between the innermost and middle rings. By comparing the distance between the nearest turning points and the contact line for the temperatures of 51, 64, and 81 °C, it was found that increasing the substrate temperature decreased the stagnation distance.

Chapter 6 Conclusions

6.1 General Conclusions

In the present experimental research, different techniques were used to study the evaporation of sessile droplets. The optical microscopy technique was used to study the motion of nano- and micro-particles in droplets and their resulting pattern formation. Infrared thermography was employed to study the thermal flow pattern of droplets at their free interfaces and the white light interferometry technique was used to investigate the final deposition pattern of particles left after complete evaporation.

The first study detailed in Chapter 3 investigated the influence of substrate temperature on the deposition of nanoparticles suspended in evaporating water droplets. The internal flow structure was found to be dependent on the substrate temperature and thus led to the formation of three distinctive deposition patterns after full evaporation: a relatively uniform pattern, a dual-ring pattern, and a stick-slip pattern. Using the microscopy technique, the existence of a stagnation point at the air-liquid interface was demonstrated which divided the flow field into two regions: first, the outward flow responsible for the formation of the peripheral rings at all studied temperatures; and second, the temperature-induced Marangoni flow, which played a crucial role in the formation of the ring-like cluster at the top surface of the drying droplets at temperatures of 51, 64, 81, and 99 °C. This ring-like cluster was deposited as a secondary ring inside the peripheral ring of drying droplets at 51, 64, and 81 °C, forming the dual-ring pattern. The size of the secondary ring increased with enhancing substrate temperatures. At the highest substrate temperature of 99 °C, the contact line slipped and sticked for several times preventing the formation of the dual-ring pattern. Instead, a stick-slip pattern formed on the substrate.

In the second study detailed in Chapter 4, the influence of adding butanol to the water-based nanofluid droplets on the deposition of nanoparticles was investigated at the same substrate temperatures listed in Chapter 3. Similarly to the drying of pure

water-based nanofluid droplets, three distinctive patterns were left behind after the complete evaporation of binary-based water-butanol nanofluid droplets: a relatively uniform pattern, a dual-ring pattern, and a stick-slip pattern. Additionally, several faint line patterns also formed inside the secondary ring of the dual-ring pattern. Using the infrared thermography technique and volume evolution of droplets, the evaporation process was categorised into three regimes. Each of these regimes corresponded to the observations of nanoparticle movement captured by the optical microscopy technique. In addition to the outward capillary flow, two Marangoni flows were also observed during the evaporation process: first, the thermal Marangoni flow induced by a temperature gradient at the free interface of droplets; and second, the solutal Marangoni flow induced by local concentration gradients arising from the addition of alcohol. A comparison between the strength of these two Marangoni flows revealed that formation of the deposition patterns was mainly affected by the thermal Marangoni flow and outward flow during the last regime of the evaporation. This regime was identical to the total evaporation process of water-based nanofluid droplets reported in Chapter 3. However, the existence of the faint lines inside the secondary ring of the dual-ring pattern was attributed to the role of the solutal Marangoni flow in the first regime.

Finally, the third study detailed in Chapter 5 revealed the effect of substrate temperature on the pattern formation of bidispersed micro-particles from evaporating water-based droplets. Depending on substrate temperature, five distinctive deposition patterns were formed: a relatively uniform pattern enclosed by a disk-shaped ring on the non-heated substrate, a nearly non-uniform pattern inside a thick outer ring at the substrate temperature of 51 °C, a dual-ring pattern at 64 and 81 °C, a rose-like pattern, and a set of concentric rings corresponding to the stick-slip pattern at 99 °C. Particle separation based on size led to the formation of three rings near the contact line: an outermost ring formed by the non-volatile additives smaller than 1 μm, a middle ring built by 1 μm particles, and an innermost ring formed by the mixture of particles with the size of 1 and 3.2 μm. At the substrate temperatures from 64 to 99 °C, the depinning of the contact line formed the same three ring structures in the interior regions of the droplets but with a larger distance between the outermost and middle rings compared to

that at the initial contact line region. This effect was attributed to the value of the contact angle at the time of ring deposition. Particle velocity in the outward flow region was measured during evaporation and was compared with a theoretical value. Results revealed that the velocity gradually increased with time and abruptly increased at the last stages of the evaporation, i.e., rush-hour behaviour. The sudden increase of velocity occurred between the normalised time of 0.7 and 0.8 for temperatures ranging from 22 to 81 °C. Furthermore, the stagnation distance between the initial contact line and the nearest turning point of particles to the contact line was measured. Results revealed a decreasing function of the substrate temperature, i.e., the higher the substrate temperature, the smaller the stagnation distance.

6.2 Future Work

The observations and findings presented in this PhD research could be beneficial for a variety of biological and industrial applications and scientific communities related to the pattern formation of nano- and micro-particles from volatile droplets. Interestingly, after the publication of Chapter 3 [26], several studies examining the effect of substrate temperature on deposition patterns of non-volatile components were published [143,184,185,227].

Notably, varying the substrate temperature affects evaporation and the strength of the Marangoni flow and thus the drying patterns. In this research, an isothermally heated substrate was proposed as a key factor for the control of pattern formation during evaporation and the manipulation of the final deposition patterns. Hence, study into the effect of substrate with a gradient of temperature on drying patterns might be crucial in this research field.

Although the influence of substrate temperature on the pattern formation of particles was thoroughly investigated in this research, some questions may remain unanswered. In Chapters 3, 4, and 5, the substrate temperature is varied but the environmental pressure remains unchanged. It would be interesting to conduct experimental research in which the environmental pressure is under control in a confined environment but the environmental pressure and substrate temperature is

changed independently. This approach would likely lead to a better understanding of the effect of evaporation kinetics on particle pattern formation.

Of particular significance for expanding current knowledge is examining substrates of various materials and hydrophobicities and particles varying in material, size, and shape, which may affect interparticle and interfacial interactions. However, this topic can be considered a permanent research focus since novel particles are continuously produced and taken to the research market.

In addition to the study on binary-based nanofluid droplets detailed in Chapter 4, investigating the effect of binary base fluids of two or more liquids of various volatilities and concentrations is also an interesting direction for future research. Notably, outcomes related to nanoparticles behaviour at the interfaces can be useful for heat transfer applications in industry where particle clogging and sedimentation should be prevented.

The study on bidispersed particles in evaporating droplets requires more research. To fully understand the effect of bidispersed particles on evaporation and pattern formation on heated substrates, different particle size ratios and concentration should be investigated.

A Appendix

A.1 Appendix Chapter 4

A.1.1 Estimation of butanol concentration

This section is based on the study by Bennacer and Sefiane [206] who estimated the evolution of the bulk and interface concentrations of ethanol for an evaporating ethanol-water mixture sessile droplet. It is well known that the more volatile component evaporates first; it diffuses from the bulk to the interface of the drop. After evaporation, the component diffuses in the form of the gas phase which is a mixture of vapour and air [206]. In order to deduce butanol concentrations and its evolution with time, the diffusion can be solved by using the convection-diffusion equation as follows:

$$\frac{\partial C}{\partial t} + U_c \nabla C = D_B . \nabla^2 C \tag{A.1}$$

where C is butanol concentration; D_B, the butanol diffusivity in water (in the form of the liquid phase); and U_c, convective velocity of butanol.

U_c can be written as follows:

$$U_c = \frac{q\dot{v}_B}{S} \tag{A.2}$$

where $q\dot{v}_B$ is the mass flow rate of butanol and S, the surface area at the liquid-air interface.

S can be written as follows:

$$S = 2\pi R^2 \tag{A.3}$$

where R is the droplet radius.

The initial conditions are defined as follows:

$C = C_0$ at $t = 0$.

The boundary conditions are as follows:

Concentration gradient at the substrate-liquid interface is $\frac{\partial C}{\partial n}|_{S/L} = 0$.

Concentration gradient at the liquid-air interface,

$$D_B.\frac{\partial C}{\partial n}|_{L/V} = h\left(C_{\mathrm{L/V}} - C_{\infty}\right) \tag{A.4}$$

where h is the diffusion-convection coefficient on the liquid-air interface. Here, there is no butanol in the air, hence $C_{\infty} = 0$.

This equation was solved by the finite element method (FEM) using a partial differential equation (PDE) solver FreeFem++ (version 3.36).

Figures A.1 and A.2 show the evolution of butanol concentration within the droplet and the butanol mass flow rate with time at ambient temperature, respectively. There is a good agreement in between the above model and the experimental data (at ambient temperature) which was obtained from an acoustic high-frequency echography technique [228].

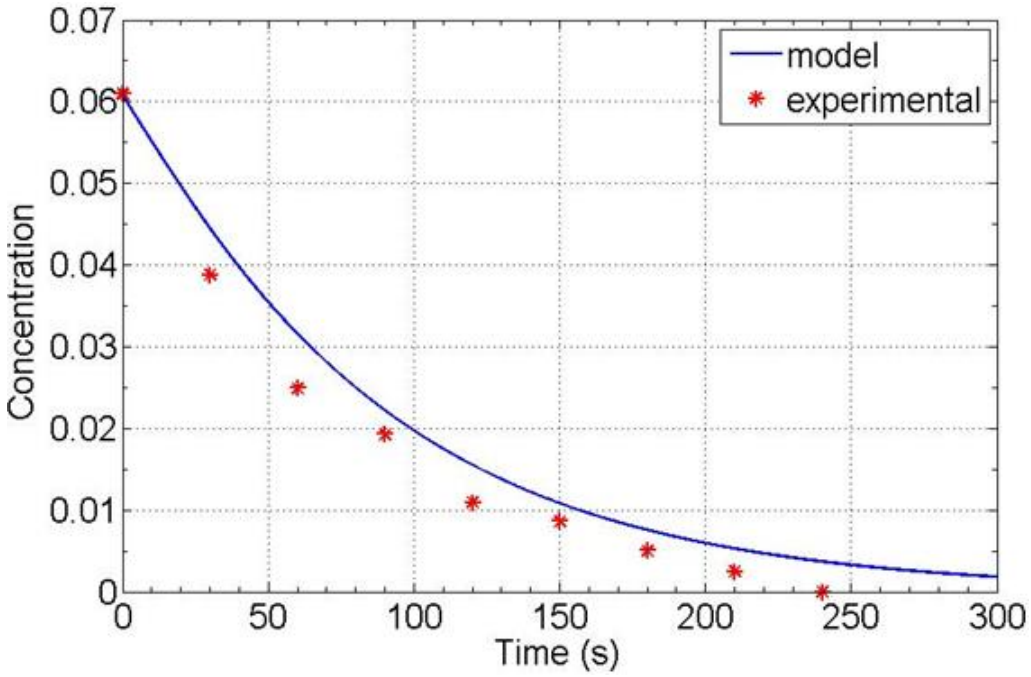

Figure A.1 Evolution of butanol concentration within the drop with time at ambient condition.

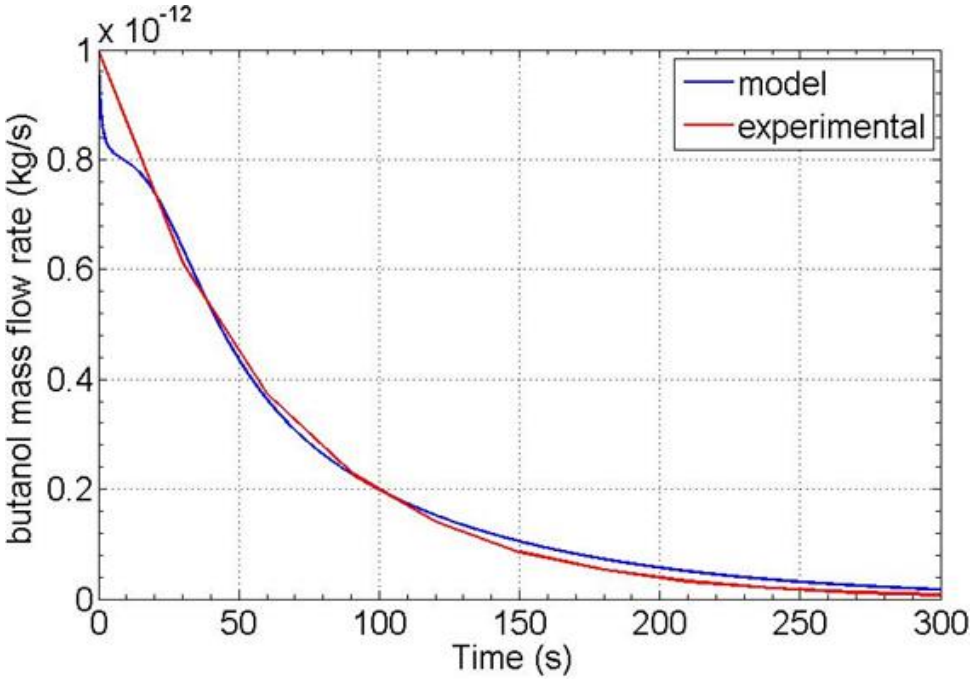

Figure A.2 Evolution of butanol mass flow rate with time at ambient condition.

A.1.2 Marangoni number

The dimensionless solutal Marangoni number can be written as

$$M_a^S = \frac{\frac{d\sigma}{dC}R}{\mu D_B}\Delta C \tag{A.5}$$

where $d\sigma/dC$ is the change of the surface tension with concentration, in N.m; ΔC is the concentration difference between the bulk and the interface; and μ is dynamic viscosity of the binary mixture, in Pa.s.

The dimensionless thermal Marangoni number is defined as

$$M_a^T = -\frac{\frac{d\sigma}{dT}R}{\mu\alpha}\Delta T \tag{A.6}$$

where $d\sigma/dT$ is the change of the surface tension with temperature, in N.m/°C, ΔT is the temperature difference between the droplet edge and the centre, in ℃; and α is thermal diffusivity, in m^2/s.

Surface tension was measured by means of a pendant droplet method using a drop shape analyser (DSA30, KRÜSS GmbH, Germany). The calculation of liquid properties at different temperatures (i.e., dynamic viscosity) showed that there is a negligible change in the values in comparison with the pure binary mixture. It can be deduced that a very low concentration of nanoparticles (0.05 wt %) has no effect on pure binary mixture properties; thus, the Marangoni numbers are calculated for pure binary mixture at different temperatures. Parsa et al. [26] have also found that there is a negligible difference between the calculated properties of CuO-water nanofluid (0.05 wt %) and pure water. Therefore, the authors calculated the Marangoni numbers for the pure water at different substrate temperatures and time.

A.1.3 Marangoni velocity

This section is based on the work by Kim et al. [86] who estimated the Marangoni effect for an evaporating binary mixture sessile droplet. For the estimation of the Marangoni velocities, an evaporating binary mixture droplet with radius R and height h_0 with a nearly spherical cap is considered. Similarly to the study of Kim et al. [86], the binary mixture droplet is thin due to $h_0/R < 1$ where $h_0 \approx 0.1$ mm and $R \approx 1$ mm at the late stages of the evaporation (e.g., after regime II). In cylindrical coordinates (r, z) and using the lubrication approximation ($h_0 \ll R$), the Navier-Stokes equations can be reduced to

$$\frac{dp}{dr} = \mu \frac{\partial^2 u}{\partial z^2} \tag{A.7}$$

where p is the pressure and u, the radial velocity.

The velocity profile can be obtained by integrating Equation (A.7) according to z as follows:

$$u(r, z, t) = \frac{1}{\mu}\frac{\partial p}{\partial r}\left(\frac{1}{2}z^2 - h(r, t)z\right) + \frac{z}{\mu}\frac{\partial \sigma}{\partial r} \tag{A.8}$$

where the boundary conditions are the no-slip condition at the liquid-solid interface, and a Marangoni shear stress $\left(\frac{\partial \sigma}{\partial r} \neq 0\right)$ at $z = h(r, t)$. The capillary pressure is

$p = -\sigma\nabla^2\tilde{h}$ where $\tilde{h}$ ($\ll h_0$) is the perturbation to the liquid-air interface arisen from the internal flow. The surface velocity at the liquid-air interface ($z = h$) can be written as

$$u(r,z,t) = -\frac{h^2}{2\mu}\frac{\partial}{\partial r}\left(\sigma\nabla^2\tilde{h}\right) + \frac{h}{\mu}\frac{\partial\sigma}{\partial r} \tag{A.9}$$

The first term on the right side of Equation (A.9) is the interfacial velocity driven by the capillary pressure gradient. The second term on the right side of Equation (A.9) is the interfacial velocity created by the Marangoni effects which can be expressed as

$$u(r,z,t) = \frac{h(t)}{\mu(t)}\frac{\Delta\sigma(t)}{R(t)} \tag{A.10}$$

Here, the sign of $\Delta\sigma$ shows the flow direction. The interfacial velocity driven by the concentration gradient (or the solutal Marangoni velocity) can be obtained as

$$U_{M_a}^{S} = \left|\frac{\Delta\sigma_S}{\mu}\frac{h}{R}\right| \tag{A.11}$$

where $\Delta\sigma_S$ is the surface tension difference caused by the concentration gradient. The interfacial velocity driven by the temperature gradient (or the thermal Marangoni velocity) is given by

$$U_{M_a}^{T} = \left|\frac{\Delta\sigma_T}{\mu}\frac{h}{R}\right| \tag{A.12}$$

where $\Delta\sigma_T$ is the surface tension difference due to the temperature gradient.

A.2 Appendix Chapter 5

An algorithm is used to separate particles of different sizes, as shown in Figures A.3-A.5.

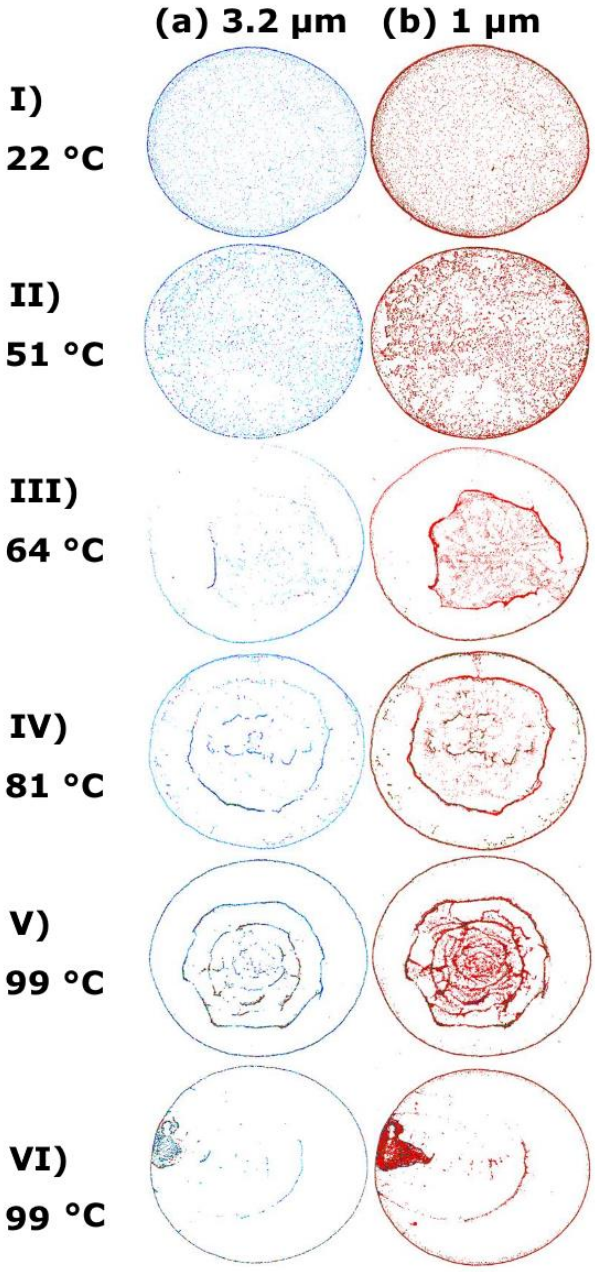

Figure A.3 Dried deposits at various temperatures: (a) Particle size of 3.2 μm, and (b) Particle size of 1 μm.

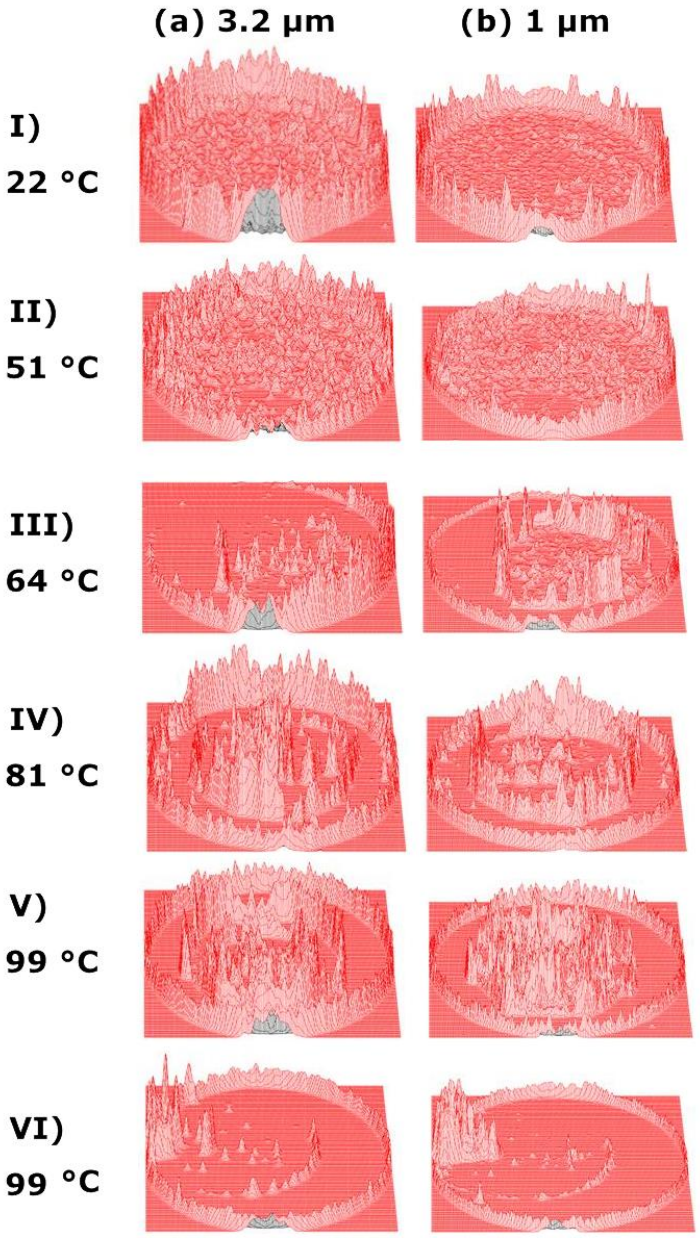

Figure A.4 Topography of the particle deposits at various temperatures: (a) Particle size of 3.2 μm, (b) Particle size of 1 μm.

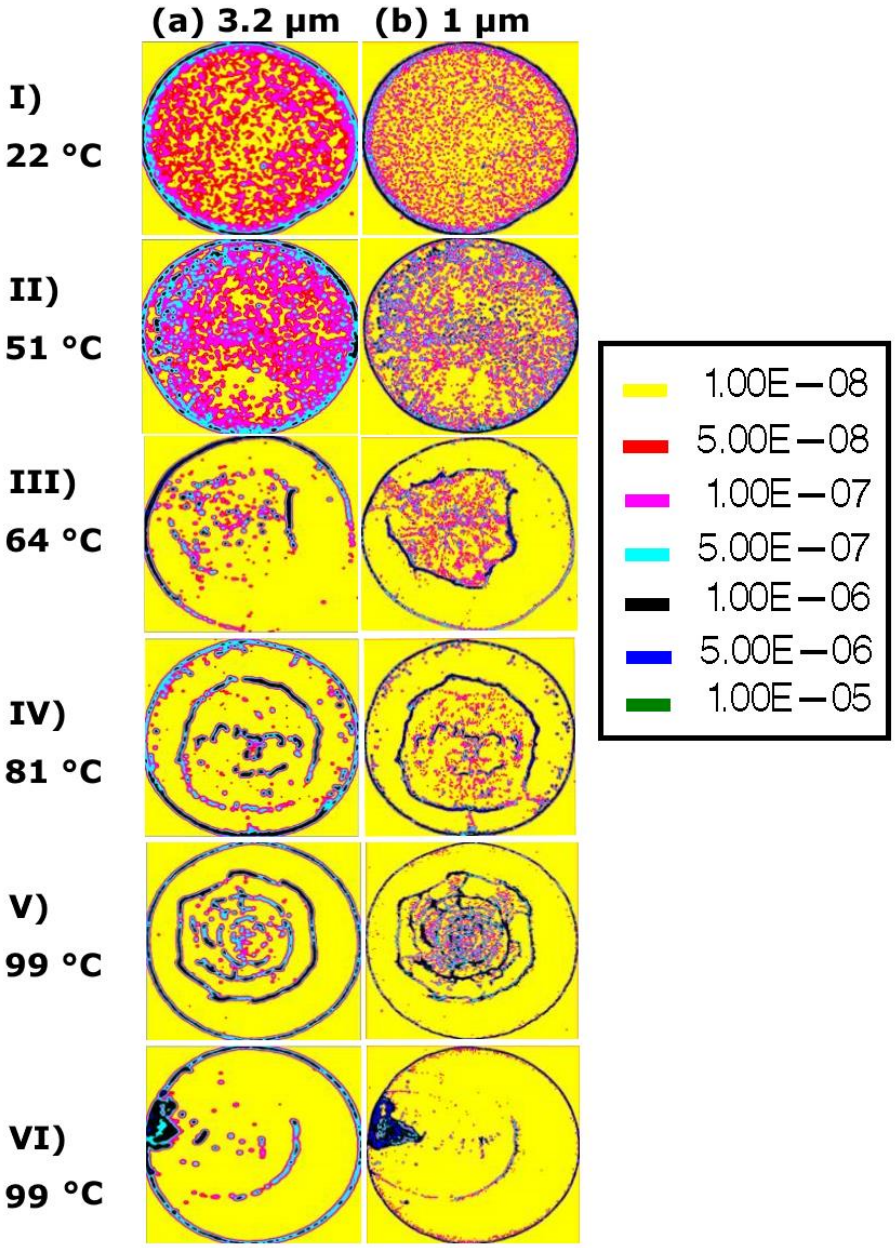

Figure A.5 Density distribution of particles at various temperatures: (a) Particle size of 3.2 μm, and (b) Particle size of 1 μm.

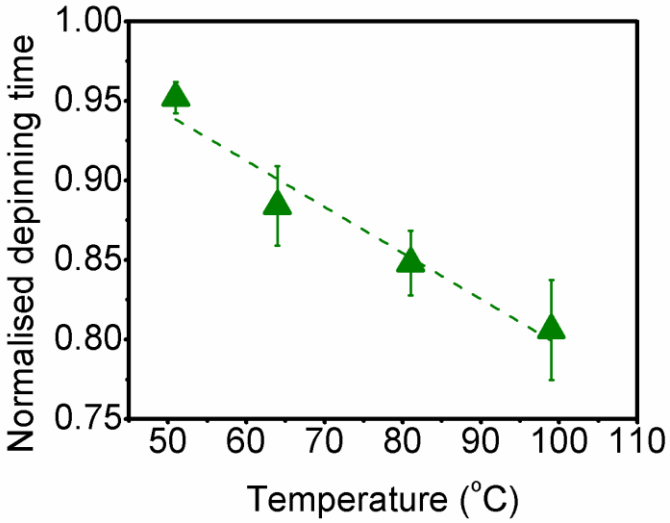

Figure A.6 Normalised depinning time versus temperature. The dashed line is the linear fitting line.

References

[1] R.J. Good, Contact angle, wetting, and adhesion: a critical review, J. Adhes. Sci. Technol. 6 (1992) 1269–1302. doi:10.1163/156856192X00629.

[2] H.Y. Erbil, The debate on the dependence of apparent contact angles on drop contact area or three-phase contact line: A review, Surf. Sci. Rep. 69 (2014) 325–365. doi:10.1016/j.surfrep.2014.09.001.

[3] T. Young, An essay on the cohesion of fluids, Philos. Trans. R. Soc. London. 95 (1805) 65–87.

[4] E.B. Dussan, On the spreading of liquids on solid surfaces: static and dynamic contact lines, Annu. Rev. Fluid Mech. 11 (1979) 371–400. doi:10.1146/annurev.fl.11.010179.002103.

[5] P.G. de Gennes, Wetting: statics and dynamics, Rev. Mod. Phys. 57 (1985) 827–863. doi:10.1103/RevModPhys.57.827.

[6] T.M. Squires, S.R. Quake, Microfluidics: Fluid physics at the nanoliter scale, Rev. Mod. Phys. 77 (2005) 977–1026. doi:10.1103/RevModPhys.77.977.

[7] G. Reiter, Dewetting of thin polymer films, Phys. Rev. Lett. 68 (1992) 75–78. doi:10.1103/PhysRevLett.68.75.

[8] Y. Xia, G.M. Whitesides, Soft lithography, Annu. Rev. Mater. Sci. 28 (1998) 153–184. doi:10.1146/annurev.matsci.28.1.153.

[9] C. Neinhuis, Characterization and distribution of water-repellent, self-cleaning plant surfaces, Ann. Bot. 79 (1997) 667–677. doi:10.1006/anbo.1997.0400.

[10] N. Gudris, L. Kulikowa, Die verdampfung kleiner wassertropfen, Zeitschrift Für Phys. 25 (1924) 121–132. doi:10.1007/BF01327514.

[11] R.F. Mangel, E. Baer, The evaporation of water drops from a “Teflon” surface, Chem. Eng. Sci. 17 (1962) 705–706. doi:10.1016/0009-2509(62)85029-5.

[12] J. Thomson, XLII. On certain curious motions observable at the surfaces of wine and other alcoholic liquors, Philos. Mag. 10 (1855) 330–333. http://www.tandfonline.com/doi/abs/10.1080/14786445508641982?journalCode=tphm15.

[13] C. Maranogni, PhD thesis: Sull' espansione delle gocce liquide, Universita di Pavia, 1865.

[14] R.D. Deegan, O. Bakajin, T.F. Dupont, G. Huber, S.R. Nagel, T.A. Witten, Capillary flow as the cause of ring stains from dried liquid drops, Nature. 389 (1997) 827–829. doi:10.1038/39827.

[15] R. Deegan, O. Bakajin, T. Dupont, G. Huber, S. Nagel, T. Witten, Contact line deposits in an evaporating drop, Phys. Rev. E. 62 (2000) 756–765. doi:10.1103/PhysRevE.62.756.

[16] R.D. Deegan, Pattern formation in drying drops, Phys. Rev. E. 61 (2000) 475–485. doi:10.1103/PhysRevE.61.475.

[17] K. Sefiane, Patterns from drying drops., Adv. Colloid Interface Sci. 206 (2014) 372–81. doi:10.1016/j.cis.2013.05.002.

[18] X. Zhong, A. Crivoi, F. Duan, Sessile nanofluid droplet drying, Adv. Colloid Interface Sci. 217 (2015) 13–30. doi:10.1016/j.cis.2014.12.003.

[19] C.H. Chon, S. Paik, J.B. Tipton, K.D. Kihm, Effect of nanoparticle sizes and number densities on the evaporation and dryout characteristics for strongly pinned nanofluid droplets, Langmuir. 23 (2007) 2953–2960. doi:10.1021/la061661y.

[20] D. Brutin, Influence of relative humidity and nano-particle concentration on pattern formation and evaporation rate of pinned drying drops of nanofluids, Colloids Surfaces A Physicochem. Eng. Asp. 429 (2013) 112–120. doi:10.1016/j.colsurfa.2013.03.012.

[21] T. Still, P.J. Yunker, A.G. Yodh, Surfactant-induced Marangoni eddies alter the coffee-rings of evaporating colloidal drops, Langmuir. 28 (2012) 4984–

4988. doi:10.1021/la204928m.

[22] X. Zhong, F. Duan, Evaporation of sessile droplets affected by graphite nanoparticles and binary base fluids, J. Phys. Chem. B. 118 (2014) 13636–13645. doi:10.1021/jp508051y.

[23] M. Parsa, S. Harmand, K. Sefiane, M. Bigerelle, Evaporation of binary mixture nanofluid drops: Pattern formation, in: M. Laudon, F. Case, B. Romanowicz (Eds.), 10th Annu. TechConnect World Innov. Conf., TechConnect, Washington, 2016: pp. 196–197. http://www.techconnect.org/proceedings/paper.html?volume=TCB2016v3&chapter=6&paper=752.

[24] M. Parsa, R. Boubaker, S. Harmand, K. Sefiane, M. Bigerelle, R. Deltombe, Patterns from dried water-butanol binary-based nanofluid drops, J. Nanoparticle Res. 19 (2017) 268. doi:10.1007/s11051-017-3951-2.

[25] A. Askounis, K. Sefiane, V. Koutsos, M.E.R. Shanahan, The effect of evaporation kinetics on nanoparticle structuring within contact line deposits of volatile drops, Colloids Surfaces A Physicochem. Eng. Asp. 441 (2014) 855–866. doi:10.1016/j.colsurfa.2012.10.017.

[26] M. Parsa, S. Harmand, K. Sefiane, M. Bigerelle, R. Deltombe, Effect of substrate temperature on pattern formation of nanoparticles from volatile drops, Langmuir. 31 (2015) 3354–3367. doi:10.1021/acs.langmuir.5b00362.

[27] E.G. Rapis, Soviet technical physics letters, 14 (1988) 679.

[28] E. Rapis, A change in the physical state of a nonequilibrium blood plasma protein film in patients with carcinoma, Tech. Phys. 47 (2002) 510–512. doi:10.1134/1.1470608.

[29] V.N. Shabalin, S.N. Shatokhina, Patent: Method of diagnosing complicated urolithiasis and prognosticating urolithiasis, EP0504409 B1, 1996.

[30] H.M. Gorr, J.M. Zueger, D.R. McAdams, J.A. Barnard, Salt-induced pattern formation in evaporating droplets of lysozyme solutions, Colloids Surfaces B

Biointerfaces. 103 (2013) 59–66. doi:10.1016/j.colsurfb.2012.09.043.

[31] D. Brutin, B. Sobac, B. Loquet, J. Sampol, Pattern formation in drying drops of blood, J. Fluid Mech. 667 (2011) 85–95. doi:10.1017/S0022112010005070.

[32] W. Bou Zeid, D. Brutin, Influence of relative humidity on spreading, pattern formation and adhesion of a drying drop of whole blood, Colloids Surfaces A Physicochem. Eng. Asp. 430 (2013) 1–7. doi:10.1016/j.colsurfa.2013.03.019.

[33] W. Bou Zeid, J. Vicente, D. Brutin, Influence of evaporation rate on cracks' formation of a drying drop of whole blood, Colloids Surfaces A Physicochem. Eng. Asp. 432 (2013) 139–146. doi:10.1016/j.colsurfa.2013.04.044.

[34] W. Bou-Zeid, D. Brutin, Effect of relative humidity on the spreading dynamics of sessile drops of blood, Colloids Surfaces A Physicochem. Eng. Asp. 456 (2014) 273–285. doi:10.1016/j.colsurfa.2014.05.004.

[35] R. Chen, L. Zhang, D. Zang, W. Shen, Blood drop patterns: Formation and applications, Adv. Colloid Interface Sci. 231 (2016) 1–14. doi:10.1016/j.cis.2016.01.008.

[36] S.U.S. Choi, J.A. Eastman, Enhancing thermal conductivity of fluids with nanoparticles, in: ASME Int. Mech. Eng. Congr. Expo., ASME, San Fransisco, 1995: pp. 99–105.

[37] C.T. Nguyen, G. Roy, C. Gauthier, N. Galanis, Heat transfer enhancement using Al2O3–water nanofluid for an electronic liquid cooling system, Appl. Therm. Eng. 27 (2007) 1501–1506. doi:10.1016/j.applthermaleng.2006.09.028.

[38] J. Barber, D. Brutin, L. Tadrist, A review on boiling heat transfer enhancement with nanofluids., Nanoscale Res. Lett. 6 (2011) 1–16. doi:10.1186/1556-276X-6-280.

[39] R.A. Taylor, P.E. Phelan, T.P. Otanicar, C.A. Walker, M. Nguyen, S. Trimble, R. Prasher, Applicability of nanofluids in high flux solar collectors, J. Renew. Sustain. Energy. 3 (2011) 23104. doi:10.1063/1.3571565.

[40] D. Peer, J.M. Karp, S. Hong, O.C. Farokhzad, R. Margalit, R. Langer, Nanocarriers as an emerging platform for cancer therapy, Nat. Nanotechnol. 2 (2007) 751–760. doi:10.1038/nnano.2007.387.

[41] M.J. Kao, C.H. Lo, T.T. Tsung, Y.Y. Wu, C.S. Jwo, H.M. Lin, Copper-oxide brake nanofluid manufactured using arc-submerged nanoparticle synthesis system, J. Alloys Compd. 434–435 (2007) 672–674. doi:10.1016/j.jallcom.2006.08.305.

[42] H. Sirringhaus, T. Kawase, R.H. Friend, T. Shimoda, M. Inbasekaran, W. Wu, E.P. Woo, High-resolution inkjet printing of all-polymer transistor circuits, Science. 290 (2000) 2123–2126. doi:10.1126/science.290.5499.2123.

[43] T. Kawase, H. Sirringhaus, R.H. Friend, T. Shimoda, Inkjet printed via-hole interconnections and resistors for all-polymer transistor circuits, Adv. Mater. 13 (2001) 1601–1605. doi:10.1002/1521-4095(200111)13:21<1601::AID-ADMA1601>3.0.CO;2-X.

[44] B.J. De Gans, P.C. Duineveld, U.S. Schubert, Inkjet printing of polymers: State of the art and future developments, Adv. Mater. 16 (2004) 203–213. doi:10.1002/adma.200300385.

[45] B. Dan, T.B. Wingfield, J.S. Evans, F. Mirri, C.L. Pint, M. Pasquali, I.I. Smalyukh, Templating of self-alignment patterns of anisotropic gold nanoparticles on ordered SWNT macrostructures, ACS Appl. Mater. Interfaces. 3 (2011) 3718–3724. doi:10.1021/am2009019.

[46] T. Yakhno, Salt-induced protein phase transitions in drying drops., J. Colloid Interface Sci. 318 (2008) 225–30. doi:10.1016/j.jcis.2007.10.020.

[47] K. Sefiane, On the formation of regular patterns from drying droplets and their potential use for bio-medical applications, J. Bionic Eng. 7 (2010) S82–S93. doi:10.1016/S1672-6529(09)60221-3.

[48] D. Bonn, J. Eggers, J. Indekeu, J. Meunier, Wetting and spreading, Rev. Mod. Phys. 81 (2009) 739–805. doi:10.1103/RevModPhys.81.739.

[49] C.W. Extrand, Origins of wetting, Langmuir. 32 (2016) 7697–7706. doi:10.1021/acs.langmuir.6b01935.

[50] A. Dupré, P. Dupré, Théorie mécanique de la chaleur, Gauthier-Villars, 1869.

[51] H.P. Kavehpour, B. Ovryn, G.H. McKinley, Microscopic and macroscopic structure of the precursor layer in spreading viscous drops, Phys. Rev. Lett. 91 (2003) 196104. doi:10.1103/PhysRevLett.91.196104.

[52] R. Chen, L. Zhang, D. Zang, W. Shen, Wetting and drying of colloidal droplets: Physics and pattern formation, in: M.M. Rahman, A.M. Asiri (Eds.), Adv. Colloid Sci., InTech, 2016: pp. 3–25. doi:10.5772/65301.

[53] K.N. Prabhu, P. Fernades, G. Kumar, Effect of substrate surface roughness on wetting behaviour of vegetable oils, Mater. Des. 30 (2009) 297–305. doi:10.1016/j.matdes.2008.04.067.

[54] M. Sakai, T. Yanagisawa, A. Nakajima, Y. Kameshima, K. Okada, Effect of surface structure on the sustainability of an air layer on superhydrophobic coatings in a water−ethanol mixture, Langmuir. 25 (2009) 13–16. doi:10.1021/la802763h.

[55] Y. Son, C. Kim, D.H. Yang, D.J. Ahn, Spreading of an inkjet droplet on a solid surface with a controlled contact angle at low Weber and Reynolds numbers, Langmuir. 24 (2008) 2900–2907. doi:10.1021/la702504v.

[56] J. Perelaer, C.E. Hendriks, A.W.M. de Laat, U.S. Schubert, One-step inkjet printing of conductive silver tracks on polymer substrates, Nanotechnology. 20 (2009) 165303. doi:10.1088/0957-4484/20/16/165303.

[57] A. Bar-Cohen, M. Arik, M. Ohadi, Direct liquid cooling of high flux micro and nano electronic components, Proc. IEEE. 94 (2006) 1549–1570. doi:10.1109/JPROC.2006.879791.

[58] X. Zhang, J. Wang, L. Bao, E. Dietrich, R.C.A. van der Veen, S. Peng, J. Friend, H.J.W. Zandvliet, L. Yeo, D. Lohse, Mixed mode of dissolving immersed nanodroplets at a solid–water interface, Soft Matter. 11 (2015)

1889–1900. doi:10.1039/C4SM02397H.

[59] A.K. Panwar, S.K. Barthwal, S. Ray, Effect of evaporation on the contact angle of a sessile drop on solid substrates, J. Adhes. Sci. Technol. 17 (2003) 1321–1329. doi:10.1163/156856103769172760.

[60] K.S. Birdi, D.T. Vu, A. Winter, A study of the evaporation rates of small water drops placed on a solid surface, J. Phys. Chem. 93 (1989) 3702–3703. doi:10.1021/j100346a065.

[61] H. Hu, R.G. Larson, Evaporation of a sessile droplet on a substrate, J. Phys. Chem. B. 106 (2002) 1334–1344. doi:10.1021/jp0118322.

[62] H.Y. Erbil, G. McHale, M.I. Newton, Drop evaporation on solid surfaces: Constant contact angle mode, Langmuir. 18 (2002) 2636–2641. doi:10.1021/la011470p.

[63] G. McHale, S.M. Rowan, M.I. Newton, M.K. Banerjee, Evaporation and the wetting of a low-energy solid surface, J. Phys. Chem. B. 102 (1998) 1964–1967. doi:10.1021/jp972552i.

[64] R.. Picknett, R. Bexon, The evaporation of sessile or pendant drops in still air, J. Colloid Interface Sci. 61 (1977) 336–350. doi:10.1016/0021-9797(77)90396-4.

[65] M.E.R. Shanahan, Simple theory of "Stick-Slip" wetting hysteresis, Langmuir. 11 (1995) 1041–1043. doi:10.1021/la00003a057.

[66] D. Orejon, K. Sefiane, M.E.R. Shanahan, Stick–Slip of evaporating droplets: Substrate hydrophobicity and nanoparticle concentration, Langmuir. 27 (2011) 12834–12843. doi:10.1021/la2026736.

[67] A. Askounis, PhD thesis: Surface nano-patterning using the coffee-stain effect, Univeristy of Edinburgh, 2014.

[68] W. Sempels, R. De Dier, H. Mizuno, J. Hofkens, J. Vermant, Auto-production of biosurfactants reverses the coffee ring effect in a bacterial system, Nat. Commun. 4 (2013) 1757. doi:10.1038/ncomms2746.

[69] H. Hu, R.G. Larson, Analysis of the microfluid flow in an evaporating sessile droplet, Langmuir. 21 (2005) 3963–3971. doi:10.1021/la047528s.

[70] H. Hu, R.G. Larson, Analysis of the effects of Marangoni stresses on the microflow in an evaporating sessile droplet., Langmuir. 21 (2005) 3972–3980. doi:10.1021/la0475270.

[71] C.A. Ward, F. Duan, Turbulent transition of thermocapillary flow induced by water evaporation, Phys. Rev. E. 69 (2004) 56308. doi:10.1103/PhysRevE.69.056308.

[72] J.-H. Kim, S.-B. Park, J.H. Kim, W.-C. Zin, Polymer transports inside evaporating water droplets at various substrate temperatures, J. Phys. Chem. C. 115 (2011) 15375–15383. doi:10.1021/jp202429p.

[73] Y. Zhang, Y. Qian, Z. Liu, Z. Li, D. Zang, Surface wrinkling and cracking dynamics in the drying of colloidal droplets, Eur. Phys. J. E. 37 (2014) 84. doi:10.1140/epje/i2014-14084-3.

[74] V. Dugas, J. Broutin, E. Souteyrand, Droplet evaporation study applied to DNA chip manufacturing, Langmuir. 21 (2005) 9130–9136. doi:10.1021/la050764y.

[75] J. Park, J. Moon, Control of colloidal particle deposit patterns within picoliter droplets ejected by ink-jet printing, Langmuir. 22 (2006) 3506–3513. doi:10.1021/la053450j.

[76] H. Hu, R.G. Larson, Marangoni effect reverses coffee-ring depositions, J. Phys. Chem. B. 110 (2006) 7090–7094. doi:10.1021/jp0609232.

[77] M. Majumder, C.S. Rendall, J.A. Eukel, J.Y.L. Wang, N. Behabtu, C.L. Pint, T.-Y. Liu, A.W. Orbaek, F. Mirri, J. Nam, A.R. Barron, R.H. Hauge, H.K. Schmidt, M. Pasquali, Overcoming the “coffee-stain” effect by compositional Marangoni-flow-assisted drop-drying, J. Phys. Chem. B. 116 (2012) 6536–6542. doi:10.1021/jp3009628.

[78] A.K. Thokchom, Q. Zhou, D.-J. Kim, D. Ha, T. Kim, Characterizing self-

assembly and deposition behavior of nanoparticles in inkjet-printed evaporating droplets, Sensors Actuators B Chem. 252 (2017) 1063–1070. doi:10.1016/j.snb.2017.06.045.

[79] D.M. Kuncicky, O.D. Velev, Surface-guided templating of particle assemblies inside drying sessile droplets, Langmuir. 24 (2008) 1371–1380. doi:10.1021/la702129b.

[80] J.R. Moffat, K. Sefiane, M.E.R. Shanahan, Effect of TiO2 nanoparticles on contact line stick−slip behavior of volatile drops, J. Phys. Chem. B. 113 (2009) 8860–8866. doi:10.1021/jp902062z.

[81] R. Bhardwaj, X. Fang, P. Somasundaran, D. Attinger, Self-assembly of colloidal particles from evaporating droplets: Role of DLVO interactions and proposition of a phase diagram, Langmuir. 26 (2010) 7833–7842. doi:10.1021/la9047227.

[82] T.P. Bigioni, X.-M. Lin, T.T. Nguyen, E.I. Corwin, T. a Witten, H.M. Jaeger, Kinetically driven self assembly of highly ordered nanoparticle monolayers, Nat. Mater. 5 (2006) 265–270. doi:10.1038/nmat1611.

[83] Y. Li, Q. Yang, M. Li, Y. Song, Rate-dependent interface capture beyond the coffee-ring effect, Sci. Rep. 6 (2016) 24628. doi:10.1038/srep24628.

[84] K. Uno, K. Hayashi, T. Hayashi, K. Ito, H. Kitano, Particle adsorption in evaporating droplets of polymer latex dispersions on hydrophilic and hydrophobic surfaces, Colloid Polym. Sci. 276 (1998) 810–815. doi:10.1007/s003960050314.

[85] X. Shen, C.-M. Ho, T.-S. Wong, Minimal size of coffee ring structure, J. Phys. Chem. B. 114 (2010) 5269–5274. doi:10.1021/jp912190v.

[86] H. Kim, F. Boulogne, E. Um, I. Jacobi, E. Button, H.A. Stone, Controlled uniform coating from the interplay of Marangoni flows and surface-adsorbed macromolecules, Phys. Rev. Lett. 116 (2016) 124501. doi:10.1103/PhysRevLett.116.124501.

[87] C. Seo, D. Jang, J. Chae, S. Shin, Altering the coffee-ring effect by adding a surfactant-like viscous polymer solution, Sci. Rep. 7 (2017) 500. doi:10.1038/s41598-017-00497-x.

[88] D. Orejon, PhD thesis: A study of nanosuspension droplets free evaporation and electrowetting, University of Edinburgh, 2013.

[89] K. Sefiane, On the role of structural disjoining pressure and contact line pinning in critical heat flux enhancement during boiling of nanofluids, Appl. Phys. Lett. 89 (2006) 44106. doi:10.1063/1.2222283.

[90] M. Anyfantakis, D. Baigl, Manipulating the coffee-ring effect: Interactions at work, ChemPhysChem. 16 (2015) 2726–2734. doi:10.1002/cphc.201500410.

[91] J. Wu, J. Xia, W. Lei, B. Wang, Generation of the smallest coffee-ring structures by solute crystallization reaction on a hydrophobic surface, RSC Adv. 3 (2013) 5328. doi:10.1039/c3ra40465j.

[92] J.R. Moffat, K. Sefiane, M.E.R. Shanahan, Nanofluid droplet evaporation kinetics and wetting dynamics on flat substrates, J. Nano Res. 7 (2009) 75–80. doi:10.4028/www.scientific.net/JNanoR.7.75.

[93] E. Adachi, A.S. Dimitrov, K. Nagayama, Stripe patterns formed on a glass surface during droplet evaporation, Langmuir. 11 (1995) 1057–1060. doi:10.1021/la00004a003.

[94] E. Pauliac-Vaujour, P. Moriarty, Meniscus-mediated organization of colloidal nanoparticles, J. Phys. Chem. C. 111 (2007) 16255–16260. doi:10.1021/jp074152t.

[95] E. Pauliac-Vaujour, A. Stannard, C.P. Martin, M.O. Blunt, I. Notingher, P.J. Moriarty, I. Vancea, U. Thiele, Fingering instabilities in dewetting nanofluids, Phys. Rev. Lett. 100 (2008) 176102. doi:10.1103/PhysRevLett.100.176102.

[96] I. Vancea, U. Thiele, E. Pauliac-Vaujour, A. Stannard, C.P. Martin, M.O. Blunt, P.J. Moriarty, Front instabilities in evaporatively dewetting nanofluids, Phys. Rev. E. 78 (2008) 41601. doi:10.1103/PhysRevE.78.041601.

[97] A. Crivoi, F. Duan, Evaporation-induced branched structures from sessile nanofluid droplets, J. Phys. Chem. C. 117 (2013) 7835–7843. doi:10.1021/jp312021w.

[98] R. De Dier, W. Sempels, J. Hofkens, J. Vermant, Thermocapillary fingering in surfactant-laden water droplets, Langmuir. 30 (2014) 13338–13334. doi:10.1021/la503655j.

[99] A.M. Cazabat, F. Heslot, S.M. Troian, P. Carles, Fingering instability of thin spreading films driven by temperature gradients, Nature. 346 (1990) 824–826. doi:10.1038/346824a0.

[100] F. Melo, J.F. Joanny, S. Fauve, Fingering instability of spinning drops, Phys. Rev. Lett. 63 (1989) 1958–1961. doi:10.1103/PhysRevLett.63.1958.

[101] B.D. Edmonstone, O.K. Matar, R.V. Craster, Surfactant-induced fingering phenomena in thin film flow down an inclined plane, Phys. D Nonlinear Phenom. 209 (2005) 62–79. doi:10.1016/j.physd.2005.06.014.

[102] B.M. Weon, J.H. Je, Fingering inside the coffee ring, Phys. Rev. E. 87 (2013) 13003. doi:10.1103/PhysRevE.87.013003.

[103] L. Pauchard, F. Parisse, C. Allain, Influence of salt content on crack patterns formed through colloidal suspension desiccation, Phys. Rev. E. 59 (1999) 3737–3740. doi:10.1103/PhysRevE.59.3737.

[104] C.C. Annarelli, J. Fornazero, J. Bert, J. Colombani, Crack patterns in drying protein solution drops, Eur. Phys. J. E. 5 (2001) 599–603. doi:10.1007/s101890170043.

[105] D. Mal, S. Sinha, T.R. Middya, S. Tarafdar, Desiccation crack patterns in drying laponite gel formed in an electrostatic field, Appl. Clay Sci. 39 (2008) 106–111. doi:10.1016/j.clay.2007.05.005.

[106] G. Jing, J. Ma, Formation of circular crack pattern in deposition self-assembled by drying nanoparticle suspension, J. Phys. Chem. B. 116 (2012) 6225–6231. doi:10.1021/jp301872r.

[107] B. Sobac, D. Brutin, Desiccation of a sessile drop of blood: Cracks, folds formation and delamination, Colloids Surfaces A Physicochem. Eng. Asp. 448 (2014) 34–44. doi:10.1016/j.colsurfa.2014.01.076.

[108] V.R. Dugyala, H. Lama, D.K. Satapathy, M.G. Basavaraj, Role of particle shape anisotropy on crack formation in drying of colloidal suspension, Sci. Rep. 6 (2016) 30708. doi:10.1038/srep30708.

[109] L. Bahmani, M. Neysari, M. Maleki, The study of drying and pattern formation of whole human blood drops and the effect of thalassaemia and neonatal jaundice on the patterns, Colloids Surfaces A Physicochem. Eng. Asp. 513 (2017) 66–75. doi:10.1016/j.colsurfa.2016.10.065.

[110] Y.Y. Tarasevich, I.V. Vodolazskaya, O.P. Bondarenko, Modeling of spatial–temporal distribution of the components in the drying sessile droplet of biological fluid, Colloids Surfaces A Physicochem. Eng. Asp. 432 (2013) 99–103. doi:10.1016/j.colsurfa.2013.04.069.

[111] T.A. Yakhno, V.G. Yakhno, A.G. Sanin, O.A. Sanina, A.S. Pelyushenko, N.A. Egorova, I.G. Terentiev, S.V. Smetanina, O.V. Korochkina, E.V. Yashukova, The informative-capacity phenomenon of drying drops, IEEE Eng. Med. Biol. Mag. 24 (2005) 96–104. doi:10.1109/MEMB.2005.1411354.

[112] G. Chen, G. J. Mohamed, Complex protein patterns formation via salt-induced self-assembly and droplet evaporation, Eur. Phys. J. E. 33 (2010) 19–26. doi:10.1140/epje/i2010-10649-4.

[113] D. Kaya, V.A. Belyi, M. Muthukumar, Pattern formation in drying droplets of polyelectrolyte and salt, J. Chem. Phys. 133 (2010) 114905. doi:10.1063/1.3493687.

[114] T.A. Yakhno, V. V. Kazakov, O.A. Sanina, A.G. Sanin, V.G. Yakhno, Drops of biological fluids drying on a hard substrate: Variation of the morphology, weight, temperature, and mechanical properties, Tech. Phys. 55 (2010) 929–935. doi:10.1134/S1063784210070030.

[115] Y.Y. Tarasevich, A.K. Ayupova, Effect of diffusion on the separation of

components in a biological fluid upon wedge-shaped dehydration, Tech. Phys. 48 (2003) 535–540. doi:10.1134/1.1576463.

[116] M.E. Buzoverya, Y.P. Shcherbak, I. V. Shishpor, Experimental investigation of the serum albumin fascia microstructure, Tech. Phys. 57 (2012) 1270–1276. doi:10.1134/S1063784212090071.

[117] T.A. Yakhno, Complex pattern formation in sessile droplets of protein-salt solutions with low protein content. What substance fabricates these patterns?, Phys. Chem. 1 (2012) 10–13. doi:10.5923/j.pc.20110101.02.

[118] T.A. Yakhno, Sodium chloride crystallization from drying drops of albumin–salt solutions with different albumin concentrations, Tech. Phys. 60 (2015) 1601–1608. doi:10.1134/S1063784215110262.

[119] X. Zhong, J. Ren, F. Duan, Wettability effect on evaporation dynamics and crystalline patterns of sessile saline droplets, J. Phys. Chem. B. 121 (2017) 7924–7933. doi:10.1021/acs.jpcb.7b03690.

[120] A. Crivoi, F. Duan, Fingering structures inside the coffee-ring pattern, Colloids Surfaces A Physicochem. Eng. Asp. 432 (2013) 119–126. doi:10.1016/j.colsurfa.2013.04.051.

[121] Y.-F. Li, Y.-J. Sheng, H.-K. Tsao, Evaporation stains: suppressing the coffee-ring effect by contact angle hysteresis, Langmuir. 29 (2013) 7802–7811. doi:10.1021/la400948e.

[122] T.A.H. Nguyen, M.A. Hampton, A. V Nguyen, Evaporation of nanoparticle droplets on smooth hydrophobic surfaces: The inner coffee ring deposits, J. Phys. Chem. C. 117 (2013) 4707–4716. doi:10.1021/jp3126939.

[123] M.E. Buzoverya, Y.P. Shcherbak, I. V Shishpor, Quantitative estimation of the microstructural inhomogeneity of biological fluid facies, Tech. Phys. 59 (2014) 1550–1555. doi:10.1134/S1063784214100119.

[124] J. Fukai, H. Ishizuka, Y. Sakai, M. Kaneda, M. Morita, A. Takahara, Effects of droplet size and solute concentration on drying process of polymer solution

droplets deposited on homogeneous surfaces, Int. J. Heat Mass Transf. 49 (2006) 3561–3567. doi:10.1016/j.ijheatmasstransfer.2006.02.049.

[125] H.H. Lee, S.C. Fu, C.Y. Tso, C.Y.H. Chao, Study of residue patterns of aqueous nanofluid droplets with different particle sizes and concentrations on different substrates, Int. J. Heat Mass Transf. 105 (2017) 230–236. doi:10.1016/j.ijheatmasstransfer.2016.09.093.

[126] J.C. Loudet, A.M. Alsayed, J. Zhang, A.G. Yodh, Capillary interactions between anisotropic colloidal particles, Phys. Rev. Lett. 94 (2005) 18301. doi:10.1103/PhysRevLett.94.018301.

[127] J.C. Loudet, A.G. Yodh, B. Pouligny, Wetting and contact lines of micrometer-sized ellipsoids, Phys. Rev. Lett. 97 (2006) 18304. doi:10.1103/PhysRevLett.97.018304.

[128] N. Bowden, F. Arias, T. Deng, G.M. Whitesides, Self-assembly of microscale objects at a liquid/liquid interface through lateral capillary forces, Langmuir. 17 (2001) 1757–1765. doi:10.1021/la001447o.

[129] A.B.D. Brown, C.G. Smith, A.R. Rennie, Fabricating colloidal particles with photolithography and their interactions at an air-water interface, Phys. Rev. E. 62 (2000) 951–960. doi:10.1103/PhysRevE.62.951.

[130] B. Madivala, S. Vandebril, J. Fransaer, J. Vermant, Exploiting particle shape in solid stabilized emulsions, Soft Matter. 5 (2009) 1717. doi:10.1039/b816680c.

[131] B. Madivala, J. Fransaer, J. Vermant, Self-assembly and rheology of ellipsoidal particles at interfaces, Langmuir. 25 (2009) 2718–2728. doi:10.1021/la803554u.

[132] B.J. Park, E.M. Furst, Attractive interactions between colloids at the oil–water interface, Soft Matter. 7 (2011) 7676. doi:10.1039/c1sm00005e.

[133] J.-B. Fournier, P. Galatola, Anisotropic capillary interactions and jamming of colloidal particles trapped at a liquid-fluid interface, Phys. Rev. E. 65 (2002)

31601. doi:10.1103/PhysRevE.65.031601.

[134] P.J. Yunker, T. Still, M.A. Lohr, A.G. Yodh, Suppression of the coffee-ring effect by shape-dependent capillary interactions, Nature. 476 (2011) 308–311. doi:10.1038/nature10344.

[135] V.R. Dugyala, M.G. Basavaraj, Control over coffee-ring formation in evaporating liquid drops containing ellipsoids, Langmuir. 30 (2014) 8680–8686. doi:10.1021/la500803h.

[136] Y. Choi, J. Han, C. Kim, Pattern formation in drying of particle-laden sessile drops of polymer solutions on solid substrates, Korean J. Chem. Eng. 28 (2011) 2130–2136. doi:10.1007/s11814-011-0084-7.

[137] S. Ryu, J.Y. Kim, S.Y. Kim, B.M. Weon, Drying-mediated patterns in colloid-polymer suspensions, Sci. Rep. 7 (2017) 1–7. doi:10.1038/s41598-017-00932-z.

[138] A.P. Sommer, M. Ben-Moshe, S. Magdassi, Size-discriminative self-assembly of nanospheres in evaporating drops, J. Phys. Chem. B. 108 (2004) 8–10. doi:10.1021/jp0363747.

[139] J.-Y. Jung, Y.W. Kim, J.Y. Yoo, Behavior of particles in an evaporating didisperse colloid droplet on a hydrophilic surface, Anal. Chem. 81 (2009) 8256–8259. doi:10.1021/ac901247c.

[140] T.S. Wong, T.H. Chen, X. Shen, C.M. Ho, Nanochromatography driven by the coffee ring effect, Anal. Chem. 83 (2011) 1871–1873. doi:10.1021/ac102963x.

[141] X. Zhong, H. Xie, F. Duan, Deposition patterns from evaporating sessile droplets with suspended mixtures of multi-sized and multi-species hydrophilic and non-adsorbing nanoparticles, Appl. Therm. Eng. 111 (2017) 1565–1572. doi:10.1016/j.applthermaleng.2016.08.040.

[142] V.H. Chhasatia, A.S. Joshi, Y. Sun, Effect of relative humidity on contact angle and particle deposition morphology of an evaporating colloidal drop,

Appl. Phys. Lett. 97 (2010) 231909. doi:10.1063/1.3525167.

[143] N.D. Patil, P.G. Bange, R. Bhardwaj, A. Sharma, Effects of substrate heating and wettability on evaporation dynamics and deposition patterns for a sessile water droplet containing colloidal particles, Langmuir. 32 (2016) 11958–11972. doi:10.1021/acs.langmuir.6b02769.

[144] V.H. Chhasatia, Y. Sun, Interaction of bi-dispersed particles with contact line in an evaporating colloidal drop, Soft Matter. 7 (2011) 10135–10143. doi:10.1039/C1SM06393F.

[145] H. Jeong, J. van Tiem, Y.B. Gianchandani, J. Park, Nano-particle separation using Marangoni flow in evaporating droplets, in: Solid-State Sensors, Actuators Microsystems Work., Hilton Head Island, 2014: pp. 223–226. http://wims2.org/publications/papers/nano-particle_j-park.pdf.

[146] Y.-C. Hu, Q. Zhou, H.-M. Ye, Y.-F. Wang, L.-S. Cui, Peculiar surface profile of poly(ethylene oxide) film with ring-like nucleation distribution induced by Marangoni flow effect, Colloids Surfaces A Physicochem. Eng. Asp. 428 (2013) 39–46. doi:10.1016/j.colsurfa.2013.03.035.

[147] A. Crivoi, F. Duan, Effect of surfactant on the drying patterns of graphite nanofluid droplets, J. Phys. Chem. B. 117 (2013) 5932–5938. doi:10.1021/jp401751z.

[148] A. Crivoi, F. Duan, Amplifying and attenuating the coffee-ring effect in drying sessile nanofluid droplets, Phys. Rev. E. 87 (2013) 42303. doi:10.1103/PhysRevE.87.042303.

[149] E.L. Talbot, A. Berson, P.S. Brown, C.D. Bain, Drying and deposition of picolitre droplets of colloidal suspensions in binary solvent mixtures, in: NIP28 28th Int. Conf. Digit. Print. Technol. Digit. Fabr., Quebec, 2012: pp. 420–423. http://www.dspace.cam.ac.uk/handle/1810/243374.

[150] H.B. Eral, D.M. Augustine, M.H.G. Duits, F. Mugele, Suppressing the coffee stain effect: how to control colloidal self-assembly in evaporating drops using electrowetting, Soft Matter. 7 (2011) 4954. doi:10.1039/c1sm05183k.

[151] D. Orejon, K. Sefiane, M.E.R. Shanahan, Evaporation of nanofluid droplets with applied DC potential, J. Colloid Interface Sci. 407 (2013) 29–38. doi:10.1016/j.jcis.2013.05.079.

[152] B. Sobac, D. Brutin, Thermal effects of the substrate on water droplet evaporation, Phys. Rev. E. 86 (2012) 21602. doi:10.1103/PhysRevE.86.021602.

[153] B.J. Fischer, Particle convection in an evaporating colloidal droplet, Langmuir. 18 (2002) 60–67. doi:10.1021/la015518a.

[154] D. Frenkel, Playing tricks with designer “atoms”, Science. 296 (2002) 65–66. doi:10.1126/science.1070865.

[155] J.P. Hartfield, P. V. Farrell, Droplet vaporization in a high-pressure gas, J. Heat Transfer. 115 (1993) 699. doi:10.1115/1.2910741.

[156] L. Zhang, Y. Nguyen, W. Chen, “Coffee ring” formation dynamics on molecularly smooth substrates with varying receding contact angles, Colloids Surfaces A Physicochem. Eng. Asp. 449 (2014) 42–50. doi:10.1016/j.colsurfa.2014.02.043.

[157] T. Heim, S. Preuss, B. Gerstmayer, A. Bosio, R. Blossey, Deposition from a drop: morphologies of unspecifically bound DNA, J. Phys. Condens. Matter. 17 (2005) S703–S716. doi:10.1088/0953-8984/17/9/025.

[158] D. Wang, S. Liu, B.J. Trummer, C. Deng, A. Wang, Carbohydrate microarrays for the recognition of cross-reactive molecular markers of microbes and host cells., Nat. Biotechnol. 20 (2002) 275–81. doi:10.1038/nbt0302-275.

[159] G.T. Carroll, D. Wang, N.J. Turro, J.T. Koberstein, Photochemical micropatterning of carbohydrates on a surface, Langmuir. 22 (2006) 2899–2905. doi:10.1021/la0531042.

[160] I. Smalyukh, O. Zribi, J. Butler, O. Lavrentovich, G. Wong, Structure and dynamics of liquid crystalline pattern formation in drying droplets of DNA, Phys. Rev. Lett. 96 (2006) 177801. doi:10.1103/PhysRevLett.96.177801.

[161] R. Blossey, A. Bosio, Contact line deposits on cDNA microarrays: A “twin-spot effect,” Langmuir. 18 (2002) 2952–2954. doi:10.1021/la0114732.

[162] R.G. Larson, T.T. Perkins, D.E. Smith, S. Chu, Hydrodynamics of a DNA molecule in a flow field, Phys. Rev. E. 55 (1997) 1794–1797. doi:10.1103/PhysRevE.55.1794.

[163] J. Jing, J. Reed, J. Huang, X. Hu, V. Clarke, J. Edington, D. Housman, T.S. Anantharaman, E.J. Huff, B. Mishra, B. Porter, A. Shenker, E. Wolfson, C. Hiort, R. Kantor, C. Aston, D.C. Schwartz, Automated high resolution optical mapping using arrayed, fluid-fixed DNA molecules, Proc. Natl. Acad. Sci. 95 (1998) 8046–8051. doi:10.1073/pnas.95.14.8046.

[164] B. Sobac, D. Brutin, Structural and evaporative evolutions in desiccating sessile drops of blood, Phys. Rev. E. 84 (2011) 11603. doi:10.1103/PhysRevE.84.011603.

[165] D. Kim, S. Jeong, B.K. Park, J. Moon, Direct writing of silver conductive patterns: Improvement of film morphology and conductance by controlling solvent compositions, Appl. Phys. Lett. 89 (2006) 264101. doi:10.1063/1.2424671.

[166] D.J. Norris, E.G. Arlinghaus, L. Meng, R. Heiny, L.E. Scriven, Opaline photonic crystals: How does self-assembly work?, Adv. Mater. 16 (2004) 1393–1399. doi:10.1002/adma.200400455.

[167] N.D. Denkov, O.D. Velev, P.A. Kralchevsky, I.B. Ivanov, H. Yoshimura, K. Nagayama, Two-dimensional crystallization, Nature. 361 (1993) 26–26. doi:10.1038/361026a0.

[168] Y. Hamamoto, J.R.E. Christy, K. Sefiane, Order-of-magnitude increase in flow velocity driven by mass conservation during the evaporation of sessile drops, Phys. Rev. E. 83 (2011) 51602. doi:10.1103/PhysRevE.83.051602.

[169] N. Zhang, W.-J. Yang, Natural convection in evaporating minute drops, J. Heat Transfer. 104 (1982) 656–662. doi:10.1115/1.3245182.

[170] W. Ristenpart, P. Kim, C. Domingues, J. Wan, H. Stone, Influence of substrate conductivity on circulation reversal in evaporating drops, Phys. Rev. Lett. 99 (2007) 234502. doi:10.1103/PhysRevLett.99.234502.

[171] C. Buffone, K. Sefiane, Investigation of thermocapillary convective patterns and their role in the enhancement of evaporation from pores, Int. J. Multiph. Flow. 30 (2004) 1071–1091. doi:10.1016/j.ijmultiphaseflow.2004.05.010.

[172] C. Buffone, K. Sefiane, J.R.E. Christy, Experimental investigation of self-induced thermocapillary convection for an evaporating meniscus in capillary tubes using micro–particle image velocimetry, Phys. Fluids. 17 (2005) 52104. doi:10.1063/1.1901688.

[173] C. Buffone, K. Sefiane, IR measurements of interfacial temperature during phase change in a confined environment, Exp. Therm. Fluid Sci. 29 (2004) 65–74. doi:10.1016/j.expthermflusci.2004.02.004.

[174] V. Nguyen, K. Stebe, Patterning of small particles by a surfactant-enhanced Marangoni-Bénard instability, Phys. Rev. Lett. 88 (2002) 164501. doi:10.1103/PhysRevLett.88.164501.

[175] V.N. Truskett, K.J. Stebe, Influence of surfactants on an evaporating drop: Fluorescence images and particle deposition patterns, Langmuir. 19 (2003) 8271–8279. doi:10.1021/la030049t.

[176] T. Kajiya, W. Kobayashi, T. Okuzono, M. Doi, Controlling the drying and film formation processes of polymer solution droplets with addition of small amount of surfactants, J. Phys. Chem. B. 113 (2009) 15460–15466. doi:10.1021/jp9077757.

[177] X. Xu, J. Luo, Marangoni flow in an evaporating water droplet, Appl. Phys. Lett. 91 (2007) 124102. doi:10.1063/1.2789402.

[178] X. Xu, L. Ma, D. Huang, J. Luo, D. Guo, Linear growth of colloidal rings at the edge of drying droplets, Colloids Surfaces A Physicochem. Eng. Asp. 447 (2014) 28–31. doi:10.1016/j.colsurfa.2014.01.068.

[179] J.R.A. Pearson, On convection cells induced by surface tension, J. Fluid Mech. 4 (2006) 489–500. doi:10.1017/S0022112058000616.

[180] G.M. Faeth, Evaporation and combustion of sprays, Prog. Energy Combust. Sci. 9 (1983) 1–76. doi:10.1016/0360-1285(83)90005-9.

[181] H.Y. Erbil, Evaporation of pure liquid sessile and spherical suspended drops: a review., Adv. Colloid Interface Sci. 170 (2012) 67–86. doi:10.1016/j.cis.2011.12.006.

[182] N.M. Kovalchuk, A. Trybala, V.M. Starov, Evaporation of sessile droplets, Curr. Opin. Colloid Interface Sci. 19 (2014) 336–342. doi:10.1016/j.cocis.2014.07.005.

[183] M. Maillard, L. Motte, M.-P. Pileni, Rings and hexagons made of nanocrystals, Adv. Mater. 13 (2001) 200–204. doi:10.1002/1521-4095(200102)13:3<200::AID-ADMA200>3.0.CO;2-P.

[184] X. Zhong, F. Duan, Disk to dual ring deposition transformation in evaporating nanofluid droplets from substrate cooling to heating, Phys. Chem. Chem. Phys. 18 (2016) 20664–20671. doi:10.1039/C6CP03231A.

[185] X. Zhong, C. Wu, F. Duan, From enhancement to elimination of dual-ring pattern of nanoparticles from sessile droplets by heating the substrate, Appl. Therm. Eng. 115 (2017) 1418–1423. doi:10.1016/j.applthermaleng.2016.11.002.

[186] S.M. Rowan, M.I. Newton, F.W. Driewer, G. McHale, Evaporation of microdroplets of azeotropic liquids, J. Phys. Chem. B. 104 (2000) 8217–8220. doi:10.1021/jp000938e.

[187] K. Sefiane, S. David, M.E.R. Shanahan, Wetting and evaporation of binary mixture drops, J. Phys. Chem. B. 112 (2008) 11317–11323. doi:10.1021/jp8030418.

[188] K. Sefiane, L. Tadrist, M. Douglas, Experimental study of evaporating water–ethanol mixture sessile drop: influence of concentration, Int. J. Heat Mass

Transf. 46 (2003) 4527–4534. doi:10.1016/S0017-9310(03)00267-9.

[189] A.K.H. Cheng, D.M. Soolaman, H.-Z. Yu, Evaporation of microdroplets of ethanol-water mixtures on gold surfaces modified with self-assembled monolayers., J. Phys. Chem. B. 110 (2006) 11267–11271. doi:10.1021/jp0572885.

[190] C. Liu, E. Bonaccurso, H.-J. Butt, Evaporation of sessile water/ethanol drops in a controlled environment., Phys. Chem. Chem. Phys. 10 (2008) 7150–7157. doi:10.1039/b808258h.

[191] J.R.E. Christy, K. Sefiane, E. Munro, A study of the velocity field during evaporation of sessile water and water/ethanol drops, J. Bionic Eng. 7 (2010) 321–328. doi:10.1016/S1672-6529(10)60263-6.

[192] J.R.E. Christy, Y. Hamamoto, K. Sefiane, Flow transition within an evaporating binary mixture sessile drop, Phys. Rev. Lett. 106 (2011) 205701. doi:10.1103/PhysRevLett.106.205701.

[193] X. Zhong, F. Duan, Flow regime and deposition pattern of evaporating binary mixture droplet suspended with particles, Eur. Phys. J. E. 39 (2016) 18. doi:10.1140/epje/i2016-16018-5.

[194] R. Vochten, G. Petre, Study of the heat of reversible adsorption at the air-solution interface. II. Experimental determination of the heat of reversible adsorption of some alcohols, J. Colloid Interface Sci. 42 (1973) 320–327. doi:10.1016/0021-9797(73)90295-6.

[195] G. Petre, M.A. Azouni, Experimental evidence for the minimum of surface tension with temperature at aqueous alcohol solution/air interfaces, J. Colloid Interface Sci. 98 (1984) 261–263. doi:10.1016/0021-9797(84)90503-4.

[196] M.C. Limbourg-Fontaine, G. Petre, J.C. Legros, Thermocapillary movements under microgravity at a minimum of surface tension, Naturwissenschaften. 73 (1986) 360–362. doi:10.1007/BF00367265.

[197] Y. Abe, A. Iwasaki, Microgravity experiments on dual vapor bubbles of self-

wetting fluid, in: AIP Conf. Proc., AIP, 2002: pp. 189–196. doi:10.1063/1.1449724.

[198] Y. Abe, K. Tanaka, M. Nakagawa, N. di Francescantonio, R. Savino, A. Iwasaki, Flexible wickless heat pipes radiator with self-rewetting fluids, in: 9th AIAA/ASME Jt. Thermophys. Heat Transf. Conf., American Institute of Aeronautics and Astronautics, Reston, Virigina, 2006: pp. 2006–3105. doi:10.2514/6.2006-3105.

[199] R. Savino, A. Cecere, R. Di Paola, Surface tension-driven flow in wickless heat pipes with self-rewetting fluids, Int. J. Heat Fluid Flow. 30 (2009) 380–388. doi:10.1016/j.ijheatfluidflow.2009.01.009.

[200] R. Savino, R. Di Paola, A. Cecere, R. Fortezza, Self-rewetting heat transfer fluids and nanobrines for space heat pipes, Acta Astronaut. 67 (2010) 1030–1037. doi:10.1016/j.actaastro.2010.06.034.

[201] R. Savino, A. Cecere, S. Van Vaerenbergh, Y. Abe, G. Pizzirusso, W. Tsevecos, M. Mojahed, Q. Galand, Some experimental progresses in the study of self-rewetting fluids for the SELENE experiment to be carried in the Thermal Platform 1 hardware, Acta Astronaut. 89 (2013) 179–188. doi:10.1016/j.actaastro.2013.03.020.

[202] R. Di Paola, R. Savino, D.M. Gattia, R. Marazzi, M.V. Antisari, Self-rewetting carbon nanofluid as working fluid for space and terrestrial heat pipes, J. Nanoparticle Res. 13 (2011) 6207–6216. doi:10.1007/s11051-011-0601-y.

[203] M. Sato, Y. Abe, Y. Urita, R. Di Paola, A. Cecere, R. Savino, Thermal performance of self-rewetting fluid heat pipe containing dilute solutions of polymer-capped silver nanoparticles synthesized by microwave-polyol process., in: Proc. 6th Interdiscip. Transp. Phenom. VI Fluid Therm. Biol. Mater. Sp. Sci., Volterra, Italy, 2009. https://www.iris.unina.it/handle/11588/352451?mode=full.22#.WNpStjuGNPY.

[204] X. Su, M. Zhang, W. Han, X. Guo, Enhancement of heat transport in oscillating heat pipe with ternary fluid, Int. J. Heat Mass Transf. 87 (2015) 258–264. doi:10.1016/j.ijheatmasstransfer.2015.04.002.

[205] X. Su, M. Zhang, W. Han, X. Guo, Experimental study on the heat transfer performance of an oscillating heat pipe with self-rewetting nanofluid, Int. J. Heat Mass Transf. 100 (2016) 378–385. doi:10.1016/j.ijheatmasstransfer.2016.04.094.

[206] R. Bennacer, K. Sefiane, Vortices, dissipation and flow transition in volatile binary drops, J. Fluid Mech. 749 (2014) 649–665. doi:10.1017/jfm.2014.220.

[207] M. Parsa, S. Harmand, K. Sefiane, M. Bigerelle, R. Deltombe, Effect of substrate temperature on pattern formation of bidispersed particles from volatile drops, J. Phys. Chem. B. 121 (2017) 11002–11017. doi:10.1021/acs.jpcb.7b09700.

[208] A.D. Bermel, D.E. Bugner, Particle size effects in pigmented ink jet inks, J. Imaging Sci. Technol. 43 (1999) 320–324. doi:10.1023/A:1010029021882.

[209] E. Sowade, T. Blaudeck, R.R. Baumann, Inkjet printing of colloidal nanospheres: Engineering the evaporation-driven self-assembly process to form defined layer morphologies, Nanoscale Res. Lett. 10 (2015) 362. doi:10.1186/s11671-015-1065-2.

[210] D.J. Harris, H. Hu, J.C. Conrad, J.A. Lewis, Patterning colloidal films via evaporative lithography, Phys. Rev. Lett. 98 (2007) 148301. doi:10.1103/PhysRevLett.98.148301.

[211] Y. Xia, B. Gates, Z.-Y. Li, Self-assembly approaches to three-dimensional photonic crystals, Adv. Mater. 13 (2001) 409–413. doi:10.1002/1521-4095(200103)13:6<409::AID-ADMA409>3.0.CO;2-C.

[212] J. Huang, F. Kim, A.R. Tao, S. Connor, P. Yang, Spontaneous formation of nanoparticle stripe patterns through dewetting, Nat. Mater. 4 (2005) 896–900. doi:10.1038/nmat1517.

[213] J.Y. Jung, H.Y. Kwak, Separation of microparticles and biological cells inside an evaporating droplet using dielectrophoresis, Anal. Chem. 79 (2007) 5087–5092. doi:10.1021/ac0702903.

[214] R.M. Erb, H.S. Son, B. Samanta, V.M. Rotello, B.B. Yellen, Magnetic assembly of colloidal superstructures with multipole symmetry., Nature. 457 (2009) 999–1002. doi:10.1038/nature07766.

[215] A.S. Sangani, C. Lu, K. Su, J.A. Schwarz, Capillary force on particles near a drop edge resting on a substrate and a criterion for contact line pinning, Phys. Rev. E. 80 (2009) 11603. doi:10.1103/PhysRevE.80.011603.

[216] B.M. Weon, J.H. Je, Capillary force repels coffee-ring effect, Phys. Rev. E. 82 (2010) 15305. doi:10.1103/PhysRevE.82.015305.

[217] C. Monteux, F. Lequeux, Packing and sorting colloids at the contact line of a drying drop, Langmuir. 27 (2011) 2917–2922. doi:10.1021/la104055j.

[218] N.R. Devlin, K. Loehr, M.T. Harris, The importance of gravity in droplet evaporation: A comparison of pendant and sessile drop evaporation with particles, AIChE J. 62 (2016) 947–955. doi:10.1002/aic.15120.

[219] N.R. Devlin, K. Loehr, M.T. Harris, The separation of two different sized particles in an evaporating droplet, AIChE J. 61 (2015) 3547–3556. doi:10.1002/aic.14977.

[220] W. Han, M. Byun, Z. Lin, Assembling and positioning latex nanoparticles via controlled evaporative self-assembly, J. Mater. Chem. 21 (2011) 16968. doi:10.1039/c1jm11603g.

[221] E. Hendarto, Y.B. Gianchandani, Size sorting of floating spheres based on Marangoni forces in evaporating droplets, J. Micromechanics Microengineering. 23 (2013) 75016. doi:10.1088/0960-1317/23/7/075016.

[222] Á.G. Marín, H. Gelderblom, D. Lohse, J.H. Snoeijer, Order-to-disorder transition in ring-shaped colloidal stains, Phys. Rev. Lett. 107 (2011) 85502. doi:10.1103/PhysRevLett.107.085502.

[223] Á.G. Marín, H. Gelderblom, D. Lohse, J.H. Snoeijer, Rush-hour in evaporating coffee drops, Phys. Fluids. 23 (2011) 91111. doi:10.1063/1.3640018.

[224] P.A. Kralchevsky, N.D. Denkov, Capillary forces and structuring in layers of colloid particles, Curr. Opin. Colloid Interface Sci. 6 (2001) 383–401. doi:10.1016/S1359-0294(01)00105-4.

[225] R. Di Leonardo, F. Saglimbeni, G. Ruocco, Very-long-range nature of capillary interactions in liquid films, Phys. Rev. Lett. 100 (2008) 106103. doi:10.1103/PhysRevLett.100.106103.

[226] A. Askounis, K. Sefiane, V. Koutsos, M.E.R. Shanahan, Effect of particle geometry on triple line motion of nano-fluid drops and deposit nano-structuring, Adv. Colloid Interface Sci. 222 (2015) 44–57. doi:10.1016/j.cis.2014.05.003.

[227] Y. Li, C. Lv, Z. Li, D. Quéré, Q. Zheng, From coffee rings to coffee eyes, Soft Matter. 11 (2015) 4669–4673. doi:10.1039/C5SM00654F.

[228] P. Chen, M. Toubal, J. Carlier, S. Harmand, B. Nongaillard, M. Bigerelle, Evaporation of binary sessile drops: Infrared and acoustic methods to track alcohol concentration at the interface and on the surface, Langmuir. 32 (2016) 9836–9845. doi:10.1021/acs.langmuir.6b02564.

Résumé: L'évaporation de gouttes de liquides contenant des particules non volatiles représente un phénomène largement présent dans la vie quotidienne, à l'image des traces laissées par le marc de café après séchage. L'étude de la morphologie des dépôts de particules présente un grand intérêt dans les domaines de la biologie et trouve de nombreuses applications dans l'industrie. De ce fait, elle a fait l'objet de nombreuses recherches durant les dernières décennies. Malgré les nombreuses récentes recherches sur les morphologies des dépôts de particules, les mécanismes les contrôlant restent encore non complétement expliqués. Certains facteurs influençant les morphologies des dépôts sont nombreux (température de substrats…) mais restent encore peu documentés dans la littérature. Cette étude expérimentale s'intéresse à l'influence de la température du substrat sur la morphologie des dépôts de nanoparticules après séchage de gouttes sessiles de liquides. L'augmentation de la température du substrat accélère le processus d'évaporation et entraine des morphologies de dépôts très différentes de celles obtenues sur des substrats à température ambiante. Dans cette étude, la microscopie combinée à la thermographie infrarouge et à l'interférométrie ont permis d'expliquer la dynamique de formation de dépôts. De plus, l'étude a permis d'analyser les effets d'autres paramètres sur la morphologie des dépôts, tel que la composition chimique du liquide composant les gouttes.

Mots clés: Goutte Sessile, Mouillage, Évaporation, Nanofluides, Effet Thermocapillaire, Effet Marangoni, Dépôt de Nanoparticules, Morphologie de Dépôt.

Abstract: Evaporation of liquid droplets containing non-volatile solutes is an omnipresent phenomenon in daily life, e.g., coffee stains on solid surfaces. The study of pattern formation of the particles left after the evaporation of a sessile droplet has attracted the attention of many researchers during the past two decades due to the wide range of biological and industrial applications. Despite the significance of controlling the deposition morphology of droplets, the underlying mechanisms involved in pattern formation are not yet fully understood. There is a varied range of factors that affect the final deposition patterns and some, e.g., substrate temperature, are poorly studied in the literature. This experimental study investigates the effect of a wide range of substrate temperatures on the deposition patterns of nanoparticles from drying sessile droplets. Increasing substrate temperature and accelerating the drying process lead to the formation of the patterns not observed on non-heated substrates. This research elucidates the formation mechanisms of these patterns by optical microscopy, infrared thermography, and white light interferometry techniques. Furthermore, the combined effects of substrate temperature and other factors such as chemical composition of base fluid and particle size on the dried patterns are studied. The underlying mechanisms involved in the formation of the patterns influenced by the combined factors are also discussed and presented.

Keywords: Sessile Droplet, Wetting, Evaporation, Nanofluids, Thermocapillary Effect, Marangoni Effect, Deposition of Nanoparticles, Pattern Formation.